The Cool State of Water

Infrared Insights into Ice

Wilbert J. Smit

The Cool State of Water

Wilbert J. Smit

The Cool State of Water
Infrared Insights into Ice

The Cool State of Water

Infrared Insights into Ice

ACADEMISCH PROEFSCHRIFT

ter verkrijging van de graad van doctor
aan de Universiteit van Amsterdam
op gezag van de Rector Magnificus
prof. dr. ir. K. I. J. Maex
ten overstaan van een door het College voor Promoties
ingestelde commissie,
in het openbaar te verdedigen in de Agnietenkapel
op donderdag 24 november 2016, te 14:00 uur

door

Wilbert Johannes Smit

geboren te Amsterdam

Promotiecommissie

Promotor:	prof. dr. H. J. Bakker	(Universiteit van Amsterdam)
Copromotor:	prof. dr. M. Bonn	(Universiteit van Amsterdam)
Overige leden:	prof. dr. D. Bonn	(Universiteit van Amsterdam)
	prof. dr. J. W. M. Frenken	(Universiteit van Amsterdam)
	prof. dr. A. F. Koenderink	(Universiteit van Amsterdam)
	dr. Y. L. A. Rezus	(AMOLF)
	prof. dr. S. Roke	(EPFL)
	prof. dr. S. Woutersen	(Universiteit van Amsterdam)

Faculteit der Natuurwetenschappen, Wiskunde en Informatica

On the cover: Hendrick Avercamp, *Winterlandschap met schaatsers*, circa 1608, Rijksmuseum, Amsterdam

ISBN 978-94-92323-07-1

The work described in this thesis was performed at the FOM Institute AMOLF, Science Park 104, 1098 XG Amsterdam, The Netherlands. This work is part of the research programme of the Foundation for Fundamental Research on Matter (FOM), which is financially supported by the Netherlands Organization for Scientific Research (NWO).

"It's the largest diamond in the world."
"No," the gypsy countered. "It's ice."

— Gabriel García Márquez, *One Hundred Years of Solitude*, 1967

Publications covered in this thesis

W. J. Smit, H. J. Bakker, Anomalous temperature dependence of the vibrational lifetime of the OD stretch vibration in ice and liquid water, *J. Chem. Phys.* **139**(20), 204504, 2013, DOI:10.1063/1.4833596 – *Chapter 4*

W. J. Smit, H. J. Bakker, Vibrational energy relaxation of water molecules in a hydrated lithium nitrate crystal, *J. Phys. Chem. C* **120**(20), 11078–11084, 2016, DOI:10.1021/acs.jpcc.6b01128 – *Chapter 5*

W. J. Smit, M. A. Sánchez, E. H. G. Backus, M. Bonn, H. J. Bakker, Probing the molecular surface structure of ice with phase-sensitive sum-frequency generation spectroscopy, *in preparation – Chapter 6*

W. J. Smit, M. A. Sánchez, E. H. G. Backus, M. Bonn, H. J. Bakker, Observation of liquid water at the surface of ice at temperatures far below the melting point, *in preparation – Chapter 7*

W. J. Smit, J. Versluis, M. A. Sánchez, E. H. G. Backus, M. Bonn, H. J. Bakker, Resonant intermolecular coupling at the surfaces of liquid water and ice, *in preparation – Chapter 8*

W. J. Smit, N. Smolentsev, J. Versluis, S. Roke, H. J. Bakker, Freezing effects of oil-in-water emulsions studied by sum-frequency scattering spectroscopy, *J. Chem. Phys.* **145**(4), 044706, 2016, DOI:10.1063/1.4959128 – *Chapter 9*

N. Smolentsev, W. J. Smit, S. Roke, H. J. Bakker, The interfacial structure of water droplets, *submitted – Chapter 10*

Other publications by the same author

D. Müller, W. J. Smit, M. Sigrist, Resonant scattering induced thermopower in one-dimensional disordered systems, *Phys. Rev. B.* **91**(20), 205401, 2015, DOI:10.1103/PhysRevB.91.205401

M. A. Sánchez, T. Kling, T. Ishiyama, M.-J. van Zadel, P. J. Bisson, M. Mezger, M. N. Jochum, J. D. Cyran, W. J. Smit, H. J. Bakker, M. J. Shultz, A. Morita, D. Donadio, Y. Nagata, M. Bonn, E. H. G. Backus, Experimental evidence for bilayer-by-bilayer surface melting of crystalline ice, *submitted to Proc. Natl. Acad. Sci. USA*

W. J. Smit, E. P. van Dam, R. Cota, H. J. Bakker, Caffeine and taurine make water fall asleep, *submitted*

Contents

1 Introduction

Ice is the coolest state of water. It only remains frozen at temperatures below 0 °C. Whereas a change from 23 to 21 °C is hardly noticeable, a transition from +1 to −1 °C can transform an entire landscape: canals and lakes freeze over and snow covers everything with a white blanket. For a long time, winter was a challenging season, when less food was available and people had to rely on their reserves. However, the ice-cold also has its upsides. Ever since prehistoric times, ice and snow made it possible to travel great distances for migration, hunting, commerce, or leisure, as beautifully illustrated by the winter landscape from Hendrick Avercamp on the cover of this thesis. Over the years ice has even been a saviour: during the Spanish siege of Haarlem in the winter of 1572–1573, the frozen Haarlemmermeer enabled the Dutch to supply the city, damsel in distress, with sledges over the ice. When the ice melted again after seventeen weeks, the city inevitably had to surrender. [1] Nowadays winters in the Netherlands are less severe and the ice over lakes and ditches only occasionally grows past the 3–4 cm required to support the weight of a single person. [2–4]

Ice floats on water, and only the top part of the water needs to freeze in order for us to skate on ice. This property that makes ice *float* on water is actually rather peculiar. Most substances become more dense when they freeze and would therefore sink. The origin of this property and of many other anomalies of water lies in its special molecular structure. In spite of its simple molecular formula H_2O, water is surprisingly complex. It consists of one oxygen atom to which two hydrogen atoms are bonded in a triangular shape (Fig. 1.1).

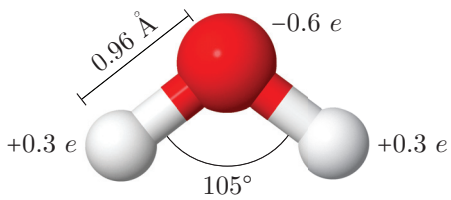

Figure 1.1: Schematic picture of the water molecule: an oxygen atom (red) with two covalently-bonded hydrogen atoms (white). In total the water molecule is charge neutral, but a charge separation is present within the molecule. This charge separation corresponds to a net point charge of +0.3 e at the hydrogen atoms and a negative charge of −0.6 e at the oxygen atom.♪

♪These values are derived by a goniometric calculation based on an electric dipole moment of $6 \cdot 10^{-30}$ C m and the electron clouds assumed to be point charges.

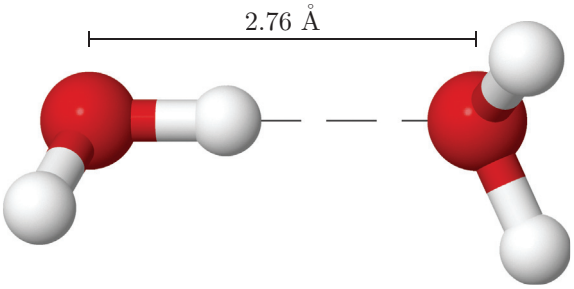

FIGURE 1.2: Two hydrogen-bonded water molecules.

The bonds between the atoms are covalent, which means that the hydrogen and oxygen atoms share their electrons. This allows them to attain the equivalent of a full outer shell, corresponding to a more stable electronic configuration. The sharing is not fair: in its greed for electrons, oxygen hogs the electrons like a selfish lover claiming most of the duvet.[5] As a result, the oxygen atom becomes partly negatively charged and the hydrogen atoms are left with a slight positive charge. These partial charges in the water molecule give rise to an attractive interaction between water molecules, called hydrogen bonds (see Fig. 1.2). This hydrogen bond is about ten times stronger than the van der Waals force that keeps "regular" liquids together,[6] but 10–100 times weaker than a covalent bond. The presence of hydrogen bonds between water molecules is the cause of the relatively high congealing and boiling temperatures, and the origin of exceptional behaviour. Hydrogen bonds have a large capacity to store energy, giving water its unusually high heat capacity, which causes sea climates to be more temperate than land climates.

Every water molecule can form up to four hydrogen bonds: two involving their own hydrogen atoms plus an additional two involving the hydrogen atoms of neighbouring water molecules. In liquid water the structure of the hydrogen bonds is very dynamic and continuously reforms on the timescale of a picosecond (10^{-12} s).[7,8] When liquid water freezes and forms ice, the arrangement of the hydrogen bonds becomes fixed and an ordered, spacious structure of water molecules is formed. The density of water decreases by 8.3 % upon freezing.[9] As a result, ice floats on water. The structure of normal ice is depicted in Fig. 1.3. The oxygen atoms are found at the summits of non-planar hexagons that have the shape of a chair. A projection of the ice crystal in the basal plane gives a regular hexagonal structure similar to honeycombs in a beehive. The hexagonal structure of ice is the origin of the sixfold symmetry of snowflakes.

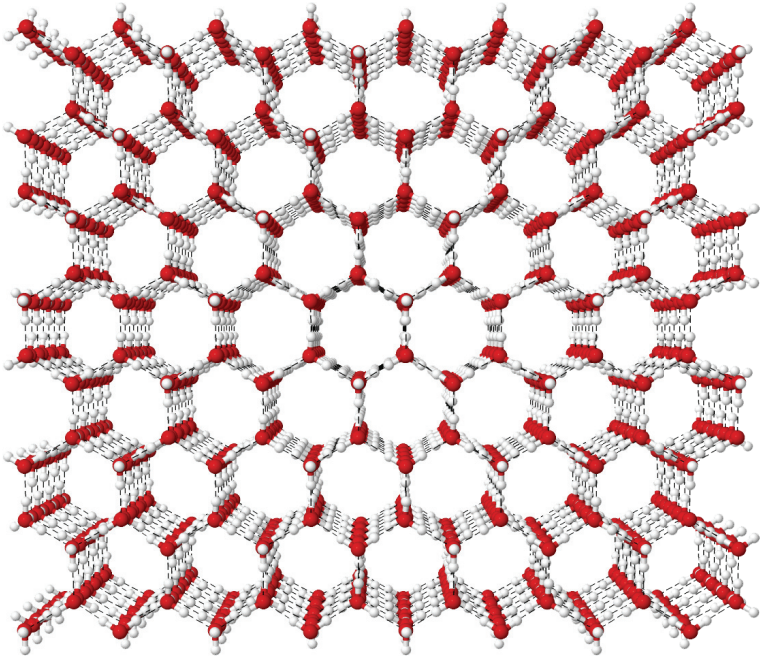

FIGURE 1.3: Hexagonal structure of ordinary ice (I_h). The crystal orientation is shown in the basal plane.

In his *Les météores* (1637) Descartes details his observations on Amsterdam's snowfalls of 4, 5, 6, and 9 February 1635:

> But what astonished me above all was that among the grains which fell lately I noticed some which had around them six little teeth, like clockmakers' wheels.
>
> These were little plates of ice, very flat, very polished, very transparent, about the thickness of a sheet of rather thick paper, ... so perfectly formed in hexagons, and of which the six sides were so straight, and the six angles so equal, that it is impossible for men to make anything so exact.[1] [10]

Today we continue to marvel at and unravel the properties of ice. Its surface structure and the reason why ice is slippery, for instance, are still not fully understood. [11] The low friction of ice is closely linked to a well-established premelting, which results in a water layer at the surface of ice at temperatures

[1] *Mais ce qui m'étonna le plus de tout, fut qu'entre ceux de ces grains qui tombèrent les derniers, j'en remarquai quelques-uns qui avaient autour de soi six petites dents semblables à celles des roues des horloges.*

C'étaient de petites lames de glace, toutes plates, fort polies, fort transparentes, environ de l'épaisseur d'une feuille d'assez gros papier, ... si parfaitement taillées en hexagones, et dont les six côtés étaient si droits, et les six angles si égaux, qu'il est impossible aux hommes de rien faire de si exact.

close to the melting point.[12,13] Premelting is not unique to ice, but occurs for all types of crystalline materials.[14,15] However, for ice it stands out due to the ubiquity and importance of the geophysical effects. Our understanding of the properties of the premelted layer on ice remain very limited, especially at the most fundamental level. Very little is known about the molecular properties of the surface layer.[12] The small size of water molecules in combination with their ultrafast dynamics makes further study challenging. Only few techniques can be deployed to acquire precise insights. This thesis uses spectroscopy to shine light on the molecular properties of ice and other related systems.

Spectroscopy Light is made up of wavelengths, and each wavelength corresponds to a particular colour. White light contains all colours of the rainbow, as can be demonstrated by shining it through a prism. Our eyes are sensitive to a small range of wavelengths, namely the range (in vacuum) from 390 nm (violet) to 700 nm (red).[17] This region coincides with the maximum of the emission spectrum of the sun,[18] which is — from an evolutionary point of view — unlikely to be a coincidence.

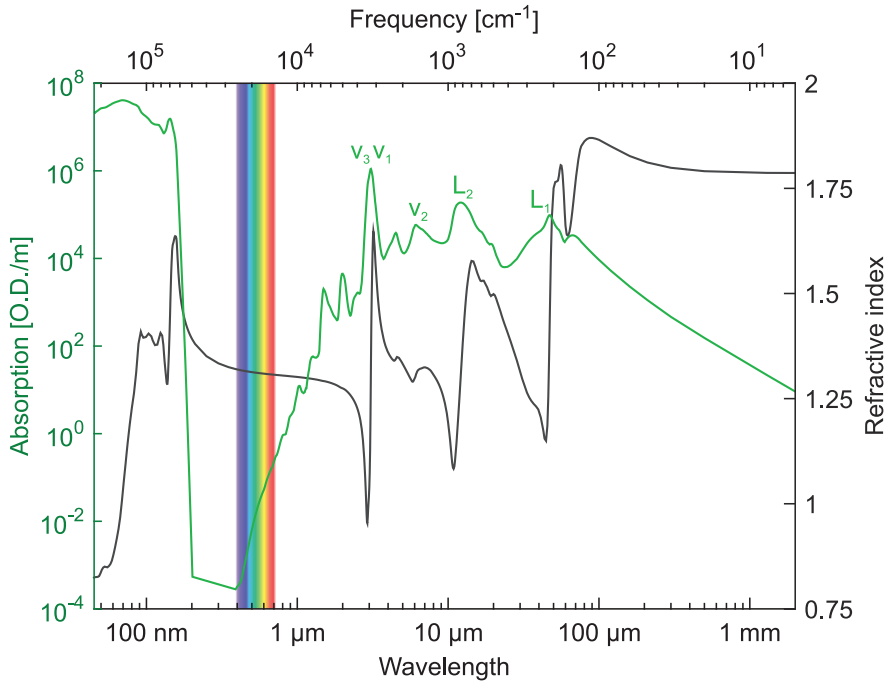

Figure 1.4: The refractive index (blue) and the absorption spectrum (green) of ice at 266 K.[16] The vibrational and librational normal modes are indicated by their abbreviation (see text).

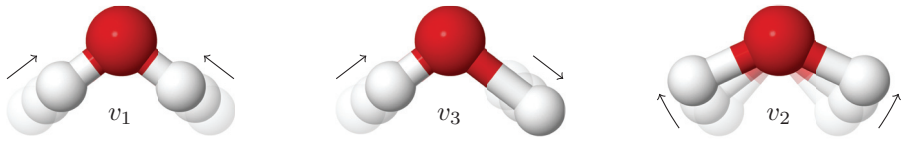

FIGURE 1.5: Vibrations of the water molecule.

Matter consists of atoms, which in turn comprise charged species like electrons and an ion core. When light is incident in matter, significant interactions can take place with the charged constituents. The light–matter interaction can be used as a measurement tool. This field of study is called spectroscopy. Spectroscopic data is often depicted by a spectrum: a plot of the absorbed or emitted light as a function of wavelength or frequency. For historic reasons, in spectroscopy the frequency is often denoted in wavenumbers in units of cm^{-1}. The wavenumber $\tilde{\nu}$ is related to the frequency f by the speed of light c:

$$\tilde{\nu}\ [\mathrm{cm}^{-1}] = \frac{1}{100}\frac{f\ [\mathrm{s}^{-1}]}{c\ [\mathrm{m\ s}^{-1}]}.$$

The absorption spectrum of ice from the extreme ultraviolet up to the far infrared is shown in Fig. 1.4. The spectrum has both regions of weak and strong absorptions. At a wavelength of 3 μm (3300 cm^{-1}), a slice of ice of 10 μm (thinner than a human hair) is already enough to absorb 99 % of the light, whereas at a wavelength of 500 nm this requires a sheet of ice of more than a kilometre. Ice is almost perfectly transparent to visible light and appears to us colourless. Only the tail of the red side of the visible spectrum is absorbed giving ice and water their intrinsic bluish shine. [19]

The features of the absorption spectrum have various origins. The absorptions in the ultraviolet part of the spectrum are caused by electronic transitions and those in the infrared are caused by molecular vibrations and rotations. In this thesis we study molecular vibrations, which field of study is called vibrational spectroscopy. The water molecule vibrates in several ways. The normal mode vibrations are illustrated in Fig. 1.5. There are symmetric and antisymmetric stretching vibrations, usually denoted as v_1 and v_3, respectively, in which the length of the covalent OH bonds oscillates. The bending vibration (v_2) is a scissor-like movement in which the angle between the two covalent OH bonds oscillates. Lastly, water molecules rotate. In the condensed phase this motion is restricted by hydrogen bonds giving rise to hindered rotations or librations (L). Each of these modes has its own oscillation frequency. The vibrations give rise to several peaks in the absorption spectrum, as marked in Fig. 1.4. The other features in the infrared spectrum are associated with overtones and combinations of vibrations.

The vibrational modes of water are very sensitive to the local environment. The spectral position, width, and amplitude of the vibrational bands depend on

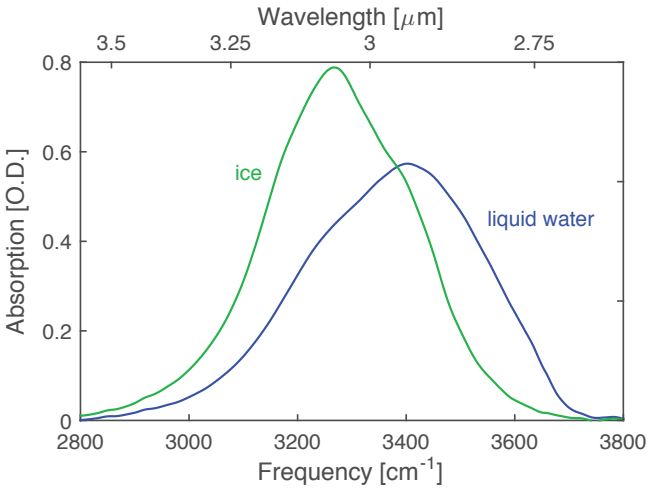

FIGURE 1.6: Absorption spectra of ice (270 K) and liquid water (295 K) in the stretching mode region.

the hydrogen-bond network.[20] Especially the stretching modes are sensitive to the strength of the hydrogen-bond interaction.[7] The hydrogen bond exerts a force on a hydrogen atom in opposite direction to the covalent OH bond, thereby lowering the effective restoring force of the hydrogen atom. As a result, the hydrogen bond lowers the oscillation frequency of the stretching mode. The absorption spectra of the H_2O stretching modes in ice and liquid water are shown in Fig. 1.6. Comparing these spectra we note that the stretching modes of ice have a lower frequency than the stretching modes of liquid water. This reflects the hydrogen bonds to be on average stronger in ice than in liquid water. The sensitivity of the stretching vibrations can be of great use as a probe for the molecular landscape.

OUTLINE In this thesis we investigate several properties of ice and ice-related systems by taking advantage of the sensitivity of the stretching vibrations to the hydrogen-bond structure. In Chapters 2 & 3 we first provide a theoretical introduction and an overview of the employed spectroscopic techniques. We will investigate aspects of the vibrational dynamics of water molecules in ice and hydrated salts in Chapters 4 & 5. Subsequently, we study the surface properties of ice and the surface premelting in Chapters 6 & 7. Chapter 8 deals with the effects of resonant molecular couplings at the surfaces of ice and liquid water. In the last two chapters we study the surface properties of water and oil emulsions. The effect of freezing water at the surface of oil droplets in water is investigated in Chapter 9. The surface structure of water droplets and ice nanocrystals immersed in a hydrophobic environment is discussed in Chapter 10.

2 Theory

Comprendre c'est avant tout unifier.

— Albert Camus, *Le Mythe de Sisyphe*, 1942

Vibrational spectroscopy is the study of the interaction between light and the vibration of molecules. In this chapter we provide the theoretical framework to describe this interaction. The interaction can be adequately described in a semi-classical way in which the electric field is considered classically, and the vibrational states of the molecule are described quantum-mechanically. The theory presented here will focus on the aspects that are needed to understand the experiments in the following chapters. More extensive treatments can be found in textbooks on light–matter interaction,[21–23] non-linear optics,[24–29] electrodynamics,[30,31] and quantum mechanics.[32,33]

2.1 Electrodynamics

Light can be depicted as a travelling electromagnetic wave propagating with the speed of light c. When an electromagnetic wave $\boldsymbol{E}$ travels through a medium, the atoms or molecules composing the medium become polarized. The induced polarization $\boldsymbol{P}$ results in oscillating charges that also emit electric waves. These fields combine with the original field. For a non-magnetic medium without any free charges, the electromagnetic fields obey the Maxwell wave equation, which reads in SI units

$$\nabla^2 \boldsymbol{E}(\boldsymbol{x},t) = \frac{1}{c^2}\frac{\partial^2}{\partial t^2}\boldsymbol{E}(\boldsymbol{x},t) + \frac{1}{\epsilon_0 c^2}\frac{\partial^2}{\partial t^2}\boldsymbol{P}(\boldsymbol{x},t), \tag{2.1}$$

with ϵ_0 the vacuum permittivity. The solutions are transverse plane waves oscillating periodically in time t with angular frequency ω and in space $\boldsymbol{x}$ with spatial frequency $\boldsymbol{k}(\omega)$:

$$\boldsymbol{E}(\boldsymbol{x},t) = \frac{1}{2\pi}\int d\omega\, \boldsymbol{E}(\omega) \mathrm{e}^{i(\boldsymbol{k}(\omega)\cdot\boldsymbol{x}-\omega t)}. \tag{2.2}$$

$\boldsymbol{E}(\omega)$ are the complex frequency components of the electromagnetic wave incorporating both the phase and the amplitude. The polarization $\boldsymbol{P}$ can be written in the same form

$$\boldsymbol{P}(\boldsymbol{x},t) = \frac{1}{2\pi}\int d\omega\, \boldsymbol{P}(\omega) \mathrm{e}^{i(\boldsymbol{k}(\omega)\cdot\boldsymbol{x}-\omega t)}. \tag{2.3}$$

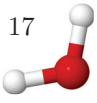

The wave equation [Eq. (2.1)] is valid for every position in space and time, a substitution of the expressions for $\boldsymbol{E}(\boldsymbol{x},t)$ and $\boldsymbol{P}(\boldsymbol{x},t)$ hence yields the following relation for the frequency components:

$$k^2\boldsymbol{E}(\omega) = \frac{\omega^2}{c^2}\boldsymbol{E}(\omega) + \frac{\omega^2}{\epsilon_0 c^2}\boldsymbol{P}(\omega). \tag{2.4}$$

The degree of polarization $\boldsymbol{P}$ induced by the electric field $\boldsymbol{E}$ is determined by the electric susceptibility χ:

$$\boldsymbol{P}(\omega) = \epsilon_0\chi(\omega)\boldsymbol{E}(\omega). \tag{2.5}$$

Depending on the frequency, the polarization $\boldsymbol{P}$ can be out of phase with respect to the original field $\boldsymbol{E}$. Hence, the susceptibility χ is a complex quantity with a real and imaginary part, i.e.

$$\chi(\omega) = \mathrm{Re}(\chi(\omega)) + i\,\mathrm{Im}(\chi(\omega)), \tag{2.6}$$

The real and imaginary parts of the susceptibility χ are related through the Kramers–Kronig relations: [28]

$$\begin{aligned}\mathrm{Re}(\chi(\omega)) &= \frac{1}{\pi}\mathcal{P}\int d\omega'\,\frac{\mathrm{Im}(\chi(\omega))}{\omega'-\omega}\\ \mathrm{Im}(\chi(\omega)) &= -\frac{1}{\pi}\mathcal{P}\int d\omega'\,\frac{\mathrm{Re}(\chi(\omega))}{\omega'-\omega},\end{aligned} \tag{2.7}$$

where $\mathcal{P}$ is the Cauchy principal value of the integral. When $\mathrm{Re}\,\chi$ is an odd function, $\mathrm{Im}\,\chi$ is an even function, and vice versa. Substitution of Eq. (2.5) into Eq. (2.4) gives the dispersion relation between the amplitude of the wavevector $\boldsymbol{k}$ and the frequency ω:

$$k(\omega) = \frac{\omega\sqrt{1+\chi(\omega)}}{c}. \tag{2.8}$$

This can be written as $k(\omega) = n(\omega)\omega/c$ by introducing the factor

$$n(\omega) = \sqrt{1+\chi(\omega)}. \tag{2.9}$$

$n(\omega)$ is denoted as the refractive index, as it also determines the angle of refraction as light passes from one medium into another. Because of the coupling with χ, the index of refraction n is a complex quantity, i.e.

$$n(\omega) = \mathrm{Re}(n(\omega)) + i\,\mathrm{Im}(n(\omega)). \tag{2.10}$$

For the physical representation of the real and imaginary parts it is insightful to consider an electromagnetic wave propagating in the x-direction. Using the dispersion relation and the complex refractive index, we can rewrite

$$\begin{aligned}\boldsymbol{E}(\boldsymbol{x},t) &= \frac{1}{2\pi}\int d\omega\,\boldsymbol{E}(\omega)\mathrm{e}^{i(k(\omega)x-\omega t)} = \frac{1}{2\pi}\int d\omega\,\boldsymbol{E}(\omega)\mathrm{e}^{i\omega(n(\omega)x/c-t)}\\ &= \frac{1}{2\pi}\int d\omega\,\boldsymbol{E}(\omega)\mathrm{e}^{i\omega(\mathrm{Re}(n(\omega))x/c-t)}\mathrm{e}^{-\omega\,\mathrm{Im}(n(\omega))x/c}.\end{aligned} \tag{2.11}$$

The real part of n determines the retardation of the phase velocity with respect to the vacuum value: $v_p(\omega) = c/\mathrm{Re}(n(\omega))$. The imaginary part of n describes the exponential damping of the electromagnetic wave in the medium, caused by light absorption. From Eq. (2.9) follows that the imaginary part of the refractive index is related to the imaginary part of the susceptibility via

$$\mathrm{Im}(n(\omega)) = \frac{\mathrm{Im}(\chi(\omega))}{2\,\mathrm{Re}(n(\omega))}. \tag{2.12}$$

Hence, the component of the polarization that is 90° out of phase with the incoming field $\boldsymbol{E}$ is responsible for the absorption of light.

NON-LINEAR EFFECTS In all materials the polarization starts to depend non-linearly on the applied electric field if the field is sufficiently intense. This response can be modelled by expanding the susceptibility

$$\chi(\omega) = \chi^{(1)}(\omega) + \chi^{(2)}(\omega)\boldsymbol{E}(\omega) + \chi^{(3)}(\omega)\boldsymbol{E}^2(\omega) + \ldots \tag{2.13}$$

Here $\chi^{(1)}$ is the linear susceptibility, and $\chi^{(2)}$ and $\chi^{(3)}$ are the second- and third-order susceptibilities, respectively. $\chi^{(n)}$ is a tensor of rank n. The polarization $\boldsymbol{P}$ [Eq. (2.5)] then consists of the series

$$\boldsymbol{P}(\omega) = \epsilon_0\chi^{(1)}(\omega)\boldsymbol{E}(\omega) + \epsilon_0\chi^{(2)}(\omega)\boldsymbol{E}^2(\omega) + \epsilon_0\chi^{(3)}(\omega)\boldsymbol{E}^3(\omega) + \ldots \tag{2.14}$$

The higher-order polarizations are typically much smaller than the linear polarization. These non-linear polarizations are employed frequently throughout this thesis. We shall refer to the term

$$\boldsymbol{P}^{(n)}(\omega) = \epsilon_0\chi^{(n)}(\omega)\boldsymbol{E}^n(\omega) \tag{2.15}$$

as the nth-order polarization.

The complex refractive index will take the following form [Eq. (2.9)]:

$$n(\omega) = \sqrt{1 + \chi^{(1)}(\omega) + \chi^{(2)}(\omega)\boldsymbol{E}(\omega) + \chi^{(3)}(\omega)\boldsymbol{E}^2(\omega) + \ldots} \tag{2.16}$$

and will hence depend on the strength of the electric field. Using a Taylor expansion for the second- and third-order terms, we get

$$n(\omega) \simeq n_0(\omega) + \underbrace{\frac{\chi^{(2)}(\omega)\boldsymbol{E}(\omega)}{2n_0}}_{\text{Pockels effect}} + \underbrace{\frac{\chi^{(3)}(\omega)\boldsymbol{E}^2(\omega)}{2n_0}}_{\text{Kerr effect}}, \tag{2.17}$$

where $n_0(\omega) = \sqrt{1 + \chi^{(1)}(\omega)}$ is the linear (complex) refractive index. The modulation of the refractive index that is proportional to the electric field is known as the Pockels effect. The Pockels effect is employed in Pockels cells, which are often used in laser cavities. In centrosymmetric materials like gases, liquids, and certain crystals, the Pockels effect is zero because the refractive index must be invariant to the reversal of $\boldsymbol{E}$. The term proportional to the electric field

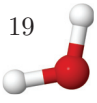

squared (and hence proportional to the intensity) is known as the Kerr effect. In many materials the Kerr effect is small in comparison with the Pockels effect, except for centrosymmetric materials where the Pockels effect is non-existing. The Kerr effect is responsible for self-focusing, which is frequently utilized to mode-lock a laser oscillator.

FREQUENCY MIXING A remarkable effect of the higher-order polarizations is that the frequency of light can change. To illustrate this let us consider a medium with a non-dispersive $\chi^{(2)}$, i.e. with an instantaneous response to the electromagnetic wave. A monochromatic electric field

$$\boldsymbol{E}(\boldsymbol{x},t) = \boldsymbol{E}_0(\boldsymbol{x})\cos(\omega t) \tag{2.18}$$

will then induce the second-order polarization

$$\begin{aligned}\boldsymbol{P}^{(2)}(\boldsymbol{x},t) &= \epsilon_0\chi^{(2)}\boldsymbol{E}^2(\boldsymbol{x},t)\\ &= \epsilon_0\chi^{(2)}\boldsymbol{E}_0^2(\boldsymbol{x})\cos^2(\omega t)\\ &= \frac{1}{2}\epsilon_0\chi^{(2)}\boldsymbol{E}_0^2(\boldsymbol{x})[1+\cos(2\omega t)].\end{aligned} \tag{2.19}$$

The first term in the brackets creates a static electric field response known as optical rectification, the second term oscillating at twice the frequency of the incident light leads to second harmonic generation.

Let us now consider the simultaneous illumination by two beams with frequencies ω_1 and ω_2 ($\omega_2 > \omega_1$). The total electric field is

$$\boldsymbol{E}(t) = \boldsymbol{E}_1(\boldsymbol{x})\cos(\omega_1 t) + \boldsymbol{E}_2(\boldsymbol{x})\cos(\omega_2 t). \tag{2.20}$$

Then additional mixing terms appear in the second-order polarization

$$\begin{aligned}\boldsymbol{P}^{(2)}(\boldsymbol{x},t) =& \epsilon_0\chi^{(2)}\boldsymbol{E}^2(\boldsymbol{x},t)\\ =& \epsilon_0\chi^{(2)}\left[\boldsymbol{E}_1(\boldsymbol{x})\cos(\omega_1 t) + \boldsymbol{E}_2(\boldsymbol{x})\cos(\omega_2 t)\right]^2\\ =& \frac{1}{2}\epsilon_0\chi^{(2)}\big\{\boldsymbol{E}_1^2(\boldsymbol{x}) + \boldsymbol{E}_2^2(\boldsymbol{x}) + \boldsymbol{E}_1^2(\boldsymbol{x})\cos(2\omega_1 t) + \boldsymbol{E}_2^2(\boldsymbol{x})\cos(2\omega_2 t)\\ &+ \boldsymbol{E}_1(\boldsymbol{x})\boldsymbol{E}_2(\boldsymbol{x})[\cos((\omega_1+\omega_2)t) + \cos((\omega_2-\omega_1)t)]\big\}.\end{aligned} \tag{2.21}$$

In this case there are polarization terms at the sum frequency $(\omega_1+\omega_2)$ and at the difference frequency $(\omega_2-\omega_1)$, giving rise to electromagnetic radiation with those frequencies.

The mixing process takes place over the whole length of the non-linear medium. In general destructive interference between the electromagnetic waves created at different positions in the material leads to small intensities of the generated light. Only when the conservation-of-momentum condition is fulfilled does constructive interference occur and are high intensities of light produced. For photons the momentum $\boldsymbol{p}$ can be expressed in the wavevector $\boldsymbol{k}$ by using de Broglie's relation $\boldsymbol{p} = \hbar\boldsymbol{k}$. The wavevector points in the direction of the phase velocity. Conservation of momentum is therefore also known as *phase matching*.

For a three-wave process the energy conservation and phase-matching conditions are:

$$\omega_1 + \omega_2 = \omega_3, \quad \boldsymbol{k}_1 + \boldsymbol{k}_2 = \boldsymbol{k}_3, \tag{2.22}$$

where subscripts 1, 2, and 3 denote the participating waves in increasing order of photon energy. These conditions must be satisfied simultaneously. In case the three waves are collinear, i.e. they travel in the same direction, we can rewrite these conditions using $k = n(\omega)\omega/c$ as

$$[n(\omega_1) - n(\omega_3)]\omega_1 = [n(\omega_3) - n(\omega_2)]\omega_2. \tag{2.23}$$

This equation cannot be fulfilled in most materials as the index of refraction normally increases with frequency, i.e. $n(\omega_1) < n(\omega_2) < n(\omega_3)$. In order to fulfill Eq. (2.23) we need $n(\omega_3)$ to lie in-between $n(\omega_1)$ and $n(\omega_2)$. This problem can be solved by employing birefringent crystals, where the index of refraction depends on the crystal orientation. The simplest and most common type of birefringence is that of crystals with an uniaxial anisotropy, like ice, sapphire, and β-barium borate (BBO). Those crystals have one axis of symmetry, denoted as the optical axis, with the perpendicular directions being optically equivalent. The optical axis has the *extraordinary* index of refraction n_e and the perpendicular directions have the *ordinary* index of refraction n_o. Let us define θ as the angle between the incoming light and the optical axis.

The oscillation orientation of the electromagnetic wave (known as the polarization) can be decomposed in two mutual perpendicular components. Because of the cylindrical symmetry we can, without loss of generality, always define the polarization of one component to lay in the plane perpendicular to the optical axis with refractive index n_o. The polarization of the other component can be projected onto the optical and ordinary axes which has a refractive index that is a combination of n_o and n_e, namely

$$\frac{1}{n^2(\theta)} = \frac{\cos^2(\theta)}{n_\mathrm{o}^2} + \frac{\sin^2(\theta)}{n_\mathrm{e}^2}. \tag{2.24}$$

The index of refraction for this normal mode can be tuned by rotating the angle θ between the optical axis and the propagation direction. The three-wave phase matching condition of Eq. (2.23) and energy conservation can be achieved by tuning the angle θ.

Another application of birefringent crystals is to change the polarization of a light wave travelling through it. A half-wave plate ($\lambda/2$-plate) can rotate the polarization of linearly polarized light by retarding one polarization component by 180° with respect to the other. The details can be found in the book of Saleh and Teich.[27] Furthermore, we use the birefringence of ice to determine its crystal orientation. The procedure is described in the Appendix.

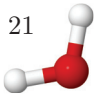

2.2 LIGHT PULSES

A light pulse is an electromagnetic wave of finite duration. For a single position in space the time-dependent electric field is described by [Eq. (2.2)]:

$$\boldsymbol{E}(t) = \frac{1}{2\pi} \int d\omega\, \boldsymbol{E}(\omega) \mathrm{e}^{-i\omega t}, \tag{2.25}$$

where $\boldsymbol{E}(\omega)$ is the continuum of frequency components, which represent the pulse envelope in the frequency domain. $\boldsymbol{E}(\omega)$ can be recognized as the Fourier transform of $\boldsymbol{E}(t)$. The inverse of the Fourier transform is given by

$$\boldsymbol{E}(\omega) = \int dt\, \boldsymbol{E}(t) \mathrm{e}^{i\omega t}. \tag{2.26}$$

Note that the time-dependent electric field $\boldsymbol{E}(t)$ is a real quantity. As a consequence, the frequency function is conjugate symmetric, i.e. $\boldsymbol{E}(\omega) = \boldsymbol{E}^*(-\omega)$ with * denoting the complex conjugate and the positive frequency components are sufficient to describe the electric field uniquely. Hence, the pulse length can be calculated from the positive frequency components. Reversely, the pulse envelope can be computed from the time dependence of the electric field. $\boldsymbol{E}(t)$ and $\boldsymbol{E}(\omega)$ are interdependent, which imposes a direct relationship between the pulse time and its spectral components. For instance, a Gaussian-shaped $\boldsymbol{E}(t)$ pulse also has a frequency envelope $\boldsymbol{E}(\omega)$ with a Gaussian profile.

With the use of some mathematics we will derive now a general property of the product of the pulse length and spectral bandwidth. The root-mean-square widths σ_t and σ_ω are measures for the pulse length and the frequency spread, respectively. They can be calculated as follows [27]

$$\sigma_t^2 = \frac{\int dt\, (t-\bar{t})^2 |\boldsymbol{E}(t)|^2}{\int dt\, |\boldsymbol{E}(t)|^2} \tag{2.27}$$

$$\sigma_\omega^2 = \frac{\int d\omega\, \omega^2 |\boldsymbol{E}(\omega)|^2}{\int d\omega\, |\boldsymbol{E}(\omega)|^2}, \tag{2.28}$$

where $\bar{t}$ is the weighted mean of the pulse time,

$$\bar{t} = \int dt\, t |\boldsymbol{E}(t)|^2. \tag{2.29}$$

Because of the conjugation symmetry of the frequency function, the mean frequency is zero. The numerator and denominator of Eq. (2.28) can be rewritten using Parseval's theorem

$$\int d\omega\, |\boldsymbol{E}(\omega)|^2 = 2\pi \int dt\, |\boldsymbol{E}(t)|^2, \tag{2.30}$$

and the moment theorem of the Fourier transform

$$\int d\omega\, \omega^2 |\boldsymbol{E}(\omega)|^2 = 2\pi \int dt \left| \frac{d\boldsymbol{E}(t)}{dt} \right|^2. \tag{2.31}$$

The quadratic product of the root-mean-square widths then becomes

$$\sigma_t^2 \sigma_\omega^2 = \frac{\int dt\, |(t-\bar{t})\boldsymbol{E}(t)|^2}{\int dt\, |\boldsymbol{E}(t)|^2} \frac{\int dt \left|\frac{d\boldsymbol{E}(t)}{dt}\right|^2}{\int dt\, |\boldsymbol{E}(t)|^2}. \tag{2.32}$$

Using the Cauchy–Schwarz inequality for the numerators we find

$$\left[\int dt\, |(t-\bar{t})\boldsymbol{E}(t)|^2\right]\left[\int dt \left|\frac{d\boldsymbol{E}(t)}{dt}\right|^2\right] \geq \left[\int dt \left|(t-\bar{t})\boldsymbol{E}(t)\frac{d\boldsymbol{E}(t)}{dt}\right|\right]^2. \tag{2.33}$$

Integration by parts yields

$$\int dt \left|(t-\bar{t})\boldsymbol{E}(t)\frac{d\boldsymbol{E}(t)}{dt}\right| = \frac{1}{2}\int dt\, |\boldsymbol{E}(t)|^2. \tag{2.34}$$

Combining the above three equations we obtain the uncertainty relation

$$\sigma_t \sigma_\omega \geq \frac{1}{2}. \tag{2.35}$$

Hence, the product of the pulse length and the spectral bandwidth cannot be less than a certain minimal value. This is of great importance for the ultrashort pulses employed in the experimental chapters of this thesis.

The time–bandwidth product for a specific pulse can be calculated using Eqs. (2.27) & (2.28). A Gaussian-shaped pulse without chirp exactly fulfills the minimal value of the time–bandwidth product [Eq. (2.35)]. Usually, the pulse length τ_p and the frequency bandwidth $\Delta\omega$ are defined in terms of their full width at half maximum (FWHM). For a Gaussian-shaped pulse the FWHM equals $2\sqrt{2\ln 2}$ times the root-mean-square width σ, i.e. $\tau_\mathrm{p} = 2\sqrt{2\ln 2}\,\sigma_t$ and $\Delta\omega = 2\sqrt{2\ln 2}\,\sigma_\omega$. In terms of the FWHM the time–bandwidth product becomes

$$\tau_\mathrm{p}\Delta\omega = 4\ln(2) \approx 2.77 \qquad \text{(Gaussian pulse)}. \tag{2.36}$$

As an example, a Gaussian pulse with a duration of 100 fs (10^{-13} s) has a minimal spectral width of 4.4 THz ($\Delta\tilde{\nu} = 150\ \mathrm{cm}^{-1}$).

2.3 HARMONIC OSCILLATOR

In this section we will describe the vibration of a molecule. To a first approximation, the vibration of a molecule can be described as a harmonic motion. We will start from a classical model of the harmonic oscillator and expand this to a quantum-mechanical description. Along the way, we will learn import aspects of vibrational spectroscopy.

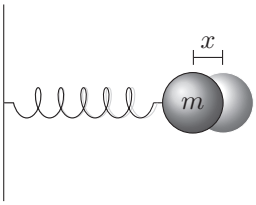

FIGURE 2.1: A mass connected to a spring. The displacement from the equilibrium position is denoted by x.

2.3.1 CLASSICAL DESCRIPTION

Figure 2.1 displays the simplest example of an harmonic oscillator with a mass m connected to a spring with spring constant κ. When the mass has a small deviation from its equilibrium position x, the spring exerts a restoring force $F = -\kappa x$ on the mass (Hooke's law). For an ideal spring without friction, this force equals the rate of momentum change following Newton's second law of motion: $F = ma$. Since the body acceleration equals the second derivative of the displacement x with respect to time t, we arrive at,

$$m\frac{d^2x}{dt^2} + \kappa x = 0. \tag{2.37}$$

The general solution of this differential equation is given by

$$x = A\sin(\omega_0 t + \phi), \tag{2.38}$$

where A and ϕ are constants depending on the boundary conditions, and

$$\omega_0 = \sqrt{\frac{\kappa}{m}} \tag{2.39}$$

is the natural frequency of oscillation of the mass on a spring. Hence, the natural frequency scales inversely proportionally to the square root of the mass.

NORMAL MODES Real molecules consist of multiple atoms and the interaction between each pair of atoms can be described in terms of a spring constant. As an example, the three coupled masses of the water molecule can be regarded classically as depicted in Fig. 2.2. Each of the N atoms fulfills Newton's second law of motion. As the position of each atom in three-dimension space is described by 3 coordinates, we thus have a set of $3N$ equations of motion. In general the equations of motion are not straightforward to solve, as the equations of motion are coupled, i.e.

$$m_i\frac{d^2x_i}{dt^2} + \sum_j \kappa_{ij}x_j = 0, \qquad i = 1, ..., 3N. \tag{2.40}$$

These equations can be expressed in compact form by defining the vector $\boldsymbol{x}$

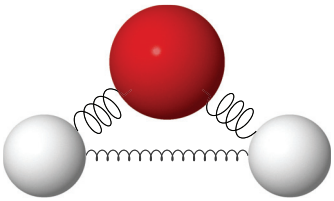

FIGURE 2.2: The interaction between each pair of atoms in a water molecule can be described as a spring connecting the masses. The coupling between the hydrogen atoms is much weaker than that of the OH bonds.

with the $3N$ elements x_i, the diagonal $3N \times 3N$ matrix M with elements m_i, and the symmetric $3N \times 3N$ matrix K with elements κ_{ij}:

$$M\frac{d^2\boldsymbol{x}}{dt^2} + K\boldsymbol{x} = 0. \tag{2.41}$$

Multiplying this equation from the left with M^{-1} yields

$$\frac{d^2\boldsymbol{x}}{dt^2} + M^{-1}K\boldsymbol{x} = 0. \tag{2.42}$$

The trick in solving these equations lies in finding the unitary transformation matrix U

$$\boldsymbol{x} = U\boldsymbol{q} \tag{2.43}$$

such that $U^{-1}M^{-1}KU$ equals the diagonal matrix Ω. With this transformation, Eq. (2.42) becomes

$$U\frac{d^2\boldsymbol{q}}{dt^2} + M^{-1}KU\boldsymbol{q} = 0. \tag{2.44}$$

Multiplying this equation now from the left with U^{-1} yields

$$\begin{aligned} \frac{d^2\boldsymbol{q}}{dt^2} + U^{-1}M^{-1}KU\boldsymbol{q} &= 0 \\ \frac{d^2\boldsymbol{q}}{dt^2} + \Omega\boldsymbol{q} &= 0. \end{aligned} \tag{2.45}$$

Since Ω is diagonal, the $3N$ coupled equations of motion in Eq. (2.40) have now become $3N$ uncoupled differential equations

$$\frac{d^2q_i}{dt^2} + \omega_i^2 q_i = 0, \qquad i = 1, ..., 3N, \tag{2.46}$$

where ω_i^2 are the (diagonal) elements of Ω. These equations are just $3N$ equations of motion of independent one-dimensional harmonic oscillators, which we already know how to solve [Eq. (2.38)].

Each independent oscillation q_i is called a *normal mode*, and any oscillation is a superposition of normal modes by Eq. (2.43). However, 3 degrees of freedom are needed to describe the translation of the centre-of-mass motion, and

3 degrees of freedom are needed to describe rotational motion (2 for molecules with a linear geometry), which are not genuine vibrational modes. Therefore, for a molecule with N atoms, the number of normal modes is $3N-6$, or $3N-5$ for a linear molecule. A molecule with M covalent bonds shall have M bond-stretching modes (for a non-cyclic molecule $M = N-1$). The remaining modes are angle-bending modes. The resonance frequencies of the bending modes are usually lower than those of the stretching modes.[34] The water molecule has a bend configuration of 3 atoms with 2 covalent bonds, thus water has one bending and two stretching modes. For normal water (H_2O) and heavy water (D_2O) the two OH/OD bond stretches combine to give symmetric and antisymmetric modes (Fig. 1.5). The symmetric stretching mode has a lower eigenfrequency than the antisymmetric stretching mode. For the water isotope HDO, the natural frequencies of the OH and OD bonds are different owing to the mass of a deuterium atom being twice the mass of a hydrogen atom [Eq. (2.39)]. As a result, the stretching modes are well localized on the OH and OD bonds.

DAMPING In real oscillators the vibration will not last, but friction will lead to damping of the oscillation. The frictional force can be me modelled as being proportional to the derivative of the normal mode coordinate with respect to time. As a consequence, the equation of motion contains one more term and becomes

$$\frac{d^2q}{dt^2} + \Gamma\frac{dq}{dt} + \omega_0^2 q = 0, \tag{2.47}$$

where Γ is the damping constant. The solution to this homogeneous equation reads

$$q = A\sin\left(\sqrt{\omega_0^2 - \Gamma^2/4}\,t + \phi\right)\mathrm{e}^{-\Gamma t/2}. \tag{2.48}$$

As can be seen from the last term, this solution is exponentially damped in time and $\Gamma/2$ can be regarded as the rate constant of the amplitude decay. The energy is proportional to the square of the amplitude, so the energy decay is twice as fast as the amplitude decay. Hence, the energy damping time τ is the inverse rate of the energy loss, i.e. $\tau = 1/\Gamma$.

Let us now drive the oscillator with an external driving force F_{driving}. For a sinusoidal driving force with driving frequency ω and force constant F_0, i.e. $F_{\mathrm{driving}} = F_0\cos(\omega t)$, the equation of motion becomes

$$\frac{d^2q}{dt^2} + \Gamma\frac{dq}{dt} + \omega_0^2 q = \frac{F_0}{m}\cos(\omega t). \tag{2.49}$$

The steady state solution is

$$q = \frac{F_0}{m}\frac{1}{\sqrt{(\omega_0^2-\omega^2)^2 + \Gamma^2\omega^2}}\cos(\omega t + \varphi) \tag{2.50}$$

with

$$\tan(\varphi) = \frac{\Gamma\omega}{\omega^2 - \omega_0^2}, \tag{2.51}$$

where $-180° < \varphi \leq 0°$. Introducing the linear susceptibility of a harmonic oscillator

$$\chi^{(1)}(\omega) = \frac{1}{m}\frac{1}{\omega_0^2 - \omega^2 + i\Gamma\omega}, \tag{2.52}$$

one can write the steady state solution more compactly as

$$q = |\chi^{(1)}(\omega)|F_0 \cos\left(\omega t + \arg(\chi^{(1)}(\omega))\right). \tag{2.53}$$

The oscillator now oscillates with the driving frequency ω. The amplitude is largest when the driving frequency ω matches the natural frequency ω_0, for which the oscillation is 90° delayed with respect to the driving force. By analogy, consider ringing the bells of a church: A bell only swings boldly when the pull frequency of the bell-ringer matches the natural frequency of the bell. Moreover, the best moment to pull the rope is at the equilibrium position of the bell when the bell moves away from the bell-ringer, i.e. when the force is 90° out of phase with the oscillation.

One can now calculate the average power absorbed by the oscillator, which is the inner product of the applied force with the velocity:

$$\langle P\rangle_t \equiv \left\langle F_{\text{driving}}\frac{dq}{dt}\right\rangle_t = -\frac{\omega F_0^2}{2m}\,\text{Im}(\chi^{(1)}(\omega)) = \frac{F_0^2}{2m^2}\frac{\Gamma}{(\omega - \omega_0^2/\omega)^2 + \Gamma^2}. \tag{2.54}$$

The maximal absorption coincides with the maximal amplitude, i.e. when the driving frequency ω matches the natural frequency ω_0. Plotting the absorbed power as a function of frequency gives the absorbed power spectrum, shown in Fig. 2.3. A typical measure of a resonance is the FWHM of the absorption spectrum, which equals here the damping constant and decay rate Γ. For a weakly damped oscillators where the damping is small compared to the resonance frequency ($\Gamma << \omega_0$), the absorption spectrum is strongly peaked at $\omega \simeq \omega_0$. Near the peak frequency we can approximate

$$(\omega - \omega_0^2/\omega)^2 = (1 + \omega_0/\omega)^2(\omega - \omega_0)^2 \simeq 4(\omega - \omega_0)^2 \tag{2.55}$$

and Eq. (2.54) approaches the Lorentzian line shape

$$\langle P\rangle_t = \frac{F_0^2}{8m^2}\frac{\Gamma}{(\omega - \omega_0)^2 + \Gamma^2/4}. \tag{2.56}$$

The model of the classical harmonic oscillator can be expanded further by including a term proportional to q^2 in the equation of motion. This will lead to non-linear susceptibilities and frequency mixing [cf. Section 2.1]. Further details can be found in for instance books by Boyd [28] and Shen. [24]

2.3.2 Quantum-mechanical description

Molecular vibrations show quantized energy levels, which cannot be described with a classical description of the harmonic oscillator. To account for quantization we need a quantum-mechanical description of the system, which is

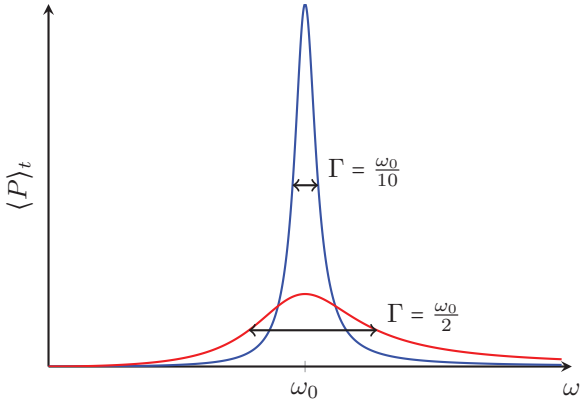

FIGURE 2.3: Absorbed power spectrum of the driven harmonic oscillator as a function of the driving frequency. The FWHM of the absorption spectrum equals the damping constant Γ. The absorption of an oscillator with a large damping constant is smeared out over a broad spectral range. A small damping constant results in a high peak absorption at the natural frequency ω_0. The spectral absorption approaches a Lorentzian line shape for $\Gamma << \omega_0$. The area underneath the absorbed power spectrum is independent of Γ.

usually described in energy-based formulations in terms of a Hamiltonian. The Hamiltonian is an operator, which acts on a state like a force on a system and corresponds to the total energy of the system. For the mass connected to a spring with force constant κ, the Hamiltonian is given by

$$\hat{H} = \frac{\hat{p}^2}{2m} + \frac{1}{2}\kappa\hat{x}^2, \tag{2.57}$$

where $\hat{p}$ and $\hat{x}$ are the momentum and position operators, respectively. The first term corresponds to the kinetic energy of the system (with $\hat{p} = -i\hbar\,\partial_x$), and the second term represents the potential energy.

The allowed stationary states ψ and the corresponding eigenenergies E are obtained by solving the time-independent Schrödinger equation, which reads in Dirac's bra–ket notation [35]

$$\hat{H}\,|\psi\rangle = E\,|\psi\rangle. \tag{2.58}$$

The solutions of this differential equation yield an orthogonal set of eigenstates of the form [32]

$$|v\rangle = (2^v v!)^{-1/2}\left(\frac{m\omega_0}{\pi\hbar}\right)^{1/4} \mathrm{e}^{-m\omega_0 x^2/2\hbar}\, H_v\left(\sqrt{m\omega_0/\hbar}\,x\right) \tag{2.59}$$

and their corresponding eigenenergies

$$E_v = \hbar\omega_0\left(v + \frac{1}{2}\right), \tag{2.60}$$

where $v \in \mathbb{N}_0$ is the vibrational quantum number and $H_v(\xi)$ are the Hermite polynomials[♪]. One can see from this equation that subsequent states are equally spaced by the energy $\hbar\omega_0$, where $\omega_0 = \sqrt{\kappa/m}$ corresponds to the classical resonance frequency of the oscillator. The first few stationary eigenstates with their corresponding energies are shown in Fig. 2.4. Note that the $v = 0$ state (also called the ground state) has an energy of $\hbar\omega_0/2$ larger than the minimum of the potential well. This is called the zero-point energy. This is in contrast with the non-driven classical oscillator, where the ground state coincides with zero oscillation.

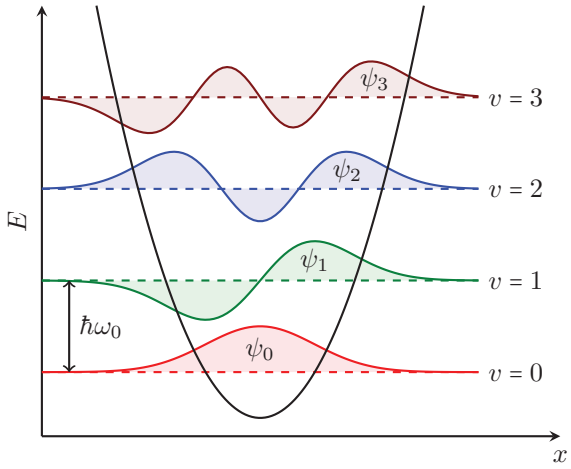

FIGURE 2.4: Wave functions and corresponding energy levels of the harmonic oscillator potential. The energy levels are spaced by $\hbar\omega_0$.

VIBRATIONAL TRANSITIONS A transition from one state to another is only possible when the Hamiltonian is perturbed by a time-dependent energy term. The effect of the perturbation on the state of a system is described by the time-dependent Schrödinger equation

$$i\hbar \frac{\partial}{\partial t}|\psi\rangle = \hat{H}(t)\,|\psi\rangle. \tag{2.61}$$

Here the Hamiltonian operator $\hat{H}(t)$ is the sum of the unperturbed harmonic Hamiltonian $\hat{H}_0$ from Eq. (2.57) and the time-dependent interaction potential $\hat{V}_{\text{int}}(t)$,

$$\hat{H}(t) = \hat{H}_0 + \hat{V}_{\text{int}}(t). \tag{2.62}$$

In the case of molecular vibrations irradiation with light can provide such a perturbation. The simplest model of the interaction potential between the electric

[♪]The first few Hermite polynomials are given by $H_0(\xi) = 1$, $H_1(\xi) = 2\xi$, $H_2(\xi) = 4\xi^2 - 2$.

field $\boldsymbol{E}(t)$ and the electric dipole moment of the molecule $\boldsymbol{\mu}$ is given by

$$\begin{aligned}\hat{V}_{\text{int}}(t) &= -\hat{\boldsymbol{\mu}} \cdot \boldsymbol{E}(t) \\ &= -\hat{\boldsymbol{\mu}} \cdot \boldsymbol{E}_0 \cos(\omega t) \\ &\equiv \frac{1}{2}\hat{V}_{\text{int}}\left(\mathrm{e}^{-i\omega t} + \mathrm{e}^{i\omega t}\right).\end{aligned} \tag{2.63}$$

We solve the time-dependent Schrödinger equation [Eq. (2.61)] using the eigenstates for the unperturbed harmonic oscillator [Eq. (2.59)]. These eigenstates form a complete set, meaning that the perturbed wave function can be expressed as a linear combination of them:

$$|\psi(t)\rangle = \sum_u a_u(\omega, t)|u\rangle, \tag{2.64}$$

where a_u are to be determined amplitudes complex functions. Inserting this into Eq. (2.61) and multiplying from the left by $\langle w|$ yields the set of differential equations:

$$\frac{\partial\, a_w(\omega,t)}{\partial t} = -\frac{i}{2\hbar}\sum_u \langle w|\hat{V}_{\text{int}}|u\rangle\left[\mathrm{e}^{-i(\omega+\omega_{wu})t} + \mathrm{e}^{i(\omega-\omega_{wu})t}\right] a_u(\omega,t), \tag{2.65}$$

where $\hbar\omega_{wu} = (E_w - E_u)$ is the energy difference between states w and u. The differential equations are coupled, i.e. a_w depends on a_u, which in turn depends on a_w and so on. This problem can be addressed using the perturbation expansion

$$a_w(\omega,t) = a_w^{(0)}(\omega) + a_w^{(1)}(\omega,t) + \ldots \tag{2.66}$$

where $a_w^{(n)}$ signifies the amplitude of nth-order expansion. In case the interaction V_{int} is small in comparison with the unperturbed Hamiltonian $\hat{H}_0$, we can solve Eq. (2.65) by a process of successive approximations. If initially only state v is populated, we have in zeroth-order $a_v^{(0)} = 1$ and $a_{w\neq v}^{(0)} = 0$. Relating the time derivatives of the first-order amplitudes only to the zeroth-order amplitudes we get

$$\frac{\partial\, a_w^{(1)}(\omega,t)}{\partial t} = -\frac{i}{2\hbar}\langle w|\hat{V}_{\text{int}}|v\rangle\left[\mathrm{e}^{-i(\omega+\omega_{wv})t} + \mathrm{e}^{i(\omega-\omega_{wv})t}\right], \tag{2.67}$$

or in integrated form

$$\begin{aligned}a_w^{(1)}(\omega,t) &= -\frac{i}{2\hbar}\langle w|\hat{V}_{\text{int}}|v\rangle \int_0^t dt' \left[\mathrm{e}^{-i(\omega+\omega_{wv})t} + \mathrm{e}^{i(\omega-\omega_{wv})t}\right] \\ &= \frac{1}{2\hbar}\langle w|\hat{V}_{\text{int}}|v\rangle\left[\frac{\mathrm{e}^{-i(\omega+\omega_{wv})t} - 1}{\omega+\omega_{wv}} + \frac{\mathrm{e}^{-i(\omega-\omega_{wv})t} - 1}{\omega-\omega_{wv}}\right] \\ &= \frac{-i}{\hbar}\langle w|\hat{V}_{\text{int}}|v\rangle\left[\frac{\mathrm{e}^{-i(\omega+\omega_{wv})t/2}\sin((\omega+\omega_{wv})t/2)}{\omega+\omega_{wv}}\right. \\ &\qquad \left. + \frac{\mathrm{e}^{-i(\omega-\omega_{wv})t/2}\sin((\omega-\omega_{wv})t/2)}{\omega-\omega_{wv}}\right].\end{aligned} \tag{2.68}$$

The probability that a particle which started out in state v will be found after time t in state w equals the squared magnitude, i.e.

$$\left|a_w^{(1)}(\omega,t)\right|^2 = \frac{1}{\hbar^2}|\langle w|\hat{V}_{\text{int}}|v\rangle|^2\left[\frac{\sin^2((\omega+\omega_{wv})t/2)}{(\omega+\omega_{wv})^2} + \frac{\sin^2((\omega-\omega_{wv})t/2)}{(\omega-\omega_{wv})^2} + \frac{2\cos(\omega_{wv}t)\sin((\omega+\omega_{wv})t/2)\sin((\omega-\omega_{wv})t/2)}{(\omega+\omega_{wv})(\omega-\omega_{wv})}\right]. \tag{2.69}$$

This expression can be simplified by realizing that as time proceeds it becomes more and more peaked near the resonance frequencies. About $\omega = \mp\omega_{wv}$ we can approximate

$$\left|a_w^{(1)}(\omega,t)\right|^2 \simeq \frac{1}{\hbar^2}|\langle w|\hat{V}_{\text{int}}|v\rangle|^2\,\frac{\sin^2((\omega\pm\omega_{wv})t/2)}{(\omega\pm\omega_{wv})^2}. \tag{2.70}$$

It is of interest to calculate the transition rate from initial state v to final state w which is defined as the time derivative of the squared magnitude $a_w^{(1)}$, i.e.

$$W_{wv}(\omega,t) \equiv \frac{\partial}{\partial t}\left|a_w^{(1)}(\omega,t)\right|^2 = \frac{2}{\hbar^2}|\langle w|\hat{V}_{\text{int}}|v\rangle|^2\,\frac{\sin((\omega\pm\omega_{wv})t)}{\omega\pm\omega_{wv}}. \tag{2.71}$$

Note that the driving frequency ω does not necessarily need to match exactly $\pm\omega_{wv}$ for a non-zero transition rate. This is a manifestation of the time–frequency uncertainty relation [Eq. (2.35)]. For $t\to\infty$ we can make use of the limit

$$\lim_{t\to\infty}\frac{\sin((\omega\pm\omega_{wv})t)}{\omega\pm\omega_{wv}} = \pi\,\delta(\omega\pm\omega_{wv}), \tag{2.72}$$

where δ is the Dirac delta function.[4] We then obtain

$$\lim_{t\to\infty} W_{wv}(\omega,t) = \frac{\pi}{2\hbar^2}|\langle w|\hat{V}_{\text{int}}|v\rangle|^2\,\delta(\omega\pm\omega_{wv}). \tag{2.73}$$

Hence, the transition rate is constant for large t. Keeping this in mind we will drop the time dependence of the transition rate and formulate the following expression of Fermi's golden rule [32]

$$\begin{aligned} W_{wv}(\omega) &= \frac{\pi}{2\hbar^2}|\langle w|\hat{V}_{\text{int}}|v\rangle|^2\,\delta(\omega\pm\omega_{wv}) \\ &= \frac{\pi}{2\hbar^2}|\langle w|\hat{\boldsymbol{\mu}}\cdot\boldsymbol{E}_0|v\rangle|^2\,\delta(\omega\pm\omega_{wv}). \end{aligned} \tag{2.74}$$

The Dirac delta function ensures the energy conservation to be fulfilled. The term $\delta(\omega-\omega_{wv})$ corresponds to the absorption of a photon with energy $\hbar\omega_{wv}$ ($E_w > E_v$) and the term $\delta(\omega+\omega_{wv})$ corresponds to stimulated emission of a photon with the same energy ($E_w < E_v$). The strength of the light–matter

[4] Strictly speaking, one should refer to the Dirac delta *distribution*, as $\delta(\omega)$ is only an analytic function once integrated over a certain frequency domain.

interaction is given by the matrix element $\langle w|\hat{\boldsymbol{\mu}} \cdot \boldsymbol{E}_0|v\rangle$. For an angle θ between the electric field polarization $\boldsymbol{E}_0$ and the dipole moment $\boldsymbol{\mu}$ we get

$$W_{wv}(\omega) = \frac{\pi E_0^2}{2\hbar^2} \cos^2(\theta) \, |\langle w|\hat{\boldsymbol{\mu}}|v\rangle|^2 \, \delta(\omega \pm \omega_{wv}). \tag{2.75}$$

The electric transition dipole moment $\langle w|\hat{\boldsymbol{\mu}}|v\rangle$ depends on the normal mode coordinate q, in which the following first-order Taylor expansion around the equilibrium position q_0 can be made:

$$\langle w|\hat{\boldsymbol{\mu}}(q)|v\rangle \simeq \boldsymbol{\mu}(q_0)\langle w|v\rangle + \left(\frac{\partial \boldsymbol{\mu}(q)}{\partial q}\right)_{q=q_0} \langle w|\hat{q}|v\rangle. \tag{2.76}$$

Because vibrational eigenstates are orthogonal, the first term is zero. Substituting this back into Eq. (2.75), we arrive at

$$W_{wv}(\omega) = \frac{\pi E_0^2}{2\hbar^2} \cos^2(\theta) \left|\frac{\partial \boldsymbol{\mu}(q)}{\partial q}\right|^2_{q=q_0} |\langle w|\hat{q}|v\rangle|^2 \, \delta(\omega \pm \omega_{wv}). \tag{2.77}$$

The absorbed power of a transition is found by multiplying the transition rate by the photon energy, e.g.

$$P_{wv}(\omega) = \hbar\omega \, W_{wv}(\omega). \tag{2.78}$$

The absorption cross section σ is defined as the absorbed power P divided by the intensity of the incident light $I = \epsilon_0 c E_0^2/2$. Using Eq. (2.77) under the assumption of an isotropic medium where $\langle \cos^2(\theta)\rangle = 1/3$, we get

$$\sigma_{wv}(\omega) = \frac{P_{wv}(\omega)}{I(\omega)} = \frac{\pi\omega}{3\hbar c\epsilon_0} \left|\frac{\partial \boldsymbol{\mu}(q)}{\partial q}\right|^2_{q=q_0} |\langle w|\hat{q}|v\rangle|^2 \, \delta(\omega \pm \omega_{wv}). \tag{2.79}$$

The proportionality to the modulo squared of the derivative of the dipole moment with respect to the vibrational coordinate entails that only vibrational motions that lead to a change in the dipole moment of the molecule are active. As a consequence molecules like O_2 and N_2 do not absorb infrared (IR) light. For the CO_2 molecule the antisymmetric stretch vibration is active while the symmetric one is not, since that vibration does not modulate the dipole moment. The three fundamental vibrational modes of the water molecule (illustrated in Fig. 1.5) are all IR active.

For the harmonic oscillator the matrix elements of the position operator $\hat{q}$ can be calculated explicitly: [32]

$$\langle w|\hat{q}|v\rangle = \sqrt{\frac{\hbar}{2m\omega}} \left(\sqrt{v+1}\,\delta_{w,v+1} + \sqrt{v}\,\delta_{w,v-1}\right). \tag{2.80}$$

Here the Kronecker delta function is unity when the indices match and zero otherwise. Hence, an optical transition on the ladder of vibrational states is only allowed between adjacent excitation levels, i.e. $w = v \pm 1$. The $v = 0 \rightarrow 1$

transition is defined as the fundamental. Other possible transitions are $v = 1 \rightarrow 2$ and $v = 2 \rightarrow 3$. Transitions such as $v = 0 \rightarrow 2$ and $v = 1 \rightarrow 3$ are forbidden for a perfect harmonic oscillator. We note that the $v \rightarrow w$ cross section (σ_{wv}) equals the $w \rightarrow v$ cross section (σ_{vw}), e.g. $\sigma_{10} = \sigma_{01}$. We also note that the cross section is larger for more highly excited states, e.g. $\sigma_{21} = 2\sigma_{10}$. Since the resonance frequency scales proportionally to $m^{-1/2}$ [Eq. (2.39)], we find $\langle w|\hat{q}|v\rangle \propto m^{-1/4}$. Hence, the cross section scales $\sigma_{wv} \propto m^{-1/2}$.

VIBRATIONAL RELAXATION States can also couple by non-optical interactions. This yields a finite lifetime for an excited state v, as the vibrational energy can be dissipated via resonant coupling to accepting modes. For vibrational transitions in the IR, spontaneous emission is negligible owing to an ω^3 dependence of the Einstein coefficient.[21] Resonant coupling to accepting modes occurs within the molecule (intramolecular coupling) and with other molecules in the vicinity (intermolecular coupling). A constant decay probability leads to an exponentially decaying vibration in time, which can also be derived more rigourously by solving the time-dependent Schrödinger equation [Eq. (2.61)].[36] The decay rate Γ_i for initial state i is given by the sum over the transition probabilities of all accepting modes integrated over all energies, i.e.

$$\Gamma_i = \frac{2\pi}{\hbar} \int d\omega \sum_f |\langle f|\hat{V}_c|i\rangle|^2 \delta(\omega - \omega_{fi}). \tag{2.81}$$

Here $\langle f|\hat{V}_c|i\rangle$ is the coupling matrix element between the initial state i and final state f. The initial state i of the system comprises the excited state v of the vibrational mode and the ground state of the accepting mode. The final state f of the system encompasses the vibrational state w with $w < v$ and the excited state of the accepting mode. In physically realistic situations the vibration is coupled to many other sates, which form a continuum of final states. This thought is often expressed by replacing the summation over the final states in Eq. (2.81) by an (energy) density of final states ρ_f, i.e.

$$\Gamma_i = \frac{2\pi}{\hbar} \int d\omega \, |\langle f|\hat{V}_c|i\rangle|^2 \delta(\omega - \omega_{fi}) \rho_f(\omega). \tag{2.82}$$

This expression for Fermi's golden rule can be used to acquire insights in the vibrational lifetime T_1, which equals the inverse decay rate ($T_1 = 1/\Gamma$).[j] A Fourier transformation of the exponential decay leads to a Lorentzian spectral line shape with FWHM Γ, like we found for the classical oscillator [Eq. (2.56)]. Spectral broadening induced by the vibrational lifetime is called lifetime broadening. In an ensemble of molecules with heterogeneous environments the absorption lines are additionally inhomogeneously broadened which can often be described by a Gaussian profile.

[j] The nomenclature T_1 is adopted from nuclear magnetic resonance (NMR) spectroscopy. Note that subscript 1 does not refer to the first excited state ($v = 1$).

2.3.3 RULES OF THUMB

In the above description the molecular vibration is described as a simple harmonic motion. Real molecules do not vibrate in a perfectly harmonic manner. Nevertheless, the harmonic oscillator model is a good starting point and carries many guidelines for vibrational spectroscopy. The harmonic oscillator functions form a complete set of basis functions and are therefore a suitable expansion set for many anharmonic oscillators. Below, we summarize some learned lessons with special emphasis on the implications for the water molecule:

(a) The natural frequency of oscillation reads $\omega_0 = \sqrt{\kappa/m}$ [Eq. (2.39)]. Therefore, the vibrational frequencies of the OH stretching modes are $\sqrt{2}$ larger than the OD stretching modes.♫ Furthermore, the effective spring constant κ depends on the hydrogen-bond strength. The hydrogen bond exerts a force in opposite direction to the covalent bond, thereby lowering the restoring force of the covalent bond. As a result, the hydrogen bond lowers the effective spring constant. A strong hydrogen bond leads to a lower effective spring constant than a weak hydrogen bond. Therefore, the stretching vibration of strongly hydrogen-bonded water has a lower frequency than that of weakly hydrogen-bonded water.

(b) The cross section scales with the magnitude square of the dipole moment derivative, i.e. $\sigma_{wv} \propto |\partial\boldsymbol{\mu}(q)/\partial q|^2_{q=q_0}$ [Eq. (2.79)]. As a consequence, only vibrations that modulate the dipole moment are IR active.

(c) The cross section scales with the magnitude square of the off-diagonal matrix element of the position operator, i.e. $\sigma_{wv} \propto |\langle w|\hat{q}|v\rangle|^2$ [Eq. (2.79)]. Therefore, transitions are only possible between adjacent levels in the harmonic approximation, i.e. $w = v \pm 1$. Anharmonic transitions such as $v = 0 \to 2$ and $v = 0 \to 3$ have in general very low cross sections. In addition, the vibrational cross sections of the OH stretching modes are $\sqrt{2}$ times larger than the OD stretching modes [Eq. (2.80)].♫ We also deduced from Eq. (2.80) that the cross section of the $v = 0 \to 1$ transition equals the cross section of the $v = 1 \to 0$ transition ($\sigma_{01} = \sigma_{10}$) and that the cross section of the $v = 1 \to 2$ transition is twice the cross section of the $v = 0 \to 1$ transition ($\sigma_{21} = 2\sigma_{10}$).

(d) The inverse lifetime dictates the minimal spectral line width, i.e. $1/T_1 = \Gamma \geq \mathrm{FWHM}$. Lifetime broadening leads to a Lorentzian spectral line shape. Additional broadening mechanisms for an ensemble of oscillators can often be described by a Gaussian line shape.

♫Taking into account the finite mass of the oxygen atom the theoretical ratio is $\sqrt{17/9} \approx 1.374$. [37]

2.3.4 ANHARMONIC OSCILLATOR

The description of the vibrational structure of a molecule in terms of a harmonic oscillator does not account for effects like the breaking of bonds at high vibrational energies and the anharmonicity. Often a Morse potential is employed as interatomic interaction model.[22] The special nature of the hydrogen bond can be accorded for with the Lippincott–Schroeder potential. This potential was designed by Lippincott and Schroeder to explain the strong dependence of the OH vibrational frequency on the O···O hydrogen-bond length. It models the problem of a hydrogen atom in a hydrogen bond as a one-dimensional water dimer. The Lippincott–Schroeder potential is given by[38]

$$V_{\mathrm{LS}}(r,R) = D_{\mathrm{a}}[1 - \mathrm{e}^{-n_{\mathrm{a}}(r-r_0)^2/2r}] + D_{\mathrm{b}}[1 - \mathrm{e}^{-n_{\mathrm{b}}(R-r-r_0)^2/2(R-r)}], \qquad (2.83)$$

where r is the OH distance, and R is the O···O distance. $D_{\mathrm{a}} = 38750\ \mathrm{cm}^{-1}$ is the binding energy of the OH bond of water, $n_{\mathrm{a}} = 9.8\ \text{Å}^{-1}$ defines the vibrational frequency of the OH stretching vibration, and $r_0 = 0.97$ Å is the gas phase OH bond length. $D_{\mathrm{b}} = 25000\ \mathrm{cm}^{-1}$ and $n_{\mathrm{b}} = 16.5\ \text{Å}^{-1}$ follow from a comparison to empirical values.[39]

The Lippincott–Schroeder potential is shown in Fig. 2.5 for an O···O distance of $R = 2.76$ Å and has a double-minimum structure. The local minimum at 1.75 Å corresponds to the auto-ionized $\mathrm{OH^-}\cdots\mathrm{H_3O^+}$ state.[39] For the given O···O distance, the energy difference between the ground state and the first excited state is about 3300 cm^{-1}. The $v = 1 \rightarrow 2$ transition has a smaller energy difference due to the anharmonicity of the potential, namely about 3000 cm^{-1}.

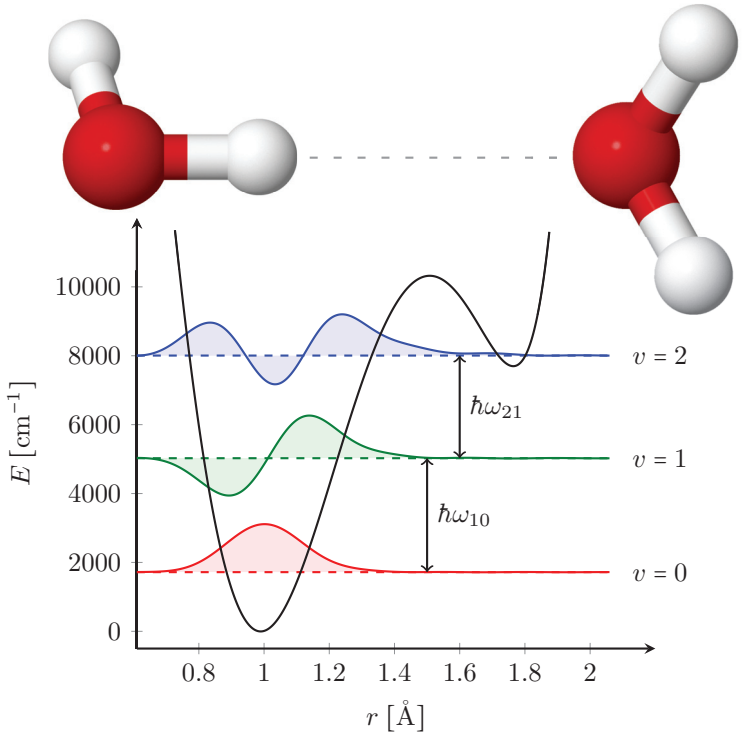

Figure 2.5: Wave functions and corresponding energy levels of the Lippincott–Schroeder potential for an O···O distance of 2.76 Å (corresponding to ice at 253 K [40]).

3 Spectroscopic techniques

The previous chapter outlined the theoretical framework of this research. We will now proceed to explore the versatile toolbox of spectroscopy, focusing on the techniques used in the experimental chapters of this thesis.

3.1 Absorption spectrum

Light with intensity I_0 travelling through an absorbing medium will leave the medium with a lower intensity I (Fig. 3.1). For an electric field travelling through a medium of thickness l, the transmission can be calculated using Eq. (2.11):

$$\frac{I(\omega)}{I_0(\omega)} = \frac{|\boldsymbol{E}(\omega)\mathrm{e}^{ik(\omega)l}|^2}{|\boldsymbol{E}(\omega)|^2} = \mathrm{e}^{-2\,\mathrm{Im}(n(\omega))\omega l/c}. \tag{3.1}$$

The absorption α is the natural logarithm of the transmission, i.e.

$$\alpha(\omega) \equiv -\ln\left(\frac{I(\omega)}{I_0(\omega)}\right) = \frac{2\omega l}{c}\,\mathrm{Im}(n(\omega)) = \frac{\omega l}{c}\frac{\mathrm{Im}(\chi(\omega))}{\mathrm{Re}(n(\omega))}, \tag{3.2}$$

where we made use of Eq. (2.12) in the last equality. Recording the attenuation of light as a function of frequency yields a linear absorption spectrum. Previously in this thesis (Fig. 1.6) we encountered the absorption spectra of ice and liquid water in the stretching region. The imaginary part of the electrical susceptibility determines the extent of the light absorption. This is a result of a cascade of effects, as we will see in the following: An electric field $\boldsymbol{E}$ induces a polarization $\boldsymbol{P}$, which in turn serves as a radiation source of an electric field $\boldsymbol{E}_{\mathrm{rad}}$. The field is radiated with a 90° phase delay with respect to the polarization,[23,26] i.e.

$$\boldsymbol{E}_{\mathrm{rad}}(\omega) \propto i\boldsymbol{P}(\omega). \tag{3.3}$$

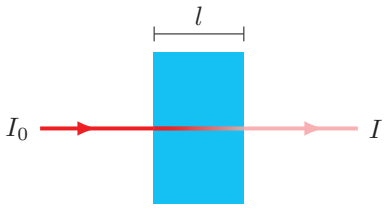

Figure 3.1: Absorbance of a beam of light with initial intensity I_0 as it travels through a sample of thickness l.

This radiated field interferes with the original field $\boldsymbol{E}$. The light transmission becomes

$$\begin{aligned}\frac{I(\omega)}{I_0(\omega)} &= \frac{|\boldsymbol{E}(\omega)+\boldsymbol{E}_{\mathrm{rad}}(\omega)|^2}{|\boldsymbol{E}(\omega)|^2}\\ &= \frac{|\boldsymbol{E}(\omega)|^2+2\,\mathrm{Re}(\boldsymbol{E}^*(\omega)\boldsymbol{E}_{\mathrm{rad}}(\omega))+|\boldsymbol{E}_{\mathrm{rad}}(\omega)|^2}{|\boldsymbol{E}(\omega)|^2}\\ &\simeq 1+\frac{2\,\mathrm{Re}(\boldsymbol{E}^*(\omega)\boldsymbol{E}_{\mathrm{rad}}(\omega))}{|\boldsymbol{E}(\omega)|^2},\end{aligned} \tag{3.4}$$

where we assumed in the last line the radiated field to be much smaller than the incoming field, i.e. $\boldsymbol{E}_{\mathrm{rad}} \ll \boldsymbol{E}$. Using a Taylor expansion of the natural logarithm of the transmission gives the absorption

$$\alpha(\omega) \equiv -\ln\left(\frac{I(\omega)}{I_0(\omega)}\right) \simeq -\frac{2\,\mathrm{Re}(\boldsymbol{E}^*(\omega)\boldsymbol{E}_{\mathrm{rad}}(\omega))}{|\boldsymbol{E}(\omega)|^2}. \tag{3.5}$$

Employing Eq. (3.3) we arrive at

$$\alpha(\omega) \propto \frac{2\,\mathrm{Im}(\boldsymbol{E}^*(\omega)\boldsymbol{P}(\omega))}{|\boldsymbol{E}(\omega)|^2}, \tag{3.6}$$

which agrees with our observation of Eq. (3.2) that the absorption scales proportionally with the imaginary part of χ.

At relatively low field intensities, the higher-order polarizations are very small and the extinction process is dominated by the first-order polarization $\boldsymbol{P}^{(1)} = \epsilon_0\chi^{(1)}\boldsymbol{E}$. The absorption is then independent of the light intensity [Eq. (3.6)]. For a medium containing a concentration C of absorbers with cross section σ, the decrease in intensity scales linearly with its magnitude according to

$$\frac{dI(\omega)}{dx} = -C\,\sigma_{wv}(\omega)I(\omega). \tag{3.7}$$

Integrating this differential equation over a length l yields the Bouguer–Lambert–Beer law

$$\frac{I(\omega)}{I_0(\omega)} = \mathrm{e}^{-Cl\,\sigma_{wv}(\omega)}. \tag{3.8}$$

Hence the light attenuates exponentially with distance, similar to Eq. (3.1). The absorption α depends linearly on all parameters, i.e.

$$\alpha(\omega) \equiv -\ln\left(\frac{I(\omega)}{I_0(\omega)}\right) = Cl\,\sigma_{wv}(\omega). \tag{3.9}$$

Combining the above equation with Eq. (3.2), we obtain a relation between the molecular cross section and the material properties:

$$\sigma_{wv}(\omega) = \frac{1}{C}\frac{\omega}{c}\frac{\mathrm{Im}(\chi(\omega))}{\mathrm{Re}(n(\omega))}. \tag{3.10}$$

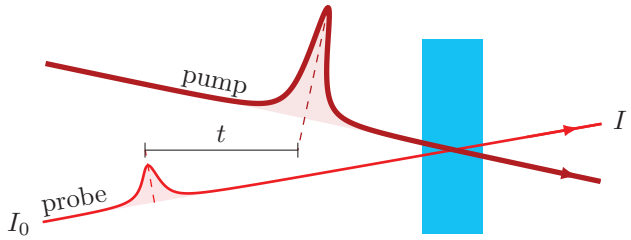

FIGURE 3.2: Schematics of a pump–probe experiment. An intense pump pulse excites molecular vibrations in a sample and a probe pulse monitors the pump-induced spectral changes. The time delay t between the pump and the probe pulse can be varied to obtain dynamic information.

3.2 PUMP–PROBE SPECTROSCOPY

Dynamical information of molecular processes can be obtained with pump–probe experiments (Fig. 3.2). This technique uses two laser pulses separated in time. An intense pump pulse brings the system in a non-equilibrium state. This state relaxes in time as described in the previous chapter. The evolution is monitored by probing the sample with another weak time-delayed pulse: the probe pulse. The time delay between the pump and probe pulse can be varied. The absorption of the probe pulse is monitored in the presence and absence of a pump pulse.

The process of excitation by the pump pulse and subsequent detection by the probe pulse is a three-field interaction process with two interactions of the pump field $\boldsymbol{E}_{\mathrm{pu}}$ and one interaction with the probe field $\boldsymbol{E}_{\mathrm{pr}}$. The interaction is described by the third-order susceptibility $\chi^{(3)}$, which yields a third-order polarization $\boldsymbol{P}^{(3)}$. Interference between the radiated field generated by $\boldsymbol{P}^{(3)}$ and the probe field $\boldsymbol{E}_{\mathrm{pr}}$ leads to the following third-order absorption [cf. Eq. (3.6)]:

$$\alpha^{(3)}(\omega) \propto \frac{2\,\mathrm{Im}(\boldsymbol{E}^{*}_{\mathrm{pr}}(\omega)\boldsymbol{P}^{(3)}(\omega))}{|\boldsymbol{E}_{\mathrm{pr}}(\omega)|^2}. \tag{3.11}$$

We will proceed with a phenomenological description of pump–probe spectroscopy, yielding good understanding of the experiments in Chapter 4 & 5.

The absorption of the probe pulse in absence of the pump pulse α_0 is given by

$$\alpha_0(\omega) = n\,\sigma_{10}(\omega), \tag{3.12}$$

where $n = Cl$ is the amount of absorbers per unit surface. The pump pulse will excite molecules from the ground state to the $v = 1$ state. Consequently, there will be less molecules in the ground state, such that the absorption of the probe pulse at the fundamental frequency will be smaller. On the other hand, the first excited state is populated after excitation by the pump pulse. In addition, stimulated emission from this excited state contributes equally to the absorption

decrease.[♪] These two contributions lead to a *bleaching* of the absorption at the fundamental frequency. Furthermore, the molecules in the first excited state can be promoted to the $v = 2$ state. This causes an increase in absorption at the $v = 1 \rightarrow 2$ transition frequency and is called *induced absorption*. The $v = 1 \rightarrow 2$ transition has in general a lower frequency than the $v = 0 \rightarrow 1$ transition owing to the anharmonicity of the vibrational potential. The bleaching and induced absorption signals give rise to the following expression for the absorption:

$$\alpha(\omega) = (n - 2n_1)\,\sigma_{10}(\omega) + n_1\,\sigma_{21}(\omega), \tag{3.13}$$

where n_1 denotes the concentration of excitations.

The difference between the pumped and unpumped spectra is called the transient absorption $\Delta\alpha$:

$$\Delta\alpha(\omega) = \alpha(\omega) - \alpha_0(\omega) = \underbrace{-2n_1\,\sigma_{10}(\omega)}_{\text{bleaching}} + \underbrace{n_1\,\sigma_{21}(\omega)}_{\substack{\text{induced}\\ \text{absorption}}}. \tag{3.14}$$

Although two signals are contributing to the bleaching signal and only one to the induced absorption, they roughly have the same intensity as $2\sigma_{10} = \sigma_{21}$ in the harmonic oscillator approximation (see Section 2.3.2). Transient absorption spectra can be obtained by blocking every second pump pulse and subtracting the absorption spectrum of the probe pulse in the absence of the pump pulse from the absorption spectrum in the presence of the pump pulse. Alternatively, one can modulate the interference of two identical pump pulses in a Mach–Zehnder and perform a Fourier transformation of the absorption of the probe pulse. The latter yields the additional information of which spectral component of the pump pulse is responsible for the transient absorption and is called two-dimensional (2D) pump–probe spectroscopy.

The transient absorption is independent of the intensity of the probe pulse but the transient absorption does dependent on the intensity of the pump pulse. The pump intensity and the spot area of the pump beam A_{pu} determine the amount of pump-excited vibrations per surface n_1 by the Bouguer–Lambert–Beer law [Eq. (3.8)]. The number of photons in the pump pulse is given by $N_{\mathrm{pu}} = \int d\omega\, N_{\mathrm{pu}}(\omega)$. Taking into account both the bandwidth of the molecular transition and the spectral width of the pump pulse we get

$$n_1 = \frac{1}{A_{\mathrm{pu}}} \int d\omega\,[1 - \mathrm{e}^{-Cl\,\sigma_{10}(\omega)}]N_{\mathrm{pu}}(\omega), \tag{3.15}$$

where A_{pu} is the spot area of the pump beam. For a sample with little absorption, we have $\mathrm{e}^{-Cl\,\sigma_{10}(\omega)} \approx 1 - Cl\,\sigma_{10}(\omega)$. Combining Eqs. (3.14) and (3.15) we find the transient absorption to scale approximately with the cross section squared for a sample with little absorption. In case the sample has a very high optical density and the pump pulse depletes, the transient absorption will scale linearly with the cross section.

[♪] It follows from Eq. (2.79) that $\sigma_{10} = \sigma_{01}$.

POLARIZATION-RESOLVED PUMP–PROBE The pump pulse excites preferentially molecules with their transition dipole moments aligned parallel to the pump polarization. As a consequence the distribution of excited molecules is anisotropic after excitation by the pump pulse. Hence, the transient absorption of the probe pulse depends on its relative polarization compared to the pump pulse. One can measure the transient absorption of the probe pulse twice, once with its polarization parallel to the pump pulse ($\Delta\alpha_\parallel$) and once with its polarization perpendicular to the pump pulse ($\Delta\alpha_\perp$). In an isotropic medium, the transient absorption initially is three times larger for the parallel polarization with respect to the perpendicular polarization. Depolarization by molecular reorientation and energy transfer could reduce this difference over time until eventually an isotropic distribution of excited molecules is reached. In that case $\Delta\alpha_\parallel$ decays faster, and the transient absorption of the probe pulse with the polarization perpendicular to the pump pulse $\Delta\alpha_\perp$ decays slower. An isotropic signal $\Delta\alpha_{\mathrm{iso}}$ that is free of depolarization processes can be constructed in the following way:

$$\Delta\alpha_{\mathrm{iso}}(\omega,t) = \frac{\Delta\alpha_\parallel(\omega,t) + 2\Delta\alpha_\perp(\omega,t)}{3}. \tag{3.16}$$

Information about the depolarization dynamics can be obtained by monitoring the difference between the parallel and perpendicular transient absorption changes. Normalized by the isotropic signal, this yields the anisotropy R, which depends exclusively on the depolarization dynamics: [41]

$$R(\omega,t) = \frac{\Delta\alpha_\parallel(\omega,t) - \Delta\alpha_\perp(\omega,t)}{3\Delta\alpha_{\mathrm{iso}}(\omega,t)} = \frac{\Delta\alpha_\parallel(\omega,t) - \Delta\alpha_\perp(\omega,t)}{\Delta\alpha_\parallel(\omega,t) + 2\Delta\alpha_\perp(\omega,t)}. \tag{3.17}$$

For a sample with an isotropic distribution of dipoles, it can be shown that the anisotropy is proportional to [42]

$$\begin{aligned} R(t) &= \frac{2}{5}\left\langle P_2(\hat{\boldsymbol{\mu}}(0)\cdot\hat{\boldsymbol{\mu}}(t))\right\rangle \\ &= \frac{3}{5}\left\langle \cos^2(\theta(t))\right\rangle - \frac{1}{5}, \end{aligned} \tag{3.18}$$

where $P_2(x) = (3x^2-1)/2$ is the second Legendre polynomial, $\hat{\boldsymbol{\mu}}(0)\cdot\hat{\boldsymbol{\mu}}(t) = \cos(\theta(t))$ is the correlation of the direction of the transition dipole moment between times 0 and t, and $\langle..\rangle$ denotes the average over all molecules. As $0 \le \cos^2 \le 1$ we find from Eq. (3.18) that $-1/5 \le R(t) \le 2/5$. At $t = 0$, the correlation function is unity and the anisotropy equals 2/5.

3.3 SUM-FREQUENCY GENERATION

Specific information about the molecular configuration at an interface can be obtained from sum-frequency generation (SFG) experiments (Fig. 3.3). We have already seen in Section 2.1 that in a non-linear medium the frequencies of two electromagnetic waves can mix. This requires strong fields. For a visible and

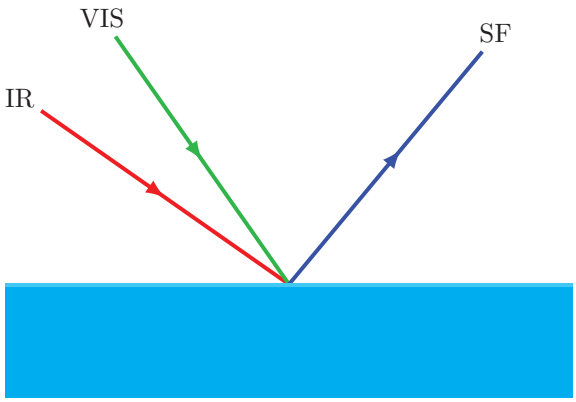

FIGURE 3.3: Schematic of a SFG experiment. At the interface (where the symmetry is broken), two pulses with different frequencies combine and generate a pulse at the sum frequency.

infrared light source, with frequencies ω_{VIS} and ω_{IR}, respectively, light can be produced at the sum of these frequencies, i.e.

$$\omega_{\mathrm{SF}} = \omega_{\mathrm{IR}} + \omega_{\mathrm{VIS}}. \tag{3.19}$$

The positive frequency part of the second-order polarization $\boldsymbol{P}^{(2)}$ can be written in vector component form as follows:

$$P_{\alpha}^{(2)}(\omega_{\mathrm{SF}}) = \epsilon_0 \chi_{\alpha\beta\gamma}^{(2)}(\omega_{\mathrm{SF}} = \omega_{\mathrm{IR}} + \omega_{\mathrm{VIS}}) E_{\beta}(\omega_{\mathrm{IR}}) E_{\gamma}(\omega_{\mathrm{VIS}}), \tag{3.20}$$

where the Einstein summation notation is used over repeated Greek indices.[43] $\mathbf{E}(\omega_{\mathrm{VIS}})$ and $\mathbf{E}(\omega_{\mathrm{IR}})$ are the electric field amplitudes of the visible and the infrared beams, respectively. The intensity of the emitted SF light is proportional to the absolute magnitude squared of the second-order polarization $\boldsymbol{P}^{(2)}$,[44] i.e.

$$I_{\alpha}^{(2)}(\omega_{\mathrm{SF}}) \propto \left| \chi_{\alpha\beta\gamma}^{(2)}(\omega_{\mathrm{SF}} = \omega_{\mathrm{IR}} + \omega_{\mathrm{VIS}}) E_{\beta}(\omega_{\mathrm{IR}}) E_{\gamma}(\omega_{\mathrm{VIS}}) \right|^2. \tag{3.21}$$

SFG is a powerful tool to study surface behaviour, because this process is bulk forbidden for an isotropic material. This is easily understood by the following argument. In a centrosymmetric material all directions are identical and the physical response of the material is independent of the axis system. This also applies for the second-order susceptibility under a parity inversion $\boldsymbol{\Pi}$ in the three spatial coordinates:

$$\Pi_{\alpha\alpha'}\Pi_{\beta\beta'}\Pi_{\gamma\gamma'}\chi_{\alpha'\beta'\gamma'}^{(2)} = \chi_{\alpha\beta\gamma}^{(2)} \qquad \text{(centrosymmetry)}. \tag{3.22}$$

In Cartesian coordinates the parity operator is represented by the matrix

$$\boldsymbol{\Pi} = \begin{pmatrix} -1 & 0 & 0 \\ 0 & -1 & 0 \\ 0 & 0 & -1 \end{pmatrix} \tag{3.23}$$

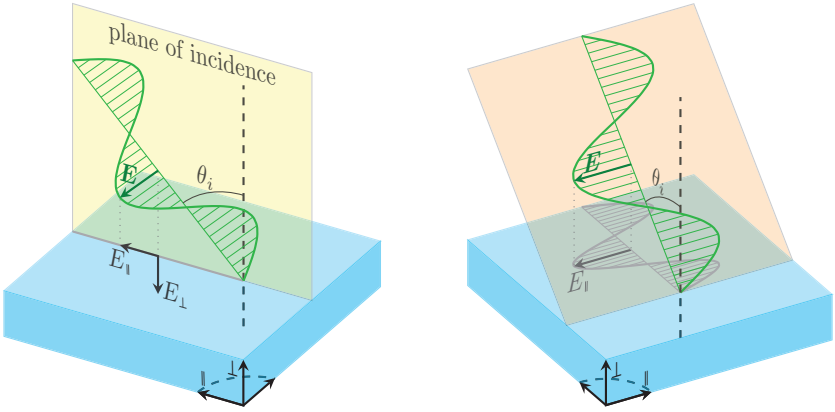

p-polarized light *s*-polarized light

FIGURE 3.4: The *p*- and *s*-polarizations of an electric field with an angle of incidence θ_i. The *p*-polarization is parallel to the plane of incidence and can be decomposed into both a perpendicular as well as a parallel component to the interface. The *s*-polarization is perpendicular to the plane of incidence and lays entirely parallel to the interface.

or in index notation $\Pi_{\alpha\beta} = -\delta_{\alpha\beta}$. Applying this on Eq. (3.22) gives $\chi^{(2)} = -\chi^{(2)}$, which can only be true if and only if $\chi^{(2)} = 0$. A direct consequence is that for centrosymmetric materials SF light can only be generated at positions with broken symmetry, i.e. at interfaces.

In general, the second-order susceptibility $\chi^{(2)}$ is a third-order tensor with 27 components. Symmetry considerations, however, reduce the number of non-zero components greatly according to Neumann's principle.[i] An achiral rotationally isotropic interface is rotation symmetric in the axis perpendicular to the surface and mirror symmetric in the interfacial plane. Therefore, the second-order susceptibility $\chi^{(2)}$ has only four independent non-zero elements.[46,47] These can be deduced by different polarization combinations of the SF, VIS, and IR fields. The polarization of these electric fields can be split up in two components, one parallel and one perpendicular to the plane of incidence, which are denoted by *p* and *s*, respectively.[j] The polarization combinations are denoted like *ssp* where the polarizations are listed in order of decreasing frequency (SF, VIS, and IR). *s*-polarized light is polarized entirely parallel to the surface, whereas *p*-polarized light has both a parallel as well as a perpendicular component. This is illustrated in Fig. 3.4. Hence, the *ppp*-polarization combination probes a combination of the four non-zero $\chi^{(2)}$ components. The effective second-order susceptibility $\chi^{(2)}_{\text{eff}}$ for a given polarization combination of the SF, VIS, and IR

[i] Neumann's principle states that all symmetries of a system are possessed by every physical property of that system.[45]

[j] *p* stands for *parallel*, and *s* stands for *senkrecht* (German for perpendicular).

beams has the following dependence on the $\chi^{(2)}$ components: [48]

$$\begin{aligned}
\chi^{(2)}_{\mathrm{eff},ssp} &\propto \chi^{(2)}_{\parallel\parallel\perp} \\
\chi^{(2)}_{\mathrm{eff},sps} &\propto \chi^{(2)}_{\parallel\perp\parallel} \\
\chi^{(2)}_{\mathrm{eff},pss} &\propto \chi^{(2)}_{\perp\parallel\parallel} \\
\chi^{(2)}_{\mathrm{eff},ppp} &\propto \chi^{(2)}_{\perp\perp\perp} - \chi^{(2)}_{\parallel\parallel\perp} - \chi^{(2)}_{\parallel\perp\parallel} + \chi^{(2)}_{\perp\parallel\parallel},
\end{aligned} \tag{3.24}$$

where we omitted the Fresnel and angular factors in the last line. These local field factors correct for the influence of the interfacial reflection and the projection in the separate components. The Fresnel and angular factors depend on the optical constants and the angles of incidence. [48]

The second-order susceptibility $\chi^{(2)}$ reveals information about the surface structure, because it is the macroscopical average over the molecular hyperpolarizabilities β,

$$\chi^{(2)}_{\alpha\beta\gamma} = \frac{N_\mathrm{s}}{\epsilon_0}\langle R_{\alpha i} R_{\beta j} R_{\gamma k}\, \beta_{ijk}\rangle, \tag{3.25}$$

where N_s is the number of surface molecules, $R_{\alpha i}$ are rotation matrices [49] using all three Euler angles to project the molecule coordinate system (Roman indices) on the surface plane coordinate system (Greek indices), and $\langle..\rangle$ denotes the ensemble average.

The resonant and hence dominant part of the hyperpolarizability β is given by [46]

$$\beta_{ijk} = \frac{1}{2\hbar}\sum_w \frac{M_{ij} A_k}{\omega_{wv} - \omega_\mathrm{IR} - i\Gamma_w/2}, \tag{3.26}$$

where the sum is taken over all resonances w with their corresponding resonance frequencies ω_{wv} and decay rates Γ_w [cf. Eq. (2.81)]. M and A are the Raman and IR transition moments, respectively, and are given by [47]

$$\begin{aligned}
M_{ij} &= \frac{1}{\hbar}\sum_s \frac{\langle v|\hat{\mu}_i|s\rangle\langle s|\hat{\mu}_j|w\rangle}{\omega_\mathrm{SF} - \omega_{sv}} - \frac{\langle v|\hat{\mu}_j|s\rangle\langle s|\hat{\mu}_i|w\rangle}{\omega_\mathrm{VIS} + \omega_{sv}} \\
&\simeq \frac{1}{\hbar}\sum_s \frac{\langle v|\hat{\mu}_i|s\rangle\langle s|\hat{\mu}_j|w\rangle}{\omega_\mathrm{SF} - \omega_{sv}} \\
A_k &= \langle w|\hat{\mu}_k|v\rangle \simeq \frac{\partial \mu_k}{\partial q}\langle w|\hat{q}|v\rangle.
\end{aligned} \tag{3.27}$$

Here s can be any state of the system and the wave functions are taken to be real. For the approximation of the Raman transition moment M we employed the condition $\omega_\mathrm{SF} + \omega_{sv} \gg \omega_\mathrm{SF} - \omega_{sv}$ and for the approximation of the IR transition moment A we employed Eq. (2.76).

An important note is that the squares of the absolute values of M and A are directly proportional to the Raman and IR cross sections, respectively. [22] Therefore, from Eq. (3.26) it follows that SFG needs the vibration to be both Raman and IR active, i.e. M and A are both non-zero. This can also be inferred from the energy diagram shown in Fig. 3.5.

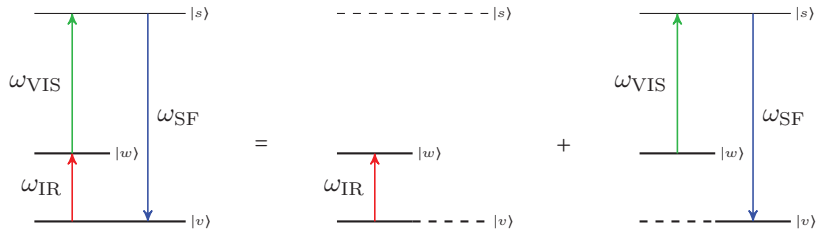

FIGURE 3.5: Diagrammatic representation of an SFG process, which can be regarded as a combination of an IR transition in combination with an anti-Stokes Raman scattering process.

SPECTRAL RESOLUTION AND NORMALIZATION Sum-frequency generation can be used to study the vibrations of molecules at an interface. As the vibrational resonances make the SFG signal species specific, varying the infrared frequency creates a vibrational spectrum. For this purpose a visible beam with a fixed and narrow wavelength is often used in combination with an infrared beam that has a broad spectrum covering the vibrational resonances to be studied. The bandwidth of the visible light defines the maximal spectral resolution. The spectral shape is determined by the effective second-order susceptibility $\chi^{(2)}_{\mathrm{eff}}$, which includes all angular and Fresnel factors.[44] Taking into account the spectral width of the VIS beam, the SF intensity can be written as

$$I_\alpha(\omega_{\mathrm{SF}}) \propto \left|\chi^{(2)}_{\mathrm{eff},\alpha\beta\gamma}(\omega_{\mathrm{SF}} = \omega_{\mathrm{IR}} + \omega_{\mathrm{VIS}})E_\beta(\omega_{\mathrm{IR}}) * E_\gamma(\omega_{\mathrm{VIS}})\right|^2, \tag{3.28}$$

where $*$ denotes the convolution operator.[50,51]

In order to divide out the spectral envelope of the IR light, the SF spectrum is often normalized with respect to a reference SF signal acquired from a material with a non-resonant and therefore non-dispersive second-order susceptibility. For this purpose often crystalline quartz is employed.[52,53] For a certain polarization combination, the normalized SF intensity is given by

$$\frac{I_{\mathrm{sample}}}{I_{\mathrm{reference}}}(\omega_{\mathrm{SF}}) \propto \left|\chi^{(2)}_{\mathrm{eff}}(\omega_{\mathrm{SF}} = \omega_{\mathrm{IR}} + \omega_{\mathrm{VIS}}) * E(\omega_{\mathrm{VIS}})\right|^2. \tag{3.29}$$

HYPERPOLARIZABILITIES FOR MOLECULAR GROUPS WITH C_{nv} SYMMETRY The strength of the $\chi^{(2)}$ response depends on the underlying hyperpolarizabilities β. The $\chi^{(2)}_{\alpha\beta\gamma}$ tensor elements are directly connected to the hyperpolarizability tensor elements $\beta_{\alpha'\beta'\gamma'}$ through transformation of the Euler angles [Eq. (3.25)]. The most general relations are given in Hirose et al.[54] They simplify considerably when we calculate the relations for molecular groups with symmetry C_{nv}[♫] on a rotational-isotropic interface. When we follow the convention of the molecular axes system given in Fig. 3.6, many hyperpolarizability elements are zero.[55,56] For a rotational-isotropic interface with a random dis-

[♫]The Schönflies symmetry notation C_{nv} stands for an n-fold rotational axis with n vertical mirror planes containing the axis of rotation.

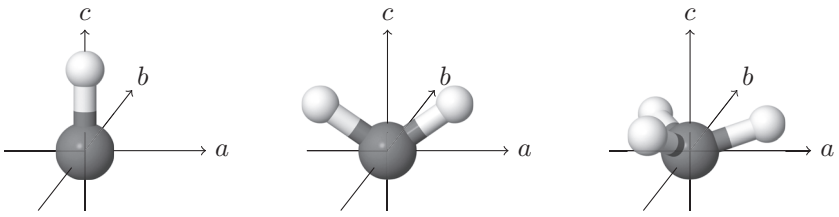

$C_{\infty v}$ C_{2v} C_{3v}

FIGURE 3.6: The molecular axes frames for molecular groups belonging to different C_{nv} symmetry groups. The c-axis coincides with the rotation axis and the ac-plane lies in one of the mirror symmetry planes.

tribution over the azimuthal and twist angles, and a tilt angle θ between the c-axis and the surface normal, the relations are

$$\begin{aligned}
\chi^{(2)}_{\parallel\parallel\perp} =& \frac{N_s}{4\epsilon_0}[(2\beta_{ccc}+\beta_{aac}+\beta_{bbc}-\beta_{aca}-\beta_{bcb}-\beta_{caa}-\beta_{cbb})\langle\cos(\theta)\rangle \\
&-(2\beta_{ccc}-\beta_{aac}-\beta_{bbc}-\beta_{aca}-\beta_{bcb}-\beta_{caa}-\beta_{cbb})\langle\cos^3(\theta)\rangle] \\
\chi^{(2)}_{\parallel\perp\parallel} =& \frac{N_s}{4\epsilon_0}[(2\beta_{ccc}-\beta_{aac}-\beta_{bbc}+\beta_{aca}+\beta_{bcb}-\beta_{caa}-\beta_{cbb})\langle\cos(\theta)\rangle \\
&-(2\beta_{ccc}-\beta_{aac}-\beta_{bbc}-\beta_{aca}-\beta_{bcb}-\beta_{caa}-\beta_{cbb})\langle\cos^3(\theta)\rangle] \\
\chi^{(2)}_{\perp\parallel\parallel} =& \frac{N_s}{4\epsilon_0}[(2\beta_{ccc}-\beta_{aac}-\beta_{bbc}-\beta_{aca}-\beta_{bcb}+\beta_{caa}+\beta_{cbb})\langle\cos(\theta)\rangle \\
&-(2\beta_{ccc}-\beta_{aac}-\beta_{bbc}-\beta_{aca}-\beta_{bcb}-\beta_{caa}-\beta_{cbb})\langle\cos^3(\theta)\rangle] \\
\chi^{(2)}_{\perp\perp\perp} =& \frac{N_s}{2\epsilon_0}[(\beta_{aac}+\beta_{bbc}+\beta_{aca}+\beta_{bcb}+\beta_{caa}+\beta_{cbb})\langle\cos(\theta)\rangle \\
&+(2\beta_{ccc}-\beta_{aac}-\beta_{bbc}-\beta_{aca}-\beta_{bcb}-\beta_{caa}-\beta_{cbb})\langle\cos^3(\theta)\rangle].
\end{aligned} \tag{3.30}$$

For the symmetric stretching (v_1) and bending (v_2) modes the dipole moment changes in the c-direction, hence only hyperpolarizability elements with the last subindex c are active, i.e. β_{aac}, β_{bbc} and β_{ccc}. Similarly, for the antisymmetric stretching modes (v_3) the dipole moment changes in the a- or b-direction. Hence only hyperpolarizability elements with the third index equal to a or b contribute, i.e. β_{aca}, β_{bcb}, β_{caa}, and β_{cbb}.

These relations can be simplified when both the SF and VIS beams are off-resonance. In that case the Kleinman's conjecture[57–59] holds and the first two subindices of the hyperpolarizability are approximately symmetric on interchange [cf. Eq. (3.27)]:

$$\beta_{ijk} \approx \beta_{jik} \tag{3.31}$$

Under Kleinman's conjecture the relations simplify to

$$\begin{aligned}
\chi^{(2)}_{\parallel\parallel\perp} =& \frac{N_s}{4\epsilon_0}[(2\beta_{ccc} + \beta_{aac} + \beta_{bbc} - 2\beta_{aca} - 2\beta_{bcb})\langle\cos(\theta)\rangle \\
&- (2\beta_{ccc} - \beta_{aac} - \beta_{bbc} - 2\beta_{aca} - 2\beta_{bcb})\langle\cos^3(\theta)\rangle] \\
\chi^{(2)}_{\parallel\perp\parallel} = \chi^{(2)}_{\perp\parallel\parallel} =& \frac{N_s}{4\epsilon_0}[(2\beta_{ccc} - \beta_{aac} - \beta_{bbc})\langle\cos(\theta)\rangle \\
&- (2\beta_{ccc} - \beta_{aac} - \beta_{bbc} - 2\beta_{aca} - 2\beta_{bcb})\langle\cos^3(\theta)\rangle] \\
\chi^{(2)}_{\perp\perp\perp} =& \frac{N_s}{2\epsilon_0}[(\beta_{aac} + \beta_{bbc} + 2\beta_{aca} + 2\beta_{bcb})\langle\cos(\theta)\rangle \\
&+ (2\beta_{ccc} - \beta_{aac} - \beta_{bbc} - 2\beta_{aca} - 2\beta_{bcb})\langle\cos^3(\theta)\rangle].
\end{aligned} \tag{3.32}$$

Furthermore, for the point groups $C_{\infty v}$, C_{3v}, C_{4v}, and C_{6v} the hyperpolarizability tensor is symmetric in a and b, i.e. $\beta_{aac} = \beta_{bbc}$ and $\beta_{aca} = \beta_{bcb}$. For the C_{2v} group $\beta_{bcb} = 0$.[48]

The non-vanishing tensor elements for certain molecular groups with C_{nv} symmetry are given in Table I. The hyperpolarizabilities are normalized to the β_{ccc} element of the corresponding mode. The hyperpolarizabilities of the H_2O v_2 bending mode are one order of magnitude smaller than the hyperpolarizabilities of the H_2O v_1 stretching mode.[60] CH modes in an alkane chain have an opposite dipole moment derivative with respect to an OH mode,[61,62] yielding an opposite sign in the hyperpolarizabilities.[63] However, care has to be taken as the dipole moment derivative of a CH mode strongly depends on the residual group and sometimes even changes its sign.[64] The factor of 2 in $\beta^{CH_3}_{aca}$ should be applied in case the two antisymmetric stretch vibrations of the methylene group are degenerate.[48] For the CH_2 group, the term $2\beta_{ccc}-\beta_{aac}-\beta_{bbc}$ vanishes at the standard bond angle 109.5°.[65] For the water molecule the bond angle is 105° and $2\beta_{ccc} - \beta_{aac} - \beta_{bbc}$ is very small.[66] The CH, CH_2, and CH_3 hyperpolarizability elements have the following relative magnitudes: $\beta^{CH}_{ccc} = 4.4\beta^{CH_3}_{ccc}$ and $\beta^{CH}_{ccc} = 2.0\beta^{CH_2}_{ccc}$.[48]

Water molecules do not always possess C_{2v} symmetry because of hydrogen bonding. As the hydrogen bonds of a single water molecule may be different in strength/length, the two stretch modes (v_1 and v_3) can decouple and become local modes, as is the case for HDO. In that case the water molecule no longer possesses C_{2v} symmetry, but C_{1v} symmetry. When the localization is strong as for HDO, $C_{\infty v}$ symmetry may be assumed for the single OH/OD branches. The stretch vibration of the free OH bond for H_2O molecules at the air–water interface is weakly coupled to the stretch vibration of the other OH bond,[73] so strictly it neither possesses $C_{\infty v}$ nor C_{2v} symmetry. However, it can be well described with $C_{\infty v}$ symmetry.[66]

The orientation of molecules or molecular groups can be determined by comparing the relative strengths of the $\chi^{(2)}$ elements, which can be probed using different polarization combinations of the SF, VIS, and IR beams [see Eq. (3.24)]. A precise analysis of the SFG spectra requires the Fresnel factors

TABLE I: Non-zero independent hyperpolarizability tensor elements of different molecular modes

Group	Symmetry	Mode	Non-zero tensor elements [a.u.]
H_2O	C_{2v}	v_1	$\beta_{ccc} = 1$, $\beta_{aac} = 1.30$, $\beta_{bbc} = 0.56$ [66]
		v_3	$\beta_{aca} = 0.74$ [66]
		v_2	$\beta_{ccc} = 1$, $\beta_{aac} = -6.64$, $\beta_{bbc} = -2.47$ [67]
OH	$C_{\infty v}$	v_1	$\beta_{ccc} = 1$, $\beta_{aac} = 0.32$ [68, 69]
OH^-	$C_{\infty v}$	v_1	$\beta_{ccc} = 1$, $\beta_{aac} = 0.52$–0.79 [70]
CH	$C_{\infty v}$	v_1	$\beta_{ccc} = -1$, $\beta_{aac} = -(0$–$0.28)$ [71]
CH_2	C_{2v}	v_1	$\beta_{ccc} = -1$, $\beta_{aac} = -1.67$, $\beta_{bbc} = -0.33$ [48]
		v_3	$\beta_{aca} = -1.38$ [48]
CH_3	C_{3v}	v_1	$\beta_{ccc} = -1$, $\beta_{aac} = -(1.7$–$3.4)$ [72]
		v_3	$\beta_{aca} = -2 \cdot (0.37$–$4.5)$ [72]

and the experimental angles of incidence of the incoming VIS and IR beams. As a guideline for the identification of the vibrational modes and the orientation of the molecules, we can formulate rules of thumb following Wang et al. [48] The polarization dependencies are as follows for the CH_3 stretching modes:

(a) The v_1 mode is stronger in the *ssp*-polarization combination than in the *ppp*-, *sps*-, or *pss*-polarization combinations.

(b) The v_3 mode is weaker in the *ssp*- than in the *ppp*-polarization combination. For both polarization combinations the v_3 mode is maximal for the magic tilt angle $\theta = \arccos(1/\sqrt{3}) \simeq 54.7°$.

(c) In the *sps*- and *pss*-polarization combinations, the v_3 mode is largest and the v_1 mode is smallest for small tilt angles θ.

(d) In the *ssp*-polarization combination the v_1 and v_3 modes have opposite signs and negatively interfere whereas they have equal signs in the *ppp*-polarization combination.

For the stretching modes of H_2O and CH_2, the following dependencies hold:

(e) The v_1 mode is stronger in the *ssp*-polarization combination than in the *ppp*-polarization combination.

(f) The v_3 mode is weaker in the *ssp*-polarization combination than in the *ppp*-polarization combination.

(g) In the *sps*- and the *pss*-polarization combinations, the v_3 mode is much stronger than the v_1 mode. The v_3 mode is largest for small tilt angles θ in both polarization combinations.

(h) No v_1 strength in the *sps*- and the *pss*-polarization in case of CH_2 and only very little strength in case of H_2O.

(i) In the *ssp*-polarization combination the v_1 and v_3 modes have opposite signs and negatively interfere, whereas they have equal signs in the *ppp*-polarization combination.

For the stretching vibrations of OH and CH groups and of OH^-, the polarization dependencies are:

(j) Strongest in the *ssp*-polarization combination for large tilt angles θ.

(k) Strongest in the *ppp*-polarization combination for small tilt angles θ.

(l) The *sps*- and *pss*-polarization combinations are largest for the magic tilt angle $\theta \simeq 54.7°$.

Similar we have for the H_2O bending mode (v_2):

(m) Stronger in the *ssp*- than in the *ppp*-polarization combination.

(n) The mode is largest for the magic tilt angle $\theta \simeq 54.7°$ in the *sps*- and *pss*-polarization combinations.

(o) The mode is much weaker in the *sps*- and *pss*-polarization combinations than in the *ssp*- and *ppp*-polarization combinations for small tilt angles θ.

3.3.1 REAL AND IMAGINARY PART OF $\chi^{(2)}$

Omitting the tensorial indices, the frequency dependence of a resonant $\chi^{(2)}$ response of a single molecular transition $v \to w$ is given by [Eq. (3.26)]

$$\chi^{(2)} \propto \frac{1}{\omega_{wv} - \omega_{\mathrm{IR}} - i\Gamma_w/2}.$$

The response can be separated into a real and imaginary part, viz.

$$\frac{1}{\omega_{wv} - \omega_{\mathrm{IR}} - i\Gamma_w/2} = \frac{\omega_{wv} - \omega_{\mathrm{IR}}}{(\omega_{wv} - \omega_{\mathrm{IR}})^2 + \Gamma_w^2/4} + i\frac{\Gamma_w/2}{(\omega_{wv} - \omega_{\mathrm{IR}})^2 + \Gamma_w^2/4}. \tag{3.33}$$

The real and imaginary parts of $\chi^{(2)}$ for a single resonance are plotted in Fig. 3.7. $\mathrm{Re}\,\chi^{(2)}$ is an odd function in $(\omega_{wv} - \omega_{\mathrm{IR}})$, whereas $\mathrm{Im}\,\chi^{(2)}$ is an even function in $(\omega_{wv} - \omega_{\mathrm{IR}})$. This is in agreement with the Kramers–Kronig relations [Eq. (2.7)]. $\mathrm{Im}\,\chi^{(2)}$ can be interpreted as a surface absorption spectrum and the maximal response strength is found on resonance, i.e. when $\omega_{\mathrm{IR}} = \omega_{wv}$. Unlike a linear absorption spectrum, $\mathrm{Im}\,\chi^{(2)}$ can be positive or negative. The sign of $\mathrm{Im}\,\chi^{(2)}$ reflects the polar orientation of the transition dipole moment derivative revealing the molecular orientation. In a conventional SFG experiment one measures the squared magnitude $|\chi^{(2)}|^2$. For a single resonance, $|\chi^{(2)}|^2$ has the same spectral shape as $\mathrm{Im}\,\chi^{(2)}$, but the information of the polar orientation is lost by squaring. In case of multiple interfering resonances or the presence of a non-resonant background, the spectral shapes of $|\chi^{(2)}|^2$ and $\mathrm{Im}\,\chi^{(2)}$ are different and the spectral shape of $\mathrm{Im}\,\chi^{(2)}$ can only be retrieved by spectral fitting. However, the

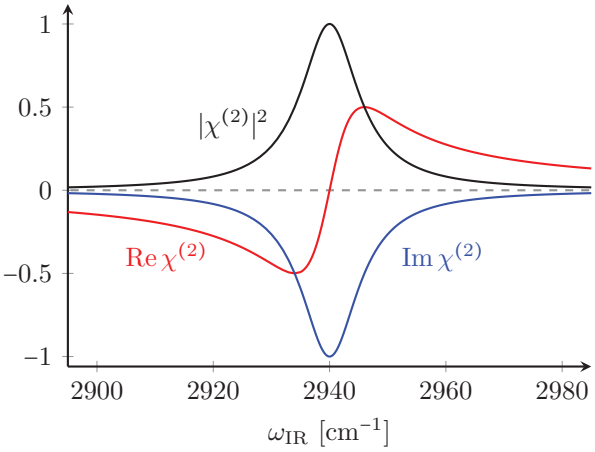

Figure 3.7: Real (red) and imaginary (blue) parts of a single $\chi^{(2)}$ resonance with a negative amplitude and a FWHM of 12 cm^{-1} as a function of the infrared frequency. The imaginary part of the second order susceptibility, Im($\chi^{(2)}$), has the same spectral shape as the squared magnitude, $|\chi^{(2)}|^2$ (black).

uniqueness of the fit is not ensured, especially when $\chi^{(2)}$ comprises a continuum of resonances like the OH stretches of hydrogen-bonded water.[74, 75] These problems can be circumvented by employing an experimental configuration in which the SF signal from the sample interferes with the SF signal generated at a local oscillator. This technique yields the phase of $\chi^{(2)}$ directly and is called phase-resolved SFG. We will discuss the theoretical and experimental approach of this technique in detail in Chapter 6.

3.3.2 Sum-frequency scattering

Sum-frequency signals can also be generated from non-planar interfaces. This method is used to probe the surface structure of dispersed particles with sum-frequency scattering experiments. In these experiments the IR and VIS beams are overlapped in a solution with dispersed particles and the SF signal is generated all around the particle's surface. Because of the phase difference at the detection point between the polarization components generated at different parts of the surface, the SF photons interfere and generate a scattering pattern (Fig. 3.8). The scattering pattern is depending on the polarization configuration, the particle size and shape, surface structure, and the experimental geometry.[76–79] The intensity of the SF light from particle n is proportional to the modulus squared of the effective particle susceptibility tensor $\chi^{(2)\sharp}_{\mathrm{eff},n}$, i.e.[82, 83]

$$I_{\alpha,n}(\omega_{\mathrm{SF}},\theta) \propto \left|\chi^{(2)}_{\mathrm{eff},\alpha\beta\gamma,n}(\omega_{\mathrm{SF}}=\omega_{\mathrm{IR}}+\omega_{\mathrm{VIS}},\theta)E_\beta(\omega_{\mathrm{IR}})*E_\gamma(\omega_{\mathrm{VIS}})\right|^2, \quad (3.34)$$

$^\sharp$In literature the effective particle susceptibility tensor is often denoted by $\Gamma^{(2)}_n$.[80–82]

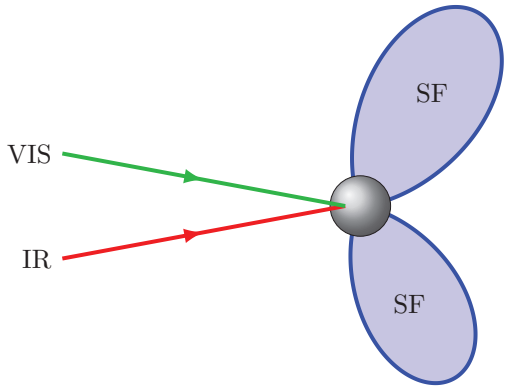

FIGURE 3.8: Schematic of a sum-frequency scattering experiment. A sum-frequency signal is generated at the surface of a particle (where $\chi^{(2)} \neq 0$). Interference of the signals generated at different parts gives rise to a scattering pattern.

where θ is the scattering angle. The total SF intensity is the incoherent sum of the SF intensities that are generated on the individual particles n,[79] i.e.

$$\begin{aligned} I_\alpha(\omega_{\mathrm{SF}},\theta) &= \sum_n I_{\alpha,n}(\omega_{\mathrm{SF}},\theta) \\ &\propto \sum_n \left|\chi^{(2)}_{\mathrm{eff},\alpha\beta\gamma,n}(\omega_{\mathrm{SF}}=\omega_{\mathrm{IR}}+\omega_{\mathrm{VIS}},\theta)E_\beta(\omega_{\mathrm{IR}})*E_\gamma(\omega_{\mathrm{VIS}})\right|^2 . \end{aligned} \tag{3.35}$$

In case the particles are homogeneous and all have the same effective particle susceptibility tensor, i.e. $\chi^{(2)}_{\mathrm{eff},n} = \chi^{(2)}_{\mathrm{eff}}$, the expression of the total SF intensity becomes equivalent to the previous obtained result for planar SFG [Eq. (3.28)]:

$$I_\alpha(\omega_{\mathrm{SF}},\theta) \propto \left|\chi^{(2)}_{\mathrm{eff},\alpha\beta\gamma}(\omega_{\mathrm{SF}}=\omega_{\mathrm{IR}}+\omega_{\mathrm{VIS}},\theta)E_\beta(\omega_{\mathrm{IR}})*E_\gamma(\omega_{\mathrm{VIS}})\right|^2 . \tag{3.36}$$

It is illustrative to examine the scattering pattern in the extreme case of particles with an infinitely small radius and collinear IR and VIS beams. Then a polarization is only created at a single point. Like an oscillating dipole, there is no emission in the forward direction and the scattered light will have the maximal intensity at an angle θ of 90°.[31] For particles with a finite radius and an arbitrary angle between the IR and VIS beams, non-linear Mie theory can be applied to calculate the scattering pattern.[76] The calculated scattering pattern for water droplets in air is given in Fig. 3.9.

The SF scattering signal increases with increasing particle size. For a spherical particle with radius r, the volume scales $\propto r^3$. For small particles with $r < c/\omega_{\mathrm{SF}}$, the scattering cross section scales $\propto r^6$.[76] Therefore, the SF scattering intensity of an emulsions with fixed volume fractions follows an r^3 dependence in the limit of small particles.

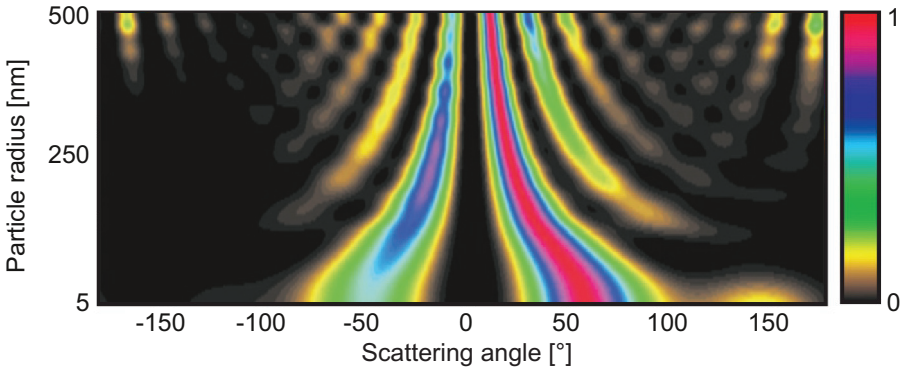

Figure 3.9: Computations of the SF scattering patterns for water droplets with in air as function of the particle radius and the scattering angle in the *ppp*-polarization combination. Every scattering pattern has been normalized to its respective peak value. The non-collinear scattering setup consists of source waves with a VIS wavelength of 800 nm and an IR wavelength of 2708 nm (3693 cm^{-1}) under a relative angle of 15°. Adapted with permission from de Beer and Roke.[76]

4 Anomalous temperature dependence of the vibrational lifetime of the OD stretch vibration

The temperature dependence of the vibrational T_1 lifetime of the OD stretch vibration of HDO in H_2O ice is measured using femtosecond mid-IR pump–probe experiments. We find an increase of T_1 from 480 ± 40 fs at 25 K to 860 ± 60 fs at 265 K. These lifetimes are remarkably shorter than the vibrational lifetime of the OD stretch vibration of HDO in H_2O in the liquid phase, which has a value of 1.7 ± 0.1 ps at 274 K and increases to 2.24 ± 0.09 ps at 343 K. The observed temperature dependence of T_1 can be well explained from a relaxation mechanism in which the OD vibration relaxes via energy transfer to the bend–libration combination tones of H_2O and HDO.

4.1 Introduction

The IR spectrum of water is strongly influenced by the formation of hydrogen bonds, which makes IR spectroscopy a powerful tool to study the properties of water molecules. The position, width, and intensity of the vibrational bands all depend on hydrogen-bond strength. [20] Especially the OH stretching vibrations of the water molecule are particularly sensitive to the local environment. [7]

In neat water the two OH stretch modes within the H_2O molecule are strongly coupled. In addition, these vibrations are coupled to other OH oscillators on nearby water molecules. These strong interactions make the OH stretch vibrations of pure water a far from ideal system to study the dynamics of individual water molecules. This study can best be performed with isotopically diluted water, i.e. dilute HDO in H_2O or D_2O, as the OH(OD) vibration of HDO will only be weakly coupled to the surrounding OD(OH) vibrations. [84]

The temperature dependence of the vibrational relaxation of the OH stretch vibration of dilute HDO in D_2O water and ice has been studied both experimentally [85–87] and theoretically, [88] and an anomalous increase of the vibrational lifetime with temperature was observed. The temperature dependence of the OD stretch of HDO in H_2O in the liquid phase has also been investigated, [89–91] and again an increase of the vibrational lifetime was found from 1.7 ± 0.1 ps at

274 K to 2.2±0.1 ps at 343 K. [89] Recently, the vibrational relaxation of this system has been studied in the ice phase at 80 and 258 K, [92, 93] but its temperature dependence has not yet been studied.

In this chapter we present a study on the temperature dependency of the OD stretch vibration of the HDO molecule in H_2O in the solid (ice I_h) phase. Combined with the results for the water regime obtained by Tielrooij et al. [89], we present and discuss the temperature dependence of the OD relaxation over the temperature range from 25 to 343 K. We also present a relaxation model that can explain the observations.

4.2 Experimental methods

The polycrystalline ice samples are prepared by inserting isotopic diluted water of 2 % D_2O in H_2O ($\triangleq$ 4 % HDO:H_2O) between two z-cut sapphire windows with a spacer of 10 μm. This dilution is low enough to prevent diffusion by resonant Föster energy transfer [87] and the samples show a desired transmission of about 10 % at the resonance frequency of the OD stretching vibration. The samples are frozen using a closed cycle cryostat (CTI-Cryogenics) with a stability of 0.5 K.

Linear absorption spectra are collected with a PerkinElmer 881 double-beam IR spectrometer. Infrared pump–probe spectroscopy measurements are performed on the OD stretch vibration of HDO in H_2O in the temperature range 25–265 K. The infrared pulses are generated using a commercial Ti:sapphire laser system (Coherent Legend) that delivers 3.5 mJ pulses at a wavelength of 800 nm and a repetition rate of 1 kHz. The 800 nm light is converted into mid-infrared light using non-linear crystals. This is done using two independent optical parametric amplifiers (OPAs) pumped by the 800 nm light. The infrared pump is produced by differential frequency mixing of a part of the 800 nm light with the doubled idler output (995 nm) produced by a commercial OPA (TOPAS Light Conversion). This process yields 10 μJ pulses at 4.1 μm (2450 cm^{-1}) with a bandwidth of 180 nm (110 cm^{-1}). The infrared probe is generated with a home-built OPA, consisting of two BBO-based amplification stages. The resulting signal and idler pulses are used in a difference-frequency mixing process in a $AgGaS_2$ crystal to produce pulses at 4.4 μm (2250 cm^{-1}) with a FWHM of 440 nm (220 cm^{-1}). From this beam two 100 nJ pulses are split off by ZnSe plates (8 % reflection). One of these pulses is overlapped with the pump beam in the sample, the other is used as a reference to correct for pulse-to-pulse fluctuations. The probe is sent over a delay stage with a resolution of 0.03 fs to vary the time delay between the pump and the probe. After the sample the probe and reference pulses are dispersed with an Oriel monochromator and detected by two 32-pixel liquid-nitrogen-cooled mercury cadmium telluride (MCT) arrays. The width of the cross-correlation of pump and probe is determined by a germanium plate to be 200 fs.

Every second pump pulse is blocked by a chopper wheel to determine the pump-induced absorption changes $\Delta\alpha$. Fluctuations in the probe intensity are

corrected for by a reference pulse in the following manner [cf. Eq. (3.9)]:

$$\Delta\alpha(\omega,t) = -\ln\left(\frac{I(\omega,t)I_{\mathrm{r},0}(\omega)}{I_0(\omega)I_{\mathrm{r}}(\omega)}\right), \tag{4.1}$$

where subscript 0 indicates the absence of the pump beam and subscript r denotes the reference beam. After the sample the probe beam passes through a rotating polarization filter which allows the selection of either the parallel or perpendicular component of the transient absorption, $\Delta\alpha_{\parallel}$ and $\Delta\alpha_{\perp}$, respectively. From these two signals the isotropic signal is constructed following Eq. (3.16).

The pump pulse is resonant with the $0 \rightarrow 1$ transition of the OD stretch vibration and excites a significant fraction (a few percent) to the first excited state. The population dynamics of the first excited state are probed with a probe pulse that covers the $1 \rightarrow 2$ transition. As a result, the measurements are not affected by scattered pump light falling on the probe array of the MCT detector, because the probe and pump pulse are dispersed differently by the monochromator. In addition, the population of the first excited state is directly probed without a contribution of the ground state recovery, which would be the case in case the transient signal at the $0 \rightarrow 1$ transition is be probed.[94]

4.3 Results

4.3.1 Linear absorption spectra

The linear absorption spectrum of HDO in H_2O at seven different temperatures is shown in Fig. 4.1. The spectrum shows two absorption peaks: a broad band centred at ~2200 cm^{-1} that can be assigned to a combination of the bend and libration (frustrated rotation) mode of H_2O (Fig. 4.1b), and a narrower peak centred at ~2450 cm^{-1} that is assigned to the OD stretch band of HDO (Fig. 4.1c).

The absorption strength and the centre frequency of the H_2O bend–libration combination both increase with decreasing temperature.[95–97] The absorption band of the OD stretch becomes narrower and its peak intensity becomes larger in the transition from the liquid to the solid phase. The narrowing results from the transition from the disordered liquid phase to the much more ordered and less inhomogeneous crystalline phase. The centre frequency of the OD stretch absorption band shifts to lower frequencies when the temperature is decreased. In addition, we observe an increase in the total absorption cross section σ_{tot} with decreasing temperature.

In a semiclassical approach with a classical treatment of the light the band strength or total cross section σ_{tot} can be expressed as:[21]

$$\sigma_{\mathrm{tot}} \equiv \int d\omega\, \sigma(\omega) = \frac{\pi}{3\hbar c\epsilon_0} \int d\omega \left|\frac{\partial \boldsymbol{\mu}(q)}{\partial q}\right|^2_{q=q_0} |\langle 1|\hat{q}|0\rangle|^2 \omega\, g(\omega), \tag{4.2}$$

where q is the vibrational coordinate, $\boldsymbol{\mu}$ the electric dipole moment, and $g(\omega)$ the distribution function that describes the initial spectral distribution of the vibra-

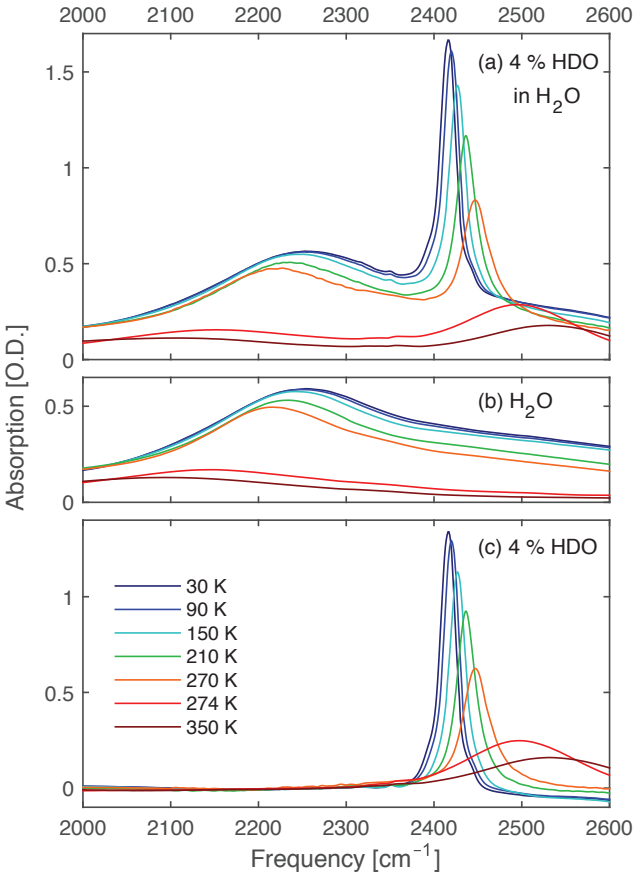

Figure 4.1: Linear absorption spectra of 4 % HDO in H_2O (a) and of H_2O (b) at seven different temperatures. The HDO spectrum (c) is obtained by subtracting the H_2O spectrum (b) from the HDO:H_2O spectrum (a). The H_2O spectrum contains the H_2O bend–libration combination (b) and the HDO spectrum gives sign of the OD stretch band of HDO (c). The sample thickness is ~10 μm.

tions ($\int d\omega\, g(\omega) = 1$). The hydrogen-bonding strength is temperature dependent and therefore the spectral shape and magnitude of the cross section also depend on temperature. The dipole moment derivative $\partial\boldsymbol{\mu}(q)/\partial q$ exhibits a strong non-Condon effect, meaning that its value strongly depends on the equilibrium position q_0 and thus on the strength of the local hydrogen-bond. [95, 98–101] Because of the increase in charge flux associated with the vibration, i.e. $\partial\boldsymbol{\mu}(q)/\partial q$, the integrated cross section increases with increasing hydrogen-bond strength and thus decreasing temperature. For the OD stretch vibration, this increase is close to linear within the liquid and solid phase. [98, 100]

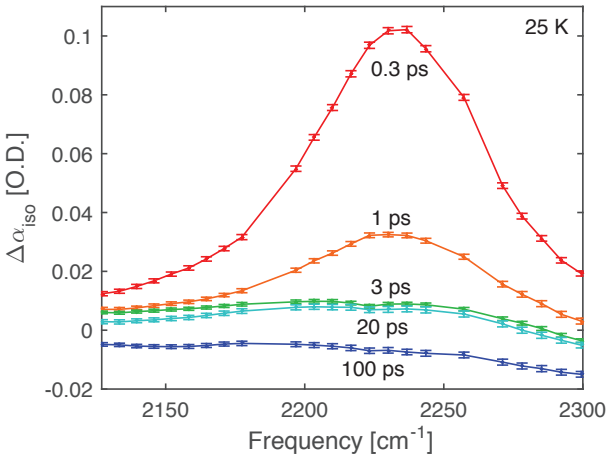

Figure 4.2: Transient absorption spectrum for different delay times at 25 K.

4.3.2 Vibrational energy relaxation dynamics

In Figure 4.2 a typical transient spectrum is shown. We observe an induced absorption that decays with increasing delay time. The subsequent thermalization of the vibrational energy leads to an absorption spectrum that differs from that of the initial state. The $1 \rightarrow 2$ transition of the OD stretch at 2230 cm^{-1} overlaps with the H_2O bend–libration combination (see Fig. 4.1b). However, this band is not observed in the transient spectrum because the (non-linear) transient absorption response scales approximately with the square of the cross section and the cross section of the H_2O bend–libration combination is much lower than that of the OD stretch vibration.

The transient spectra are fitted with a population relaxation model where the vibration decays exponentially and the heating effect grows in with the same rate. Up to 0.3 ps, the overlap between the pump and the probe pulses gives rise to artifacts due to coherent coupling and cross-phase modulation. After the vibrational relaxation is complete (after ~3 ps), we observe additional dynamics at timescales of 20–100 ps, which can be attributed to a thermally induced reorganization of the ice lattice.[102] Therefore, we fit the relaxation dynamics to the data in the time interval 0.3–3 ps. A typical fit result is shown in Fig. 4.3.

Based on linear difference spectra we estimate the local heating caused by energy deposition of the pump pulse to be maximally 10 K. The temperature jump due to the relaxation of the OD stretch vibration only takes place after the relaxation of the vibration, and therefore does not affect the lifetime. The direct excitation of the H_2O bend–libration combination by the pump pulse might lead to an early heating of a few degrees.

We performed measurements at different temperatures between 25–265 K. A selection of delay traces with corresponding fits are shown in Fig. 4.4. In this figure both uncorrected (Fig. 4.4a) and heat-subtracted delay traces (Fig. 4.4b)

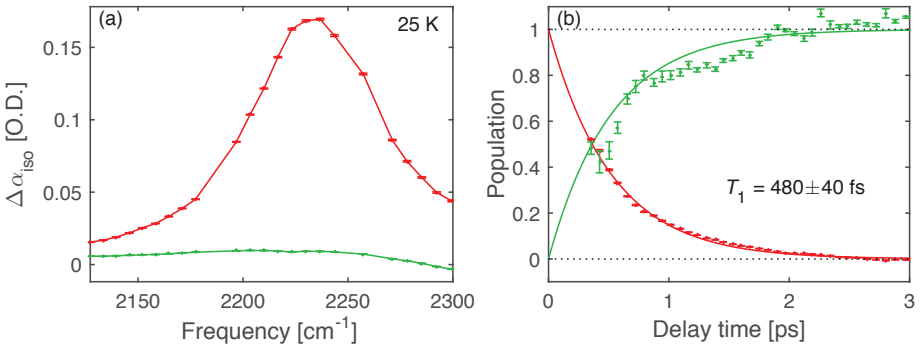

Figure 4.3: Spectral decomposition (a) and population dynamics (b) of the $1 \rightarrow 2$ transition of the OD stretch vibration (red) and the heated ground state (green) at 25 K.

are shown.

In Table II we present the fitted vibrational lifetimes T_1 at different temperatures, supplemented with the results in the liquid phase measured by Tielrooij et al. [89] These lifetimes are plotted as a function of temperature in Fig. 4.5.

Table II: T_1 lifetime of the OD stretch vibration of HDO in H_2O for different temperatures.

Solid phase		Liquid phase [89]	
Temperature [K]	T_1 [ps]	Temperature [K]	T_1 [ps]
25	0.48 ± 0.04	274	1.71 ± 0.10
35	0.49 ± 0.07	278	1.81 ± 0.10
40	0.48 ± 0.06	283	1.81 ± 0.10
80	0.48 ± 0.05	288	1.79 ± 0.03
130	0.56 ± 0.05	293	1.80 ± 0.02
160	0.59 ± 0.05	298	1.86 ± 0.03
180	0.66 ± 0.06	303	1.90 ± 0.06
200	0.71 ± 0.06	313	1.96 ± 0.08
225	0.75 ± 0.05	323	2.07 ± 0.13
250	0.80 ± 0.07	333	2.14 ± 0.04
265	0.86 ± 0.06	343	2.24 ± 0.09

The lifetime increases from 480 ± 40 fs to 860 ± 60 fs in the temperature range from 25 K to 265 K. At the solid-liquid transition, the lifetime increases by a factor of two to 1.7 ± 0.1 ps at 274 K. The vibrational lifetime at 80 K of 480 ± 40 fs is somewhat longer than the value previously found by Perakis et al. [92] In this study vibrational lifetimes of 410 ± 20 fs for the $0 \rightarrow 1$ transition and 360 ± 40 fs for the $1 \rightarrow 2$ transition were reported at this temperature. This difference could be due to a difference in the modelling of the rise of the thermal

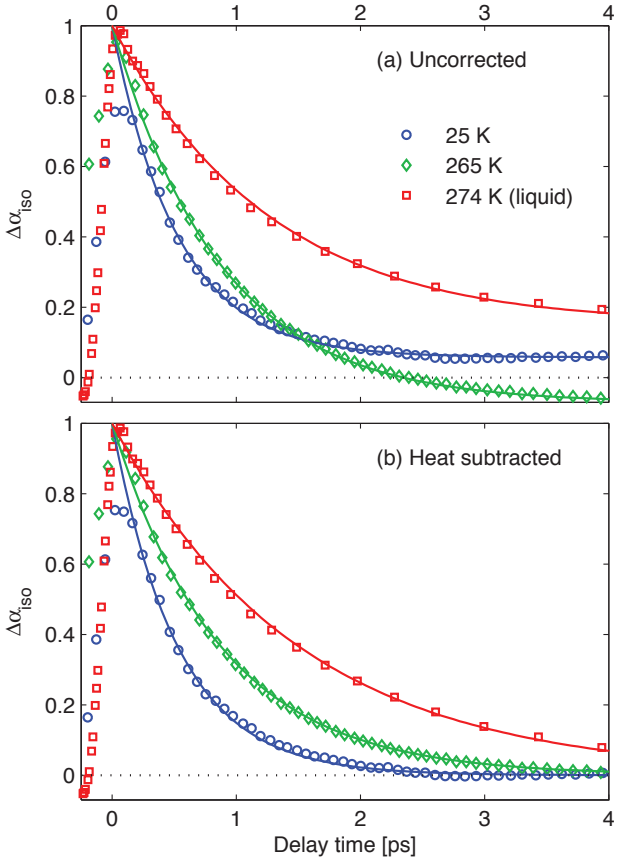

Figure 4.4: Uncorrected (a) and heat subtracted (b) normalized absorption changes as a function of delay time. The signals are at the centre frequency of the $1 \rightarrow 2$ transition of the OD stretch vibration of HDO at 25 K and 265 K. For comparison a measurement at 274 K in the liquid phase is included from Tielrooij et al.[89] The data are fitted with a monoexponential decay and heat ingrowth (see text). The fits yield lifetimes of 0.48 ± 0.04, 0.86 ± 0.06, and 1.7 ± 0.1 ps, respectively.

effect on the transient spectrum. We find that the relaxation does not slow down with decreasing temperature, as most theories for vibrational relaxation would predict.[103,104] In fact even the reverse is observed: the lower the temperature, the faster the vibrational decay. A similar anomalous temperature dependence of T_1 has been observed for the OH vibration of HDO in D_2O.[85–88]

4.3.3 Vibrational energy relaxation pathways

The vibrational lifetime is largely determined by non-radiative decay channels, see Section 2.3.2. The transfer probability to a specific channel depends on its spectral overlap, the amount of accepting modes, and the coupling strength with the initial vibration.

The OD stretch vibration is resonant with the H_2O bend–libration combination tone (see Fig. 4.1), and energy transfer to this combination tone forms a possible relaxation pathway. Another, similar relaxation channel is formed by energy transfer to the combination tone of the HDO bend vibration and a librational mode. This combination tone is redshifted by about 300 cm^{-1} with respect to the H_2O bend–libration combination.[105] Yet another relaxation channel is formed by energy transfer to the OD···O hydrogen-bond.[106] We do not have quantitative information about the specific coupling strengths of these three possible relaxation channels. However, we can determine the temperature dependencies of the three channels, and by comparing these to the experimental data we can get more information on their likeliness.

For the two relaxation channels to the H_2O and HDO bend–libration combination tones we can determine the temperature dependence of the relaxation rate from the effect of temperature on the spectral overlap of their respective absorption bands and the absorption band of the OD stretch vibration. Following Fermi's golden rule [Eq. (2.82)], the relaxation rate of the OD stretch vibration (v_1) to a bend–libration combination ($v_2 + L_2$) can be expressed in the following manner:

$$\frac{1}{T_1} = \frac{2\pi}{\hbar} \int d\omega \left| \langle 0_{v_1} 1_{v_2} 1_{L_2} | \hat{V}_{v_1, v_2+L_2} | 1_{v_1} 0_{v_2} 0_{L_2} \rangle \right|^2 g_{v_1}(\omega) \rho_{v_2+L_2}(\omega). \tag{4.3}$$

Here $g_{v_1}(\omega)$ is the spectral distribution of the OD stretch vibration ($\int d\omega\, g_{v_1}(\omega) = 1$) and $\rho_{v_2+L_2}(\omega)$ is the density of states of the bend–libration combination. In this expression we assume rapid spectral diffusion over the stretch band. This clearly is an approximation as the OD stretch vibration shows slow spectral diffusion components both in the liquid phase and the ice phase. However, the homogeneous linewidth is relatively large, especially in the ice phase.[107]

We assume the density of states of the H_2O $v_2 + L_2$ combination to be proportional to its spectral distribution, i.e. $\rho_{v_2+L_2}(\omega) \propto g_{v_2+L_2}(\omega)$. For the HDO $v_2 + L_2$ combination we take the spectral shape of the H_2O $v_2 + L_2$ combination band redshifted by 300 cm^{-1}. Furthermore, we assume the interaction potential responsible for the coupling to be proportional to the product of the local mode coordinates of the vibrations, i.e.

$$\hat{V}_{v_1, v_2+L_2} \propto \hat{q}_{v_1} \hat{q}_{v_2} \hat{q}_{L_2}. \tag{4.4}$$

Because the coordinate operators act on the corresponding states only, we can decompose the coupling matrix as follows,

$$\langle 0_{v_1} 1_{v_2} 1_{L_2} | \hat{q}_{v_1} \hat{q}_{v_2} \hat{q}_{L_2} | 1_{v_1} 0_{v_2} 0_{L_2} \rangle = \langle 0_{v_1} | \hat{q}_{v_1} | 1_{v_1} \rangle \langle 1_{v_2} 1_{L_2} | \hat{q}_{v_2} \hat{q}_{L_2} | 0_{v_2} 0_{L_2} \rangle. \tag{4.5}$$

Inserting this expression for Fermi's golden rule [Eq. (4.3)], we find that the relaxation rate is proportional to

$$\frac{1}{T_1} \propto \int d\omega \, |\langle 1_{v_1}|\hat{q}_{v_1}|0_{v_1}\rangle|^2 g_{v_1}(\omega) \, |\langle 1_{v_2} 1_{L_2}|\hat{q}_{v_2}\hat{q}_{L_2}|0_{v_2} 0_{L_2}\rangle|^2 g_{v_2+L_2}(\omega). \tag{4.6}$$

This equation can be rearranged to an expression for the spectral overlap of the cross sections of the OD stretch and the bend–libration combination bands, using Eq. (4.2)

$$\frac{1}{T_1} \propto \int d\omega \, \frac{\sigma_{v_1}(\omega)\sigma_{v_2+L_2}(\omega)}{\omega^2 \left\langle \left| \frac{\partial \boldsymbol{\mu}}{\partial q_{v_1}} \right|^2 \right\rangle_\omega \left\langle \left| \frac{\partial \boldsymbol{\mu}}{\partial q_{v_2+L_2}} \right|^2 \right\rangle_\omega}. \tag{4.7}$$

We take the spectral average of the squared dipole moment derivative $\langle|\partial\boldsymbol{\mu}/\partial q|^2\rangle_\omega$ proportional to the integrated cross section at each temperature. We fit this expression for both the H_2O $v_2 + L_2$ and HDO $v_2 + L_2$ bands to the measured lifetimes. The only free parameter in these fits is an overall scaling parameter, which is chosen to fit the data in the ice regime. The result of the fits is depicted by the red (HDO $v_2 + L_2$) and blue (H_2O $v_2 + L_2$) lines in Fig. 4.5.

For the relaxation channel to the OD···O hydrogen-bond the vibrational lifetime is highly correlated to the hydrogen-bond induced frequency shift $\delta\omega_{v_1}$ of the OD stretch vibration with respect to its gas phase value. This dependence has been described with a power law relation $T_1 \propto (\delta\omega_{v_1})^{-1.8}$.[106] To determine the hydrogen-bond induced frequency shift $\delta\omega_{v_1}$ we used the maximal value of the linear absorption spectrum (Fig. 4.1) and 2723.7 cm^{-1} as the gas phase OD stretching frequency.[108] The proportionality constant was again chosen to obtain the best fit to the data in the ice regime (green line in Fig. 4.5).

The results of Fig. 4.5 show that relaxation to the HDO $v_2 + L_2$ band yields a temperature dependence of T_1 that agrees surprisingly well with the experimental data in the ice phase. The relaxation channel to the H_2O $v_2 + L_2$ band provides a lower quality description of the temperature dependence of T_1 in the ice phase, but is superior in describing the change of T_1 at the phase transition from ice to water. Finally, the relaxation channel to the hydrogen-bond does not provide a quantitative description in either the ice or the water phase or at the transition between these phases.

4.4 Discussion

We considered three possible decay channels for the excited OD stretch vibration of HDO. The relaxation channel to the HDO bending–libration combination tone probably involves the strongest anharmonic coupling, as the HDO bending mode is located in the same molecule as the excited OD stretch vibration. On the other hand, the HDO bending–libration combination tone is redshifted by ~300 cm^{-1} with respect to the H_2O bending–libration combination tone, thereby introducing a significant energy gap with the OD stretch vibration and a spectral overlap that is ~3 times smaller. In addition, as the HDO molecule is

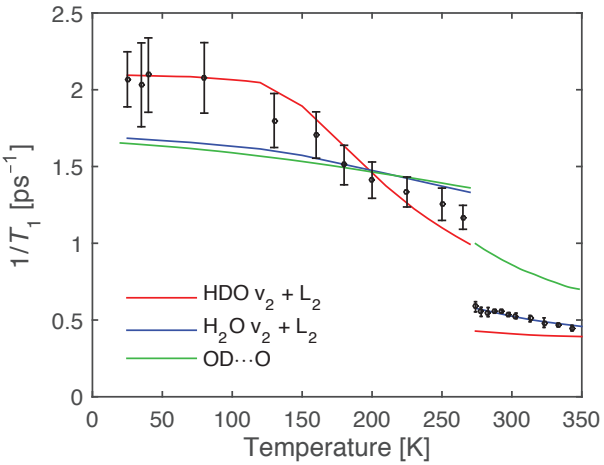

Figure 4.5: The lifetime of the OD stretch vibration of HDO as function of temperature. The data in the liquid water range (274–348 K) were published previously by Tielrooij et al.[89] The solid curves represent calculated lifetimes according to different theoretical models (explained in the text). Red: a decay via HDO bend–libration combination. Blue: a decay via the H_2O bend–libration combination. Green: a decay via the hydrogen-bond mode.

surrounded by H_2O molecules, the density of possible accepting HDO bending modes is obviously lower than that of H_2O bending modes, which will also favour relaxation to the H_2O bending–libration combination tone.

We found the experimentally observed temperature dependence of T_1 to be in excellent agreement with the temperature dependence of the relaxation channel to the HDO bend–libration combination, while the large change in T_1 at the phase transition from ice to water is best described by the relaxation channel to the H_2O bending–libration combination tone. These findings suggest that both relaxation channels may be important. It is even possible that relaxation to the HDO combination tone dominates in the ice phase, while relaxation to the H_2O combination tone is more important in the water phase. We think that relaxation to the hydrogen-bond mode can be excluded as a significant relaxation channel, as the expected temperature dependence of this relaxation channel poorly agrees with the experimental observations.

It is striking that the temperature dependence of the lifetime of the OD stretch of HDO in H_2O shows many similarities with the OH stretch lifetime of HDO in D_2O. In ice the OH stretch lifetime is a factor of two shorter than in the liquid phase.[86] In the liquid regime T_1 increases further from 740 ± 20 fs at 270 K to 900 ± 20 ps at 363 K.[86] The vibrational lifetime is determined by the available decay channels. Since a deuterium atom has twice the mass of a hydrogen atom, the OD stretch frequency is about a factor of 1.37 lower than the OH stretch frequency. Therefore, the vibrational relaxation channels of the OH and the OD vibration will likely differ. Whereas the OD stretch

vibration probably decays via the H_2O or HDO bend–librational combination, the dominant relaxation pathway of the OH stretch vibration likely involves the bend overtone ($v_2 = 0 \rightarrow 2$) of HDO.[109–111] Both mechanisms have in common that they become less probable when temperature increases owing to the redshift of the bending modes, thus yielding an increase in energy gap with the stretching modes. As a result, both relaxation mechanisms show an analogous (anomalous) temperature dependence.

4.5 Conclusions

We measured the vibrational energy relaxation dynamics of the OD stretch vibration of HDO in ice I_h at different temperatures. We observed an increase in lifetime from 480 ± 40 fs at 25 K to 860 ± 60 fs at 265 K, which is remarkably faster than the 1.7 ± 0.1 ps at 274 K in the water phase. The temperature dependence of the vibrational lifetime of the OD stretch vibration of HDO in H_2O is thus anomalous in both its condensed phases. This anomalous behaviour can be well explained from the decrease in spectral overlap of the OD stretch and the bend–libration combinations of H_2O and HDO vibration when temperature increases. This result suggests that these modes form the main accepting modes of the energy of the OD stretching vibration of HDO in H_2O.

5 Vibrational energy relaxation of water molecules in a hydrated lithium nitrate crystal

Water molecules in hydrated salts often have a well-defined geometrical arrangement and form an excellent model system for studying the effects of the hydrogen-bond environment on vibrational energy relaxation. Hydrated lithium nitrate contains two distinct types of crystal water molecules. One water molecule makes strong and weak hydrogen bonds, the other water molecule makes two bifurcated hydrogen bonds. We use femtosecond two-dimensional infrared spectroscopy to probe the vibrational relaxation dynamics of the OD stretch vibration of dilute HDO molecules in lithium nitrate trihydrate. In the temperature range from 22 to 295 K we observe a decrease in vibrational lifetime from 3.76 ± 0.16 to 2.83 ± 0.12 ps for the strongly hydrogen-bonded species, from 5.41 ± 0.08 to 4.14 ± 0.05 ps for the bifurcated hydrogen-bonded species, and from 10.4 ± 0.2 to 8.8 ± 0.4 ps for weakly hydrogen-bonded species. This temperature dependence is opposite to that of the OD stretch vibration of dilute HDO:H_2O ice, for which the vibrational lifetime increases from 480 ± 40 fs at 25 K to 850 ± 60 fs at 265 K. We discuss the origin of this difference in temperature dependence.

5.1 Introduction

The frequency of the OH stretching vibrations strongly depends on the hydrogen-bond strength: the stronger the hydrogen bond, the lower its frequency. [6] In liquid water a broad variation of hydrogen-bond strengths exists. The vibrational lifetime of the hydroxyl stretching modes shows a pronounced variation with frequency and thus with hydrogen-bond strength. [88, 112–114] The underlying mechanism of the vibrational relaxation remains an active field of study. [88, 109–111, 115, 116]

Recently, hydrated salts have emerged as a model system for studying the effects of the hydrogen-bond environment on vibrational energy relaxation. [117–120] Crystal water in hydrated salts has a well-defined geometrical arrangement with an accordingly well-defined hydrogen-bond strength. The IR

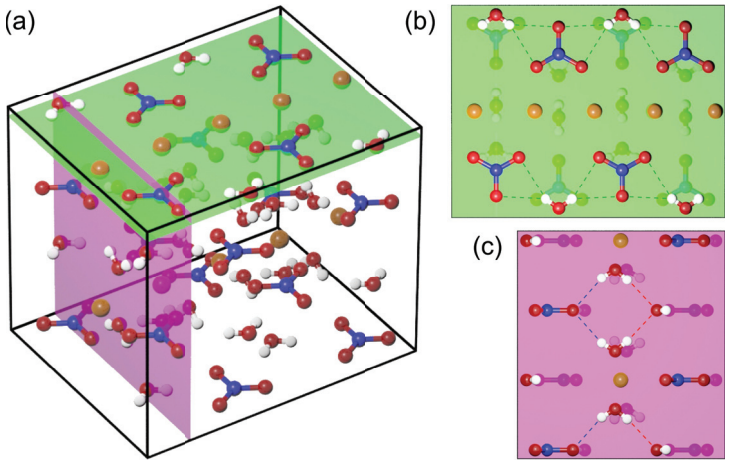

FIGURE 5.1: Crystal structure of lithium nitrate trihydrate.[128,129] The crystal structure belongs to the orthorhombic group D_{2h}^{17} (Cmcm) and has two different types of water molecules. The OH groups of the two types of water molecules lie in mutually perpendicular planes, which are projected in panels b and c for clarification. (b) Plane with the bifurcated hydrogen bonds (green dashed lines). (c) Plane with the strong hydrogen bonds (red dashed lines) and the weak hydrogen bonds (blue dashed lines). The colour scheme is as follows: H (white), Li (brown), N (blue), and O (red).

fingerprint of crystal water has recently led to the discovery of hydrated salts on Mars, demonstrating the presence of water on Mars.[121] Here we study the properties of water molecules present as crystal water in lithium nitrate trihydrate using femtosecond mid-infrared spectroscopy. Lithium nitrate contains crystal water with three different types of hydrogen bonds, leading to spectrally well-separated absorption lines of the OH stretch vibrations.[118,122,123] Lithium nitrate trihydrate is of interest as a thermal energy storage material because of its low melting point (30 °C) and its relatively large latent heat of fusion of 452 MJ/m^3 for the solid phase.[124–127]

The crystal structure of $LiNO_3{\cdot}3H_2O$ contains two different water species as illustrated in Fig. 5.1. The nitrate anion, lithium cation and one of the two non-equivalent water molecules lie in the crystal plane indicated as b in Fig. 5.1. This water molecule donates bifurcated hydrogen bonds to two oxygen atoms of a nitrate ion. Adjacent planes of type b are linked transversely by water molecules of the other type, forming the planes indicated as c in Fig. 5.1. One of the OH groups of this water molecule donates a relatively strong hydrogen bond to the water molecule in plane b, while the other OH group donates a relatively weak hydrogen bond to the nitrate ion. The vibrational lifetimes of the three distinct hydrogen-bonded OH stretch modes have been measured for HDO molecules in $LiNO_3{\cdot}HDO(D_2O)_2$ at a temperature of 220 K.[118,119]

In this chapter we study the temperature dependence of the vibrational

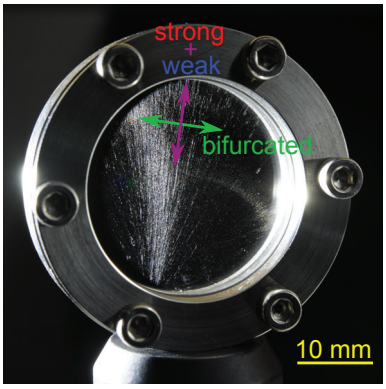

Figure 5.2: Lithium nitrate trihydrate crystal grown in a sprinkle shape from a nucleation point and the visible structure of the sample indicates the crystal orientation (see text).

energy relaxation of the three different hydroxyl vibrations. We perform this study by probing the OD stretch vibrations of HDO molecules embedded in $LiNO_3{\cdot}HDO(H_2O)_2$. We observe that the vibrational lifetime increases with decreasing temperature, opposite to what is observed for pure water and ice. We present a model that accounts for the observed temperature dependence of the relaxation.

5.2 Experimental methods

The lithium nitrate trihydrate samples are prepared as follows. A solution of 18.5 M $LiNO_3$ is dissolved in isotopically diluted water (10 % D_2O in H_2O). The $LiNO_3$ is fully dissolved by heating the solution above 304 K.[126] The solution is subsequently pressed between two z-cut sapphire windows, resulting in a sample thickness of ~5 μm. The hydrate is formed by lowering the temperature to 250 K in a closed cycle cryostat (CTI-Cryogenics) with a stability of 0.5 K. The lithium nitrate trihydrate crystal grows in a sprinkle shape from a nucleation point (see Fig. 5.2). Once the lithium nitrate trihydrate is formed, it remains stable up to its melting temperature of 303.3 K.[126]

By recording polarized IR transmission spectra of the sample using a FTIR microscope (Bruker Vertex 80v with Hyperion 3000) we have found that the macroscopic structure of the sample (Fig. 5.2) directly reflects the crystal orientation. The polarized linear spectra are shown in Fig. 5.3 and will be discussed in more detail below. The water molecules donating bifurcated hydrogen bonds lie in the plane perpendicular to the needle lines. The water molecules forming strong and weak hydrogen bonds lie in the plane parallel to the needle lines and perpendicular to the bifurcated water molecules hydrogen bonds. We measure unpolarized linear absorption spectra of the sample at different temperatures

with a PerkinElmer 881 double-beam IR spectrometer.

The vibrational dynamics of the OD stretch vibrations of the HDO molecules in the lithium nitrate crystal are studied with two-dimensional infrared (2D-IR) spectroscopy. These measurements are performed in the temperature range 22–295 K. The transient absorption of the OD stretch vibrations is measured as a function of the pump and probe frequencies and as a function of the time delay between the pump and probe pulses. The excitation from the ground state $v = 0$ to the first excited $v = 1$ state results in a transient spectrum. For each vibration this transient spectrum consists of a bleaching component, due to ground state depletion and stimulated emission of the $1 \rightarrow 0$ transition, and an induced absorption component corresponding to the $1 \rightarrow 2$ transition. The $1 \rightarrow 2$ transition has a lower frequency than the fundamental $0 \rightarrow 1$ transition because the vibrational potential of the OD stretch vibration is anharmonic.

The experimental setup is an upgraded version of the laser setup described in the previous chapter: The femtosecond Ti:sapphire laser system (Coherent Legend) delivers 3.7 mJ pulses at a wavelength of 800 nm and at a repetition rate of 1 kHz to generate mid-infrared pulses at ~4 μm that are resonant with the OD stretch vibrations of HDO. Approximately two-thirds of the laser output is used to generate the pump pulse, and one-third is used to generate the probe pulse. The pump pulse is generated with a commercial optical parametric amplifier (Spectra-Physics OPA-800C) with an additional amplification stage in BBO. The generated signal and idler pulses are subsequently difference-frequency mixed in $AgGaS_2$ yielding pulses in the mid-IR spectral region. The pump pulse has a central wavelength of 3.9 μm (2570 cm^{-1}), a FWHM of 410 nm (270 cm^{-1}), and a pulse energy of ~20 μJ. The pump pulse is sent into a Mach–Zehnder interferometer. The mirror in one of the two arms of the interferometer is placed on a motorized stage and its position is controlled with a fast scanning routine, as described by Helbing and Hamm.[130] The delay between the two split pump pulses is tracked with a HeNe beam aligned above the IR beams and a quadrature counter. One interferometric output is focused to a spot size of ~150 μm in the sample. The other interferometer output is focused onto a pyroelectric detector (Eltec 420M7-27) to record a linear interferogram of the pump pulse, which is used to calculate the absolute delay between the two pump pulses.

The probe pulse is generated in a home-built optical parametric amplifier with two BBO-based amplification stages. The generated signal and idler pulses are used in a difference frequency mixing process in a $AgGaS_2$ crystal to produce 3 μJ pulses at 4.0 μm (2500 cm^{-1}) with a FWHM of 600 nm (370 cm^{-1}). Using wedged ZnSe plates we split off two ~200 nJ pulses of the generated pulse. These pulses are the probe and reference pulse. The probe pulse is guided over a motorized delay stage to vary its time delay with respect to the pump pulse. The probe and reference pulses are focused to a spot of ~100 μm at different positions in the sample. The probe pulse is spatially overlapped with the pump pulse in the sample. The probe pulse has the same direction of polarization as the pump pulse.

Delay time zero is determined in a Ge plate and the cross-correlation time

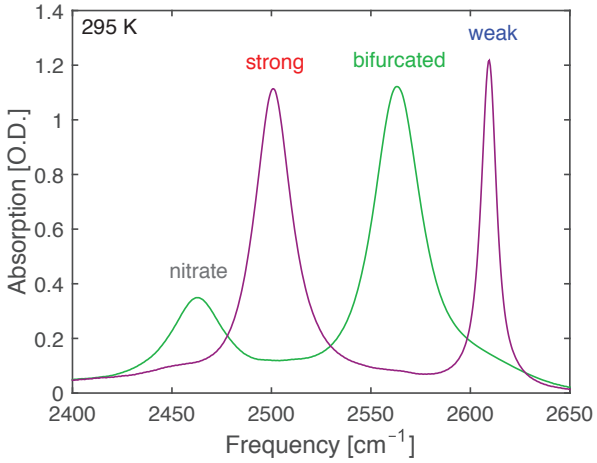

Figure 5.3: Polarized linear spectra at 295 K. In one polarization direction the OD stretch modes with strong and weak hydrogen bonds are observed (purple). In the other polarization direction the bifurcated hydrogen-bonded OD stretch modes are observed (green).

between the pump and probe pulses is ~250 fs. The reference is used to correct for pulse-to-pulse intensity and spectral fluctuations. After passing the sample the probe and the reference beams are dispersed with an Oriel monochromator and their spectrally resolved intensities are measured by two 32 pixel liquid-N_2-cooled MCT arrays. The pump frequency axis in the 2D spectrum is generated by Fourier transformation of the signal as a function of the delay between the two split pump pulses. Before Fourier transformation the time-domain is zero padded by a factor of 2 and multiplied with a Hamming window function.[23, 131] The 2D-IR setup is purged with nitrogen gas to reduce the strong CO_2 absorption around 2345 cm^{-1}. A librating CaF_2 window around the Brewster angle phase-cycles the pump pulse to average out interference effects between the probe pulse and scattered light of the pump pulse.[132]

5.3 Results

In Fig. 5.3 we present linear infrared absorption spectra for two distinct polarization directions of the infrared light. The spectra show the three distinct kinds of HDO molecules in the hydrated lithium nitrate crystal. We find a frequency of 2501 cm^{-1} with a FWHM of 23 cm^{-1} for the stretch vibration of the OD group with a strong hydrogen bond, 2563 cm^{-1} with a FWHM of 29 cm^{-1} for the stretch vibration of the OD group with a bifurcated hydrogen bond, and 2610 cm^{-1} with a FWHM of 9 cm^{-1} for the stretch vibration of the OD group with a weak hydrogen bond. The peak at 2463 cm^{-1} can be assigned

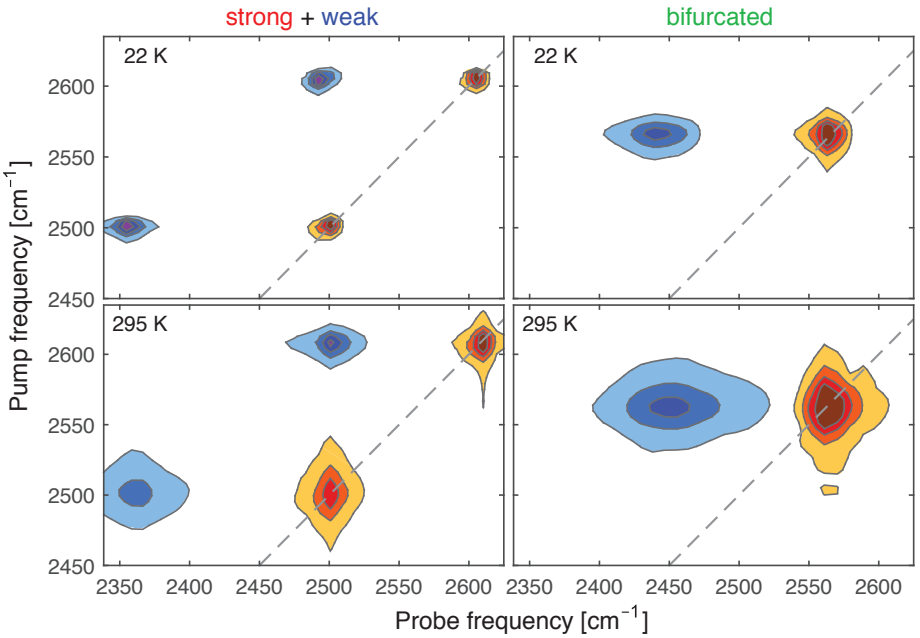

FIGURE 5.4: 2D-IR spectra at 22 and 295 K of the strongly and weakly hydrogen-bonded OD groups (left) and the bifurcated hydrogen-bonded OD groups (right). The delay between the pump and probe pulses is 0.5 ps. The positive absorption changes are shown in red, and the negative absorption changes are shown in blue. The colour steps correspond to a 10 % intensity increase and are truncated at 70 % of the maximal transient absorption differences. The spectra show distinct resonances and no cross-peaks.

to a combination of two stretch vibrations of the nitrate ion.[133] The cross section of the nitrate band is low in comparison with the OD modes. Therefore, it is not observed in the nonlinear spectrum because the transient absorption response scales approximately with the cross section squared (see Section 3.2). The observation that the OD modes can be completely suppressed by changing the polarization points out that the crystal grows in such a way that planes b and c in Fig. 5.1 are perpendicular to the window.

We measure 2D-IR spectra with the pump and probe pulses polarized parallel to the plane of the OD groups with strong and weak hydrogen bonds and with the pump and probe pulses polarized parallel to the plane of the OD groups with bifurcated hydrogen bonds. The spectra are measured at eight different temperatures. In Fig. 5.4 we present 2D-IR spectra measured at temperatures of 22 and 295 K for a delay of 0.5 ps between the pump and probe pulses.

In Fig. 5.5 we show transient absorption spectra for pump frequencies that correspond to the maxima of the bleaching signals of the weakly, bifurcated, and strongly bonded OD groups shown in the 2D spectra of Fig. 5.4. Besides

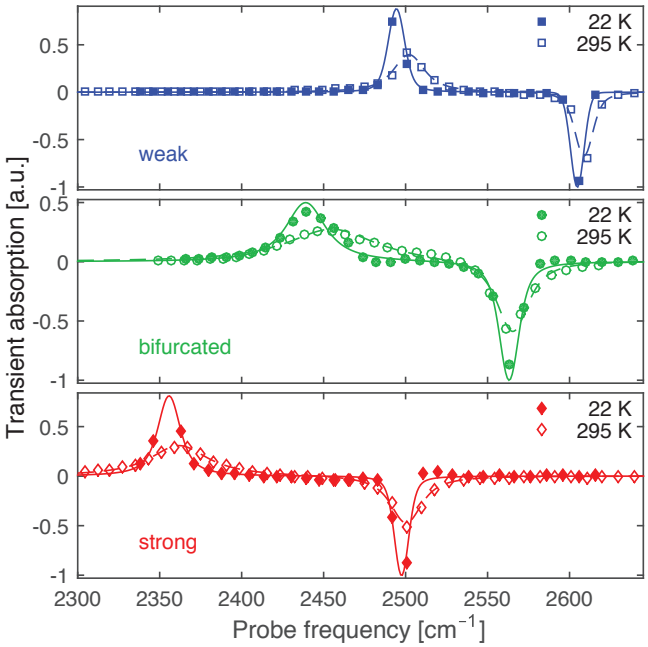

FIGURE 5.5: Normalized slices at pump frequencies that correspond to the maximal bleaching signals of the weakly, bifurcated, and strongly bonded OD groups of the 2D spectra from Fig. 5.4. The transient spectra are fitted by two Lorentzian functions at 22 K (solid line and filled symbols) and at 295 K (dashed line and open symbols).

the $0 \rightarrow 1$ bleaching signals, the transient spectra also show the presence of the $1 \rightarrow 2$ excited state absorption bands. These bands are redshifted with respect to the fundamental $0 \rightarrow 1$ transition by 139 cm^{-1} for the OD group with a strong hydrogen bond, 110 cm^{-1} for the OD group with a bifurcated hydrogen bond, and 107 cm^{-1} for the OD group with a weak hydrogen bond. The $1 \rightarrow 2$ excited state absorption bands are about 2–3 times broader than the $0 \rightarrow 1$ bleaching signals. Possible explanations for this additional broadening are the short vibrational lifetime of the $v = 2$ state [23] and the quantum nature of the hydrogen bonds [92].

The vibrational lifetimes are determined by fitting the decay of the $1 \rightarrow 2$ excited state absorption signals. For this purpose the areas of the $1 \rightarrow 2$ induced absorption bands are integrated for each delay time. The resulting signal is plotted as a function of delay and fitted between 0.5 and 100 ps with a population relaxation model in which the vibration decays exponentially and a heating effect grows in with the same rate. In Fig. 5.6 we present delay traces at 22 and 295 K. The vibrational lifetimes T_1 resulting from the fit are listed in Table III. The errors represent 95 % confidence intervals of the fitting procedure.

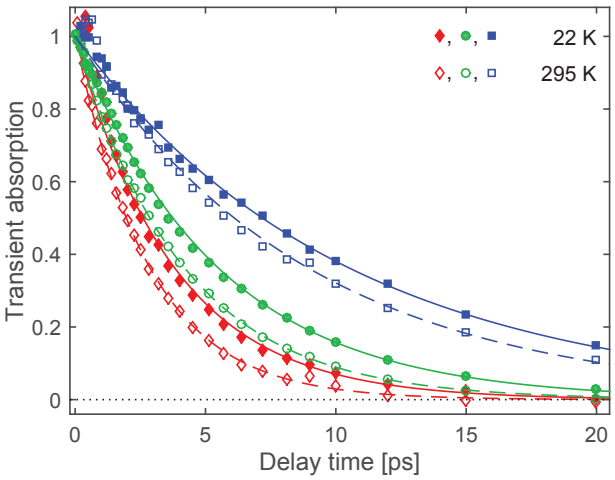

FIGURE 5.6: Fitted normalized absorption changes as a function of delay for the OD groups with strong (red), bifurcated (green) and weak (blue) hydrogen bonds, at 22 K (solid line and filled symbols) and at 295 K (dashed line and open symbols).

TABLE III: T_1 vibrational lifetimes of the three distinct hydrogen-bonded OD stretch vibrations of HDO in lithium nitrate trihydrate at different temperatures.

Temperature [K]	T_1 [ps]		
	strong	bifurcated	weak
22	3.76 ± 0.16	5.41 ± 0.08	10.4 ± 0.2
60	3.58 ± 0.15	5.20 ± 0.16	9.9 ± 0.3
100	3.47 ± 0.05	5.2 ± 0.2	10.8 ± 0.2
140	3.30 ± 0.08	5.19 ± 0.13	7.8 ± 0.8
180	3.27 ± 0.11	4.65 ± 0.13	10.3 ± 0.9
220	3.07 ± 0.18	4.54 ± 0.11	9.1 ± 1.8
250	3.13 ± 0.08	4.35 ± 0.07	9.1 ± 0.3
295	2.83 ± 0.12	4.14 ± 0.05	8.8 ± 0.4

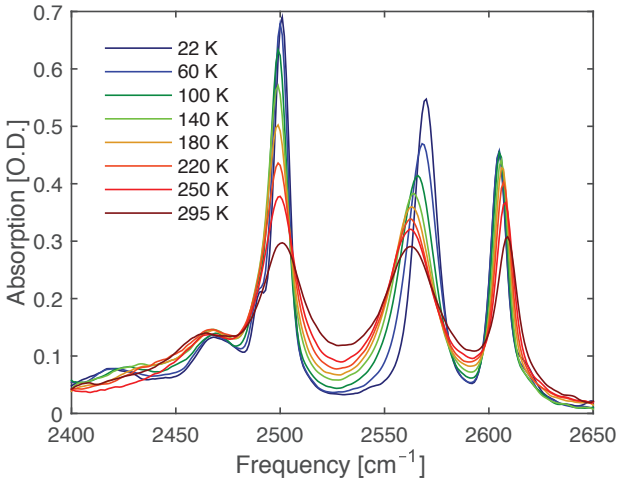

Figure 5.7: Unpolarized linear infrared absorption spectra of $LiNO_3{\cdot}HDO(H_2O)_2$ at different temperatures. The line widths of the OD stretch vibrational absorption bands increase when temperature rises.

5.4 Discussion

From Table III it is clear that the vibrational lifetime of the OD stretch vibration in lithium nitrate trihydrate is shorter for the OD groups with strong hydrogen bonds than that for the OD groups with bifurcated hydrogen bonds, which are in turn shorter than that for the OD groups with weak hydrogen bonds. This observation agrees with the typical behaviour of the hydroxyl stretch vibration of decreasing vibrational lifetime with increasing hydrogen-bond strength, as observed in bulk liquid water,[88,112–114] frozen reverse micelles,[134] and zeolites.[135] We find that the vibrational lifetimes of the OD stretch vibrations of HDO molecules in lithium nitrate trihydrate are ~3 times larger than the lifetimes of the OH stretch vibration, which are at 220 K 1.1 ± 0.1, 1.9 ± 0.2, and 3.4 ± 0.3 ps for strongly, bifurcated, and weakly hydrogen-bonded OD groups, respectively.[119]

We observe a decrease of the vibrational lifetime with increasing temperature for all three hydrogen-bonded OD stretching modes. The vibrational energy relaxation rate is determined by the coupling and spectral overlap with (combination tones) of other modes that accept the energy. For the OD vibration of HDO molecules in dilute $HDO{:}H_2O$ ice, the temperature dependence of the vibrational lifetime of the OD stretching vibration in ice could be well accounted for by considering the temperature dependence of the spectral overlap of the excited OD vibration and a single accepting combination mode.

TABLE IV: Peak positions (ω_{v_1}) and FWHM line widths (Γ_{v_1}) of the three different hydrogen-bonded OD stretch vibrations of HDO in lithium nitrate trihydrate at different temperatures determined from the linear spectra shown in Fig. 5.7.

Temperature [K]	strong		bifurcated		weak	
	ω_{v_1} [cm^{-1}]	Γ_{v_1} [cm^{-1}]	ω_{v_1} [cm^{-1}]	Γ_{v_1} [cm^{-1}]	ω_{v_1} [cm^{-1}]	Γ_{v_1} [cm^{-1}]
22	2501	8	2570	13	2605	8
60	2500	9	2568	17	2605	8
100	2499	10	2566	20	2605	8
140	2499	12	2564	22	2606	8
180	2499	15	2563	24	2606	8
220	2499	18	2562	26	2607	9
250	2500	21	2563	28	2608	10
295	2500	30	2562	34	2609	12

Using Fermi's golden rule [Eq. (2.82)], the relaxation rate of the OD stretch vibration (v_1) to a single accepting (combination) mode can be expressed as

$$\begin{aligned}\frac{1}{T_1} &= \frac{2\pi}{\hbar}\iint d\omega\, d\omega'\, |\langle f|\hat{V}_{v_1,a}|i\rangle|^2 g_{v_1}(\omega)\rho_a(\omega')\delta(\omega-\omega') \\ &= \frac{2\pi}{\hbar}\int d\omega\, |\langle f|\hat{V}_{v_1,a}|i\rangle|^2 g_{v_1}(\omega)\rho_a(\omega),\end{aligned} \tag{5.1}$$

where $g_{v_1}(\omega)$ is the spectral distribution of the OD stretch vibration ($\int d\omega\, g_{v_1}(\omega) = 1$), $\rho_a(\omega)$ the density of states of the acceptor mode, and $\langle f|\hat{V}_{v_1,a}|i\rangle$ the coupling matrix element between the final and initial states. The Dirac delta function ensures conservation of energy. In this expression we assume rapid spectral diffusion due to fluctuations in the thermal bath. Assuming the density of states of the acceptor mode to be proportional to its spectral distribution, i.e. $\rho_a(\omega) \propto g_a(\omega)$, and the coupling strength to be independent of frequency, we arrive at

$$\frac{1}{T_1} \propto |\langle f|\hat{V}_{v_1,a}|i\rangle|^2 \int d\omega\, g_{v_1}(\omega) g_a(\omega). \tag{5.2}$$

When the two spectral distributions have Lorentzian line shapes, the overlap integral can be calculated analytically, i.e.

$$\int d\omega\, g_{v_1}(\omega) g_a(\omega) = \frac{2}{\pi}\frac{\Gamma_{v_1}+\Gamma_a}{4(\omega_{v_1}-\omega_a)^2+(\Gamma_{v_1}+\Gamma_a)^2}, \tag{5.3}$$

where ω_{v_1} and Γ_{v_1} are the centre frequency and FWHM of the OD stretch mode, and ω_a and Γ_a denote the centre frequency and FWHM of the acceptor mode. The relaxation rate of the OD stretch vibration is then proportional to

$$\frac{1}{T_1} \propto |\langle f|\hat{V}_{v_1,a}|i\rangle|^2 \int d\omega\, \frac{\Gamma_{v_1}+\Gamma_a}{4(\omega_{v_1}-\omega_a)^2+(\Gamma_{v_1}+\Gamma_a)^2}. \tag{5.4}$$

We fit the experimentally observed vibrational relaxation rates with a model in which we assume that the three OD groups relax to the same acceptor mode. This acceptor mode is assumed to have a Lorentzian shape and to be temperature independent. We fit the spectral position and the width of the acceptor mode. In the fitting we calculate the spectral overlap of the three OD vibrations with the acceptor mode. The positions and widths of the OD stretch modes are determined from the linear spectra shown in Fig. 5.7 and given in Table IV. In the fitting we take the value of the coupling strength $|\langle f|\hat{V}_{v_1,a}|i\rangle|^2$ to be equal for the strong and the weak hydrogen bonds, as they are situated on the same type of water molecules in the crystal structure. The coupling matrix element of the bifurcated hydrogen-bonded OD group is allowed to be different from that of the strong and weak hydrogen bonds. The results of the fit are plotted in Fig. 5.8. We find the ratio of the coupling strengths of the strong/weak:bifurcated hydrogen bonds to be 1:1.3. The accepting mode resulting from the fit is centred at 2354 ± 12 cm^{-1} with a FWHM of 65 ± 17 cm^{-1}. Hence, the three OD modes and the found accepting mode only weakly overlap. Therefore, the OD modes and the accepting modes are only brought into resonance due to spectral diffusion caused by thermal bath fluctuations. We do not observe any IR active mode in the spectral range 2200–2400 cm^{-1}. However, it is likely that the accepting mode is a combination band composed of several excitation quanta in different vibrations, which makes it invisible in the infrared and Raman spectra. The HDO and H_2O bending modes have frequencies of about 1460 cm^{-1} and 1650 cm^{-1}, respectively.[136] Therefore it appears likely that the accepting mode is a combination of the $v = 1$ of the HDO or H_2O bending mode in combination with one or two quanta in low-frequency intermolecular modes.

The observed temperature dependence is opposite to what has been observed for the vibrational lifetime of the OD stretch vibration of HDO molecules in dilute HDO:H_2O ice, for which the vibrational lifetime increases from 480 ± 40 fs at 25 K to 850 ± 60 fs at 265 K (see previous chapter), although a similar relaxation mechanism is proposed. For HDO:H_2O ice, the line width of the OD stretch increases when the temperature rises, and the peak position of the excited OD stretch vibration increases from 2415 cm^{-1} at 20 K to 2447 cm^{-1} at 270 K, i.e. on average 0.13 cm^{-1}/K. As a result, the spectral overlap of the absorption band of the OD vibration with the absorption band of the bending and libration combination mode decreases, thus explaining the increase of the vibrational lifetime with increasing temperature. For $LiNO_3{\cdot}HDO(H_2O)_2$ the change in peak position of the OD vibrations with temperature is one order of magnitude smaller than for dilute HDO:H_2O ice; hence, the change of the vibrational lifetime is dominated by the increase of the line width rather than the peak position (see Table IV). As this line width increases with temperature, the overlap with a combination band of the bending and low-frequency modes increases, which thus explains the observed decrease of the vibrational lifetime when temperature increases.

In studies of the vibrational relaxation of hydroxyl groups in crystals[137,138] the relaxation was described to occur via crystal vibrations that are assumed to be harmonic. The temperature dependence of the relaxation was described with

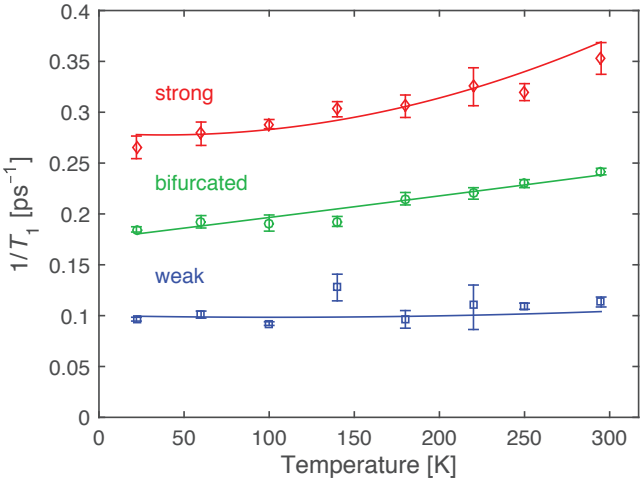

FIGURE 5.8: Vibrational lifetimes of the OD stretch vibrations of HDO molecules in three different hydrogen-bond configurations in lithium nitrate trihydrate as a function of temperature. The lifetimes are fitted utilizing Eq. (5.4), using the central frequencies and line widths of the different OD vibrations obtained from the linear absorption spectra, which yields a Lorentzian-shaped accepting mode centred at 2354 ± 12 cm^{-1} with a FWHM of 65 ± 17 cm^{-1}.

the multi-phonon relaxation model of Nitzan et al.[103,139] In this model the accepting mode is formed by a combination tone that consists of a number of low-frequency phonon excitations. The model describes a strong increase in the vibrational relaxation rate with temperature as a result of the increased thermal occupation of the harmonic phonon modes. Due to the harmonic character of the phonon modes, the vibrational amplitudes of these modes increase when they are thermally excited, and these larger amplitudes lead to an increase of the anharmonic coupling with the excited hydroxyl vibration, thus accelerating the vibrational relaxation.

Following the model of Nitzan et al.[103,139] the value of the coupling matrix element $\langle f|\hat{V}_{v_1,a}|i\rangle$ of Eq. (5.4) is expected to increase with temperature, because the accepting modes get thermally excited. We did not include such a temperature dependence in modelling the data, and assumed the coupling matrix element to be temperature independent. For all three OD vibrations the temperature dependence of T_1 can be well explained from the temperature dependence of the spectral overlap of the excited OD vibrations and an accepting mode that likely consists of a bending mode in combination with low-frequency intermolecular modes of the water molecule (librations, hydrogen-bond stretch vibrations). For this accepting mode the coupling matrix element is indeed expected to show very little temperature dependence in the temperature range 22–295 K. The HDO and H_2O bending modes have frequencies of about 1460 cm^{-1} and 1650 cm^{-1}, respectively,[136] both being much larger than the thermal excitation energy k_BT (corresponding to 205 cm^{-1} at 295 K). This implies that the thermal excitation of the bending mode is negligible over the whole studied temperature range of 22–295 K. Hence, an increase in temperature from 22 to 295 K will lead to a negligible thermal excitation of this mode and thus negligible acceleration of the vibrational relaxation. The intermolecular librational and hydrogen-bond modes have much lower frequencies and their thermal occupation will increase in the studied temperature range. However, these modes are strongly anharmonic, showing a double-well potential,[38,140] which means that the vibrational amplitude will not strongly increase when the temperature is raised. Hence, for an accepting mode that consists of the $v = 1$ state of the bending mode and a few quanta of excitation in low-frequency intermolecular water modes, the assumption of a temperature independent coupling appears to be justified, at least at relatively low temperatures up to 295 K.

The present results show that the vibrational relaxation mechanism of the OH stretching vibrations of water is quite anomalous, even when the water molecules are contained in a highly-ordered crystal structure. While most high-frequency vibrations like covalently bound hydroxyl vibrations[137,138] relax via multi-phonon decay, following the relaxation model of Nitzan et al.[103,139], water molecules relax via the bending mode vibration in combination with anharmonic low-frequency intermolecular modes. This relaxation mechanism leads to a very different temperature dependence of the relaxation that in some cases, even leads to a deceleration of the relaxation with temperature, as we found in the previous chapter for the OD stretching vibration of HDO in neat H_2O.

5.5 Conclusions

We studied the vibrational dynamics of the OD stretch vibrations of HDO molecules in lithium nitrate trihydrate. Water molecules are located in the hydrated lithium nitrate crystal at specific positions, leading to hydroxyl groups with three different well-defined hydrogen-bond interaction strengths, including hydroxyl groups with strong hydrogen bonds, weak hydrogen bonds, and bifurcated (intermediate) hydrogen bonds. We measured the vibrational lifetimes of the OD stretch vibrations over a wide temperature range from 22 to 295 K. The vibrational lifetime of the strongly hydrogen-bonded OD groups is shorter than that for the bifurcated hydrogen-bonded OD groups, which in turn is shorter than that for the weakly hydrogen-bonded OD groups. For all three types of OD groups, the vibrational lifetime decreases when temperature increases: from 3.76 ± 0.16 ps at 22 K to 2.83 ± 0.12 ps at 295 K for the strongly hydrogen-bonded species, from 5.41 ± 0.08 ps at 22 K to 4.14 ± 0.05 ps at 295 K for the bifurcated hydrogen-bonded species, and from 10.4 ± 0.2 ps at 22 K to 8.8 ± 0.4 ps at 295 K for the weakly hydrogen-bonded species. This temperature dependence can be well explained from an increase in the line width of the OD stretch absorption bands when temperature increases and the resulting increase in spectral overlap with a single (combination) accepting mode centred at 2354 ± 12 cm^{-1} with a FWHM of 65 ± 17 cm^{-1}. This accepting mode likely consists of the $v = 1$ state of the H_2O or HDO bending vibration in combination with one or two quanta in low-frequency intermolecular modes.

6 Probing the molecular surface structure of ice with phase-sensitive sum-frequency generation spectroscopy

The surface structure of ice is studied between 150–245 K using phase-resolved sum-frequency generation, which measures the second-order surface susceptibility $\chi^{(2)}$. At 150 K we observe a correspondence between 5 modes in the surface spectrum with modes in the analogue bulk spectra, indicating a strong influence of vibration couplings on the $\chi^{(2)}$ spectrum of ice. The mode associated with the bilayer-stitching bonds (3110 cm^{-1}) is observed to be phase-rotated, consonant with the previous reported quadrupole contribution of this mode. The surface spectrum contains two modes at higher frequencies that are not present in the IR and Raman bulk spectra. These modes are assigned to the outermost water molecules that have an incomplete hydrogen-bond configuration. When temperature increases, the features in the modes in the $\chi^{(2)}$ spectrum become less pronounced, which likely results from a decrease in the intermolecular couplings due to an increasing disorder of the surface. Starting from a temperature of ~185 K, the $\chi^{(2)}$ response strongly increases with temperature around 3400 cm^{-1} which is not observed for the Raman and IR spectra, probably due to the formation of a premelted layer at the surface of ice.

6.1 Introduction

Ice plays a key geophysical role. Glaciers shape the Earth's surface, and ice particles in the atmosphere facilitate the occurrence of lightning and the depletion of the ozone layer.[13,141–143] At least 16 distinct crystalline phases of ice exist,[144] but the only stable phase that naturally occurs on the Earth surface is ice I_h.[145] Ice I_h has a crystal structure of hexagonal prisms as is illustrated in Fig. 1.3. The oxygen atoms lie on a wurtzite lattice. The hydrogens are distributed quasi-randomly following the Bernal–Fowler ice rules.[146] These rules state that each oxygen is covalently bonded to two hydrogen atoms, and that the surrounding water molecules are oriented in such a way that only one hy-

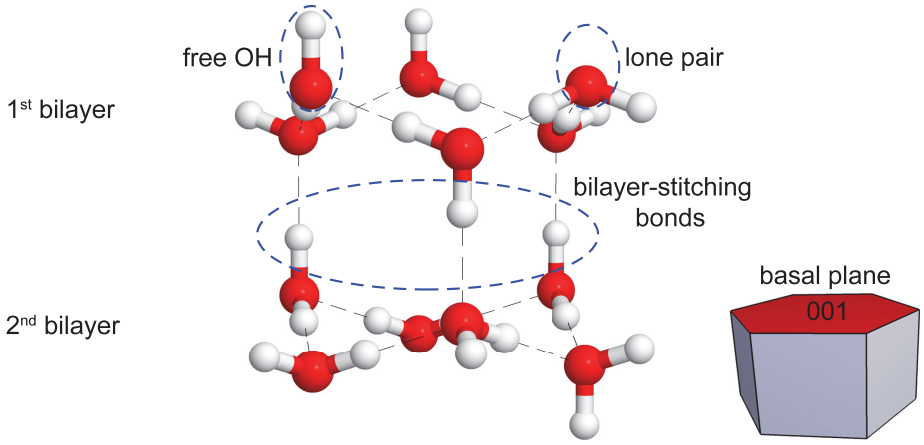

FIGURE 6.1: Fragment of the crystalline basal surface of ice I_h. Bilayers are formed by water molecules in a chair configuration. The bilayers are interconnected by stitching bonds. The upper part of the 1st bilayer consists of water molecules with a free OH group and of water molecules with a lone pair.

drogen atom lays between each pair of oxygen atoms. At the surface the crystal structure terminates, leaving the outermost water molecules with an incomplete hydrogen-bond configuration.

At low temperatures the surface of ice is highly ordered: the basal plane of ice I_h has a full-bilayer termination and the outer molecules have either a free OH group or an oxygen atom with a free electron pair as illustrated in Fig. 6.1.[147–149] Starting from a temperature of 180–200 K[69,150] a limited amount of surface disorder is observed to set in, finally resulting in a premelting of the surface at temperatures just below the bulk melting point.[12] This premelted layer governs many chemical and physical processes.[13]

In order to acquire a better understanding of the molecular surface structure of ice we study the surface of basal ice with phase-resolved SFG spectroscopy. SFG spectroscopy is an ideal tool as it combines surface-selectivity with molecular sensitivity. Since SFG is an even-order ($\chi^{(2)}$) non-linear optical process, SFG is bulk-forbidden for water and ice under the electric dipole approximation.[75,151] The frequency of the SFG signal of the OH stretching vibrations is strongly correlated with the strength of the hydrogen bonds,[7,84] providing insights in the molecular configuration at the surface. Previously, the surface properties of ice have been studied with conventional intensity SFG spectroscopy.[69,151–155] Here we will employ an even more powerful method: phase-resolved SFG. In this technique the sum-frequency (SF) signal is interfered with a local oscillator, thus enabling a direct determination of the amplitude and the phase of the generated SF electric field. The SFG field can be directly related to the amplitude and phase of the second-order susceptibility $\chi^{(2)}$ (conventional SFG determines $|\chi^{(2)}|^2$), which allows a direct identification of the surface vibrational resonances. Moreover, phase-resolved SFG allows

the separation between the resonant part of the signal and the non-resonant background, which simplifies the interpretation.[73] In this chapter we will use phase-resolved SFG to investigate the surface of ice between 150 and 245 K.

6.2 Experimental methods and analysis

Monocrystalline ice is grown by applying the method of seed extraction from the melt:[156] A monocrystalline seed is frozen to a copper pin. The copper pin is cooled by a processor cooler (LD PC-V2) and the temperature is initially set to 270 K by adjusting the current through a resistance. The surface of the seed is molten by a heat gun. Thereupon the seed is dipped in a pan with ultrapure water maintained at 273.8 K and allowed to grow in the melt. After one hour, the seed is pulled from the melt with 5 mm/hour. Meanwhile the temperature of the copper pin is gradually decreased to 240 K. After 10 hours, a crystal of height ~50 mm and diameter ~70 mm is produced (Fig. 6.2a). The crystal is stored in a freezer for further handling.

The ice crystal is cut into convenient parts by a bandsaw (Proxxon MBS 240/E) with a nickel-plated saw. One piece is frozen to an aluminum bar for convenient handling. A slice is cut off to determine the orientation of the basal plane using a Rigsby stage (Fig. 6.2b) following the procedure described in the Appendix. Next the ice is cut to the correct crystal orientation. A smooth surface is obtained by repeatedly shaving the ice using a blade of cemented carbide (Fig. 6.2c). Best results are obtained by shaving at a freezer temperature of ~270 K with the blade heated to ~300 K. A piece of ~4 mm thickness is cut off and used in the experiment.

The SFG measurements are carried out using a closed temperature cell that is cooled with liquid N_2 and allows transmittance of the laser beams through a CaF_2 window (Fig. 6.2d). The desired temperature is set by a heating foil resistance covered by a copper plate. The ice sample is placed on the copper plate. A temperature sensor is welded onto the ice surface with a water droplet in order to accurately monitor the surface temperature. For reference purposes a z-cut quartz crystal is placed adjacent to the ice. After positioning, the sample cell is thoroughly flushed with N_2 gas in order to remove the deposited frost that enters during the loading of the sample cell. The sample cell can be moved in the horizontal plane by two motorized actuators (Thorlabs) to prevent the accumulation of heat and damage of the ice crystal during the measurements.

The laser source for the SFG experiments is a regenerative Ti:sapphire amplifier system (Coherent Legend) delivering 35 fs pulses with a pulse energy of 3.2 mJ at a wavelength of 798 nm (FWHM 70 nm) and a repetition rate of 1 kHz. The VIS pulse is prepared by transmitting 20 % of the amplifier output through an etalon to reduce its spectral bandwidth, yielding a 15 μJ pulse with a FWHM of 0.9 nm (15 cm^{-1}). The IR pulse is generated by the other 80 % of the amplifier output power in a home-built OPA with two BBO-based amplification stages. The generated signal and idler pulses are difference-frequency mixed in a $AgGaS_2$ crystal, producing 5 μJ broadband pulses centred at 3.0 μm

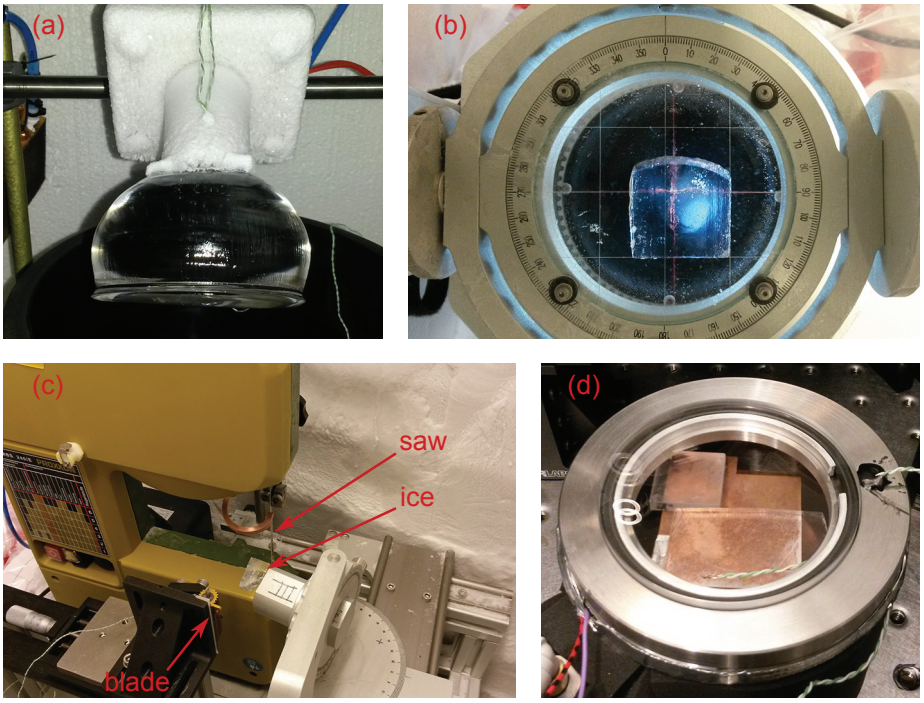

Figure 6.2: Ice growth and sample preparation. (a) Monocrystalline ice is grown by seed extraction from the melt. (b) The basal plane orientation is determined using a Rigsby stage. (c) Correctly oriented ice is shaved by a blade to smoothen the surface. Subsequently the sample is cut off by a bandsaw. (d) The ice sample in the sample cell. A thermocouple on the ice monitors the surface temperature. A z-cut quartz crystal is placed adjacent to the ice for reference purposes.

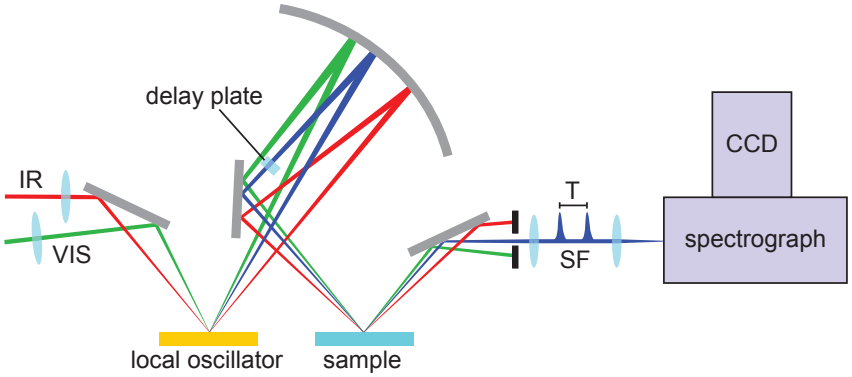

FIGURE 6.3: Schematic of the phase-resolved SFG setup.

(3300 cm^{-1}) with a FWHM of 600 nm (650 cm^{-1}). The VIS and IR pulses are set to *s*- and *p*-polarizations, respectively, using a combination of a $\lambda/2$-plate and a polarizer.

The geometry of the phase-resolved SFG setup is depicted in Fig. 6.3. First the IR and VIS pulses are spatially overlapped on a gold surface to generate broadband sum-frequency light, which is used as local oscillator. Then the pulses are refocused by a concave mirror onto the sample surface with angles of incidence of 44° and 39° for the IR and VIS, respectively. The SF signal stemming from the local oscillator is delayed by $T \simeq 2$ ps by transmission through a glass plate and creates an interference pattern with the SF signal generated at the sample, of which the *s*-polarization component is dispersed by a grating and recorded with a CCD camera. The detected intensity spectrum is proportional to

$$\begin{aligned} I(\omega_{\mathrm{SF}}) \propto\ & |E_{\mathrm{sample}}(\omega_{\mathrm{SF}}) + r_{\mathrm{sample}}(\omega_{\mathrm{SF}}) E_{\mathrm{LO}}(\omega_{\mathrm{SF}}) \mathrm{e}^{i\omega_{\mathrm{SF}}T}|^2 \\ =\ & |E_{\mathrm{sample}}(\omega_{\mathrm{SF}})|^2 + |r_{\mathrm{sample}} E_{\mathrm{LO}}(\omega_{\mathrm{SF}})|^2 \\ & + r^*_{\mathrm{sample}}(\omega_{\mathrm{SF}}) E_{\mathrm{sample}}(\omega_{\mathrm{SF}}) E^*_{\mathrm{LO}}(\omega_{\mathrm{SF}}) \mathrm{e}^{-i\omega_{\mathrm{SF}}T} \\ & + r_{\mathrm{sample}}(\omega_{\mathrm{SF}}) E^*_{\mathrm{sample}}(\omega_{\mathrm{SF}}) E_{\mathrm{LO}}(\omega_{\mathrm{SF}}) \mathrm{e}^{i\omega_{\mathrm{SF}}T}, \end{aligned} \tag{6.1}$$

where r is the reflection coefficient,[31] and E_{LO} and E_{sample} are the sum-frequency fields of the local oscillator and sample, respectively. The cross terms are responsible for the interference pattern and contain the phase information. Because the cross terms carry a phase factor owing to the delay T, they can be isolated by Fourier filtering in the time domain.[63] The term with positive time is extracted and divided by the corresponding term of a reference spectrum measured on z-cut quartz. The resulting quotient is proportional to the ratio of the frequency-dependent second-order susceptibilities of the sample ($\chi^{(2)}_{\mathrm{sample}}$)

and the frequency-independent susceptibility of quartz ($\chi^{(2)}_{\text{quartz}}$):

$$\frac{r^*_{\text{sample}} E_{\text{sample}} E^*_{\text{LO}} \mathrm{e}^{-i\omega_{\text{SF}} T}}{r^*_{\text{quartz}} E_{\text{quartz}} E^*_{\text{LO}} \mathrm{e}^{-i\omega_{\text{SF}} T}} = \frac{r^*_{\text{sample}} F_{\text{sample}}}{r^*_{\text{quartz}} F_{\text{quartz}}} \frac{\chi^{(2)}_{\text{sample}}}{i\chi^{(2)}_{\text{quartz}}}. \tag{6.2}$$

The F factors are dispersive constants comprising the product of geometrical factors and Fresnel factors.[48,63,157] The latter can be calculated using literature values of the optical constants.[16,158,159] For ice, the infrared optical constants are taken at the closest determined temperature[158] and the effective refractive index of the interfacial layer is calculated using a slab model.[44] The factor i in front of $\chi^{(2)}_{\text{quartz}}$ reflects the bulk origin of the quartz response, which causes a 90° phase-shift with respect to a surface response.[157,160,161] The bulk $\chi^{(2)}$ value of quartz is taken to be $8 \cdot 10^{-13}$ m V^{-1} and the coherence length is calculated to be ~40 nm for our experimental configuration.[162] The achieved $\chi^{(2)}_{\text{sample}}$ is independent of experimental parameters. The *ssp*-polarization configuration of the SF, VIS, and IR beams yields the $\chi^{(2)}_{\parallel\parallel\perp}$ component, with the projections of the parallel Raman polarizability in the surface plane and the IR transition dipole moment perpendicular to the surface plane.

Linear absorption spectra are obtained with a PerkinElmer 881 double-beam IR spectrometer. The sample is prepared by pressing a water droplet between two sapphire windows. The sample is placed in a cryostat where the desired temperature is set.

6.3 RESULTS AND DISCUSSION

The real and imaginary parts of $\chi^{(2)}$ of basal ice at 150 K are shown in Fig. 6.4a. The imaginary part of $\chi^{(2)}$ contains direct information on the resonances. The real part of $\chi^{(2)}$ complements the imaginary part, and contains additionally a negative non-resonant background contribution.[163] A $\chi^{(2)}$ resonance is proportional to the product of its Raman and IR transition moments [Eq. (3.26)]. Since $\chi^{(2)}$ is an even-order optical response, only surface vibrations contribute to the $\chi^{(2)}$ response under the electric dipole approximation. The sign of $\operatorname{Im}\chi^{(2)}$ reflects the net orientation of the transition dipole moment of the corresponding OH mode, e.g. the positive $\operatorname{Im}\chi^{(2)}$ response at 3694 cm^{-1} corresponds to non-hydrogen-bonded OH groups sticking out of the surface.

Although the surface modes possibly differ from the bulk modes, it is insightful to compare the $\chi^{(2)}$ spectrum with the bulk Raman and IR line shapes (Fig. 6.4b–c). Together, the IR and Raman bulk spectra exhibit five main resonances, at about 3110, 3150, 3228, 3350, and 3420 cm^{-1} (as indicated by the vertical dashed lines),[165] which we label from low to high frequency by I–V. Although all modes are both Raman and IR active, peaks I, III, IV, and V are apparent in the Raman spectrum, and peaks II–IV are observable in the IR spectrum. These features are caused by strong and weak couplings between OH oscillators on different molecules,[165–167] and do not directly refer to species

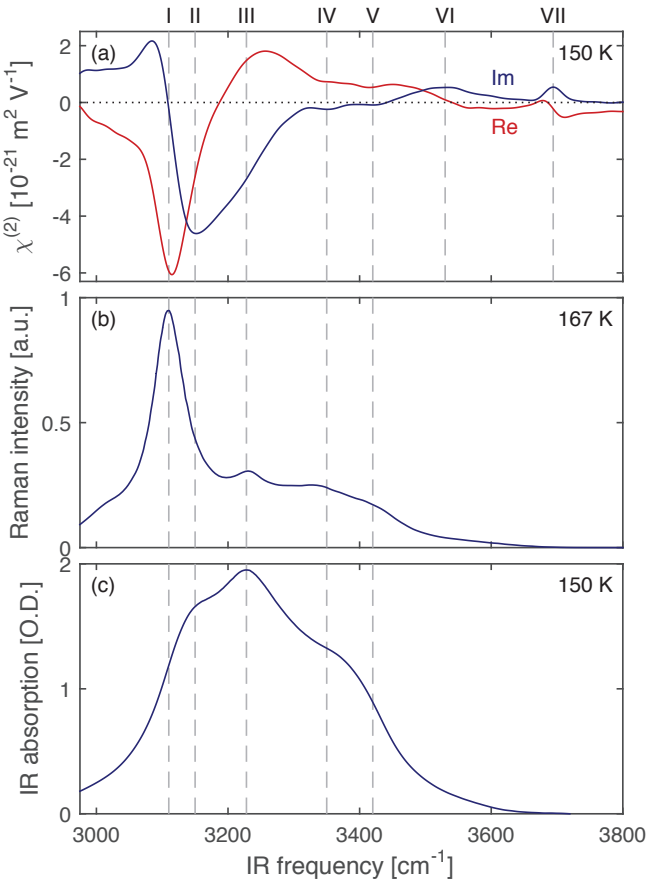

FIGURE 6.4: (a) Real and imaginary parts of $\chi^{(2)}_{\parallel\perp}$ of basal ice at 150 K. (b) Parallel-polarized Raman spectrum (aa) of basal ice at 167 K.[164] (c) IR absorption spectrum of polycrystalline ice at 150 K.

with a certain hydrogen-bond strength. In particular the strong Raman peak I has been assigned to a collective in-phase vibration.[165,167,168] Peaks II–V can also be observed in the Im $\chi^{(2)}$ spectrum and have negative amplitudes. Peak I does not coincide with a mode in the Im $\chi^{(2)}$ spectrum, but it does coincide with a strong peak in the Re $\chi^{(2)}$ spectrum. SFG experiments using the polarization null-angle method have shown that peak I (with a frequency of 3098 cm^{-1} at 113 K) contains a significant quadrupole component.[151,169] Hence, mode I has been associated with the bilayer-stitching hydrogen bonds (see Fig. 6.1), which form numerous oppositely aligned dipoles (constituting quadrupoles).[169] This mode has a significant bulk component,[154,169] which has a 90° phase-shift in the $\chi^{(2)}$ response with respect to a pure surface response.[161,170,171] Hence, the bulk component causes the $\chi^{(2)}$ response to be phase-shifted by a value close to 90°. This explains the correspondence of peak I with a peak in the real part

of $\chi^{(2)}$ and the dispersive line shape of $\mathrm{Im}\,\chi^{(2)}$ around 3100 cm^{-1} (cf. Fig. 3.7). Peaks II–V remain unassigned.

The $\chi^{(2)}$ response shows additional bands at 3530 cm^{-1} (peak VI) and 3694 cm^{-1} (peak VII) that are not present in the IR and Raman bulk spectra. The latter mode can be assigned to non-hydrogen-bonded free OH groups that are sticking out of the ice surface. We assign the 3530 cm^{-1} band to water molecules with 2 donor and 1 acceptor hydrogen bonds. A similar band has been observed in the $\chi^{(2)}$ spectrum of liquid water.[73, 172] The OH groups of these molecules are oriented with both hydrogen atoms pointing away from the surface (see Fig. 6.1), and intramolecular coupling gives rise to an antisymmetric mode contributing positively to $\mathrm{Im}\,\chi^{(2)}$ in an *ssp*-polarization configuration. Similar water molecules are present at the surface of basal ice (see Fig. 6.1). A purely parallel mode would in fact be $\chi^{(2)}$ inactive.[155, 173] The 3530 cm^{-1} mode can be observed because it is coupled to OH vibrations of neighbouring water molecules. As these neighbouring water molecules constitute a highly asymmetric environment in the direction perpendicular to the surface, the transition dipole moment acquires a non-zero perpendicular component, therefore making the 3530 cm^{-1} mode observable in the $\chi^{(2)}$ spectrum.

In Fig. 6.5 the $\chi^{(2)}$ response is shown at several temperatures in the range 150–245 K. The spectra exhibit a strong temperature dependence. All modes shift to higher frequency when temperature increases. This can be explained by a weakening of the hydrogen-bonds.[167] Surprisingly, we also observe a shift in the frequency of the non-hydrogen-bonded free OH mode from 3694 cm^{-1} at 150 K to 3700 cm^{-1} at 245 K (Fig. 6.6). This shift can be explained from the coupling of this mode to the companion OH group that is located on the same water molecule. The latter OH group is hydrogen bonded and this hydrogen bond weakens when temperature increases. Hence, the difference in frequency between the two OH oscillators becomes smaller, leading to a stronger frequency splitting due to intramolecular coupling.[73] As a result, the free OH mode shifts to higher frequency when temperature increases.

The amplitude of the low frequency modes I–III decreases when the temperature rises. In particular the bilayer-stitching mode (I) exhibits a strong temperature dependence and has been reported to gain further strength below 150 K.[153] The strong temperature dependence of the $\chi^{(2)}$ response has been explained by a decreasing order of the crystal structure with increasing temperature leading to a less strong delocalization of the OH stretch vibrations.[169, 174, 175] The bulk Raman spectrum shows a comparable decrease in spectral intensity when temperature increases.[166, 176]

The spectral features of the $\chi^{(2)}$ spectrum become less pronounced at higher temperatures. Modes I–III combine into a single broad band. Moreover, modes IV and V, quite distinct at 150 K, broaden and converge into a single broad feature at higher temperatures. There is also a strong increase in amplitude around 3400 cm^{-1} when temperature increases. The available Raman spectra[164, 167] also display the merge of modes IV and V, but do not show an increase in amplitude. Temperature dependent IR absorption spectra are shown in Fig. 6.7 and exhibit only a slight increase in amplitude around 3400 cm^{-1} when the

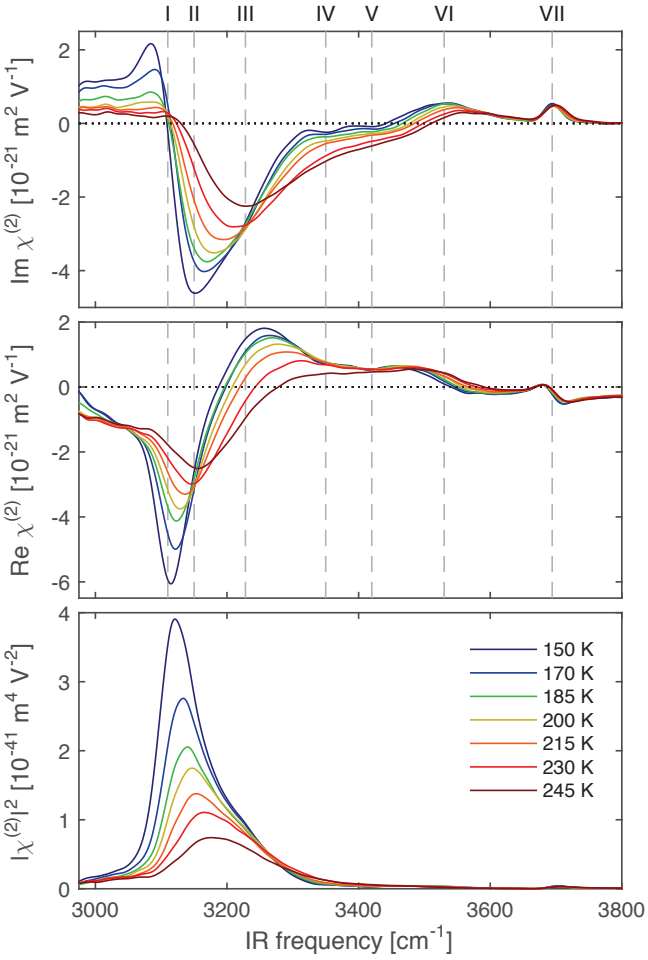

FIGURE 6.5: $\chi^{(2)}$ spectrum of basal ice at different temperatures. The top panel shows the imaginary component ($\mathrm{Im}\,\chi^{(2)}$), the central panel the real component ($\mathrm{Re}\,\chi^{(2)}$), and the bottom panel the squared amplitude ($|\chi^{(2)}|^2$).

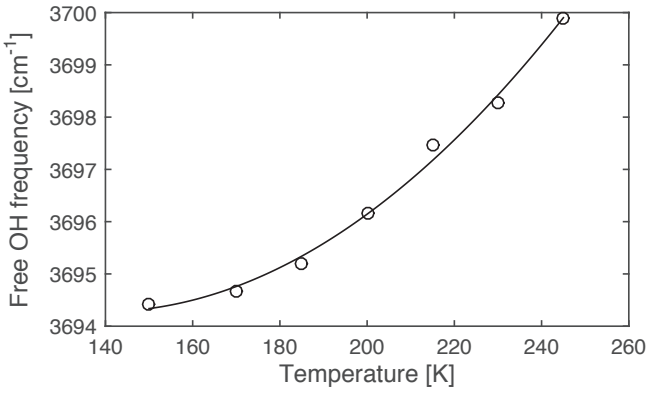

FIGURE 6.6: Peak position of the free OH stretching mode as a function of temperature. The data are fitted by a quadratic function.

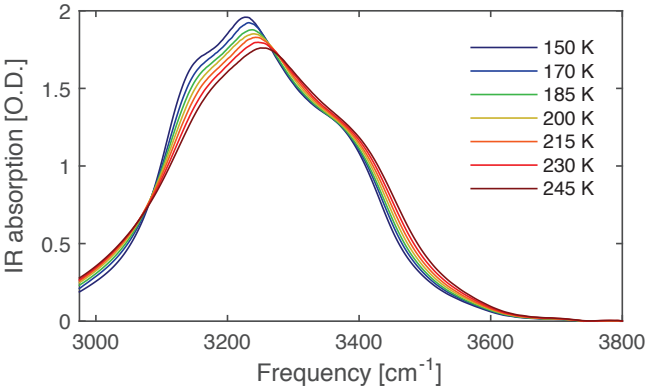

FIGURE 6.7: IR absorption spectrum of polycrystalline ice as a function of temperature.

temperature is increased. Because the Raman and IR spectra do not show a significant change in spectral shape in the temperature range 150–245 K, we explain the strong rise of the $\chi^{(2)}$ response around 3400 cm^{-1} from an increase in disorder of the structure of the ice surface. A disordering of the ice surface [177] has been reported to set in around 180–200 K. [69, 150] An increase in disorder leads to a reduction of the delocalization of the OH vibrations of the surface water molecules. [165, 167] Increasing the temperature from 150 to 245 K has little effect on the order in the bulk. As a result, the delocalization of the bulk modes hardly changes, and thus the Raman and IR spectra show a much smaller change in spectral shape with temperature. As the frequency of ~3400 cm^{-1} coincides with the surface sum-frequency response of liquid water, the observed disorder could well be associated with the formation of a premelted layer, i.e. a layer of supercooled water on the crystalline ice surface.

6.4 CONCLUSIONS

We studied the surface structure of basal ice in the temperature range 150–245 K using phase-resolved surface sum-frequency generation. The obtained second-order susceptibility $\chi^{(2)}$ spectrum provides information on the vibrational resonances on the ice surface. At 150 K the structure of the low-frequency $\chi^{(2)}$ spectrum and the structure of the IR and Raman bulk spectra correspond. This indicates that the OH vibrations at the surface of ice show a similarly strong intermolecular coupling as in the bulk. We observe five distinct modes in the $\chi^{(2)}$ spectrum. The lowest frequency mode (3110 cm^{-1}) is associated with the bilayer-stitching bonds and is observed to be phase-shifted with respect to the other modes, in agreement with the previously reported quadrupole contribution to this mode. The modes at 3530 and 3694 cm^{-1} in the $\chi^{(2)}$ spectrum are absent in the IR and Raman bulk spectra. These two modes are associated with the outermost water molecules on the basal surface. We assign the band at 3530 cm^{-1} to the antisymmetric mode of surface water molecules that are oriented in such a way that both hydrogen atoms point away from the surface and have a lone pair. The peak at 3694 cm^{-1} originates from non-hydrogen-bonded free OH groups that are sticking out of the ice surface.

The modes in the $\chi^{(2)}$ spectrum are observed to shift to higher frequency when temperature increases because of a weakening of the hydrogen bonds. The blueshift of the free OH mode finds its origin in the blueshift of the other hydrogen-bonded OH mode that is located on the same water molecule. Due to the blueshift of this latter mode, the frequency splitting between the uncoupled OH vibrations decreases, leading to a stronger mixing of the two modes and a higher frequency of the high-frequency mode resulting from the coupling. When temperature increases, the individual hydrogen-bonded OH modes become less pronounced and the surface structure becomes more disordered resulting in a reduction of the intermolecular coupling. As a result, the 3 modes with the lowest frequency combine into a single broad band. Furthermore, the 2 modes near 3400 cm^{-1} also merge. In addition the Im $\chi^{(2)}$ amplitude around 3400 cm^{-1}

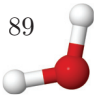

increases from 185 to 245 K. The latter increase is not observed in the Raman and IR spectra, which primarily probe the bulk OH modes. Hence the increase of $\mathrm{Im}\,\chi^{(2)}$ around 3400 cm^{-1} points at an increased disorder of the ice surface, probably associated with the formation of a premelted layer.

7 Observation of liquid water at the surface of ice at temperatures far below the melting point

We employ phase-resolved sum-frequency generation (SFG) spectroscopy to study the molecular properties of the premelted layer on ice. We observe that even at temperatures far below the melting point (<245 K), the surface of ice is covered by a liquid layer, that is indistinguishable from supercooled liquid water.

7.1 Introduction

It has been well-established that the surface of ice is covered by a liquid-like layer. This layer governs processes as diverse as glacier motion, frost heave, the occurrence of lightning and chemical reactions at the surface of ice particles in the atmosphere.[13] In spite of its importance, the precise nature of the liquid-like layer is still under debate. For decades, the surface properties of ice have been the subject of numerous studies employing a large variety of experimental techniques. Much of this previous work reached seemingly inconsistent conclusions about the structure of the liquid-like layer and the temperature at which it forms. For example, the top surface layer has been reported to resemble bulk liquid water,[178–180] but also to have a much higher viscosity than liquid water.[69, 181–186] The onset temperature for the formation of a liquid-like layer reported from experiments varies between 200 and 271 K.[69, 178, 186–191]

SFG spectroscopy is an ideal tool to provide information on the molecular structure at the surface of ice as it combines surface-selectivity with molecular sensitivity. In the previous chapter we have studied the surface structure of ice using phase-resolved SFG between 150 and 245 K. In this chapter we employ the same technique at higher temperatures to probe the molecular nature of the premelting layer at the surface of ice.

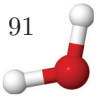

7.2 Experimental methods

The preparation of the ice sample and the experimental configuration of the phase-resolved sum-frequency setup have been described in the previous chapter. The spectra are obtained in an *ssp*-polarization configuration and divided by a reference spectrum taken from z-cut quartz. The Fresnel factors are calculated using literature values for the optical constants of ice,[16] water,[158,192] and quartz,[159] and calculating the effective refractive index of the interfacial layers by the use of a slab model.[44] For an accurate determination of the phase of $\chi^{(2)}$, it is essential that the sample and reference are measured at the same height. The heights of the sample and reference are set to a precision of 10 μm, resulting in a phase inaccuracy of 10°. Following previous work, the obtained $\chi^{(2)}$ spectra are precisely phased such that the imaginary part is zero in the off-resonance part of the spectrum between 3800–3900 cm^{-1}.[73] During the SFG experiment, the ice sample is continuously moved to prevent the accumulation of heat and damage of the crystal. The heating effect of the laser pulses is found to be negligible (see Fig. 7.5).

7.3 Results

In Fig. 7.1 we present the phase-resolved SFG response of the ice surface at different temperatures in the range 245–270 K for an *ssp*-polarization configuration. The imaginary part of $\chi^{(2)}$ contains direct information at the surface resonances. The real part of $\chi^{(2)}$ complements the imaginary part, and additionally contains a negative non-resonant background contribution.[163] The constructed $|\chi^{(2)}|^2$ spectra allow for a direct comparison with conventional intensity SFG measurements. At 245 K the spectrum is dominated by an intense band at 3230 cm^{-1} with a shoulder around 3400 cm^{-1}. With increasing temperature the 3230 cm^{-1} band decreases in amplitude and the shoulder around ~3400 cm^{-1} increases in amplitude. The Im $\chi^{(2)}$ spectrum also shows a clear band at ~3580 cm^{-1}. The low amplitude of this band makes it hardly visible in the constructed $|\chi^{(2)}|^2$ spectra. This band can be assigned to water molecules with 2 donor and 1 acceptor hydrogen bonds and a lone pair.[73,172] These molecules are oriented with both hydrogen atoms pointing towards the bulk, which implies that the antisymmetric mode will be oriented nearly parallel to the surface. Nevertheless, this mode contributes with a positive sign to the Im $\chi^{(2)}$ in the *ssp*-polarization combination.[73] This mode shows a very small blue shift when the temperature increases reflecting a weakening of the hydrogen bonds. The resonance at ~3700 cm^{-1} is assigned to free OH groups sticking out of surface. The positive sign of the imaginary part reflects their outward orientation from the bulk. The amplitude of the free OH band changes only moderately with temperature, which is in agreement with previous work.[152]

In Fig. 7.2a we show the Im $\chi^{(2)}$ spectra of ice at 245 K, ice at 270 K, and supercooled liquid water at 270 K. To facilitate the comparison, the amplitude of the ice spectra are multiplied by 1.6. The lower amplitude of the ice spectrum

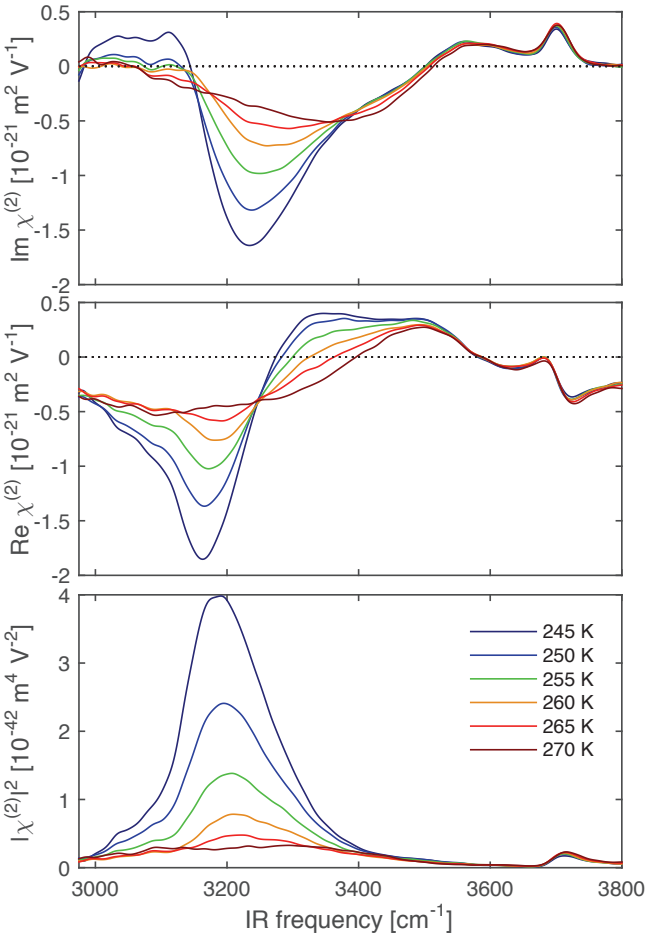

Figure 7.1: Second-order susceptibility of the basal ice surface as a function of temperature. The top panel shows the imaginary component ($\mathrm{Im}\,\chi^{(2)}$), the central panel the real component ($\mathrm{Re}\,\chi^{(2)}$), and the bottom panel the squared amplitude ($|\chi^{(2)}|^2$).

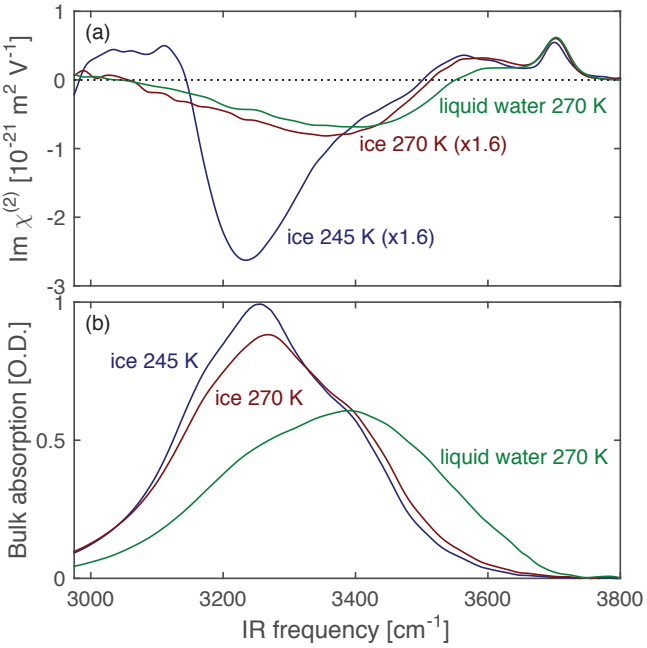

FIGURE 7.2: (a) Comparison of the imaginary parts of the second-order susceptibility ($\mathrm{Im}\,\chi^{(2)}$) of the surfaces of basal ice and supercooled water. (b) Bulk absorption spectra of ~0.5 mm polycrystalline ice and supercooled liquid water.

is likely caused by some remaining surface roughness resulting from the ice sample preparation, which causes SFG light to be scattered outside the range of detection angles (the detection path has a numerical aperture of ~0.1). It is clearly seen that the surface spectrum of ice at 270 K is more similar to that of supercooled liquid water than to that of ice at 245 K. This conclusion is not influenced by the applied corrections for the Fresnel factors (see Fig. 7.6).

The bottom panel of Fig. 7.2b shows bulk infrared absorption spectra of equivalent systems that were shown in Fig. 7.2a. The absorption bands of ice at 245 K and ice at 270 K are quite similar. Ice at 245 K has its maximum infrared absorption at 3255 cm^{-1}, and ice at 270 K has its maximum absorption at 3265 cm^{-1}. Hence, the strength of the hydrogen bonds in bulk ice decreases only slightly going from 245 to 270 K. For supercooled water at 270 K the infrared absorption maximum is found at a frequency of 3390 cm^{-1}, much higher than is observed for ice at 270 K, which implies that the hydrogen bonds are significantly stronger in bulk ice at 270 K than in bulk liquid water at 270 K. It is thus clearly seen that for ice at 270 K the bulk response is similar to that of ice at much lower temperatures, whereas the surface response is similar to that of liquid water. This result indicates that the surface response of ice at 270 K has a large contribution from a layer that resembles liquid water.

To obtain more quantitative information on the properties of the ice surface we perform a spectral decomposition (Fig. 7.3). First we fit the $\mathrm{Im}\,\chi^{(2)}$ spectrum of supercooled water by 3 Gaussian bands of which 2 have asymmetric widths to account for the inhomogeneity in hydrogen-bond strengths. The broad band with the maximum at 3407 cm^{-1} corresponds to hydrogen-bonded OH modes of liquid water, the band at 3587 cm^{-1} corresponds to the mode involving 2 donor and 1 acceptor hydrogen bonds and a lone pair,[73, 172] to be denoted as the lone-pair band, and the band at 3702 cm^{-1} corresponds to the free OH mode. Next we fit the ice spectra with these three bands plus another asymmetric Gaussian-shaped band to account for the response around 3230 cm^{-1}, which represents the OH vibrations of crystalline ice. In this fit of the ice spectra we keep the spectral shapes shapes and widths of the four bands constant. Furthermore, the peak position of the lone-pair band is kept constant and obtained from a global fit. The peak position of the band corresponding to liquid water is taken to be 3407 cm^{-1} at 270 K and to shift by 1 cm^{-1}/K. This latter shift per Kelvin is determined from the liquid water spectra at 270 and 295 K (Fig. 7.7). The peak position of the crystalline ice band is also fitted globally to all ice spectra and is also set to shift by 1 cm^{-1}/K. The fitting of the ice spectra yields the amplitudes of the 4 bands. The areas of the fitted bands as a function of temperature are shown in Fig. 7.4.

The results of Fig. 7.3 show that at all measured temperatures the $\mathrm{Im}\,\chi^{(2)}$ spectrum of ice can be well described with the four bands described above. This implies that the surface response of ice contains a contribution of (supercooled) liquid water, even at 245 K, i.e. at 28 K below the melting point. It also follows from Fig. 7.4 that the liquid water band still shows a significant amplitude at 245 K, that is only ~3 times smaller than the amplitude of the liquid water band of ice at 270 K. This observation indicates that the surface of even very cold ice (at −28 °C) is covered with a water layer. In contrast, the amplitude of the crystalline ice response strongly depends on temperature, and vanishes when approaching the melting point at 273 K (Fig. 7.4). The amplitudes of the free OH band and the lone-pair band involving the OH groups of water molecules with a lone pair change only moderately with temperature. The frequency position of the lone-pair band is shifted 30 cm^{-1} to lower frequencies in comparison to the spectrum of supercooled liquid water. This frequency shift indicates that the two OH groups of the water molecule on which this mode is located, are pointing into the bulk of crystalline ice instead of liquid water. This means that the observed lone pair modes are likely located at the water molecules in the top layer of the crystalline ice phase, i.e. at the boundary of the crystalline ice phase and its overlying liquid water layer.

7.4 Discussion

The surface properties of ice have been studied before with conventional intensity SFG spectroscopy.[69, 152] In this study it was found that the free OH groups sticking out the ice–air interface show orientation disorder at tempera-

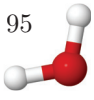

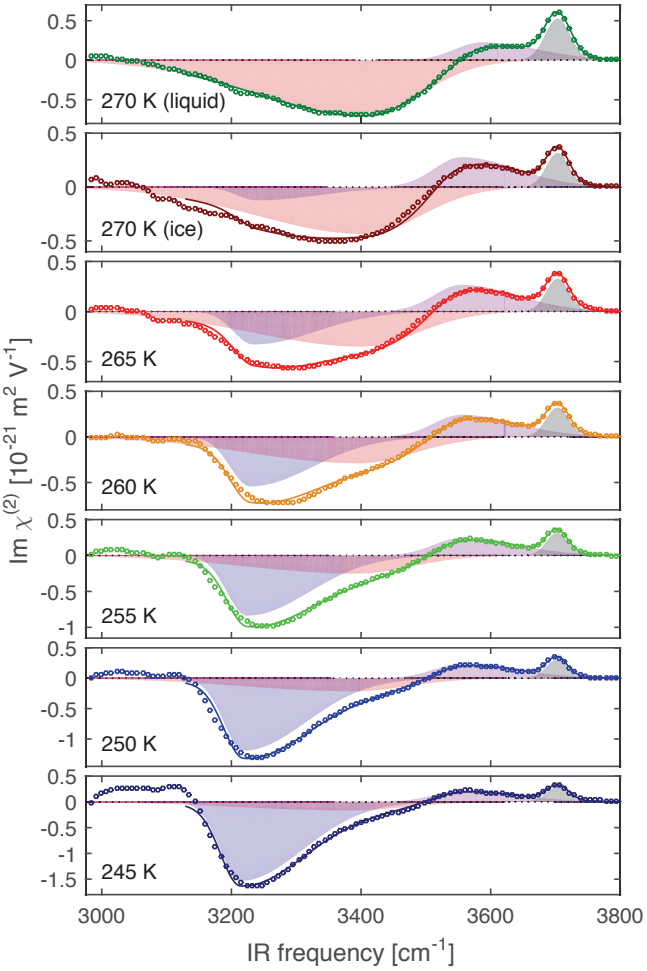

Figure 7.3: Spectral decomposition of the imaginary part of the susceptibility ($\mathrm{Im}\,\chi^{(2)}$) of the surface of supercooled water at 270 K and basal ice at temperatures between 245 and 270 K. The supercooled water spectrum (top) is fitted by a sum of two asymmetric Gaussian-shaped bands and one symmetric Gaussian-shaped band. The ice spectra are fitted with the three bands resulting from the fit to liquid water and an additional asymmetric Gaussian-shaped band (see text). The data are represented by the symbols and the fitted spectra by the solid lines. The four spectral bands that together form the fitted spectra are indicated by shaded areas.

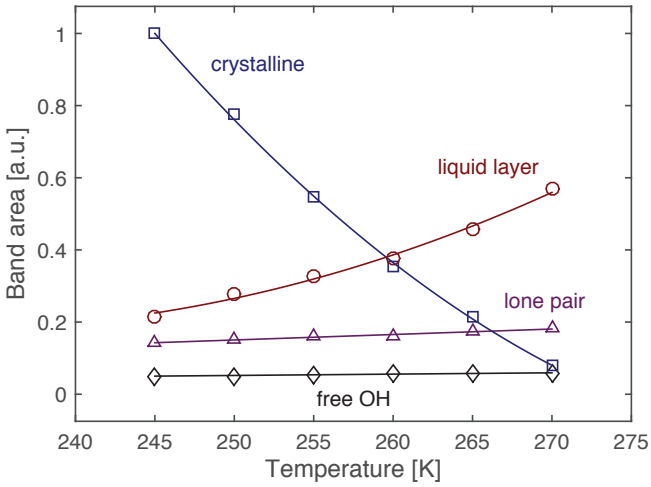

Figure 7.4: Area of the bands resulting from the spectral decomposition of the ice spectra shown in Fig. 7.3.

tures ≥200 K,[69, 152] pointing at a disordered character of the top surface layer of ice. However, the exact nature of this disorder was not revealed, in particular to what extent the disordered surface would resemble liquid water. In this study we measure the spectrum of the ice surface with phase-resolved SFG, and we find that the spectrum of the premelted layer is indistinguishable from the spectrum of supercooled liquid water at the same temperature.

As the premelted layer is indistinguishable from supercooled water, the hydrogen-bond structure and dynamics of this layer will also likely be similar to the structure and dynamics of supercooled liquid water. In view of this finding it seems unlikely that the viscosity of the premelted layer would be 300–4000 times larger than the viscosity of (supercooled) water, as has been reported in interfacial and atomic force microscopy studies of the ice surface.[184–186] The observed extremely high viscosity may find its origin in the strong confinement of the liquid-like layer between the probing tip of the atomic force microscope and the ice crystal surface.[12] Indeed, in an interfacial force microscopy study it was reported that the measurements may be affected by the formation of a frustrated capillary between the probing tip and the ice surface.[186]

7.5 Conclusions

We studied the surface of ice between 245–270 K using phase-resolved SFG spectroscopy. At all temperatures in this range, we find the ice surface to be covered with a layer of supercooled liquid water. We observe that the magnitude of the water signal decreases only by a factor of 3 when the temperature is decreased from the melting point down to 245 K.

7.6 Supplementary figures

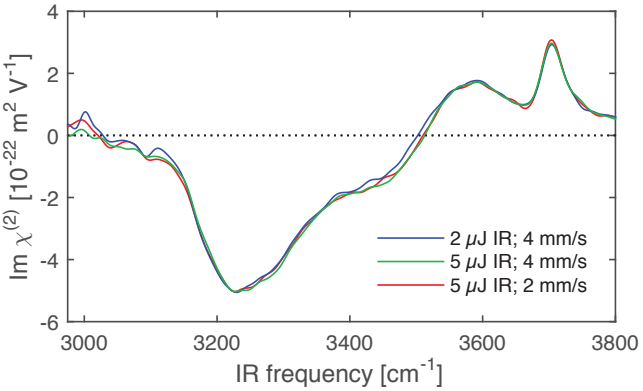

Figure 7.5: SFG spectra at various IR intensities and moving speeds of the ice sample. Both a reduction in IR intensity from 5 μJ to 2 μJ as well as a reduction in the scanning speed from 4 mm/s to 2 mm/s do not affect the spectral shape. From this we conclude that the laser pulses used in the experiment lead to a negligible heating effect.

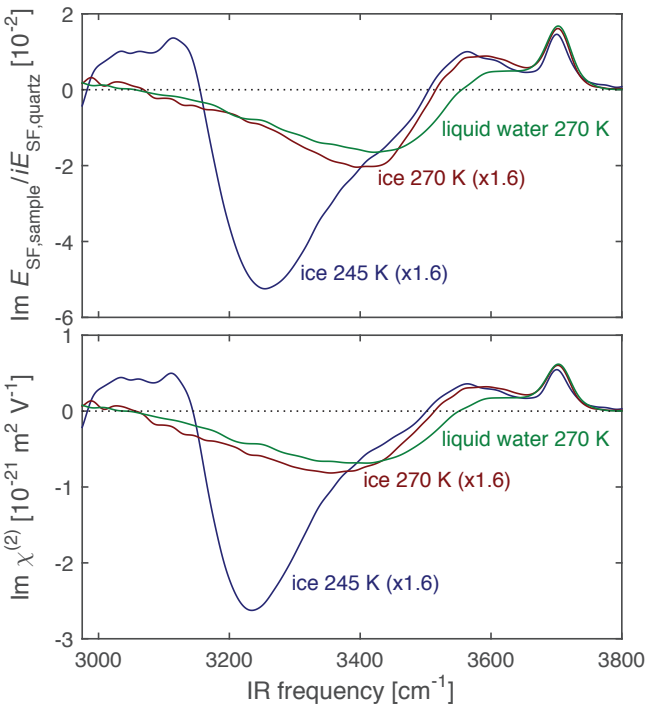

Figure 7.6: The imaginary part of the second-order susceptibility ($\mathrm{Im}\,\chi^{(2)}$) of the surfaces of basal ice and supercooled water. The top panel shows the division of the sum-frequency field generated from ice/liquid water ($E_{\mathrm{SF,sample}}$) by the sum-frequency field generated from z-cut quartz ($E_{\mathrm{SF,quartz}}$). The bottom panel shows this division and a correction for the Fresnel effects.

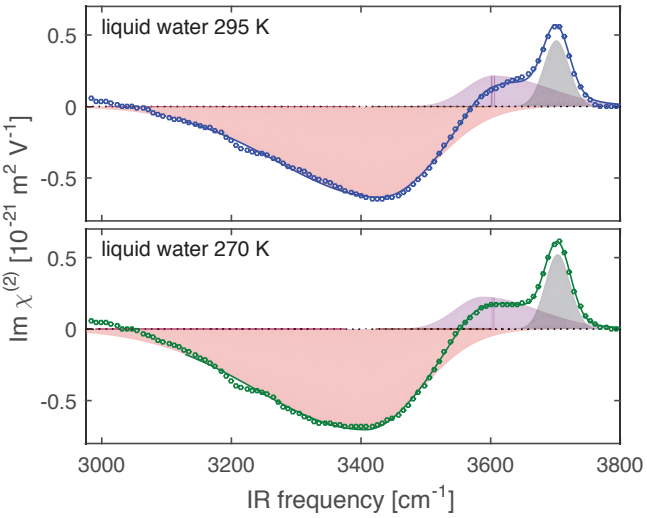

Figure 7.7: Spectral decomposition of the $\mathrm{Im}\,\chi^{(2)}$ spectrum of the liquid water–air interface at 270 and 295 K. The spectra are decomposed in two asymmetric Gaussian bands and one symmetric Gaussian band. The maximum of the negative imaginary band is found to be located at 3407 cm^{-1} for 270 K and at 3430 cm^{-1} for 295 K, corresponding to a shift of ~1 cm^{-1}/K.

8 Resonant intermolecular coupling at the surfaces of liquid water and ice

We study the strength of hydrogen-bond interactions and effects of resonant intermolecular coupling at the surfaces of liquid water and ice using phase-resolved sum-frequency generation spectroscopy. The effect of intermolecular resonant vibrational coupling is determined by isotope substitution, i.e. by comparing the response of the OH stretching vibrations of H_2O with that of the OH stretch vibration of dilute HDO in D_2O. The HDO:D_2O spectra are not affected by resonant intermolecular vibration coupling. For liquid water, the surface spectra of H_2O and HDO:D_2O are surprisingly similar, in contrast to the bulk infrared absorption spectra of H_2O and HDO:D_2O that strongly differ. This indicates that the OH stretch vibrations are far less delocalized at the surface of liquid H_2O than in the bulk. For ice, the surface spectra of H_2O and HDO:D_2O strongly differ, and this difference is comparable to the difference observed between the bulk infrared absorption spectra of H_2O and HDO:D_2O ice. This indicates that the surface OH stretch vibrations of H_2O ice are strongly delocalized, in contrast to H_2O liquid water. The delocalization of the OH stretch vibrations at the surface of H_2O ice is likely caused by the highly ordered crystal structure of ice that persists at the ice surface. Comparison of the SFG spectra of HDO with bulk infrared spectra of HDO reveals that the hydrogen-bond strengths at the surface and the bulk are quite similar, both for liquid water and for ice.

8.1 Introduction

Water is a remarkable substance owing to the presence of a strong spatial network of hydrogen bonds. This network is truncated at the surface, which gives rise to unique properties like water's high surface tension. These properties in turn govern a broad variety of biological and environmental processes. [13, 142, 193] The understanding of the physical properties of the surface structure of water and ice at the molecular level is thus of broad scientific interest. Unfortunately, the detailed study of the surface properties of water and ice is complicated because the surface region is very thin compared to the bulk and not many techniques are sufficiently surface-specific. [194]

Over the last three decades, sum-frequency generation (SFG) spectroscopy has emerged as an extremely useful tool to study the molecular structure of water surfaces.[68, 75, 194] SFG is a second-order ($\chi^{(2)}$) optical process that is forbidden in centrosymmetric media like bulk water, but allowed at its surface. As detailed in Chapter 3, the method involves the frequency mixing of an IR and a VIS laser pulse, yielding a signal at the sum frequency. The SFG response is strongly enhanced when the IR frequency matches a vibrational resonance, making it a selective probe for surface vibrations. For the OH stretching vibrations of water, the frequency is strongly influenced by the strength of the hydrogen bonds. As a result, the $\mathrm{Im}\,\chi^{(2)}$ spectrum is a sensitive probe of the molecular structure of the water surface.

The spectrum of water is not only affected by the strength of the hydrogen-bond interactions, but also by resonant intermolecular interactions, often resulting from dipole–dipole (Föster) coupling. In neat H_2O the stretching vibration of an OH group couples both with the other OH group of the same molecule (intramolecular coupling) and to other OH oscillators in the vicinity (intermolecular coupling). As a result, the vibrational modes are delocalized over many OH oscillators, which has a profound effect on the spectrum and impedes a direct connection between the hydrogen-bond strength and the resonance frequency.[101, 195] Resonant intermolecular interactions can even change the apparent orientation of molecular groups.[73]

In this chapter we examine the effect of resonant intermolecular interactions at the surface of liquid water and ice by studying different isotopic mixtures of H_2O and D_2O using phase-resolved SFG spectroscopy. For isotopically dilute HDO in D_2O, OH oscillators are effectively uncoupled from the surrounding OD oscillators and other local modes, owing to the large frequency mismatches. As a result, the $\mathrm{Im}\,\chi^{(2)}$ spectrum of HDO:D_2O can be interpreted in terms of isolated well-localized OH stretch oscillators.

8.2 Experimental methods and analysis

Water samples of various isotopic mixtures are prepared by mixing ultrapure water H_2O (with a resistivity of 18.2 MΩ cm at 25 °C) with D_2O (>99.9 %D, Cambridge Isotope). The liquid water samples are measured in a teflon cup. The growth and handling of single crystal ice are detailed in Chapter 6. For the growth of $H_2O : 3\,D_2O$ ice, the maintaining temperatures of the water bath and the seed crystal are increased by 2.7 K to account for the higher melting point with respect to H_2O.

The experimental configuration of the phase-resolved SFG laser setup is described in Chapter 6. The spectra are collected in an *ssp*-configuration of the polarizations (SF,VIS,IR) and normalized to a reference spectrum obtained from z-cut quartz. The Fresnel factors[48] are calculated using literature values for the optical constants of water,[192, 196] ice,[16] and quartz.[159] The dielectric constant of liquid HDO:D_2O is approximated by taking the average of the dielectric constants of H_2O and D_2O, weighted by their relative concentrations.

In the calculation of the dielectric constant of HDO:D_2O ice, the dielectric constant of D_2O ice is calculated by frequency shifting the optical constants of H_2O ice by a factor of 1/1.35. This simplification is justified because D_2O has no strong vibrational resonances above 2900 cm^{-1}. We verify the validity of the approximation for the liquid phase, for which literature values of the optical constants are available.[192, 196] The effective refractive index of the interfacial layers has been calculated using a slab model.[44] We take the effective $\chi^{(2)}$ value of quartz to be $3 \cdot 10^{-20}\,m^2\,V^{-1}$ for our experimental configuration, based on a bulk response of $8 \cdot 10^{-13}\,m\,V^{-1}$.[162]

In phase-resolved SFG it is essential that the sample and reference are measured at the same height, as a difference in height will lead to a phase offset in the recorded $\chi^{(2)}$ spectrum. The height of the reference and sample is set to a precision of 10 μm, as determined by the height of the sum-frequency signal on the CCD camera. Evaporation of the liquid water sample during the typical acquisition time of 300 s is a potential threat to an accurate determination of the phase.[172] We account for this by setting the initial height of the sample slightly higher, i.e. by half the height loss due to evaporation. This procedure leads to an overall phase uncertainty of the acquired $\chi^{(2)}$ of ~10°. At low isotopic concentrations, the $\mathrm{Im}\,\chi^{(2)}$ value is very sensitive to the correct reference phase, due to a large non-resonant background contribution (described below). Therefore, we phase-shift the spectra within the phase accuracy to an average $\mathrm{Im}\,\chi^{(2)}$ of zero between 2850–3000 cm^{-1} conforming previous work.[53, 73, 197] The mean applied phase shift is 6°. After phasing, 10–20 spectra are averaged for each isotopic dilution.

8.3 Results and discussion

The $\mathrm{Im}\,\chi^{(2)}$ of the liquid water–air interface at different isotopic concentrations is presented in Fig. 8.1. The signal scales with the number of chromophores and decreases consequently with increasing isotopic dilution. The spectra show a main negative band with a peak at ~3425 cm^{-1} and a positive band near 3700 cm^{-1}. We observe an isosbestic point at ~3570 cm^{-1} near the zero-crossing. The spectrum also shows a feature at ~3620 cm^{-1} that strongly decreases with isotopic dilution. This feature has been assigned to water molecules with 2 donor and 1 acceptor hydrogen bonds.[73, 172] The OH groups of such molecules are oriented away from the surface, and intramolecular coupling gives rise to an antisymmetric mode which contributes positively to the $\mathrm{Im}\,\chi^{(2)}$ response in an *ssp*-polarization configuration. Intramolecular coupling also effects the frequency of the free OH mode: The position of the free OH mode shifts from ~3702 cm^{-1} in pure H_2O to ~3692 cm^{-1} for diluted HDO. In a previous study by Stiopkin et al.[73] a similar shift of ~17 cm^{-1} has been observed for the free OD mode. The observed shift of ~10 cm^{-1} for the free OH mode exactly agrees with their predictions and is smaller than for the free OD mode because the natural frequency is a factor of $\sim\sqrt{2}$ larger for the free OH mode.[73] In addition, the intramolecular coupling is somewhat weaker in H_2O than in D_2O.[73, 167]

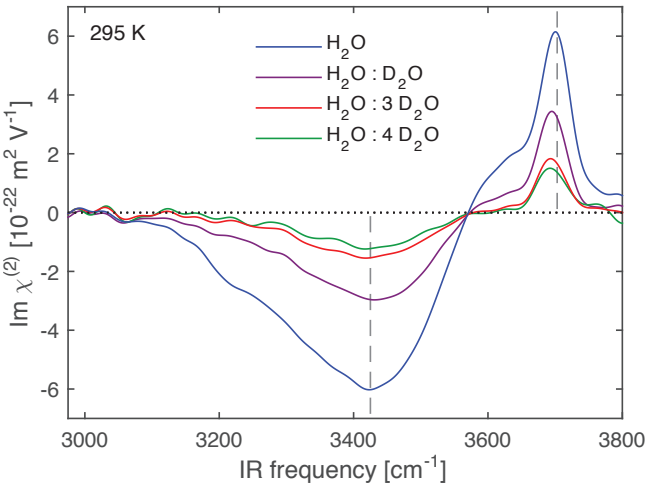

Figure 8.1: Imaginary part of the second-order susceptibility of the water–air interface at 295 K with various isotopic concentrations. The indicated $H_2O : n\,D_2O$ ratios quickly exchange to a mixture of $H_2O : HDO : D_2O \approx 1 : 2n : n^2$.[198] The maximum of the negative band and the position of the free OH mode of H_2O are indicated by dashed lines.

The positive amplitude of the free OH mode in the $\mathrm{Im}\,\chi^{(2)}$ spectrum reflects its orientation outward from the bulk. The negative imaginary band below 3570 cm^{-1} correspond to hydrogen-bonded OH groups with a net orientation toward the bulk. The peak position is ~3425 cm^{-1} and does not change with isotopic concentration (within experimental uncertainty). The spectra with isotopic dilutions of $H_2O : 3\,D_2O$ and $H_2O : 4\,D_2O$ have similar spectral shapes, indicating that the spectrum with an isotopic dilution of $H_2O : 3\,D_2O$ (corresponding to $H_2O : HDO : D_2O \approx 1 : 6 : 9$) can be regarded to represent the spectra of OH vibrations of HDO molecules that are not coupled to other nearby OH oscillators.

A comparison between the sum-frequency spectra of liquid H_2O and HDO:D_2O is shown in Fig. 8.2a. The spectral shapes of the main hydrogen-bonded bands are surprisingly similar. For HDO the band is somewhat narrower (by ~20 %) at the low frequency wing of the band. This difference is likely the result of the complete switching off of the resonant intermolecular coupling upon isotopic dilution of the OH oscillators.[199]

Previously, the hydrogen-bonded region of the $\mathrm{Im}\,\chi^{(2)}$ spectrum of the liquid water–air interface has been reported to contain a positive band at low frequency.[199,200] The presence of this band likely results from a small offset in the determined phase,[53,197,201] which leads to a transfer from the real part of $\chi^{(2)}$ to its imaginary part. Because $\mathrm{Re}\,\chi^{(2)}$ contains a non-resonant background contribution.[163] A phase offset significantly distorts the spectral shape of $\mathrm{Im}\,\chi^{(2)}$, especially in the low frequency region where $\mathrm{Im}\,\chi^{(2)}$ is small compared to $\mathrm{Re}\,\chi^{(2)}$. The $\chi^{(2)}$ spectrum of HDO:D_2O contains a relatively large

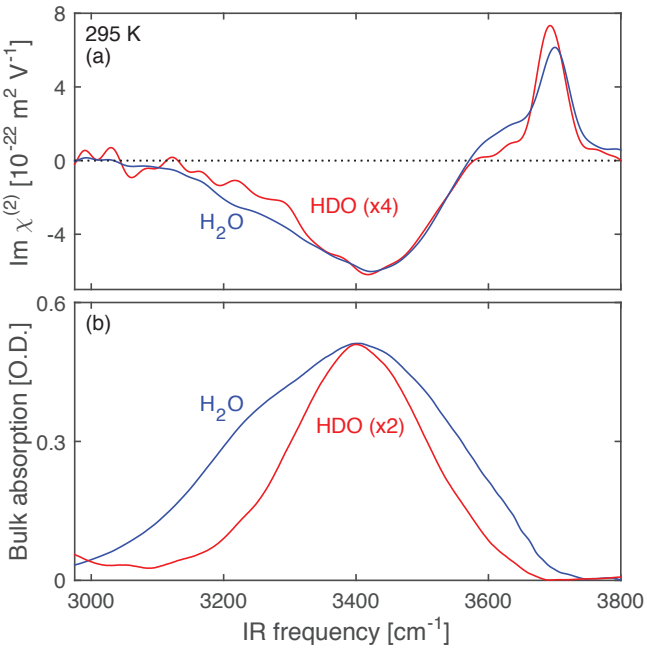

Figure 8.2: (a) Imaginary part of the second-order susceptibility of H_2O and $H_2O:3\,D_2O$ at 295K. (b) Linear absorption spectra of H_2O and a mixture of 4 % HDO in D_2O at 295K.

non-resonant background contribution in comparison to the $\chi^{(2)}$ spectrum of pure H_2O. As a result, a phase offset leads to a much stronger spectral distortion for HDO:D_2O than for pure H_2O. Hence, the difference between the present and previous observations for the Im $\chi^{(2)}$ spectrum of HDO:D_2O, can be explained from a phase offset in the previous data.[199,200] The present Im $\chi^{(2)}$ spectrum of the liquid H_2O–air interface is very similar to the recently reported spectra of Yamaguchi,[197] Nihonyanagi et al.,[53] and Sun et al.[161]

Figure 8.2b shows (bulk) infrared absorption spectra of H_2O and isotopically diluted water (HDO:D_2O). The H_2O absorption spectrum is strongly affected by intermolecular coupling.[101] The intermolecular coupling leads to a significant broadening of the H_2O spectrum by 65 % with respect to the HDO:D_2O absorption spectrum. The broadening in the bulk spectrum is much larger than in the sum-frequency spectrum. This indicates that the amount of vibrational delocalization is much smaller at the surface of liquid H_2O than in the bulk of the liquid. This observation agrees with the results of molecular dynamics simulations performed by Auer and Skinner.[101,202] These simulations show the vibrational eigenstates to be delocalized over up to 12 OH groups in the bulk and only few OH groups close to the surface boundary.[101,202]

For HDO:D_2O, the maximum of the Im $\chi^{(2)}$ spectrum is blueshifted by only ~20 cm^{-1} with respect to the maximum of the bulk infrared spectrum. The sur-

face and bulk spectra of HDO:D_2O also show a quite similar width and spectral shape. These observations show that the hydrogen bonds at the surface are comparable in strength to the hydrogen bonds in the bulk, which supports the observation by other work of a remarkably fast onset of a bulk-phase hydrogen-bond structure when entering the surface of water.[73, 114, 203]

In contrast to the observations for the $\mathrm{Im}\,\chi^{(2)}$ spectrum, the intensity spectra ($|\chi^{(2)}|^2$) of the liquid water–air interface of H_2O and HDO:D_2O differ substantially.[204–207] In Fig. 8.3 we show the experimentally obtained $\mathrm{Im}\,\chi^{(2)}$ (top panel), $\mathrm{Re}\,\chi^{(2)}$ (middle panel), and the constructed $|\chi^{(2)}|^2$ (bottom panel), both of liquid H_2O and HDO:D_2O. It is clearly seen that the intensity spectra of H_2O and HDO:D_2O strongly differ. From the $\mathrm{Im}\,\chi^{(2)}$ spectra it is clear that this difference is not caused by resonant intermolecular coupling effects on the spectrum of the OH stretch vibrations of H_2O. The origin of this difference can in fact be found in the $\mathrm{Re}\,\chi^{(2)}$ spectra. These spectra show that $\chi^{(2)}$ also possesses a quite strong non-resonant contribution as a frequency-independent contribution with a negative sign to $\mathrm{Re}\,\chi^{(2)}$.[163] The non-resonant background is relatively larger for isotopically diluted water than for neat water. As a result, the non-resonant contribution has a much stronger effect on the intensity spectrum for HDO:D_2O than for H_2O, leading to a strong difference between these spectra. For instance, due to the non-resonant contribution, the peak position of the free OH mode is far more strongly shifted in the intensity spectrum of HDO:D_2O than in the intensity spectrum of H_2O. We can correct the spectra for the non-resonant contribution by subtracting a frequency-independent contribution from the experimentally obtained $\mathrm{Re}\,\chi^{(2)}$. In the middle panel of Fig. 8.3 we show the experimentally obtained $\mathrm{Re}\,\chi^{(2)}$ (dashed lines) and the corrected $\mathrm{Re}\,\chi^{(2)}$ (solid lines). Using the corrected (resonant-only) $\mathrm{Re}\,\chi^{(2)}$ we can construct corrected intensity spectra for HDO:D_2O and H_2O. These spectra are shown as the solid lines in the lower panel of Fig. 8.3. Correction for the non-resonant background yields intensity spectra for H_2O and HDO:D_2O that are strikingly similar, again indicative of the weak effect of resonant intermolecular coupling on the OH stretch vibrations at the surface of liquid water. It is thus clearly seen that the shape of the intensity spectra of isotopically diluted water is strongly influenced by the non-resonant background. Furthermore, the peak at 3200 cm^{-1} in the H_2O spectrum, which has been previously assigned to ice-like water,[194, 208] is suppressed in the intensity spectra if these spectra are corrected for the non-resonant background.

The current observations show that the SFG response of the OH stretch vibrations at the liquid water-air interface is quite similar for HDO:D_2O and H_2O, which indicates that at the water surface the effects of intermolecular coupling are small, and that the OH vibrations of H_2O are only weakly delocalized. This result does not necessarily hold for charged aqueous interfaces, as in these studies the depth over which water molecules contribute to the sum-frequency signal can be substantially larger.[170, 209] It has indeed been observed that the $\mathrm{Im}\,\chi^{(2)}$ responses of pure and isotopically diluted water can show profound differences in case the liquid-water surface is charged.[207, 210, 211] Apparently, if liquid water is probed over a larger depth, the intermolecular coupling and

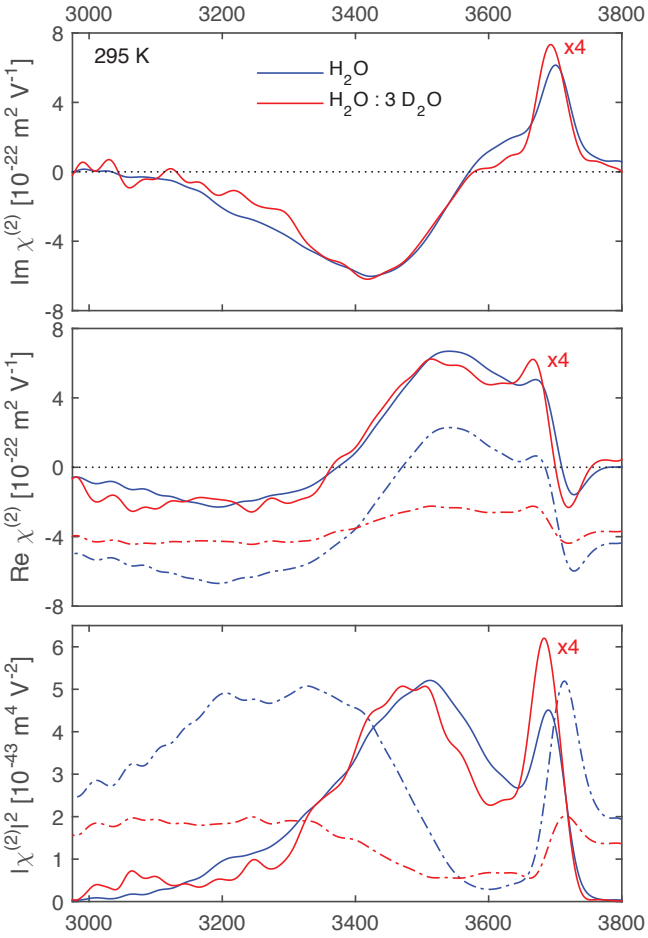

Figure 8.3: Effect of the non-resonant background on the spectral shape of $|\chi^{(2)}|^2$ for H_2O and $H_2O:3\,D_2O$ at 295 K. The resonant $\chi^{(2)}$ response (solid lines) is obtained by subtracting a real background constant from the experimentally obtained $\chi^{(2)}$ (dash-dotted lines).

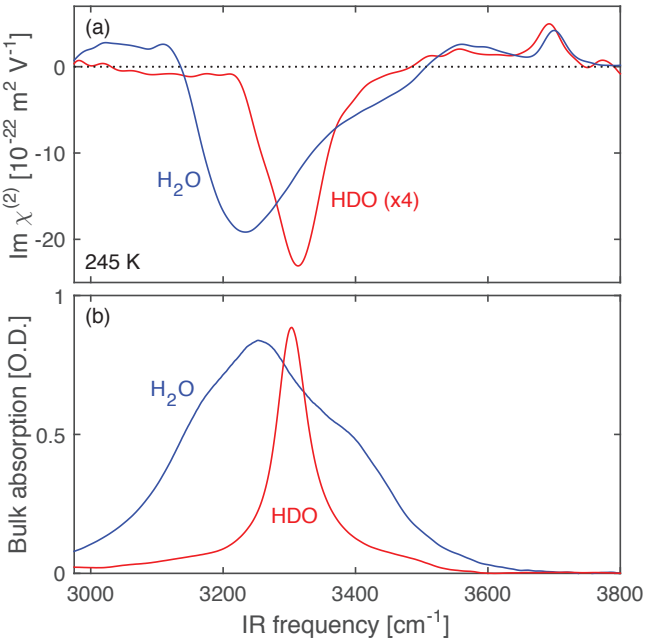

Figure 8.4: (a) Imaginary part of the second-order susceptibility of the basal face of H_2O ice and $H_2O:3\,D_2O$ ice at 245K. (b) Linear absorption spectra of H_2O ice and a mixture of 4 % HDO in D_2O ice at 245K.

delocalization of the OH vibrations does play an important role for the shape of the observed $\mathrm{Im}\,\chi^{(2)}$ spectrum of H_2O.

We also investigated the role of resonant intermolecular coupling for the surface of ice. In Fig. 8.4a we show the $\mathrm{Im}\,\chi^{(2)}$ spectrum of the basal faces of H_2O and $H_2O:3\,D_2O$ ice crystals at 245 K. Above 3500 cm^{-1}, the $\mathrm{Im}\,\chi^{(2)}$ spectrum is positive and contains two features: a resonance at ~3700 cm^{-1} corresponding to non-hydrogen-bonded free OH groups sticking out of the ice surface, and a band at ~3570 cm^{-1}. We assign the latter band to an antisymmetric OH mode involving surface water molecules with two OH groups pointing away from the surface and a dangling electron pair, equivalent to the mode observed at ~3620 cm^{-1} in the liquid H_2O spectrum.[73] The redshift of ~50 cm^{-1} can be well explained from the stronger hydrogen bonds of ice compared to liquid water. The position of the free OH is ~8 cm^{-1} higher for H_2O ice than for HDO:D_2O ice, caused by the presence of near-resonant intramolecular coupling for H_2O, similar to what is observed for the surface of liquid water. The observed frequency shift for ice is slightly smaller than the ~10 cm^{-1} shift observed for liquid water, which can be well explained from the larger frequency difference between the free OH oscillator and the other OH group located on the same H_2O molecule of H_2O ice compared to H_2O water.[73]

The spectral shapes for H_2O and HDO:D_2O ice are very different below 3500 cm^{-1}. The negative imaginary band of the H_2O spectrum can be described by two bands, of which the strongest is located at 3230 cm^{-1}. The other, less strong negative imaginary band is located at ~3440 cm^{-1}. The HDO spectrum below 3500 cm^{-1} consists of a single negative imaginary band at ~3310 cm^{-1}. The marked difference between the $\mathrm{Im}\,\chi^{(2)}$ spectra of H_2O and HDO:D_2O ice indicates that the OH vibrations at the surface of ice are strongly delocalized, which clearly deviates from the results obtained for liquid water for which we observed the $\mathrm{Im}\,\chi^{(2)}$ spectra of H_2O and HDO to be quite similar.

In Fig. 8.4b we present (bulk) infrared absorption spectra of H_2O and isotopically diluted ice at 245 K. The HDO spectrum has a single mode at ~3300 cm^{-1}. This mode is much narrower and has a lower frequency for ice than for liquid HDO:D_2O, reflecting the narrower distribution of hydrogen bonds in ice and their increased strength. For HDO:D_2O ice, the bulk resonance frequency is close to the maximum of the sum-frequency spectrum, redshifted by only ~10 cm^{-1}. Hence, the strength of the hydrogen bonds at the ice surface is similar to the bulk ice value, as was the case for liquid water.

The infrared absorption spectra of HDO:D_2O and H_2O ice strongly differ, which can be explained from the effect of intermolecular coupling and resulting delocalization of the OH oscillators in pure H_2O.[165,167] The difference observed in the linear infrared absorption spectrum is comparable to the difference observed in the $\mathrm{Im}\,\chi^{(2)}$ spectrum. The observation of a similar difference between HDO and H_2O for the surface $\mathrm{Im}\,\chi^{(2)}$ spectra indicates that the OH vibrations of H_2O ice are approximately equally strongly delocalized at the surface of H_2O ice at 245 K as in the bulk. This observation is supported by previous theoretical work by Ishiyama et al.[174,175] Their molecular dynamics simulations indicate that the persistence of the tetrahedral structure at the ice surface augments the delocalization of the surface OH vibrations.[174]

8.4 Conclusions

In summary, we studied the strength of the hydrogen-bond interactions and the effects of resonant intermolecular interaction at the surfaces of liquid water and ice using phase-resolved SFG experiments. We observe the $\mathrm{Im}\,\chi^{(2)}$ spectra of isotopically diluted (HDO:D_2O) and pure water to be rather similar, which indicates that the OH vibrations are only weakly delocalized at the liquid-water surface. In contrast, the bulk absorption spectrum of pure H_2O is much broader than for HDO:D_2O. This indicates that the OH stretch vibrations are strongly delocalized in the bulk. For ice at 245 K, the $\mathrm{Im}\,\chi^{(2)}$ spectrum of H_2O strongly differs from that of HDO:D_2O. A comparable difference is found in the linear absorption spectra of H_2O and HDO:D_2O, which indicates that the OH stretch vibrations of H_2O ice are strongly delocalized both in the bulk and at the surface of ice at 245 K. This is likely caused by the persistence of the bulk tetrahedral structure of ice towards the surface at temperatures well below the melting point.

9 Freezing effects of oil-in-water emulsions

Sum-frequency scattering spectroscopy is used to study the properties of hexadecane and dodecane oil droplets in water. The sum-frequency scattering spectra contain vibrational bands that correspond to the symmetric and antisymmetric CH stretching vibrations of the methylene (CH_2) and methyl (CH_3) groups of the alkane molecules. The relative amplitudes of the vibrational bands provide information on the surface structure and the shape of the oil droplets. We study the emulsions over a temperature range of −48 to 24 °C, including the freezing transitions of the water matrix and the oil droplets. Hexadecane oil droplets freeze at a higher temperature than the surrounding water, whereas dodecane oil droplets freeze at a lower temperature than the surrounding water. This allows us to independently study the freezing effect of oil and water on the surface structure of the oil droplets. In both cases freezing leads to a change in the polarization dependencies that are valid in the case of the spherical-symmetric shapes that the oil droplets assume when both water and oil are liquid. We find that the freezing of water leads to a strong distortion of the liquid dodecane surface but has little effect on the surface of already solidified hexadecane. For completely frozen emulsions a further decrease in temperature is observed to lead to a further distortion of the surface of the solid oil particles, which might be caused by increasing hardness of the ice matrix encapsulating the particles.

9.1 Introduction

Oil-in-water emulsions are omnipresent in oil-based products, including foods, cosmetics, paints, crop protectors, and pharmaceuticals.[212–214] The emulsion properties are determined by the molecular-scale structure of the adjacent oil and water layers, as this structure determines the free energy of the oil–water interface. The freezing of oil-in-water emulsions affects many functional properties like their stability,[215] which is relevant in many applications, for instance in the chilled storage of frozen ready meals. Previously the liquid–solid phase transitions of emulsified oils have extensively been studied with differential scanning calorimetry[215–220] and ultrasonics.[221–224] The bulk properties of frozen emulsified oils have been investigated using X-ray scattering experiments[225–227] and electron microscopy.[228] However, until now no direct study on the molecular structure of the oil droplet surface upon freezing has been

performed. To this purpose, temperature-dependent sum-frequency scattering is a powerful technique.

Recently, SF scattering made it possible to obtain information about the molecular structure of the oil droplet–water interface.[79, 83] In this chapter we investigate the effects of phase changes on the interface of oil-in-water emulsions using SF scattering spectroscopy. We investigate two oil-in-water emulsions: a hexadecane-in-water emulsion with the oil freezing temperature above the freezing point of water, and a dodecane-in-water emulsion with the oil freezing temperature below the freezing point of water.[215] In this chapter we present and discuss SF scattering spectra at room temperature and at different temperatures during cooling down to −48 °C. This is the first reported study employing temperature-dependent SF scattering spectroscopy.

9.2 Experiment

The SF scattering experiments are performed using a commercial Ti:sapphire laser system (Coherent Legend) that delivers 3.2 mJ pulses at a wavelength of 800 nm (FWHM 70 nm) and at a repetition rate of 1 kHz. The VIS pulse is made by spectrally narrowing 20 % of the laser output to a FWHM of 0.6 nm (10 cm^{-1}) by a pulse shaper.[229] The IR pulse is generated using a home-built OPA, pumped by the other 80 % of the laser output. This process yields 20 μJ pulses at 3.4 μm (2900 cm^{-1}) with a FWHM bandwidth of 280 nm (240 cm^{-1}). The polarizations of the VIS and IR light are independently adjusted by a combination of a $\lambda/2$-plate and a polarizer.

A schematic of the experimental geometry is shown in Fig. 9.1. The IR and VIS light are focused by the same 90° off-axis parabolic gold mirror with an effective focal length of 10 cm to a spot size of about 150 μm and are incident under a relative angle of 6° (as measured in air). To match the focused spot sizes of the IR and VIS beams,[27] the VIS beam size is reduced by a telescope before the parabolic mirror.

The SF scattering signal is collected by a collimating lens with a focal distance of 4 cm under an angle of 45° and an effective diameter of 23 mm, corresponding to an acceptance angle of 21–41° of the SF signal of a water sample. A shortpass filter (Semrock FF01-775/SP-25) and bandpass filter (Semrock FF02-650/100-25) are used to suppress background scattering of the VIS beam and light generated at other frequencies by higher-order processes. A final polarizer cube is used to select the polarization of the SF light. The SF light is detected by a Princeton Instruments spectrometer system consisting of a Pixis 100 CCD camera in conjunction with an Acton SP 2356 monochromator. We use an integration time of 300 s per spectrum.

The sample is cooled in two stages. A processor cooler (LD PC-V2) with a cooling power of 300 W at −30 °C cools a copper board on which a 40 W double stage Peltier element is mounted. On top of the Peltier element a movable copper holder is placed, which can hold both an emulsion between two Raman grade CaF_2 windows (Crystran) with a 100 μm spacer and a z-cut quartz crystal

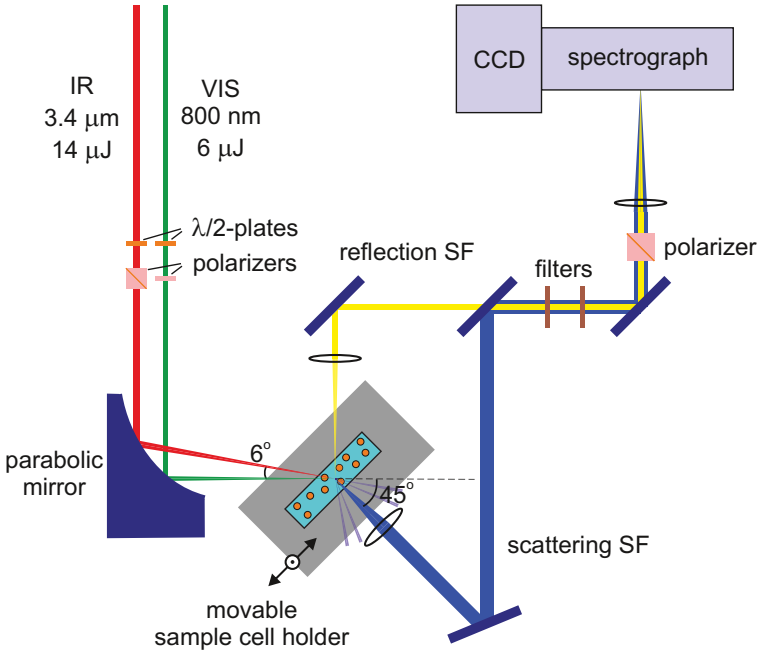

FIGURE 9.1: Schematic of the experimental setup in the horizontal plane. An IR beam (red) and a VIS beam (green) are collimated by the same parabolic mirror and overlapped in the sample cell containing an emulsion. SF scattered light (blue) is generated in a wide angular range. A collimating lens selects an angular range which is conducted into the spectrograph. The reflection detection scheme, which is used for referencing of the IR spectrum, is indicated in yellow.

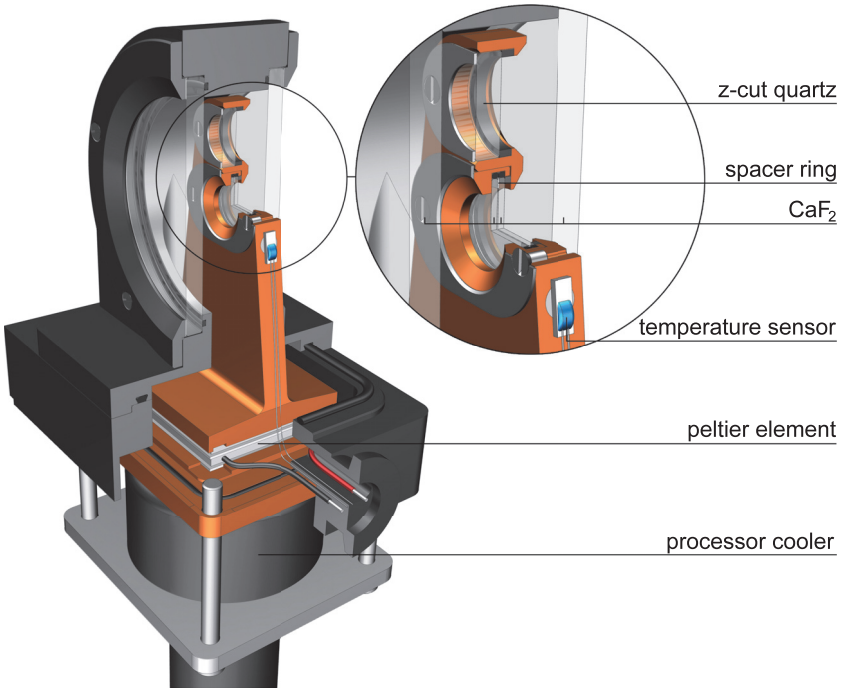

Figure 9.2: Schematic drawing of the sample cell holder.

(see Fig. 9.2). The copper holder is held in place by a flexible spring steel plate which acts as a pressure release. By adjusting the current through the Peltier element, temperatures down to −60 °C can be achieved. During the experiments, we used a cooling rate of maximally 2 °C/min. In order to prevent condensation on the windows of the sample cell holder, the last part of the setup is enclosed and continuously purged with dry nitrogen.

Recorded SF spectra are shown as a function of IR frequency in units of wavenumber (cm^{-1}). The spectra are baseline subtracted and corrected for the air–CaF_2 reflection losses in *s*-polarization. The polarization combinations are given in order of decreasing frequency of the interacting light fields, i.e. *ssp* stands for *s*-polarized SF, *s*-polarized VIS, and *p*-polarized IR light. For spherical liquid droplets the non-zero polarization configurations are *ppp*, *ssp*, *sps*, and *pss*, and the latter two have nearly identical spectral shapes.[78] All spectra are normalized to a SF spectrum of z-cut quartz measured in reflection geometry in the *ssp*-polarization combination in order to divide out the spectral shape of the IR beam.[52] We switched between measuring emulsions in the scattering geometry and quartz reference spectra by shifting the height of our sample cell holder (see Fig. 9.2).

The emulsions are prepared by adding 1 vol% dodecane or 2 vol% hexadecane to a solution of 10 mM deuterated sodium dodecyl sulfate (SDS) in D_2O. Hexadecane and dodecane are from Sigma–Aldrich and have analytical

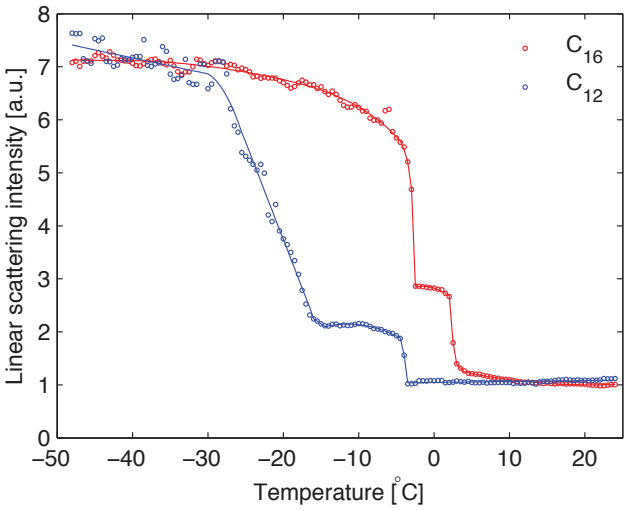

FIGURE 9.3: Temperature dependence of the linear scattering intensity of a diode laser for the C_{16} and C_{12} emulsions by cooling from 24 to −48 °C. Intensity changes are an indicator of phase transitions.

purity (≥ 99.8 %). Deuterated SDS (98 % D) is obtained from Cambridge Isotopes. The emulsions are ultrasonicated to decrease the average droplet radii, which is characterized by dynamic light scattering (using a Malvern Zetasizer Nano ZS) to be 116 ± 21 nm for the hexadecane emulsion and 59 ± 14 nm for the dodecane emulsion. Both emulsions have a surface to volume ratio of about $5 \cdot 10^5$ m^{-1} in the hard sphere approximation. The addition of SDS makes the emulsions stable, even over years.[230] With the droplet concentrations used the scattering is in the linear regime,[79] multiple scattering will thus be negligible. Hereafter, we will denote the hexadecane-in-D_2O emulsion as the C_{16} emulsion and the dodecane-in-D_2O emulsion as the C_{12} emulsion after the number of carbon atoms in the alkane.

Due to supercooling, the freezing temperatures in emulsions are lower than in bulk, which are reported to be 3.8 °C for D_2O, 18.1 °C for hexadecane, and −9.6 °C for dodecane.[9] We measure the freezing transition temperatures of the C_{16} and C_{12} emulsions by linear light scattering,[231,232] shown in Fig. 9.3. During the linear light scattering experiment the water phase crystallizes rapidly in the whole sample at −3 and −4 °C for the C_{16} and C_{12} emulsion, respectively. However, given that the water solvent can nucleate from a single nucleation core, the water crystallization temperature can vary by a couple of degrees, even for samples of the same composition.[217,233] The oil droplet solidification takes place over a broad range due to the polydispersity in droplet size.[216,220,221] This finding agrees with differential scanning calorimetry experiments.[215] The oil solidification takes place in the C_{16} emulsion from 2.5 to 1 °C and in the C_{12} emulsion over a broader temperature range from −15 to −27 °C.[234]

9.3 Results and discussion

9.3.1 Room temperature

SF scattering spectra of the two alkane-in-water emulsions taken at room temperature are shown in Fig. 9.4. The different polarization combinations allows to assign the resonances. Similar to the guidelines we have given for reflective SFG in Section 3.3, we can formulate rules of thumb for the dependence of the scattering SF signals on the polarization configuration. For our experimental configuration, the following dependencies on the polarization configurations are expected: [77, 235]

(a) Symmetric CH_2 and CH_3 vibrations are stronger in the *ssp*- than in the *ppp*-polarization combination and negligible in the *pss*-polarization combination.

(b) Antisymmetric CH_2 and CH_3 vibrations are strongest in the *ppp*-, intermediate in the *pss*-, and weakest in the *ssp*-polarization combination.

Therefore, we can assign the symmetric CH_2 stretch mode (d^+, at ~2857 cm^{-1}), the symmetric CH_3 stretch mode (r^+, at ~2878 cm^{-1}), and the nearly degenerate antisymmetric CH_3 stretch mode (r^-, at ~2970 cm^{-1}). The antisymmetric CH_2 stretch mode (d^-, at ~2928 cm^{-1}) overlaps with a Fermi Resonance of the r^+ with the overtone of the antisymmetric bending vibration (r^+_{FR}, at ~2940 cm^{-1}). [236, 237] In the *pss*-polarization combination the d^- dominates and in the *ssp*-combination the r^+_{FR} dominates. In the *ppp*-polarization combination both the d^- and the r^+_{FR} are strong and they are observed as a single broad band. The deviation of a few wavenumbers with other literature values [65, 83, 235, 237, 238] falls within the uncertainty in the calibration of the spectrometer.

The solid lines in Fig. 9.4 are fitted using Eq. (3.29) with five Lorentzian-shaped resonances and a spectral width of 10 cm^{-1} for the VIS beam. To decrease the covariant noise in the fitting procedure, we assumed the resonance widths of the CH_2 and CH_3 symmetric stretch vibrations to be equal.

An alkane molecule with an even number of carbon atoms in an all-*trans* configuration has local inversion symmetry at the centre of each C–C bond. Therefore, symmetry considerations impose that no SF photons can be emitted from the symmetric CH_2 stretch (d^+) vibration of an alkane in all-*trans* conformation. [239] Therefore, the amplitude ratio of the d^+ and the r^+ vibrations is a measure of the deviation from an all-*trans* conformation of the alkyl chains. [83, 238–243] In the *ssp*-polarization combination we find a d^+/r^+ ratio of 0.49 ± 0.14 for the C_{12} emulsion and a d^+/r^+ ratio of 0.89 ± 0.13 for the C_{16} emulsion. The latter is in agreement with the value of 0.88 ± 0.42 found by de Aguiar et al. [83] It follows that the d^+/r^+ ratio is 1.8 ± 0.6 times larger for hexadecane than for dodecane. Thus, hexadecane molecules have more gauche defects than dodecane molecules, which agrees with their difference in alkyl chain length. This ratio is in reasonable agreement with reflective SF studies on the liquid alkane–air interface by Esenturk et al. [243] where the d^+/r^+ amplitude ratio (as

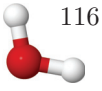

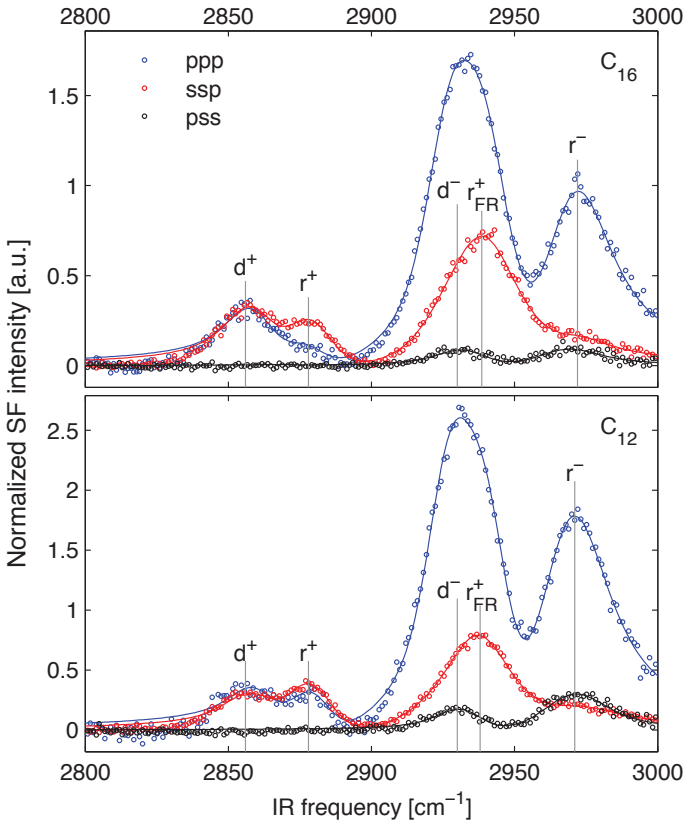

FIGURE 9.4: SF scattering spectra of the liquid–liquid interface of the C_{16} emulsion (top) and the C_{12} emulsion (bottom) at 24°C. Circles represent experimental data and solid lines are fitted curves to the experimental data (see text). The different CH_2 and CH_3 modes are indicated by their abbreviations.

determined from the intensity ratio) was found to be 1.12 ± 0.07 for dodecane and 1.8 ± 0.3 for hexadecane.

The d^+/r^+ ratio depends on the polarization combination. In the *ppp*-polarization combination we find a d^+/r^+ ratio of 1.6 ± 0.4 for the C_{16} emulsion and 0.76 ± 0.13 for the C_{12} emulsion. The d^+/r^+ ratios in the *ppp*-polarization combination are thus 1.8±0.4 (hexadecane) and 1.6±0.2 (dodecane) times higher than in the *ssp*-polarization combination. This result agrees with calculations using the theoretical framework provided by de Beer and Roke,[77] predicting the d^+/r^+ ratio to be 1.5 times larger in the *ppp*- than in *ssp*-polarization combination.

The antisymmetric CH_3 stretch (r^-) and symmetric CH_3 stretch (r^+) vibrations both originate from the same part of the alkane molecule and the r^-/r^+ amplitude ratio gives information about the average molecular tilt of the end group.[235] In the *ssp*-polarization combination we find a r^-/r^+ ratio of 0.38 ± 0.15 for the C_{16} emulsion and 0.26 ± 0.07 for the C_{12} emulsion. Calculations by Chen et al.[235] show that these ratios correspond to average tilt angles of the CH_3 group with respect to the droplet surface normal of $30 \pm 30°$ for the C_{16} emulsion and $55 \pm 15°$ for the C_{12} emulsion.[235] The r^-/r^+ ratio strongly depends on the polarization combination.

9.3.2 C_{16} EMULSION FREEZING

In the top panel of Fig. 9.5 we present SF scattering spectra in the *ssp*-polarization configuration at a selection of temperatures. For the liquid emulsion, we do not observe any significant changes in the amplitude and shape of the SF scattering spectra when we vary the temperature. The spectrum at 24 °C represents an average of several SF scattering spectra measured in the liquid phase. This spectrum is fitted using Eq. (3.29).

When we cool the C_{16} emulsion down to −48 °C, we observe discontinuous intensity increments in the SF scattering signal at temperatures that correspond with the phase transition temperatures (Fig. 9.3). The oil solidification, visible from 2 °C, induces both spectral changes as well as an overall increase in SF intensity. Note that the bulk crystal structure of frozen hexadecane is triclinic pinacoid[217,244,245] which is centrosymmetric and thus SF forbidden. Hence, the changes in SF spectrum are manifestations of the interfacial changes.

The formation of crystallites leads to an increase in the SF intensity as a result of (a combination of) the following three effects:

1. Ordering of the alkyl chains at the interface.[246]

2. Deviations from the spherical shape of liquid oil droplets leading to a larger interfacial area.[76,78]

3. The formation of multiple crystalline domains per frozen oil droplet. At the interfaces of the crystalline domains the symmetry is broken and additional SF light can be generated.[247]

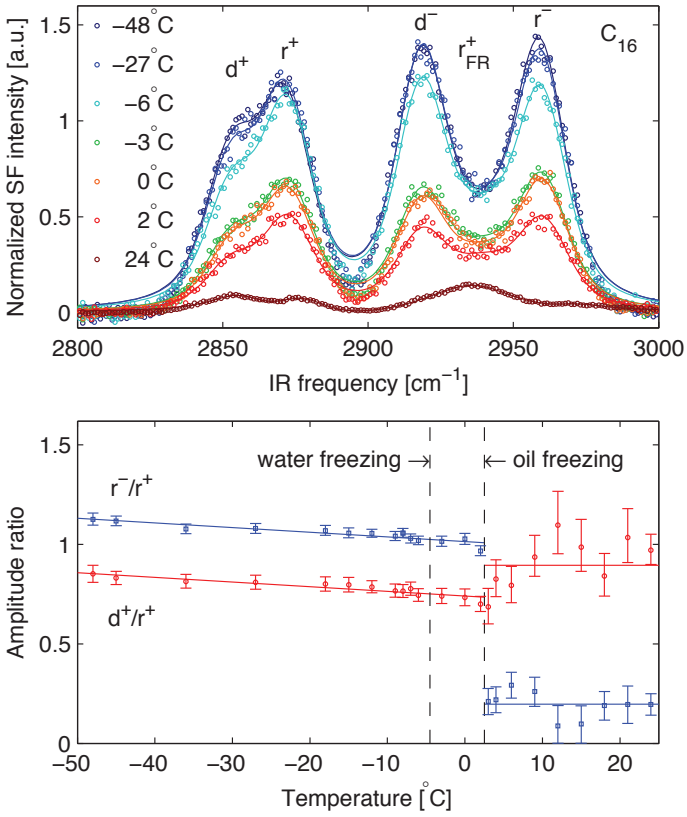

FIGURE 9.5: Top: SF scattering spectra in the *ssp*-polarization combination of the C_{16} emulsion at a selection of temperatures by cooling from 24 to −48 °C. Circles represent experimental data and solid lines are fits based on five resonances (see text). Bottom: The d^+/r^+ (red) and r^-/r^+ (blue) amplitude ratios of the C_{16} emulsion as determined by the fitting procedure. The dashed lines are the freezing points of the water and the oil. Error bars represent 95 % confidence intervals of the spectral fitting procedure and the solid lines are trends.

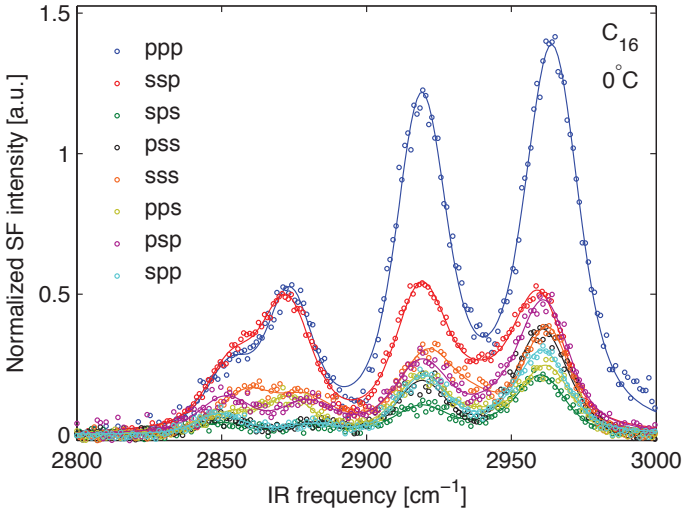

FIGURE 9.6: SF scattering spectra for all eight possible polarization combinations of the C_{16} emulsion at 0°C with frozen oil droplets and liquid water. SF scattering signal is observed for all eight polarization combinations, indicating less strict polarization selection rules than for the spherical symmetric droplets in the liquid emulsion (see text).

Effects 2 and 3 additionally lead to an increase in the SF signal due to a relaxation of the polarization selection rules,[78,247] i.e. more second-order susceptibility elements are non-zero than for spherical symmetric droplets. The random crystal orientation of the frozen oil droplets also contributes to the relaxation of the polarization selection rules.[247] The relaxation of the polarization selection rules is confirmed by the fact that oil freezing results in the observation of SF signal for all eight polarization configurations (Fig. 9.6). Combined molecular dynamics and quantum-chemical calculations would be required to determine the relative importance of these effects.

As oil freezing can result in a large variety of particles with different shapes, crystal orientations, and crystalline domains, the effective surface second-order susceptibility that determines the SF response of a particle can be different for each particle [cf. Eq. (3.35)]. As a result, the responses of the different vibrations no longer have well-defined phase relations. To illustrate the influence of a modification of the selection rules on the phase relations, one can compare the polarization dependencies for an isotropic interface in the *ssp*-polarization combination with respect to the *ppp*-polarization combination. For the *ssp*-polarization combination, the second-order susceptibilities of the symmetric CH_2 stretch (d^+) and antisymmetric CH_2 stretch (d^-) modes of the same molecular group have opposite signs, whereas they have equal signs for the *ppp*-polarization combination.[48,77] The same holds for the symmetric (r^+) and antisymmetric (r^-) stretch modes of a CH_3 group. To obtain structural information, we fit the intensity spectra with an incoherent sum of Lorentzians,

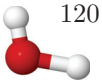

representing the d^+, r^+, d^-, r^+_{FR} and r^- bands. The d^+/r^+ and r^-/r^+ amplitude ratios are shown in the bottom panel of Fig. 9.5.

The crystallization of the hexadecane oil droplets leads to an increase of the r^-/r^+ ratio from 0.38±0.15 to 0.96±0.03 at 2 °C. The value of 0.38 is observed for the all-liquid phase for which there is no polarization mixing. This r^-/r^+ ratio corresponds to an average tilt angle of the terminal CH_3 group of 30 °C. [235] The r^-/r^+ ratio of 0.96 observed at 2 °C cannot be related to a tilt angle as there is strong polarization mixing (Fig. 9.6), leading to a significant *ppp*-type signal for an *ssp*-polarization combination configuration. The d^+/r^+ ratio is observed to decrease from 0.89 ± 0.13 to 0.70 ± 0.04 at 2 °C, which tentatively indicates an enhanced polar ordering and a decrease of the number of gauche defects of the hexadecane molecules at the interface. A decrease of the d^+/r^+ ratio has also been found in the case of hexadecane freezing at a hexadecane–sapphire interface. [248] However, as freezing also leads to a change of the polarization selection rules, it is not possible to draw unambiguous structural conclusions from the change in d^+/r^+ ratio.

The freezing of the water matrix at −4 °C does not lead to an abrupt change in the shape of the SF spectrum: neither the d^+/r^+ nor the r^-/r^+ ratio changes. This observation implies that water freezing has no effect on the shape and surface structure of already solid oil particles. This can be explained from the fact that the ice matrix is not very solid just below the freezing point: apparently the amorphous liquid-like layers of water molecules at the ice-oil interface fully accommodate the shape of the frozen oil droplets. This scenario is illustrated in the top panel of Fig. 9.9. The freezing of the water matrix does lead to an increase in the intensity of the SF signal. This is likely an effect of the clustering of the oil particles induced by the water freezing [212, 215, 249] because clustered oil particles scatter SF light at much higher intensities than isolated particles. [76, 250]

When the temperature is further decreased, the d^+/r^+ and r^-/r^+ ratios both gradually increase. The d^+/r^+ ratio increases from 0.74 ± 0.03 at −6 °C to 0.85 ± 0.04 at −48 °C. The r^-/r^+ ratio increases from 1.02±0.02 at −6 °C to 1.13±0.03 at −48 °C. The increase of these ratios indicates that the oil particles become more distorted with decreasing temperature. This can be explained by a hardening of the liquid-like water layer on the ice surface with decreasing temperature as we have observed in Chapter 7.

9.3.3 C_{12} EMULSION FREEZING

We also cool the C_{12} emulsion down to −48 °C. The SF scattering spectra at a selection of temperatures during the cooling process are shown in the top panel of Fig. 9.7. The spectra for the liquid emulsion do not show any significant changes as a function of temperature. The spectrum at 24 °C represents an average of the several SF scattering spectra measured in the liquid phase, which is fitted using Eq. (3.29).

For the C_{12} emulsion the water phase freezing occurs at −7 °C with the oil still being liquid. This causes an increases in SF intensity, which is likely a result

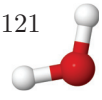

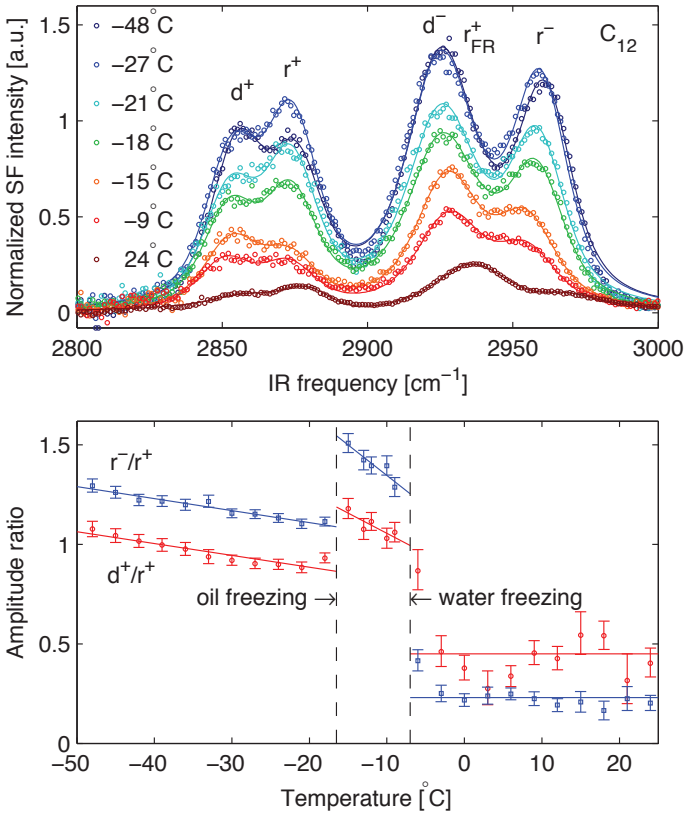

FIGURE 9.7: Top: SF scattering spectra in the *ssp*-polarization combination of the C_{12} emulsion at a selection of temperatures by cooling from 24 to −48 °C. Circles represent experimental data points and solid lines are fits based on five resonances (see text). Bottom: The d^+/r^+ (red) and r^-/r^+ (blue) amplitude ratios of the C_{12} emulsion as determined by the fitting procedure. The dashed lines are the freezing points of the oil and the water. Error bars represent 95 % confidence intervals of the spectral fitting procedure and the solid lines are trends.

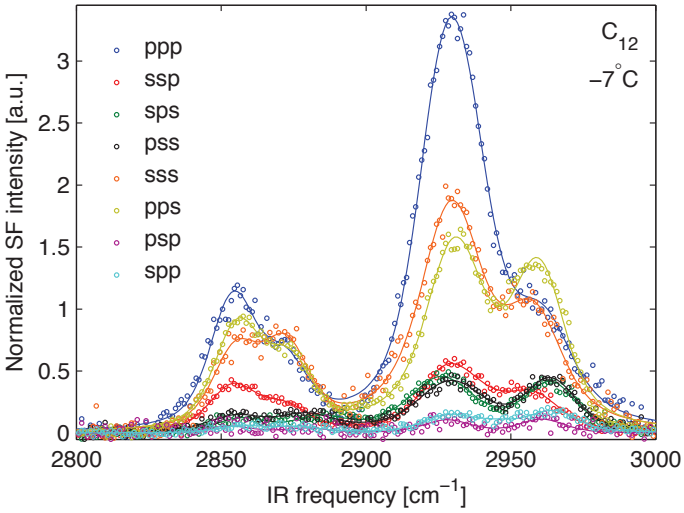

FIGURE 9.8: SF scattering spectra for all eight possible polarization combinations of the C_{12} emulsion at −7 °C with a frozen water phase and liquid oil droplets. SF signal is observed for all eight polarization combinations, indicating non-spherical droplet shapes.

of the clustering of the oil droplets.[212, 215, 249] Since we observe scattered SF photons for all eight polarization combinations (Fig. 9.8) which is not allowed for spherical droplets, we conclude that the water freezing induces a strong deformation of the liquid oil droplets,[78] probably as a result of the water expansion upon freezing. The water freezing likely leads to a large variety of droplet shapes, each with their own effective second-order susceptibility. We fit the intensity spectra with an incoherent sum of five Lorentzians as we did for the C_{16} emulsion with frozen oil droplets. The d^+/r^+ and r^-/r^+ amplitude ratios are shown in the bottom panel of Fig. 9.5. Both the d^+/r^+ and r^-/r^+ ratios increase upon freezing. At −9 °C the r^-/r^+ ratio is 1.29 ± 0.04. The increase of the r^-/r^+ ratio follows from the deformation of the oil droplets induced by the frozen water matrix. Freezing of the water matrix also leads to an increase of the d^+/r^+ ratio from 0.49 ± 0.14 to 1.06 ± 0.05 at −9 °C. This change is likely due to an increase in the number of gauche defects of the dodecane molecules at the droplet interface. However, it may in part also result from the modification of the polarization dependencies due to the fact that the droplets become non-spherical. A strong increase of the d^+/r^+ and the r^-/r^+ ratios is observed in the temperature range from −9 down to −15 °C, which can be explained from a hardening of the ice matrix, leading to a stronger deformation of the liquid oil droplets.

The dodecane oil droplets freeze at temperatures below −17 °C. The solidification of the oil droplets leads to larger SF signals and the crystallization causes a modification in the polarization dependencies, like we observed for the C_{16} emulsion. The oil solidification is accompanied by a decrease in oil

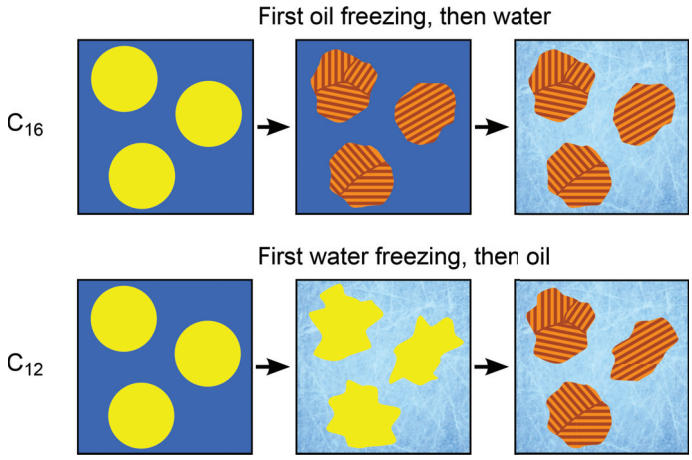

FIGURE 9.9: Illustration of the effect of a decrease in temperature on the oil droplets for the C_{16} emulsion (top) and the C_{12} emulsion (bottom). The liquid–solid transitions are indicated by the black arrows. Freezing of the water matrix has very little effect when the oil is solid (C_{16} emulsion) and a large influence on the oil droplet surface when the oil is liquid (C_{12} emulsion). Freezing of the oil droplets in liquid water leads to a distortion of the spherical droplet surface (C_{16} emulsion), whereas freezing of dodecane oil droplets in ice reduces the distortion that resulted from the freezing of the water matrix (C_{12} emulsion).

volume[251, 252] and is observed to lead to a decrease of the r^-/r^+ ratio from 1.51 ± 0.05 at $-15\,°C$ to 1.11 ± 0.02 at $-18\,°C$, which indicates that the surface deformation that was induced by the freezing of the water matrix gets somewhat reduced when the oil freezes. The bottom illustration of Fig. 9.9 illustrates this scenario. The d^+/r^+ ratio decreases from 1.18 ± 0.05 at $-15\,°C$ to 0.93 ± 0.03 at $-18\,°C$. This observation tentatively shows that the freezing of the oil leads to an increased ordering of the dodecane alkyl chains, thereby decreasing the number of gauche defects and thus the d^+/r^+ ratio. A further decrease of the temperature again increases both the d^+/r^+ ratio and the r^-/r^+ ratio. This observation indicates that the surface of the oil particle becomes more distorted at lower temperatures. As in the case of the C_{16} emulsion, this effect is probably caused by the hardening of the ice matrix with decreasing temperature.

In the temperature range where the oil droplets are frozen the r^-/r^+ ratio is larger for the C_{12} emulsion than for the C_{16} emulsion. This finding indicates that the frozen dodecane droplets are stronger deformed than the frozen hexadecane particles.

9.4 Conclusions

We studied the molecular interfacial properties of hexadecane and dodecane oil droplets in aqueous emulsions with sum-frequency scattering spectroscopy in the temperature range from 24 to −48 °C temperatures including the water–ice and liquid–solid oil transitions. The SF scattering spectra show vibrational bands corresponding to the symmetric CH_2 vibration (d^+), the antisymmetric CH_2 vibration (d^-), the symmetric CH_3 vibration (r^+) and its Fermi resonance (r^+_{FR}), and the antisymmetric CH_3 vibration (r^-). The d^+/r^+ and the r^-/r^+ amplitude ratios provide information on the conformation of the alkane molecules and the shape of the oil droplets. Both oil and water freezing lead to a distortion of the spherical-symmetry of the droplets and a modification of the polarization dependencies, which in turn affects the d^+/r^+ and r^-/r^+ ratios. Whereas the freezing of hexadecane oil droplets in liquid water leads to changes in the oil surface, the subsequent freezing of the water phase has little effect on the oil surface, probably because the amorphous liquid-like ice layer at the ice–oil interface is soft in comparison with the surface of already frozen oil droplets. Freezing of the water matrix is observed to lead to a strong distortion of the surface of the oil droplets in case the oil is liquid (dodecane). Freezing of liquid dodecane oil droplets within an ice matrix reduces the distortion that resulted from freezing of the water matrix. Further decreasing the temperature for solid oil particles embedded in ice leads to a further distortion of the oil surface, probably because the ice matrix hardens at lower temperatures, thereby imposing a stronger deformation of the solid oil particle.

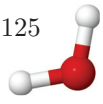

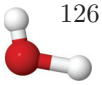

10 Cool behaviour of water droplets in oil

We report on the surface structure of nanoscopic water droplets and ice nanocrystals in hydrophobic oil as obtained from vibrational sum-frequency scattering measurements. The interface of a water droplet shows significantly stronger hydrogen bonds than the air–water interface and previously reported planar hydrophobic–water interfaces at room temperature. The observed spectral difference is similar to that of a planar air–water surface at a temperature that is ~60 K lower. Supercooling the droplets to 263 K does not affect the surface structure. Below the homogeneous ice nucleation temperature a single vibrational mode is present with a similar mean hydrogen-bond strength as for a planar ice–air interface. The observed differences suggest that the interface of a liquid water droplet in a hydrophobic environment — such as marine aerosols and cloud droplets — is much less reactive than expected.

10.1 Introduction

Aqueous hydrophobic interfaces play a defining role on nano- and microscopic length scales. Pockets and droplets of water in a hydrophobic environment are omnipresent in the atmosphere (as ice particles, marine aerosols, and cloud droplets [253]), the earth [254] (in e.g. oil fields), and in chemical [255, 256] and biological processes [257–259] (as vehicles for medicine delivery [260]). For all of these processes the hydrophobic interface of nanoscopic water droplets plays a critical role in determining the fate of the system. The molecular surface properties of such water droplets are commonly inferred from data obtained from the macroscopic water–air interface [48, 66, 194, 261–263] or from aqueous solutions of solvated hydrophobes, [264] systems that are possible very different in both their size, chemical composition and temperature dependence from actual droplet surfaces. As such, the surface structure of a water droplet remains elusive.

In this chapter we present temperature controlled sum-frequency scattering experiments on nanoscopic water droplets in a liquid hydrophobic environment. We find that compared to the water–air interface the spectrum reveals a greater order corresponding to that of a planar water surface at a ~60 K lower temperature. In addition, upon supercooling the droplets the surface spectrum does not change shape. Cooling the water droplets below the homogeneous ice nucleation temperature results in a spectrum with a single symmetric peak that

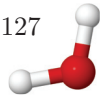

is similar to the one found for the ice–air interface.

10.2 Experimental methods

Water-in-oil emulsions are prepared by 1 vol% D_2O to a solution of 5 mM Span80 in hexadecane or in a 1:1 mixture of decane and cyclohexane. The emulsions are sonicated in an ultrasonic bath to an average droplet radius of ~100 nm and a polydispersity index of ~0.2. Span80 is a hydrophobic non-ionic surfactant that partially covers the interface and stabilizes the droplets.

Temperature dependent SF scattering measurements are performed using a custom made temperature cell (Quantum Northwest) with a metallic holder for the sample cuvette. The temperature is regulated by an attached Peltier element. The hot side of the Peltier element is cooled with a flow of liquid ethanol pumped by a peristaltic pump (Ismatec ISM1200). The liquid ethanol is cooled to ~220 K with a copper coil placed in a bath containing a mixture of dry ice and ethanol. The windows of the temperature cell are from CaF_2 (for the incoming beams) and quartz (for the scattered SF beam). The enclosed sample chamber is filled with N_2 gas to avoid condensation of water vapour.

The SF scattering experiments are performed with a comparable experimental setup as the one described in Chapter 9. The angle between the 10 μJ VIS beam (800 nm, FWHM 15 cm^{-1}) and the 6 μJ IR beam (3–4.5 μm, FWHM 160 cm^{-1}) is 20° (as measured in air). The focused beams are overlapped in a sample cuvette with a path length of 200 μm. The scattered SF photons are detected under an angle of 55° (as measured in air). The experimental setup is purged with N_2 gas to reduce the strong CO_2 absorption around 2345 cm^{-1} of the IR pulse and to prevent the condensation of water vapour on the temperature cell windows.

All spectra are acquired in an *ssp*-polarization configuration and baseline subtracted. Because the scattering experiments are performed in transmission, we have to take into account that the oil phase absorbs part of the IR spectrum. For that purpose the SF scattering spectra are corrected by a linear absorption spectrum as measured from the same cuvette. Next the spectra are corrected for refraction of the electromagnetic fields at the droplet interface using non-linear Mie theory [76, 77] and literature values for the optical constants of oil [265] and D_2O. [266] The spectral envelope of the IR light is divided out by a SF spectrum of z-cut quartz measured in reflection geometry.

10.3 Results and discussion

The scattered SF spectrum of D_2O nanodroplets in d-hexadecane (296 K) as well as the SF spectrum of a planar liquid D_2O–air interface are shown in Fig. 10.1. The SF spectrum of the D_2O–air interface has three main features at 2370 cm^{-1}, 2510 cm^{-1}, and 2745 cm^{-1}. The latter corresponds to free OD bonds sticking out of the surface. [68] The 296 K droplet–hydrophobic interface spectrum contains the same 2370 cm^{-1} and 2510 cm^{-1} features (indicated by the

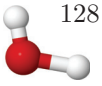

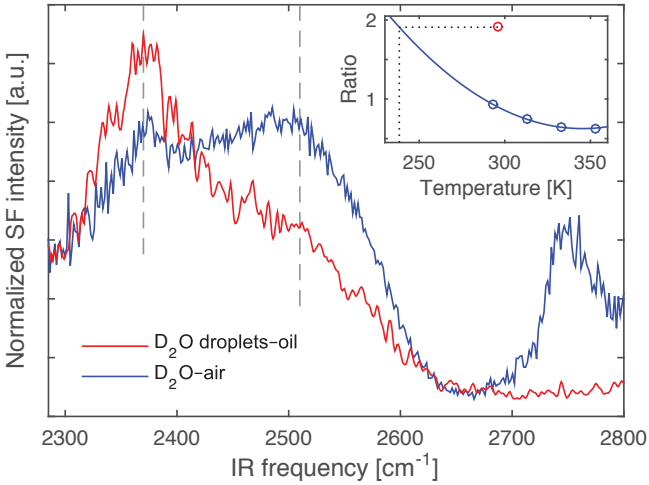

FIGURE 10.1: SF scattering spectrum of D_2O droplets in d-hexadecane (red) and SF spectrum of the D_2O–air interface measured in reflection geometry (blue). The inset shows the ratio between the low and high frequency bands of the SF spectrum of the planar water–air interface [267] (blue markers) and an extrapolation with a quadratic polynomial fit to a lower temperature range (blue line). The ratio for the room temperature water nanodroplet spectrum is depicted by the red marker. The SF spectra are collected in the *ssp*-polarization configuration.

dashed lines), but the higher frequency components are significantly less intense. The frequency of the OD stretching vibrations is correlated to the strength of the interfacial hydrogen-bond interaction: the OD frequency decreases when the hydrogen-bond strength increases. Hence, there are relatively more strongly hydrogen-bonded water molecules at the water droplet interface than at the water–air interface of the same temperature. This difference implies a higher degree of tetrahedral ordering at the water droplet interface.

The peak ratio of the 2370 cm^{-1} and 2510 cm^{-1} features changes with temperature for the water–air interface. The inset in Fig. 10.1 shows that the ratio increases with decreasing temperature, [267] indicating that the population of stronger hydrogen bonds increases over that of weaker hydrogen bonds. The peak ratio obtained for the water droplets is also indicated (red marker). Based on extrapolating the ratios found for the water–air spectra (blue line) we find that the same ratio as for the water droplets would be found at a hypothetical planar water–air interface of ~240 K (i.e. ~60 K colder). Thus, the water molecules of the water droplet–hydrophobic interface appear to be much more structured than the water molecules at a planar water–air interface. This result is in qualitative agreement with previous studies on macroscopic water–hydrophobic interfaces, [267–269] but the change in the peak ratio with respect to the air–water interface (100 %) is much bigger than that observed for the planar liquid–hydrophobic interfaces (~20 % [267–269]). The absence of a non-

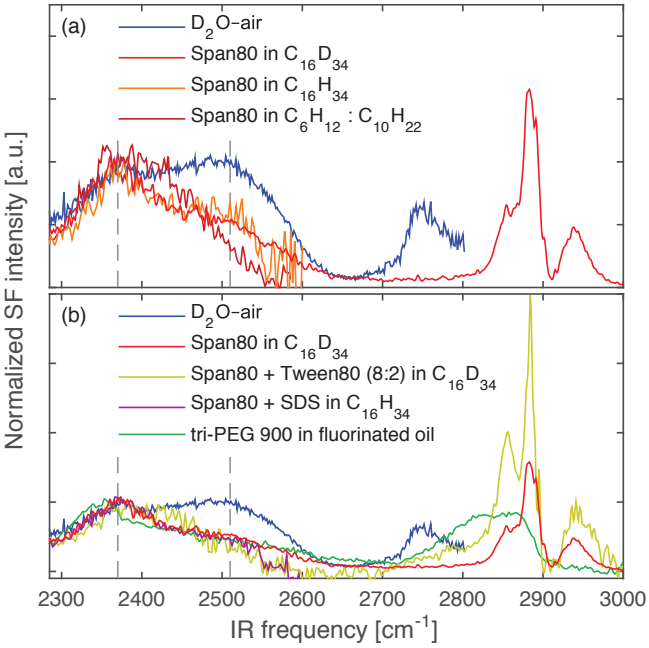

Figure 10.2: Room temperature SF scattering spectra of D_2O droplets in different solvents (a) and stabilized with different surfactants. (b) The planar D_2O–air SF spectrum is shown for comparison. (a) D_2O droplets (1 vol%) in deuterated and hydrogenated hexadecane and in a mixture of cyclohexane and decane, stabilized with 5 mM Span80. (b) D_2O droplets in 5 mM Span80 in deuterated hexadecane, a 5 mM mixture of 84:16 weight fraction Span80:Tween80 in deuterated hexadecane, a mixture of 10 mM SDS with 5 mM Span80 in hexadecane, tri-block PEG-900 in fluorinated oil HFE-7500 (prepared with microfluidics).

hydrogen-bonded free OD mode in the droplet spectrum can be explained by the presence of OH groups on the Span80 molecule that can form hydrogen bonds with interfacial water molecules.

To estimate the influence of the precise chemical structure of the hydrophobic environment on the interfacial water structure we measure water droplets in different hydrophobic solvents. SF scattering spectra for other combinations of hydrophobic oils (mixtures of decane and cyclohexane, fluorinated oil) and surfactants (Tween80, tri-block PEG-900) are presented in Fig. 10.2. The spectra of dispersed water droplets in various hydrophobic environments are all redshifted with respect to a planar water–air interface. Besides, the addition of either an anionic (SDS) or a hydrophilic non-ionic surfactants (Tween80) does not result in a significant spectral change. This indicates that the spectral redshift is a common phenomenon of water droplets in an hydrophobic environment.

The SF spectra of D_2O droplets in a mixture of decane and cyclohexane

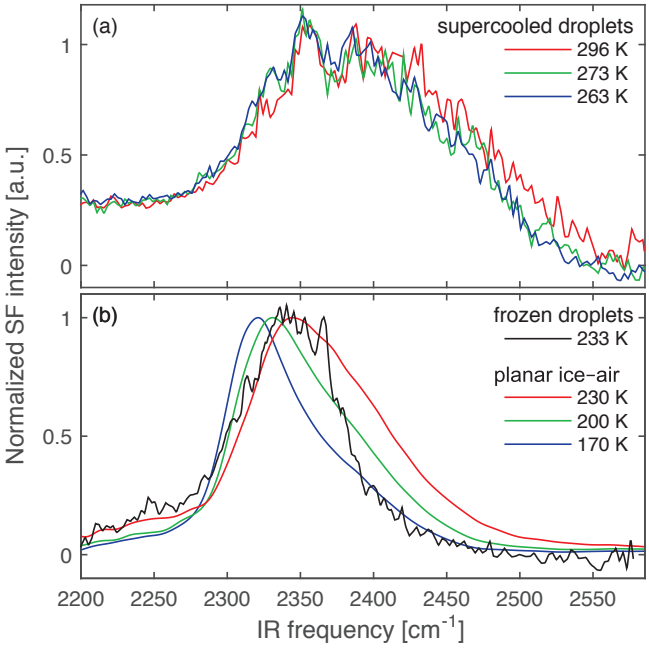

FIGURE 10.3: (a) SF scattering spectra of D_2O droplets in a mixture of decane and cyclohexane at room temperature and under supercooled conditions. (b) SF scattering spectrum of frozen D_2O droplets in a mixture of decane and cyclohexane at 233 K and SF spectra of the basal surface of the H_2O ice–air at 230 K, 200 K, and 170 K. The H_2O spectra are converted to D_2O spectra [263] by multiplying the frequencies by a factor of 1/1.35.

at different temperatures are shown in Fig. 10.3. Supercooling the droplets results in a slight redshift of the spectrum, but the spectral shape does not change (Fig. 10.3a). Further cooling the droplets down to 233 K let all droplets freeze (the homogeneous ice nucleation point of D_2O is 237 K [270]) and yields a spectrum of ice nanocrystals (Fig. 10.3b). The spectrum of the nanocrystals is redshifted and much narrower than the spectrum of liquid droplets, reflecting the narrower distribution of hydrogen bonds in the ice nanocrystals and their increased strength. For comparison, Figure 10.3b also shows normalized intensity spectra of the planar ice–air interface (see Chapter 6). The H_2O frequencies are converted to corresponding D_2O frequencies [263] by multiplication with 1/1.35. The resonance in the SF spectrum of the ice nanocrystals has a similar frequency as is observed for the planar ice surface of the same temperature. This indicates that the difference in surface structure observed for the liquid interface is not present in the solid phase. The absence of the effect for the frozen droplets can be understood from the fact that when the droplets freeze, the mutual water–water interactions become relatively more important for the resulting water spectrum (and the detected hydrogen-bond strength) than the interactions with the hydrophobic oil molecules. For crystalline planar ice, the

observed SF ice–air spectrum originates in part from OH groups connecting the different layers in the ice crystal.[169,174] These deeper layers of water molecules are much less influenced by the hydrophobic groups at the interface. Hence, for planar ice and frozen water droplets of the same temperature the hydrogen bonds of the probed OH groups are of similar strength.

Thermodynamics[271,272] and Raman-MCR measurements on solvated alkanols[264] show that hydrophobic solute perturbed water molecules are more tetrahedrally ordered and thus more constrained in configurational space. These solutes are very small and fulfill the criterion of Chandler[255] that states that hydrophobic solutes lead to an enhancement of the tetrahedral ordering of water if the radius of the solute is <1 nm.[255] In this perspective the present observations of an enhanced ordering of water molecules at the surface of water nanodroplets embedded in oil is surprising, as the droplet radius is very large compared to the criterion defined by Chandler. However, the interaction with oil can lead to a significant local corrugation of the water droplet surface, yielding a similar structure for the interfacial water as is observed for water surrounding small hydrophobic solutes.

10.4 Conclusions

Vibrational sum-frequency scattering spectra from water droplets with a radius of ~100 nm embedded in a hydrophobic liquid at different temperatures show that the hydrogen-bond network of the interfacial water possesses a much enhanced tetrahedral structure compared to a planar air–water interface. This greater order manifests itself as a redshifted spectrum. This increase is much larger than observed in previous studies of planar liquid hydrophobic–water interfaces. The observed surface structure of the water droplets corresponds to that of a water–air interface that is ~60 K colder. Upon supercooling the droplets, the surface spectrum does not change shape. Cooling the sample below the homogeneous ice nucleation temperature results in a spectrum with a single symmetric peak at a comparable frequency as that of a planar ice–air interface of the same temperature.

The presented experiments demonstrate the possibility of quantifying the interfacial structure of water droplets and illustrate the large impact of nanoscopic hydrophobic surfaces on the hydrogen-bond structure of water. With a reduction of the effective 'surface temperature' we expect that the reactivity of water droplets embedded in a hydrophobic environment such as in marine aerosols and cloud droplets[253] or medicine carriers[260] is lower than what one might think based on the actual temperature. Future studies on such nanoscopic systems may reveal important information on the role and reactivity of interfacial water in aerosol formation, protein folding, pore functioning[255,257,258,273] and the charging and stabilization of hydrophobic interfaces.

The work presented in this chapter has been performed in collaboration with the group of Prof. Dr. Sylvie Roke at the EPFL. The sum-frequency scattering experiments on liquid water droplets have been carried out by Nikolay Smolentsev. The author has cooperated with Nikolay Smolentsev on the conduction of the sum-frequency scattering experiments on frozen water droplets.

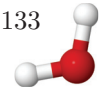

Appendix: Determination of the crystal orientation of ice

Hexagonal ice (I_h) is a uniaxial birefringent crystal and its birefringence can be used to determine the crystal orientation. The ordinary axes have a refractive index of n_o = 1.3091 and the extraordinary or optical axis has a refractive index of n_e = 1.3105 for light at a wavelength of 589 nm (daylight mean).[274] We exploit the birefringence of ice to determine the orientation of the optical axis, which coincides with the basal plane of ice.

For that purpose we constructed a Rigsby-type universal stage with four independent axes of rotation (Fig. A1).[275–277] The stage can rotate around an inner vertical axis (IV), an outer vertical axis (OV), a north–south axis (NS), and an east–west axis (EW). The point of intersection of NS and EW lays in IV.

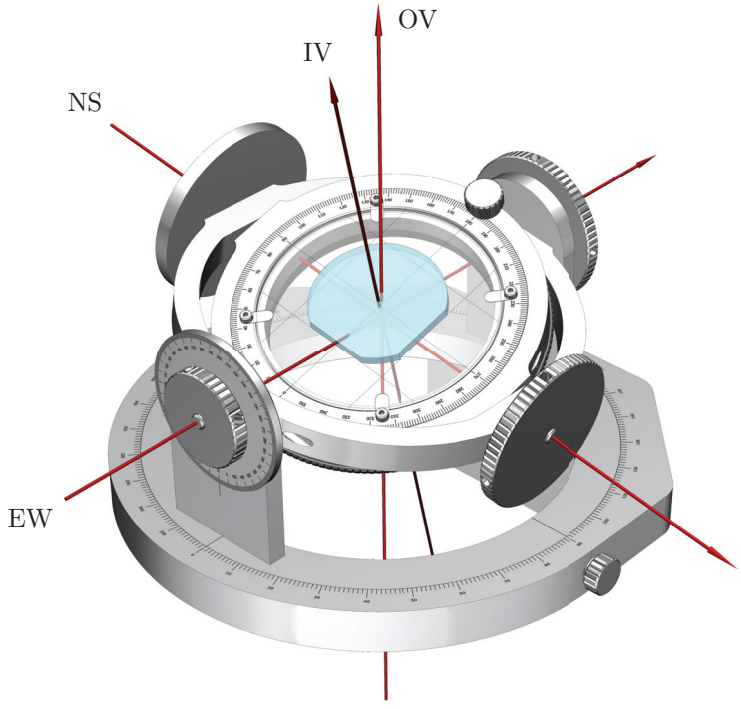

Figure A1: The four independent axes of rotation of the Rigsby stage.

The Rigsby stage comprises two crossed polarizing filters in front of a diffuse lamp. The OV coincides with the line of sight. The bottom polarizer is oriented to transmit light that is vibrating in a north–south direction and the top polarizer (or analyser) to transmit light vibrating in an east–west direction. During crystal orientation determination it is of paramount importance to keep the eye centred above the ice, especially at higher angles of inclination. We ensure the alignment of the eye with two cross hairs on top of the polarizers.

The optical axis orientation can be determined by the following routine, as described by Fairbairn: [275]

1. Rotate on IV to extinction.
2. Test the extinction by rotation on NS. If the ice does not remain dark, then return on NS to 0°, rotate 90° on IV to the alternative extinction position and test in the same manner on NS. In this position it will remain dark, indicating that the east–west plane contains the optical axis.
3. Turn about 20–30° on EW and rotate on NS to an extinction position. If two positions are available, select the one of least inclination.
4. Rotate on EW to the zero position. Then rotate around OV. If the ice remains dark, then the optical axis coincides with the line of sight; if it is illuminated, then the optical axis is normal to the line of sight and to NS.
5. Note the readings on IV and NS.

Special orientation cases arise where, in its initial position, the crystal remains dark for all positions of IV (optical axis parallel, or nearly so, to the line of sight) or where the manipulation in step 3 gives extinction in both IV positions (optical axis perpendicular to the line of sight). In the former case, a more exact determination can be obtained by the following additional steps:

1. Rotate on NS until the ice is illuminated.
2. Rotate on IV to restore extinction.
3. Return NS to 0°, retaining the IV position.
4. Proceed with the standard procedure, omitting steps 1 and 2.

The second case is treated as follows:

1. With the crystal at one of the two extinction positions, rotate an arbitrary amount on EW.
2. Then vary NS. If the crystal remains dark, the horizontal optical axis lies in the north–south plane; if extinction is lost, the optical axis lies in the east–west plane.

Care has to be taken that the difference in refractive index of ice and air gives a distorted view of the optical axis. This should be properly corrected for by Snell's law, especially for larger tilt angles. [276]

Fundamental constants

Quantity	Symbol	Numerical value	Unit
number π	π	3.14159265358979323...	
number e	e	2.71828182845904523...	
speed of light in vacuum	c	299792458	m s^{-1}
vacuum permeability	μ_0	$4\pi \cdot 10^{-7}$	N A^{-2}
vacuum permittivity $1/\mu_0 c^2$	ϵ_0	$8.854187817... \cdot 10^{-12}$	F m^{-1}
elementary charge	e	$1.6021766208(98) \cdot 10^{-19}$	C
Planck constant	h	$6.626070040(81) \cdot 10^{-34}$	J s
reduced Planck constant $h/2\pi$	$\hbar$	$1.054571800(13) \cdot 10^{-34}$	J s
Avogardo constant	N_A	$6.022140857(74) \cdot 10^{-23}$	mol^{-1}
Boltzmann constant	k_B	$1.38064852(79) \cdot 10^{-23}$	J K^{-1}

Values are taken from the National Institute of Standards and Technology. [278]

Bibliography

[1] J. Buisman, *Bar en boos. Zeven eeuwen winterweer in de Lage Landen*. Westland, 1984, ISBN:90-246-4412-7

[2] A. D. Kerr, The bearing capacity of floating ice plates subjected to static or quasi-static loads. *J. of Glaciol.*, **17**(76):229–268, 1976, DOI:10.3198/1976JoG17-76-229-268

[3] A. D. Kerr, Bearing capacity of floating ice covers subjected to static, moving, and oscillatory loads. *Appl. Mech. Rev*, **49**(11):463–476, 1996, DOI:10.1115/1.3101919

[4] L. Fransson, *Ice handbook for engineers*. Luleå University of Technology, 2009, version 1.2

[5] P. Ball, *H_2O: A biography of water*. Phoenix, 2015, ISBN:978-0-7538-1092-7

[6] Y. Maréchal, *The Hydrogen Bond and the Water Molecule*. Elsevier, 2007, ISBN:0-444-51957-2

[7] C. J. Fecko, J. D. Eaves, J. J. Loparo, A. Tokmakoff, and P. L. Geissler, Ultrafast hydrogen-bond dynamics in the infrared spectroscopy of water. *Science*, **301**(5640):1698–1702, 2003, DOI:10.1126/science.1087251

[8] J. B. Asbury, T. Steinel, K. Kwak, S. A. Corcelli, C. P. Lawrence, J. L. Skinner, and M. D. Fayer, Dynamics of water probed with vibrational echo correlation spectroscopy. *J. Chem. Phys.*, **121**(24):12431–12446, 2004, DOI:10.1063/1.1818107

[9] D. R. Lide (editor), *CRC Handbook of Chemistry and Physics*. CRC Press, 88th edition, 2007, ISBN:0-8493-0488-1

[10] F. C. Frank, Descartes' observations on the Amsterdam snowfalls of 4, 5, 6 and 9 February 1635. *J. Glaciol.*, **13**(69):535–539, 1974, DOI:10.3198/1974JoG13-69-535-539

[11] R. M. Rosenberg, Why is ice slippery? *Phys. Today*, **58**(12):50–55, 2005, DOI:10.1063/1.2169444

[12] Y. Li and G. A. Somorjai, Surface premelting of ice. *J. Phys. Chem. C*, **111**(27):9631–9637, 2007, DOI:10.1021/jp071102f

[13] J. G. Dash, A. W. Rempel, and J. S. Wettlaufer, The physics of premelted ice and its geophysical consequences. *Rev. Mod. Phys.*, **78**(3):695–741, 2006, DOI:10.1103/RevModPhys.78.695

[14] J. W. M. Frenken and J. F. v. d. Veen, Observation of surface melting. *Phys. Rev. Lett.*, **54**(2):134–137, 1985, DOI:10.1103/PhysRevLett.54.134

[15] J. G. Dash, Surface melting. *Contemporary Physics*, **30**(2):89–100, 1989, DOI:10.1080/00107518908225509

[16] S. G. Warren and R. E. Brandt, Optical constants of ice from the ultraviolet to the microwave: A revised compilation. *J. Geophys. Res.*, **113**:D14220, 2008, DOI:10.1029/2007JD009744

[17] C. Starr, C. Evers, and L. Starr, *Biology: Concepts and Applications*. Cengage Learning, 9th edition, 2014, ISBN:978-1-285-42781-2

[18] C. A. Gueymard, The sun's total and spectral irradiance for solar energy applications and solar radiation models. *Sol. Energy*, **76**(4):423–453, 2004, DOI:10.1016/j.solener.2003.08.039

[19] C. L. Braun and S. N. Smirnov, Why is water blue? *J. Chem. Educ.*, **70**(8):612–614, 1993, DOI:10.1021/ed070p612

[20] B. A. Zilles and W. B. Person, Interpretation of infrared intensity changes on molecular complex formation. I. Water dimer. *J. Chem. Phys.*, **79**(1):65–77, 1983, DOI:10.1063/1.445515

[21] P. F. Bernath, *Spectra of Atoms and Molecules*. Oxford University Press, 1995, ISBN:0-19-507598-6

[22] J. L. McHale, *Molecular Spectroscopy*. Pearson, 1999, ISBN:0-13-229063-4

[23] P. Hamm and M. Zanni, *Concepts and Methods of 2D Infrared Spectroscopy*. Cambridge University Press, 2011, ISBN:978-1-107-00005-6

[24] Y. R. Shen, *The principles of nonlinear optics*. Wiley, 1984, ISBN:0-474-88998-9

[25] P. N. Butcher and D. Cotter, *The Elements of Nonlinear Optics*. Cambridge University Press, 1991, ISBN:0-521-42424-0

[26] S. Mukamel, *Principles of Nonlinear Optical Spectroscopy*. Oxford University Press, 1995, ISBN:0-19-513291-2

[27] B. E. A. Saleh and M. C. Teich, *Fundamentals of photonics*. Wiley, 2nd edition, 2007, ISBN:978-0-471-35832-9

[28] R. W. Boyd, *Nonlinear Optics*. Academic Press, 2008, ISBN:978-0-12-369470-6

[29] P. E. Powers, *Fundamentals of Nonlinear Optics*. CRC Press, 2011, ISBN:1-4200-9351-7

[30] J. D. Jackson, *Classical Electrodynamics*. Wiley, 3rd edition, 1998, ISBN:0-471-30932-X

[31] D. J. Griffiths, *Introduction to Electrodynamics*. Pearson, 3rd edition, 2008, ISBN:0-13-919960-8

[32] J. J. Sakurai, *Modern Quantum Mechanics*. Addison-Wesley, revised edition, 1994, ISBN:0-201-53929-2

[33] D. J. Griffiths, *Introduction to Quantum Mechanics*. Pearson, 2nd edition, 2005, ISBN:0-13-191175-9

[34] D. R. Dalton, *Foundations of Organic Chemistry: Unity and Diversity of Structures*. Wiley, 2011, ISBN:978-0-470-47908-7

[35] P. A. M. Dirac, A new notation for quantum mechanics. *Math. Proc. Cambridge Philos. Soc.*, **35**(3):416–418, 1939, DOI:10.1017/S0305004100021162

[36] A. Nitzan, *Chemical Dynamics in Condensed Phases*. Oxford University Press, 2006, ISBN:0-19-852979-1

[37] N. Bonanos, A. Huijser, and F. Poulsen, H/D isotope effects in high temperature proton conductors. *Solid State Ionics*, **275**:9–13, 2015, DOI:10.1016/j.ssi.2015.03.028

[38] E. R. Lippincott and R. Schroeder, One-dimensional model of the hydrogen bond. *J. Chem. Phys.*, **23**(6):1099–1106, 1955, DOI:10.1063/1.1742196

[39] H. J. Bakker and H. K. Nienhuys, Delocalization of protons in liquid water. *Science*, **297**(5581):587–590, 2002, DOI:10.1126/science.1073298

[40] V. F. Petrekno and R. W. Whitworth, *Physics of Ice*. Oxford University Press, 2002, ISBN:0-19-158134-8

[41] Y.-S. Lin, P. A. Pieniazek, M. Yang, and J. L. Skinner, On the calculation of rotational anisotropy decay, as measured by ultrafast polarization-resolved vibrational pump-probe experiments. *J. Chem. Phys.*, **132**(17):174505, 2010, DOI:10.1063/1.3409561

[42] T. Lipari and A. Szabo, Effect of librational motion on fluprescence depolarization and nuclear magnetic resonance relaxation in macromolecules and membranes. *Biophys. J.*, **30**(3):489–506, 1980, DOI:10.1016/S0006-3495(80)85109-5

[43] A. Einstein, Die Grundlage der allgemeinen Relativitätstheorie. *Ann. Phys. (Berlin)*, **354**(7):769–822, 1916, DOI:10.1002/andp.19163540702

[44] X. Zhuang, P. B. Miranda, D. Kim, and Y. R. Shen, Mapping molecular orientation and conformation at interfaces by surface nonlinear optics. *Phys. Rev. B*, **59**(19):12632–12640, 1999, DOI:10.1103/PhysRevB.59.12632

[45] F. F. Neumann, *Vorlesungen über die Theorie der Elastizität der festen Körper und des Lichtäthers*. B.G.Teubner-Verlag, 1885

[46] A. J. Moad and G. J. Simpson, A unified treatment of selection rules and symmetry relations for sum-frequency and second harmonic spectroscopies. *J. Phys. Chem. B*, **108**(11):3548–3562, 2004, DOI:10.1021/jp035362i

[47] A. G. Lambert, P. B. Davies, and D. J. Neivandt, Implementing the theory of sum frequency generation vibrational spectroscopy: A tutorial review. *Appl. Spectrosc. Rev.*, **40**:103–145, 2005, DOI:10.1081/ASR-200038326

[48] H.-F. Wang, W. Gan, R. Lu, Y. Rao, and B.-H. Wu, Quantitative spectral and orientational analysis in surface sum frequency generation vibrational spectroscopy (SFG-VS). *Int. Rev. Phys. Chem.*, **24**(2):191–256, 2005, DOI:10.1080/01442350500225894

[49] H. Goldstein, C. P. Poole, Jr., and J. L. Safko, *Classical Mechanics*. Addison-Wesley, 3rd edition, 2002, ISBN:978-0-201-65702-9

[50] I. V. Stiopkin, H. D. Jayathilake, C. Weeraman, and A. V. Benderskii, Temporal effects on spectroscopic line shapes, resolution, and sensitivity of the broad-band sum frequency generation. *J. Chem. Phys.*, **132**(23):234503, 2010, DOI:10.1063/1.3432776

[51] L. Velarde and H.-F. Wang, Unified treatment and measurement of the spectral resolution and temporal effects in frequency-resolved sum-frequency generation vibrational spectroscopy (SFG-VS). *Phys. Chem. Chem. Phys.*, **15**(46):19970–19984, 2013, DOI:10.1039/C3CP52577E

[52] D. K. Hore, M. Y. Hamamoto, and G. L. Richmond, Mid-infrared second-order susceptibility of α-quartz and its application to visible-infrared surface sum-frequency spectroscopy. *J. Chem. Phys.*, **121**(24):12589–12594, 2004, DOI:10.1063/1.1826055

[53] S. Nihonyanagi, R. Kusaka, K.-I. Inoue, A. Adhikari, S. Yamaguchi, and T. Tahara, Accurate determination of complex $\chi^{(2)}$ spectrum of the air/water interface. *J. Chem. Phys.*, **143**(12):124707, 2015, DOI:10.1063/1.4931485

[54] C. Hirose, N. Akamatsu, and K. Domen, Formulas for the analysis of the surface SFG spectrum and transformation coefficients of cartesian SFG tensor components. *Appl. Spectrosc.*, **46**(6):1051–1072, 1992, DOI:10.1366/0003702924124385

[55] P. Fischer and A. D. Buckingham, Surface second-order nonlinear optical activity. *J. Opt. Soc. Am. B*, **15**(12):2951–2957, 1998, DOI:10.1364/JOSAB.15.002951

[56] W.-K. Zhang, H.-F. Wang, and D.-S. Zheng, Quantitative measurement and interpretation of optical second harmonic generation from molecular interfaces. *Phys. Chem. Chem. Phys.*, **8**(35):4041–4052, 2006, DOI:10.1039/B608005G

[57] D. A. Kleinman, Nonlinear dielectric polarization in optical media. *Phys. Rev.*, **126**(6):1977–1979, 1962, DOI:10.1103/PhysRev.126.1977

[58] C. A. Dailey, B. J. Burke, and G. J. Simpson, The general failure of Kleinman symmetry in practical nonlinear optical applications. *Chem. Phys. Lett.*, **390**(1–3):8–13, 2004, DOI:10.1016/j.cplett.2004.03.109

[59] W.-K. Zhang, D.-S. Zheng, Y.-Y. Xu, H.-T. Bian, Y. Guo, and H.-F. Wang, Reconsideration of second-harmonic generation from isotropic liquid interface: Broken Kleinman symmetry of neat air/water interface from dipolar contribution. *J. Chem. Phys.*, **123**(22):224713, 2005, DOI:10.1063/1.2136875

[60] Y. Ni. Personal communication

[61] K. B. Wiberg and J. J. Wendoloski, Charge redistribution in the molecular vibrations of acetylene, ethylene, ethane, methane, silane and the ammonium ion. signs of the M–H bond moments. *J. Phys. Chem.*, **88**(3):586–593, 1984, DOI:10.1021/j150647a051

[62] H. Takahashi and S. Yabushita, Theoretical analysis of weak adjacent substituent effect on the overtone intensities of XH (X = C, O) stretching vibrations. *J. Phys. Chem. A*, **117**(26):5491–5502, 2013, DOI:10.1021/jp312674r

[63] S. Nihonyanagi, S. Yamaguchi, and T. Tahara, Direct evidence for orientational flip-flop of water molecules at charged interfaces: A heterodyne-detected vibrational sum frequency generation study. *J. Chem. Phys.*, **130**(20):204704, 2009, DOI:10.1063/1.3135147

[64] R. Superfine, J. Huang, and Y. Shen, Experimental determination of the sign of molecular dipole moment derivatives: an infrared–visible sum frequency generation absolute phase measurement study. *Chem. Phys. Lett.*, **172**(3):303–306, 1990, DOI: 10.1016/0009-2614(90)85408-5

[65] R. Lu, W. Gan, B.-H. Wu, H. Chen, and H.-F. Wang, Vibrational polarization spectroscopy of CH stretching modes of the methylene group at the vapor/liquid interfaces with sum frequency generation. *J. Phys. Chem. B*, **108**(22):7297–7306, 2004, DOI: 10.1021/jp036674o

[66] W. Gan, D. Wu, Z. Zhang, R.-R. Feng, and H.-F. Wang, Polarization and experimental configuration analyses of sum frequency generation vibrational spectra, structure, and orientational motion of the air/water interface. *J. Chem. Phys.*, **124**(11):114705, 2006, DOI:10.1063/1.2179794

[67] Y. Ni and J. L. Skinner, IR and SFG vibrational spectroscopy of the water bend in the bulk liquid and at the liquid–vapor interface, respectively. *J. Chem. Phys.*, **143**(1):014502, 2015, DOI:10.1063/1.4923462

[68] Q. Du, R. Superfine, E. Freysz, and Y. R. Shen, Vibrational spectroscopy of water at the vapor/water interface. *Phys. Rev. Lett.*, **70**(15):2313–2316, 1993, DOI:10.1103/ PhysRevLett.70.2313

[69] X. Wei, P. B. Miranda, and Y. R. Shen, Surface vibrational spectroscopic study of surface melting of ice. *Phys. Rev. Lett.*, **86**(8):1554–1557, 2001, DOI:10.1103/PhysRevLett.86. 1554

[70] D. P. Chong and S. R. Langhoff, Theoretical study of polarizabilities and hyperpolarizabilities of Ne, HF, F^-, and OH^-. *J. Chem. Phys.*, **93**(1):570–578, 1990, DOI: 10.1063/1.459558

[71] R. Lu, W. Gan, B.-H. Wu, Z. Zhang, Y. Guo, and H.-F. Wang, C–H stretching vibrations of methyl, methylene and methine groups at the vapor/alcohol (n = 1–8) interfaces. *J. Phys. Chem.*, **109**(29):14118–14129, 2005, DOI:10.1021/jp051565q

[72] H. Wu, W.-K. Zhang, W. Gan, Z.-F. Cui, and H.-F. Wang, An empirical approach to the bond additivity model in quantitative interpretation of sum frequency generation vibrational spectra. *J. Chem. Phys.*, **125**(13):133203, 2006, DOI:10.1063/1.2352746

[73] I. V. Stiopkin, C. Weeraman, P. A. Pieniazek, F. Y. Shalhout, J. L. Skinner, and A. V. Benderskii, Hydrogen bonding at the water surface revealed by isotopic dilution spectroscopy. *Nature*, **474**(7350):192–195, 2011, DOI:10.1038/nature10173

[74] B. Busson and A. Tadjeddine, Non-uniqueness of parameters extracted from resonant second-order nonlinear optical spectroscopies. *J. Phys. Chem. C*, **113**(52):21895–21902, 2009, DOI:10.1021/jp908240d

[75] Y. R. Shen, Phase-sensitive sum-frequency spectroscopy. *Annu. Rev. Phys. Chem.*, **64**(1):129–150, 2013, DOI:10.1146/annurev-physchem-040412-110110

[76] A. G. F. de Beer and S. Roke, Nonlinear Mie theory for second-harmonic and sum-frequency scattering. *Phys. Rev. B*, **79**(15):155420, 2009, DOI:10.1103/PhysRevB.79. 155420

[77] A. G. F. de Beer and S. Roke, Obtaining molecular orientation from second harmonic and sum frequency scattering experiments in water: Angular distribution and polarization dependence. *J. Chem. Phys.*, **132**(23):234702, 2010, DOI:10.1063/1.3429969

[78] A. G. F. de Beer, S. Roke, and J. I. Dadap, Theory of optical second-harmonic and sum-frequency scattering from arbitrarily shaped particles. *J. Opt. Soc. Am. B*, **28**(6):1374–1384, 2011, DOI:10.1364/JOSAB.28.001374

[79] H. B. de Aguiar, J.-S. Samson, and S. Roke, Probing nanoscopic droplet interfaces in aqueous solution with vibrational sum-frequency scattering: A study of the effects of path length, droplet density and pulse energy. *Chem. Phys. Lett.*, **512**(1):76–80, 2011, DOI:10.1016/j.cplett.2011.06.081

[80] S. Roke, W. G. Roeterdink, J. E. G. J. Wijnhoven, A. V. Petukhov, A. W. Kleyn, and M. Bonn, Vibrational sum frequency scattering from a submicron suspension. *Phys. Rev. Lett.*, **91**(25):258302, 2003, DOI:10.1103/PhysRevLett.91.258302

[81] S. Roke, M. Bonn, and A. V. Petukhov, Nonlinear optical scattering: The concept of effective susceptibility. *Phys. Rev. B*, **70**:115106, 2004, DOI:10.1103/PhysRevB.70.115106

[82] S. Roke, J. Buitenhuis, J. C. van Miltenburg, M. Bonn, and A. van Blaaderen, Interface–solvent effects during colloidal phase transitions. *J. Phys.: Condens. Matter*, **17**(45):S3469–S3479, 2005, DOI:10.1088/0953-8984/17/45/036

[83] H. B. de Aguiar, M. L. Strader, A. G. F. de Beer, and S. Roke, Surface structure of sodium dodecyl sulfate surfactant and oil at the oil-in-water droplet liquid/liquid interface: A manifestation of a nonequilibrium surface state. *J. Phys. Chem. B*, **115**(12):2970–2978, 2011, DOI:10.1021/jp200536k

[84] H. J. Bakker and J. L. Skinner, Vibrational spectroscopy as a probe of structure and dynamics in liquid water. *Chem. Rev.*, **110**(3):1498–1517, 2010, DOI:10.1021/cr9001879

[85] S. Woutersen, U. Emmerichs, H. K. Nienhuys, and H. J. Bakker, Anomalous temperature dependence of vibrational lifetimes in water and ice. *Phys. Rev. Lett.*, **81**(5):1106–1109, 1998, DOI:10.1103/PhysRevLett.81.1106

[86] H.-K. Nienhuys, S. Woutersen, R. A. van Santen, and H. J. Bakker, Mechanism for vibrational relaxation in water investigated by femtosecond infrared spectroscopy. *J. Chem. Phys.*, **111**(4):1494–1500, 1999, DOI:10.1063/1.479408

[87] R. L. A. Timmer and H. J. Bakker, Vibrational Förster transfer in ice Ih. *J. Phys. Chem. A*, **114**(12):4148–4155, 2010, DOI:10.1021/jp911726s

[88] C. P. Lawrence and J. L. Skinner, Vibrational spectroscopy of HOD in liquid D_2O. VII. temperature and frequency dependence of the OH stretch lifetime. *J. Chem. Phys.*, **119**(7):3840–3848, 2003, DOI:10.1063/1.1591178

[89] K. J. Tielrooij, C. Petersen, Y. L. A. Rezus, and H. J. Bakker, Reorientation of HDO in liquid H_2O at different temperatures: Comparison of first and second order correlation functions. *Chem. Phys. Lett.*, **471**:71–74, 2009, DOI:10.1016/j.cplett.2009.02.003

[90] F. Perakis and P. Hamm, Two-dimensional infrared spectroscopy of supercooled water. *J. Phys. Chem. B*, **115**(18):5289–5293, 2011, DOI:10.1021/jp1092288

[91] R. A. Nicodemus, S. A. Corcelli, J. L. Skinner, and A. Tokmakoff, Collective hydrogen bond reorganization in water studied with temperature-dependent ultrafast infrared spectroscopy. *J. Phys. Chem. B*, **115**(18):5604–5616, 2011, DOI:10.1021/jp111434u

[92] F. Perakis, S. Widmer, and P. Hamm, Two-dimensional infrared spectroscopy of isotope-diluted ice Ih. *J. Chem. Phys.*, **134**:204505, 2011, DOI:10.1063/1.3592561

[93] F. Perakis, J. A. Borek, and P. Hamm, Three-dimensional infrared spectroscopy of isotope-diluted ice Ih. *J. Chem. Phys.*, **139**:014501, 2013, DOI:10.1063/1.4812216

[94] A. Shalit, F. Perakis, and P. Hamm, Two-dimensional infrared spectroscopy of isotope-diluted low density amorphous ice. *J. Phys. Chem. B*, **117**(49):15512–15518, 2013, DOI:10.1021/jp4053743

[95] A. Millo, Y. Raichlin, and A. Katzir, Mid-infrared fiber-optic attenuated total reflection spectroscopy of the solid-liquid phase transition of water. *Appl. Spectrosc.*, **59**(4):460–466, 2005, DOI:10.1366/0003702053641469

[96] L. Chieffo, J. Shattuck, J. J. Amsden, S. Erramilli, and L. D. Ziegler, Ultrafast vibrational relaxation of liquid H_2O following librational combination band excitation. *Chem. Phys.*, **341**(1–3):71–80, 2007, DOI:10.1016/j.chemphys.2007.06.024l

[97] A. B. McCoy, T. L. Guasco, C. M. Leavitt, S. G. Olesence, and M. A. Johnson, Vibrational manifestations of strong non-Condon effects in the $H_3O^+ \cdot X_3$ (X = Ar, N_2, CH_4, H_2O) complexes: A possible explanation for the intensity in the 'association band' in the vibrational spectrum of water. *Phys. Chem. Chem. Phys.*, **14**(20):7205–7214, 2012, DOI:10.1039/C2CP24110B

[98] S. A. Corcelli and J. L. Skinner, Infrared and Raman line shapes of dilute HOD in liquid H_2O and D_2O from 10 to 90°C. *J. Phys. Chem. A*, **109**:6154–6165, 2005, DOI: 10.1021/jp0506540

[99] J. R. Schmidt, S. A. Corcelli, and J. L. Skinner, Pronounced non-Condon effects in the ultrafast infrared spectroscopy of water. *J. Chem. Phys.*, **123**:044513, 2005, DOI: 10.1063/1.1961472

[100] J. J. Loparo, S. T. Roberts, R. A. Nicodemus, and A. Tokmakoff, Variation of the transition dipole moment across the OH stretching band of water. *Chem. Phys.*, **341**(1–3):218–229, 2007, DOI:10.1016/j.chemphys.2007.06.056

[101] B. M. Auer and J. L. Skinner, IR and Raman spectra of liquid water: Theory and interpretation. *J. Chem. Phys.*, **128**:224511, 2008, DOI:10.1063/1.2766943

[102] A. M. Dokter and H. J. Bakker, Transient absorption of vibrationally excited ice Ih. *J. Chem. Phys.*, **128**:024502, 2008, DOI:10.1063/1.2820765

[103] A. Nitzan, S. Mukamel, and J. Jortner, Some features of vibrational relaxation of a diatomic molecule in a dense medium. *J. Chem. Phys.*, **60**(10):3929–3934, 1974, DOI: 10.1063/1.1680840

[104] V. M. Kenkre, A. Tokmakoff, and M. D. Fayer, Theory of vibrational relaxation of polyatomic molecules in liquids. *J. Chem. Phys.*, **101**(12):10618–10629, 1994, DOI:10. 1063/1.467876

[105] D. F. Hornig, H. F. White, and F. P. Reding, The infrared spectra of crystalline H_2O, D_2O and HDO. *Spectrochim. Acta*, **12**(4):338–349, 1958, DOI:10.1016/0371-1951(58) 80060-0

[106] A. Staib and J. T. Hynes, Vibrational predissociation in hydrogen-bonded OH...O complexes via OH stretch–OO stretch energy transfer. *Chem. Phys. Lett.*, **204**(1–2):196–205, 1993, DOI:10.1016/0009-2614(93)85627-Z

[107] G. Seifert, K. Weidlich, and H. Graener, Picosecond ir hole-burning spectroscopy on HDO ice Ih. *Phys. Rev. B*, **56**(22):R14231–R14234, 1997, DOI:10.1103/PhysRevB.56.R14231

[108] N. F. Zobov, O. L. Polyansky, C. R. Le Sueur, and J. Tennyson, Vibration-rotation levels of water beyond the Born–Oppenheimer approximation. *Chem. Phys. Lett.*, **260**(3–4):381–387, 1996, DOI:10.1016/0009-2614(96)00872-X

[109] J. C. Deàk, S. T. Rhea, L. K. Iwaki, and D. D. Dlott, Vibrational energy relaxation and spectral diffusion in water and deuterated water. *J. Phys. Chem. A*, **104**(21):4866–4875, 2000, DOI:10.1021/jp994492h

[110] C. P. Lawrence and J. L. Skinner, Vibrational spectroscopy of HOD in liquid D_2O. I. vibrational energy relaxation. *J. Chem. Phys.*, **117**(12):5827–5838, 2002, DOI:10.1063/ 1.1502248

[111] A. Kandratsenka, J. Schroeder, D. Schwarzer, and V. S. Vikhrenko, Nonequilibrium molecular dynamics simulations of vibrational energy relaxation of HOD in D_2O. *J. Chem. Phys.*, **130**:174507, 2009, DOI:10.1063/1.3126781

[112] S. Woutersen, U. Emmerichs, and H. J. Bakker, Femtosecond mid-IR pump-probe spectroscopy of liquid water: Evidence for a two-component structure. *Science*, **278**(5338):658–660, 1997, DOI:10.1126/science.278.5338.658

[113] G. Gale, G. Gallot, and N. Lascoux, Frequency-dependent vibrational population relaxation time of the OH stretching mode in liquid water. *Chem. Phys. Lett.*, **311**(3–4):123–125, 1999, DOI:10.1016/S0009-2614(99)00820-9

[114] S. T. van der Post, C.-S. Hsieh, M. Okuno, Y. Nagata, H. J. Bakker, M. Bonn, and J. Hunger, Strong frequency dependence of vibrational relaxation in bulk and surface water reveals sub-picosecond structural heterogeneity. *Nat. Commun.*, **6**:8384, 2015, DOI:10.1038/ncomms9384

[115] W. J. Smit and H. J. Bakker, Anomalous temperature dependence of the vibrational lifetime of the OD stretch vibration in ice and liquid water. *J. Chem. Phys.*, **139**(20):204504, 2013, DOI:10.1063/1.4833596

[116] H. Liu, Y. Wang, and J. M. Bowman, Ab initio deconstruction of the vibrational relaxation pathways of dilute HOD in ice Ih. *J. Am. Chem. Soc.*, **136**(16):5888–5891, 2014, DOI:10.1021/ja501986t

[117] S. Pandelov, B. M. Pilles, J. C. Werhahn, and H. Iglev, Time-resolved dynamics of the OH stretching vibration in aqueous NaCl hydrate. *J. Phys. Chem. A*, **113**(38):10184–10188, 2009, DOI:10.1021/jp904558m

[118] J. C. Werhahn, S. Pandelov, S. S. Xantheas, and H. Iglev, Dynamics of weak, bifurcated, and strong hydrogen bonds in lithium nitrate trihydrate. *J. Phys. Chem. Lett.*, **2**(13):1633–1638, 2011, DOI:10.1021/jz200591v

[119] M. Bradler, J. C. Werhahn, D. Hutzler, S. Fuhrmann, R. Heider, E. Riedle, H. Iglev, and R. Kienberger, A novel setup for femtosecond pump–repump–probe IR spectroscopy with few cycle CEP stable pulses. *Opt. Express*, **21**(17):20145–20158, 2013, DOI:10.1364/OE.21.020145

[120] D. Hutzler, J. C. Werhahn, R. Heider, M. Bradler, R. Kienberger, E. Riedle, and H. Iglev, Highly selective relaxation of the OH stretching overtones in isolated HDO molecules observed by infrared pump–repump–probe spectroscopy. *J. Phys. Chem. A*, **119**(26):6831–6836, 2015, DOI:10.1021/acs.jpca.5b05145

[121] L. Ojha, M. B. Wilhelm, S. L. Murchie, A. S. McEwen, J. J. Wray, J. Hanley, M. Masse, and M. Chojnacki, Spectral evidence for hydrated salts in recurring slope lineae on mars. *Nat. Geosci.*, **8**:829–832, 2015, DOI:10.1038/ngeo2546

[122] S. Pandelov, J. C. Werhahn, B. M. Pilles, S. S. Xantheas, and H. Iglev, An empirical correlation between the enthalpy of solution of aqueous salts and their ability to form hydrates. *J. Phys. Chem. A*, **114**(38):10454–10457, 2010, DOI:10.1021/jp106050r

[123] F. Muniz-Miranda, M. Pagliai, G. Cardini, and R. Righini, Bifurcated hydrogen bond in lithium nitrate trihydrate probed by ab initio molecular dynamics. *J. Phys. Chem. A*, **116**(9):2147–2153, 2012, DOI:10.1021/jp2120115

[124] V. M. van Essen, J. Cot Gores, L. P. J. Bleijendaal, H. A. Zondag, R. Schuitema, M. Bakker, and W. G. J. van Helden, Characterization of salt hydrates for compact seasonal thermochemical storage. In *Proceedings of the ASME 3rd International Conference of Energy Sustainability*, volume 2, pp. 825–830, American Society of Mechanical Engineers, 2009, ISBN:978-0-7918-4890-6

[125] G. Balasubramanian, M. Ghommem, M. R. Hajj, W. P. Wong, J. A. Tomlin, and I. K. Puri, Modeling of thermochemical energy storage by salt hydrates. *Int. J. Heat Mass Transfer*, **53**(25–26):5700–5706, 2010, DOI:10.1016/j.ijheatmasstransfer.2010.08.012

[126] P. J. Shamberger and T. Reid, Thermophysical properties of lithium nitrate trihydrate from (253 to 353) K. *J. Chem. Eng. Data*, **57**(5):1404–1411, 2012, DOI:10.1021/je3000469

[127] L. F. Cabeza, A. Gutierrez, C. Barreneche, S. Ushak, A. G. Fernández, A. I. Fernádez, and M. Grágeda, Lithium in thermal energy storage: A state-of-the-art review. *Renew. Sust. Energ. Rev.*, **42**:1106–1112, 2015, DOI:10.1016/j.rser.2014.10.096

[128] K. Hermansson, J. O. Thomas, and I. Olovsson, Hydrogen bond studies. CXX. An X-ray determination of the crystal structure of $LiNO_3.3H_2O$. *Acta Crystallogr. Sect. B*, **33**(9):2857–2861, 1977, DOI:10.1107/S0567740877009637

[129] K. Hermansson, J. O. Thomas, and I. Olovsson, Hydrogen bond studies. CXXXVIII. Neutron diffraction studies of $LiNO_3.3H_2O$ at 120 and 295 K. *Acta Crystallogr. Sect. B*, **36**(5):1032–1040, 1980, DOI:10.1107/S0567740880005237

[130] J. Helbing and P. Hamm, Compact implementation of Fourier transform two-dimensional IR spectroscopy without phase ambiguity. *J. Opt. Soc. Am. B*, **28**(1):171–178, 2011, DOI:10.1364/JOSAB.28.000171

[131] E. Bartholdi and R. R. Ernst, Fourier spectroscopy and the causality principle. *J. Magn. Resonance*, **11**(1):9–19, 1973, DOI:10.1016/0022-2364(73)90076-0

[132] R. Bloem, S. Garrett-Roe, H. Strzalka, P. Hamm, and P. Donaldson, Enhancing signal detection and completely eliminating scattering usingquasi-phase-cycling in 2D IR experiments. *Opt. Express*, **18**(26):27067–27078, 2010, DOI:10.1364/OE.18.027067

[133] M. Tsuboi and I. C. Hisatsune, Infrared spectrum of matrix-isolated nitrate ion. *J. Chem. Phys.*, **57**(5):2087–2093, 1972, DOI:10.1063/1.1678533

[134] A. M. Dokter, C. Petersen, S. Woutersen, and H. J. Bakker, Vibrational dynamics of ice in reverse micelles. *J. Chem. Phys.*, **128**(4):044509, 2008, DOI:10.1063/1.2826376

[135] M. J. P. Brugmans, H. J. Bakker, and A. Lagendijk, Direct vibrational energy transfer in zeolites. *J. Chem. Phys.*, **104**(1):64–84, 1996, DOI:10.1063/1.470876

[136] M. Falk, Frequencies of H–O–H, H–O–D and D–O–D bending fundamentals in liquid water. *J. Raman Spectrosc.*, **21**(9):563–567, 1990, DOI:10.1002/jrs.1250210907

[137] M. P. Casassa, E. J. Heilweil, J. C. Stephenson, and R. R. Cavanagh, Time-resolved measurements of OH(v = 1) vibrational relaxation on SiO_2 surfaces: Isotope and temperature dependence. *J. Chem. Phys.*, **84**(4):2361–2364, 1986, DOI:10.1063/1.450350

[138] T. Fujino, M. Kashitani, K. Fukuyama, J. Kubota, J. Kondo, A. Wada, K. Domen, C. Hirose, F. Wakabayashi, and S. Kano, Population lifetimes of the OH stretching band of water molecules on zeolite surfaces. *Chem. Phys. Lett.*, **261**(4–5):534–538, 1996, DOI:10.1016/0009-2614(96)01006-8

[139] A. Nitzan and J. Jortner, Electronic relaxation of small molecules in a dense medium. *Mol. Phys.*, **25**(3):713–734, 1973, DOI:10.1080/00268977300100651

[140] V. P. Tayal, B. K. Srivastava, D. P. Khandelwal, and H. D. Bist, Librational modes of crystal water in hydrated solids. *Appl. Spectrosc. Rev.*, **16**(1):43–134, 1980, DOI:10.1080/05704928008081709

[141] J. G. Dash, H. Fu, and J. S. Wettlaufer, The premelting of ice and its environmental consequences. *Rep. Prog. Phys.*, **58**(1):115, 1995, DOI:10.1088/0034-4885/58/1/003

[142] M. J. Molina, T.-L. Tso, L. T. Molina, and F. C.-Y. Wang, Antarctic stratospheric chemistry of chlorine nitrate, hydrogen chloride, and ice: Release of active chlorine. *Science*, **238**(4831):1253–1257, 1987, DOI:10.1126/science.238.4831.1253

[143] K. Bolton and J. B. C. Pettersson, Ice-catalyzed ionization of hydrochloric acid. *J. Am. Chem. Soc.*, **123**(30):7360–7363, 2001, DOI:10.1021/ja010096c

[144] A. Falenty, T. C. Hansen, and W. F. Kuhs, Formation and properties of ice XVI obtained by emptying a type sII clathrate hydrate. *Nature*, **516**(7530):231–233, 2014, DOI:10.1038/nature14014

[145] B. J. Murray, D. A. Knopf, and A. K. Bertram, The formation of cubic ice under conditions relevant to Earth's atmosphere. *Nature*, **434**(7030):202–205, 2005, DOI:10.1038/nature03403

[146] J. D. Bernal and R. H. Fowler, A theory of water and ionic solution, with particular reference to hydrogen and hydroxyl ions. *J. Chem. Phys.*, **1**:515–548, 1933, DOI:10.1063/1.1749327

[147] N. Materer, Molecular surface structure of ice(0001): dynamical low-energy electron diffraction, total-energy calculations and molecular dynamics simulations. *Surf. Sci.*, **381**(2–3):190–210, 1997, DOI:10.1016/S0039-6028(97)00090-3

[148] J. Braun, A. Glebov, A. P. Graham, A. Menzel, and J. P. Toennies, Structure and phonons of the ice surface. *Phys. Rev. Lett.*, **80**(12):2638–2641, 1998, DOI:10.1103/PhysRevLett.80.2638

[149] A. Glebov, A. P. Graham, A. Menzel, J. P. Toennies, and P. Senet, A helium atom scattering study of the structure and phonon dynamics of the ice surface. *J. Chem. Phys.*, **112**(24):11011–11022, 2000, DOI:10.1063/1.481741

[150] M. T. Suter, P. U. Andersson, and J. B. C. Pettersson, Surface properties of water ice at 150–191 K studied by elastic helium scattering. *J. Chem. Phys.*, **125**(17):174704, 2006, DOI:10.1063/1.2359444

[151] H. Groenzin, I. Li, and M. J. Shultz, Sum-frequency generation: Polarization surface spectroscopy analysis of the vibrational surface modes on the basal face of ice I_h. *J. Chem. Phys.*, **128**(21):214510, 2008, DOI:10.1063/1.2920489

[152] X. Wei, P. B. Miranda, C. Zhang, and Y. R. Shen, Sum-frequency spectroscopic studies of ice interfaces. *Phys. Rev. B*, **66**(8):085401, 2002, DOI:10.1103/PhysRevB.66.085401

[153] H. Groenzin, I. Li, V. Buch, and M. J. Shultz, The single-crystal, basal face of ice I_h investigated with sum frequency generation. *J. Chem. Phys.*, **127**(21):214502, 2007, DOI:10.1063/1.2801642

[154] I. Li Barnett, H. Groenzin, and M. J. Shultz, Hydrogen bonding in the hexagonal ice surface. *J. Phys. Chem. A*, **115**(23):6039–6045, 2011, DOI:10.1021/jp110431j

[155] P. J. Bisson and M. J. Shultz, Hydrogen bonding in the prism face of ice Ih via sum frequency vibrational spectroscopy. *J. Phys. Chem. A*, **117**(29):6116–6125, 2013, DOI: 10.1021/jp400129f

[156] D. S. Roos, Rapid production of single crystals of ice. *J. Glaciol.*, **14**(71):975, 1975, DOI:10.3198/1975jog14-71-325-328

[157] L. Fu, S.-L. Chen, and H.-F. Wang, Validation of spectra and phase in sub-1 cm^{-1} resolution sum-frequency generation vibrational spectroscopy through internal heterodyne phase-resolved measurement. *J. Phys. Chem. B*, **120**(8):1579–1589, 2016, DOI: 10.1021/acs.jpcb.5b07780

[158] A. Y. Zasetsky, A. F. Khalizov, M. E. Earle, and J. J. Sloan, Frequency dependent complex refractive indices of supercooled liquid water and ice determined from aerosol extinction spectra. *J. Phys. Chem. A*, **109**(12):2760–2764, 2005, DOI:10.1021/jp044823c

[159] I. H. Malitson, Interspecimen comparison of the refractive index of fused silica. *J. Opt. Soc. Am.*, **55**(10):1205–1209, 1965, DOI:10.1364/JOSA.55.001205

[160] N. Bloembergen and P. S. Pershan, Light waves at the boundary of nonlinear media. *Phys. Rev.*, **128**(2):606–622, 1962, DOI:10.1103/PhysRev.128.606

[161] S. Sun, R. Liang, X. Xu, H. Zhu, Y. R. Shen, and C. Tian, Phase reference in phase-sensitive sum-frequency vibrational spectroscopy. *J. Chem. Phys.*, **144**(24):244711, 2016, DOI:10.1063/1.4954824

[162] X. Wei, S.-C. Hong, X. Zhuang, T. Goto, and Y. R. Shen, Nonlinear optical studies of liquid crystal alignment on a rubbed polyvinyl alcohol surface. *Phys. Rev. E*, **62**:5160–5172, 2000, DOI:10.1103/PhysRevE.62.5160

[163] S. Yamaguchi, K. Shiratori, A. Morita, and T. Tahara, Electric quadrupole contribution to the nonresonant background of sum frequency generation at air/liquid interfaces. *J. Chem. Phys.*, **134**(18):184705, 2011, DOI:10.1063/1.3586811

[164] J. R. Scherer and R. G. Snyder, Raman intensities of single crystal ice I_h. *J. Chem. Phys.*, **67**(11):4794–4811, 1977, DOI:10.1063/1.434683

[165] F. Li and J. L. Skinner, Infrared and Raman line shapes for ice Ih. II. H_2O and D_2O. *J. Chem. Phys.*, **133**(24):244504, 2010, DOI:10.1063/1.3516460

[166] M. S. Bergren and S. A. Rice, An improved analysis of the OH stretching region of the vibrational spectrum of ice Ih. *J. Chem. Phys.*, **77**:583–602, 1982, DOI:10.1063/1.443924

[167] L. Shi, S. M. Gruenbaum, and J. L. Skinner, Interpretation of IR and Raman line shapes for H_2O and D_2O ice Ih. *J. Phys. Chem. B*, **116**(47):13821–13830, 2012, DOI: 10.1021/jp3059239

[168] P. T. T. Wong and E. Whalley, Optical spectra of orientationally disordered crystal. V. Raman spectrum of ice Ih in the range 4000–350 cm^{-1}. *J. Chem. Phys.*, **62**(6):2418–2425, 1975, DOI:10.1063/1.430768

[169] M. J. Shultz, P. Bisson, H. Groenzin, and I. Li, Multiplexed polarization spectroscopy: Measuring surface hyperpolarizability orientation. *J. Chem. Phys.*, **133**(5):054702, 2010, DOI:10.1063/1.3463449

[170] Y.-C. Wen, S. Zha, X. Liu, S. Yang, P. Guo, G. Shi, H. Fang, Y. R. Shen, and C. Tian, Unveiling microscopic structures of charged water interfaces by surface-specific vibrational spectroscopy. *Phys. Rev. Lett.*, **116**(1):016101, 2016, DOI:10.1103/PhysRevLett.116.016101

[171] Y. R. Shen, *Fundamentals of Sum-Frequency Spectroscopy*. Cambridge University Press, 2016, ISBN:978-1-107-09884-8

[172] Y. Nagata, T. Hasegawa, E. H. G. Backus, K. Usui, S. Yoshimune, T. Ohto, and M. Bonn, The surface roughness, but not the water molecular orientation varies with temperature at the water–air interface. *Phys. Chem. Chem. Phys.*, **17**(36):23559–23564, 2015, DOI:10.1039/C5CP04022A

[173] M. J. Shultz, P. Bisson, and T. H. Vu, Insights into hydrogen bonding via ice interfaces and isolated water. *J. Chem. Phys.*, **141**(18):18C521, 2014, DOI:10.1063/1.4896603

[174] T. Ishiyama, H. Takahashi, and A. Morita, Origin of vibrational spectroscopic response at ice surface. *J. Phys. Chem. Lett.*, **3**(20):3001–3006, 2012, DOI:10.1021/jz3012723

[175] T. Ishiyama and A. Morita, A direct evidence of vibrationally delocalized response at ice surface. *J. Chem. Phys.*, **141**(18):18C503, 2014, DOI:10.1063/1.4895547

[176] T. C. Sivakumar, D. Schuh, M. G. Sceats, and S. A. Rice, The 2500–4000 cm^{-1} Raman and infrared spectra of low density amorphous solid water and of polycrystalline ice I. *Chemical Physics Letters*, **48**(2):212–218, 1977, DOI:10.1016/0009-2614(77)80302-3

[177] C. L. Bishop, D. Pan, L. M. Liu, G. A. Tribello, A. Michaelides, E. G. Wang, and B. Slater, On thin ice: surface order and disorder during pre-melting. *Faraday Discuss.*, **141**:277–292, 2009, DOI:10.1039/B807377P

[178] Y. Furukawa, M. Yamamoto, and T. Kuroda, Ellipsometric study of the transition layer on the surface of an ice crystal. *J. Cryst. Growth*, **82**(4):665–677, 1987, DOI:10.1016/S0022-0248(87)80012-X

[179] V. Sadtchenko and G. E. Ewing, Interfacial melting of thin ice films: An infrared study. *J. Chem. Phys.*, **116**:4686, 2002, DOI:10.1063/1.1449947

[180] B. F. Henson, L. F. Voss, K. R. Wilson, and J. M. Robinson, Thermodynamic model of quasiliquid formation on H_2O ice: Comparison with experiment. *J. Chem. Phys.*, **123**(14):144707, 2005, DOI:10.1063/1.2056541

[181] H. H. G. Jellinek, Liquid-like (transition) layer on ice. *J. Colloid Interface Sci.*, **25**(2):192 – 205, 1967, DOI:10.1016/0021-9797(67)90022-7

[182] S. Barer, N. Churaev, B. Derjaguin, O. A. Kiseleva, and V. D. Sobolev, Viscosity of nonfreezing thin interlayers between the surfaces of ice and quartz. *J. Colloid Interface Sci.*, **74**(1):173–180, 1980, DOI:10.1016/0021-9797(80)90180-0

[183] N. V. Churaev, S. A. Bardasov, and V. D. Sobolev, On the non-freezing water interlayers between ice and a silica surface. *Colloids Surf., A*, **79**(1):11–24, 1993, DOI:10.1016/0927-7757(93)80155-8

[184] H. J. Butt, A. Döppenschmidt, G. Hüttl, E. Müller, and O. I. Vinogradova, Analysis of plastic deformation in atomic force microscopy: Application to ice. *J. Chem. Phys.*, **113**(3):1194–1203, 2000, DOI:10.1063/1.481898

[185] B. Pittenger, S. C. Fain, M. J. Cochran, J. M. K. Donev, B. E. Robertson, A. Szuchmacher, and R. M. Overney, Premelting at ice-solid interfaces studied via velocity-dependent indentation with force microscope tips. *Phys. Rev. B*, **63**:134102, 2001, DOI:10.1103/PhysRevB.63.134102

[186] M. P. Goertz, X.-Y. Zhu, and J. E. Houston, Exploring the liquid-like layer on the ice surface. *Langmuir*, **25**(12):6905–6908, 2009, DOI:10.1021/la9001994

[187] M. Elbaum, S. G. Lipson, and J. G. Dash, Optical study of surface melting on ice. *J. Cryst. Growth*, **129**(3):491–505, 1993, DOI:10.1016/0022-0248(93)90483-D

[188] A. Lied, H. Dosch, and J. H. Bilgram, Surface melting of ice I_h single crystals revealed by glancing angle X-ray scattering. *Phys. Rev. Lett.*, **72**(22):3554–3557, 1994, DOI:10.1103/PhysRevLett.72.3554

[189] H. Dosch, A. Lied, and J. Bilgram, Glancing-angle X-ray scattering studies of the premelting of ice surfaces. *Surf. Sci.*, **327**(1–2):145–164, 1995, DOI:10.1016/0039-6028(94)00801-9

[190] A. Döppenschmidt and H.-J. Butt, Measuring the thickness of the liquid-like layer on ice surfaces with atomic force microscopy. *Langmuir*, **16**(16):6709–6714, 2000, DOI:10.1021/la990799w

[191] H. Bluhm, D. F. Ogletree, C. S. Fadley, Z. Hussain, and M. Salmeron, The premelting of ice studied with photoelectron spectroscopy. *J. Phys.: Condens. Matter*, **14**(8):L227, 2002, DOI:10.1088/0953-8984/14/8/108

[192] M. R. Querry, D. M. Wieliczka, and D. J. Segelstein, Water (H_2O). In *Handbook of Optical Constants of Solids II* (edited by E. D. Palik), pp. 1059–1077, Academic Press, 1991, ISBN:0-12-544422-2

[193] G. L. Richmond, Molecular bonding and interactions at aqueous surfaces as probed by vibrational sum frequency spectroscopy. *Chem. Rev.*, **102**:2693–2724, 2002, DOI:10.1021/cr0006876

[194] Y. R. Shen and V. Ostroverkhov, Sum-frequency vibrational spectroscopy on water interfaces: Polar orientation of water molecules at interfaces. *Chem. Rev.*, **106**(4):1140–1154, 2006, DOI:10.1021/cr040377d

[195] B. M. Auer and J. L. Skinner, Vibrational sum-frequency spectroscopy of the liquid/vapor interface for dilute HOD in D_2O. *J. Chem. Phys.*, **129**(21):214705, 2008, DOI:10.1063/1.3012568

[196] J.-J. Max and C. Chapados, Isotope effects in liquid water by infrared spectroscopy. III. H_2O and D_2O spectra from 6000 to 0 cm^{-1}. *J. Chem. Phys.*, **131**(18):184505, 2009, DOI:10.1063/1.3258646

[197] S. Yamaguchi, Development of single-channel heterodyne-detected sum frequency generation spectroscopy and its application to the water/vapor interface. *J. Chem. Phys.*, **143**(3):034202, 2015, DOI:10.1063/1.4927067

[198] J. C. Duplan, L. Mahi, and J. L. Brunet, NMR determination of the equilibrium constant for the liquid H_2O–D_2O mixture. *Chem. Phys. Lett.*, **413**(4–6):400–403, 2005, DOI:10.1016/j.cplett.2005.07.005

[199] S. Nihonyanagi, T. Ishiyama, T.-k. Lee, S. Yamaguchi, M. Bonn, A. Morita, and T. Tahara, Unified molecular view of the air/water interface based on experimental and theoretical $\chi^{(2)}$ spectra of an isotopically diluted water surface. *J. Am. Chem. Soc.*, **133**(42):16875–16880, 2011, DOI:10.1021/ja2053754

[200] C. Tian and Y. Shen, Sum-frequency vibrational spectroscopic studies of water/vapor interfaces. *Chem. Phys. Lett.*, **470**(1–3):1–6, 2009, DOI:10.1016/j.cplett.2009.01.016

[201] Y. Ni and J. L. Skinner, Communication: Vibrational sum-frequency spectrum of the air-water interface, revisited. *J. Chem. Phys.*, **145**(3):031103, 2016, DOI:10.1063/1.4958967

[202] B. M. Auer and J. L. Skinner, Vibrational sum-frequency spectroscopy of the water liquid/vapor interface. *J. Phys. Chem. B*, **113**(13):4125–4130, 2009, DOI:10.1021/jp806644x

[203] Z. Zhang, L. Piatkowski, H. J. Bakker, and M. Bonn, Ultrafast vibrational energy transfer at the water/air interface revealed by two-dimensional surface vibrational spectroscopy. *Nat. Chem.*, **3**(11):888–893, 2011, DOI:10.1038/nchem.1158

[204] E. A. Raymond, T. L. Tarbuck, and G. L. Richmond, Isotopic dilution studies of the vapor/water interface as investigated by vibrational sum-frequency spectroscopy. *J. Phys. Chem. B*, **106**(11):2817–2820, 2002, DOI:10.1021/jp013967d

[205] E. A. Raymond, T. L. Tarbuck, M. G. Brown, and G. L. Richmond, Hydrogen-bonding interactions at the vapor/water interface investigated by vibrational sum-frequency spectroscopy of $HOD/H_2O/D_2O$ mixtures and molecular dynamics simulations. *J. Phys. Chem. B*, **107**(2):546–556, 2003, DOI:10.1021/jp021366w

[206] M. Sovago, R. K. Campen, G. W. H. Wurpel, M. Müller, H. J. Bakker, and M. Bonn, Vibrational response of hydrogen-bonded interfacial water is dominated by intramolecular coupling. *Phys. Rev. Lett.*, **100**(17):173901, 2008, DOI:10.1103/PhysRevLett.100.173901

[207] R. A. Livingstone, Y. Nagata, M. Bonn, and E. H. G. Backus, Two types of water at the water–surfactant interface revealed by time-resolved vibrational spectroscopy. *J. Am. Chem. Soc.*, **137**(47):14912–14919, 2015, DOI:10.1021/jacs.5b07845

[208] Q. Du, E. Freysz, and Y. R. Shen, Surface vibrational spectroscopic studies of hydrogen bonding and hydrophobicity. *Science*, **264**(5160):826–828, 1994, DOI:10.1126/science.264.5160.826

[209] D. E. Gragson and G. L. Richmond, Investigations of the structure and hydrogen bonding of water molecules at liquid surfaces by vibrational sum frequency spectroscopy. *J. Phys. Chem. B*, **102**(20):3847–3861, 1998, DOI:10.1021/jp9806011

[210] S. Nihonyanagi, S. Yamaguchi, and T. Tahara, Water hydrogen bond structure near highly charged interfaces is not like ice. *J. Am. Chem. Soc.*, **132**(20):6867–6869, 2010, DOI:10.1021/ja910914g

[211] K.-i. Inoue, S. Nihonyanagi, P. C. Singh, S. Yamaguchi, and T. Tahara, 2D heterodyne-detected sum frequency generation study on the ultrafast vibrational dynamics of H_2O and HOD water at charged interfaces. *J. Chem. Phys.*, **142**(21):212431, 2015, DOI:10.1063/1.4918644

[212] B. M. Degner, C. Chung, V. Schlegel, R. Hutkins, and D. J. McClements, Factors influencing the freeze-thaw stability of emulsion-based foods. *Compr. Rev. Food Sci. F.*, **13**(2):98–113, 2014, DOI:10.1111/1541-4337.12050

[213] S. Arima, S. Ueno, A. Ogawa, and K. Sato, Scanning microbeam small-angle X-ray diffraction study of interfacial heterogeneous crystallization of fat crystals in oil-in-water emulsion droplets. *Langmuir*, **25**(17):9777–9784, 2009, DOI:10.1021/la901115x

[214] D. J. McClements, Crystals and crystallization in oil-in-water emulsions: Implications for emulsion-based delivery systems. *Adv. Colloid Interface Sci.*, **174**(0):1–30, 2012, DOI:10.1016/j.cis.2012.03.002

[215] G. L. Cramp, A. M. Docking, S. Ghosh, and J. N. Coupland, On the stability of oil-in-water emulsions to freezing. *Food Hydrocolloids*, **18**(6):899–905, 2004, DOI:10.1016/j.foodhyd.2003.10.007

[216] R. Montenegro, M. Antonietti, Y. Mastai, and K. Landfester, Crystallization in miniemulsion droplets. *J. Phys. Chem. B*, **107**(21):5088–5094, 2003, DOI:10.1021/jp0262057

[217] R. Montenegro and K. Landfester, Metastable and stable morphologies during crystallization of alkanes in miniemulsion droplets. *Langmuir*, **19**(15):5996–6003, 2003, DOI:10.1021/la027019v

[218] I. Gülseren and J. Coupland, The effect of emulsifier type and droplet size on phase transitions in emulsified even-numbered n-alkanes. *J. Am. Oil Chem. Soc.*, **84**(7):621–629, 2007, DOI:10.1007/s11746-007-1093-x

[219] I. Gülseren and J. N. Coupland, Surface melting in alkane emulsion droplets as affected by surfactant type. *J. Am. Oil Chem. Soc.*, **85**(5):413–419, 2008, DOI:10.1007/s11746-008-1216-z

[220] C. Lin, G. He, C. Dong, H. Liu, G. Xiao, and Y. Liu, Effect of oil phase transition on freeze/thaw-induced demulsification of water-in-oil emulsions. *Langmuir*, **24**(10):5291–5298, 2008, DOI:10.1021/la704079s

[221] E. Dickinson, D. J. McClements, and M. J. W. Povey, Ultrasonic investigation of the particle size dependence of crystallization in *n*-hexadecane-in-water emulsions. *J. Colloid Interface Sci.*, **142**(1):103–110, 1991, DOI:10.1016/0021-9797(91)90037-9

[222] D. J. McClements, E. Dickinson, S. R. Dungan, J. E. Kinsella, J. G. Ma, and M. J. W. Povey, Effect of emulsifier type on the crystallization kinetics of oil-in-water emulsions containing a mixture of solid and liquid droplets. *J. Colloid Interface Sci.*, **160**(2):293–297, 1993, DOI:10.1006/jcis.1993.1399

[223] E. Dickinson, F. J. Kruizinga, M. J. W. Povey, and M. van der Molen, Crystallization in oil-in-water emulsions containing liquid and solid droplets. *Colloids Surf., A*, **81**:273–279, 1993, DOI:10.1006/jcis.1993.1399

[224] D. J. McClements, S. R. Dungan, J. B. German, C. Simoneau, and J. E. Kinsella, Droplet size and emulsifier type affect crystallization and melting of hydrocarbon-in-water emulsions. *J. Food Sci.*, **58**(5):1148–1151, 1993, DOI:10.1111/j.1365-2621.1993.tb06135.x

[225] Y. Shinohara, N. Kawasaki, S. Ueno, I. Kobayashi, M. Nakajima, and Y. Amemiya, Observation of the transient rotator phase of *n*-hexadecane in emulsified droplets with time-resolved two-dimensional small- and wide-angle X-ray scattering. *Phys. Rev. Lett.*, **94**(9):097801, 2005, DOI:10.1103/PhysRevLett.94.097801

[226] Y. Shinohara, T. Takamizawa, S. Ueno, K. Sato, I. Kobayashi, M. Nakajima, and Y. Amemiya, Microbeam X-ray diffraction analysis of interfacial heterogeneous nucleation of *n*-hexadecane inside oil-in-water emulsion droplets. *Cryst. Growth Des.*, **8**(9):3123–3126, 2008, DOI:10.1021/cg701018x

[227] M. L. Schlossman and A. M. Tikhonov, Molecular ordering and phase behavior of surfactants at water-oil interfaces as probed by X-ray surface scattering. *Annu. Rev. Phys. Chem.*, **59**(1):153–177, 2008, DOI:10.1146/annurev.physchem.59.032607.093822

[228] V. Klang, N. B. Matsko, C. Valenta, and F. Hofer, Electron microscopy of nanoemulsions: An essential tool for characterisation and stability assessment. *Micron*, **43**(2–3):85–103, 2012, DOI:10.1016/j.micron.2011.07.014

[229] J. Wang, H. Dubost, A. Ghalgaoui, W. Zheng, S. Carrez, A. Ouvrard, and B. Bourguignon, Effect of visible pulse shaping on the accuracy of relative intensity measurements in BBSFG vibrational spectroscopy. *Surf. Sci.*, **626**(0):26–39, 2014, DOI:10.1016/j.susc.2014.03.017

[230] T. Delmas, H. Piraux, A.-C. Couffin, I. Texier, F. Vinet, P. Poulin, M. E. Cates, and J. Bibette, How to prepare and stabilize very small nanoemulsions. *Langmuir*, **27**(5):1683–1692, 2011, DOI:10.1021/la104221q

[231] N. Michel, A.-S. Fabiano, A. Polidori, R. Jack, and B. Pucci, Determination of phase transition temperatures of lipids by light scattering. *Chem. Phys. Lipids*, **139**(1):11–19, 2006, DOI:10.1016/j.chemphyslip.2005.09.003

[232] Y. M. S. Micheletto, N. P. da Silveira, D. M. Barboza, M. C. dos Santos, V. R. de Lima, F. C. Giacomelli, J. C. V. Martinez, T. E. A. Frizon, and A. G. Dal Bó, Investigation of self-association between new glycosurfactant *N*-acetyl-β-D-glucosaminyl-PEG-docosanate and soybean phosphatidylcholine into vesicles. *Colloids Surf., A*, **467**:166–172, 2015, DOI:10.1016/j.colsurfa.2014.11.052

[233] R. P. Sear, Nucleation: theory and applications to protein solutions and colloidal suspensions. *J. Phys.: Condens. Matter*, **19**(3):033101, 2007, DOI:10.1088/0953-8984/19/3/033101

[234] D. J. McClements, E. Dickinson, and M. J. W. Povey, Crystallization in hydrocarbon-in-water emulsions containing a mixture of solid and liquid droplets. *Chem. Phys. Lett.*, **172**(6):449–452, 1990, DOI:10.1016/0009-2614(90)80137-3

[235] Y. Chen, K. C. Jena, and S. Roke, From hydrophobic to hydrophilic: The structure and density of the hexadecane droplet / alkanol / water interface. *J. Phys. Chem. C*, **119**(31):17725–177.4, 2015, DOI:10.1021/acs.jpcc.5b04904

[236] R. A. MacPhail, H. L. Strauss, R. G. Snyder, and C. A. Elliger, C–H stretching modes and the structure of *n*-alkyl chains. 2. Long, all-trans chains. *J. Phys. Chem.*, **88**(3):334–341, 1984, DOI:10.1021/j150647a002

[237] G. Sefler, Q. Du, P. Miranda, and Y. Shen, Surface crystallization of liquid *n*-alkanes and alcohol monolayers studied by surface vibrational spectroscopy. *Chem. Phys. Lett.*, **235**(3–4):347–354, 1995, DOI:10.1016/0009-2614(95)00147-V

[238] E. Tyrode and J. Hedberg, A comparative study of the CD and CH stretching spectral regions of typical surfactants systems using VSFS: Orientation analysis of the terminal CH3 and CD3 groups. *J. Phys. Chem. C*, **116**(1):1080–1091, 2012, DOI:10.1021/jp210013g

[239] C. D. Bain, Sum-frequency vibrational spectroscopy of the solid/liquid interface. *J. Chem. Soc., Faraday Trans.*, **91**(9):1281–1296, 1995, DOI:10.1039/FT9959101281

[240] R. G. Snyder, H. L. Strauss, and C. A. Elliger, Carbon-hydrogen stretching modes and the structure of n-alkyl chains. 1. Long, disordered chains. *J. Phys. Chem.*, **86**(26):5145–5150, 1982, DOI:10.1021/j100223a018

[241] J. C. Conboy, M. C. Messmer, and G. L. Richmond, Effect of alkyl chain length on the conformation and order of simple ionic surfactants adsorbed at the D_2O/CCl_4 interface as studied by sum-frequency vibrational spectroscopy. *Langmuir*, **14**(23):6722–6727, 1998, DOI:10.1021/la980132u

[242] K. M. Wilkinson, L. Qunfang, and C. D. Bain, Freezing transitions in mixed surfactant/alkane monolayers at the air–solution interface. *Soft Matter*, **2**(1):66–76, 2006, DOI:10.1039/b511561b

[243] O. Esenturk and R. A. Walker, Surface vibrational structure at alkane liquid/vapor interfaces. *J. Chem. Phys.*, **125**(17):174701, 2006, DOI:10.1063/1.2356858

[244] A. M. Taggart, F. Voogt, G. Clydesdale, and K. J. Roberts, An examination of the nucleation kinetics of *n*-alkanes in the homologous series $C_{13}H_{28}$ to $C_{32}H_{66}$, and their relationship to structural type, associated with crystallization from stagnant melts. *Langmuir*, **12**(23):5722–5728, 1996, DOI:10.1021/la9600816

[245] P. Espeau, L. Roblès, D. Mondieig, Y. Haget, M. A. Cuevas-Diarte, and H. A. J. Oonk, Mise au point sur le comportement énergétique et cristallographique des n-alcanes I. Série de C_8H_{18} à $C_{21}H_{44}$. *J. Chim. Phys.*, **93**(7–8):1217–1238, 1996

[246] X.-Y. Liu and P. Bennema, On the morphology of crystals of triclinic even normal alkanes: theory and observation. *J. Cryst. Growth*, **135**(1–2):209–223, 1994, DOI:10.1016/0022-0248(94)90743-9

[247] A. G. F. de Beer, H. B. de Aguiar, J. F. W. Nijsen, and S. Roke, Detection of buried microstructures by nonlinear light scattering spectroscopy. *Phys. Rev. Lett.*, **102**(9):095502, 2009, DOI:10.1103/PhysRevLett.102.095502

[248] K. Nanjundiah and A. Dhinojwala, Confinement-induced ordering of alkanes between an elastomer and a solid surface. *Phys. Rev. Lett.*, **95**(15):154301, 2005, DOI:10.1103/PhysRevLett.95.154301

[249] H. Saito, A. Kawagishi, M. Tanaka, T. Tanimoto, S. Okada, H. Komatsu, and T. Handa, Coalescence of lipid emulsions in floating and freeze–thawing processes: Examination of the coalescence transition state theory. *J. Colloid Interface Sci.*, **219**(1):129–134, 1999, DOI:10.1006/jcis.1999.6452

[250] J. I. Dadap, H. B. de Aguiar, and S. Roke, Nonlinear light scattering from clusters and single particles. *J. Chem. Phys.*, **130**(21):214710, 2009, DOI:10.1063/1.3141383

[251] A. A. Schaerer, C. J. Busso, A. E. Smith, and L. B. Skinner, Properties of pure normal alkanes in the c_{17} to c_{36} range. *J. Am. Chem. Soc.*, **77**(7):2017–2019, 1955, DOI:10.1021/ja01612a097

[252] D. M. Small, *The Physical Chemistry of Lipids: From Alkanes to Phospholipids. Handbook of Lipid Res. 4*. Plenum Press, 1986, ISBN:0-306-41763-4

[253] G. de Leeuw, E. L. Andreas, M. D. Anguelova, C. W. Fairall, E. R. Lewis, C. O'Dowd, M. Schulz, and S. E. Schwartz, Production flux of sea spray aerosol. *Rev. Geophys.*, **49**(2):RG2001, 2011, DOI:10.1029/2010RG000349

[254] A. Putnis, Why mineral interfaces matter. *Science*, **343**(6178):1441–1442, 2014, DOI:10.1126/science.1250884

[255] D. Chandler, Interfaces and the driving force of hydrophobic assembly. *Nature*, **437**(7059):640–647, 2005, DOI:10.1038/nature04162

[256] L. Zhang, K. Chen, B. Chen, J. L. White, and D. E. Resasco, Factors that determine zeolite stability in hot liquid water. *J. Am. Chem. Soc.*, **137**(36):11810–11819, 2015, DOI:10.1021/jacs.5b07398

[257] H. J. Dyson, P. E. Wright, and H. A. Scheraga, The role of hydrophobic interactions in initiation and propagation of protein folding. *Proc. Natl. Acad. Sci. USA*, **103**(35):13057–13061, 2006, DOI:10.1073/pnas.0605504103

[258] P. Ball, Water as an active constituent in cell biology. *Chem. Rev.*, **108**(1):74–108, 2008, DOI:10.1021/cr068037a

[259] D. T. F. Möhlmann, Are nanometric films of liquid undercooled interfacial water biorelevant? *Cryobiology*, **58**(3):256–261, 2009, DOI:10.1016/j.cryobiol.2009.01.004

[260] E. Amstad, S.-H. Kim, and D. A. Weitz, Photo- and thermoresponsive polymersomes for triggered release. *Angew. Chem. Int. Ed.*, **124**(50):12667–12671, 2012, DOI:10.1002/ange.201206531

[261] C. M. Johnson and S. Baldelli, Vibrational sum frequency spectroscopy studies of the influence of solutes and phospholipids at vapor/water interfaces relevant to biological and environmental systems. *Chem. Rev.*, **114**(17):8416–8446, 2014, DOI:10.1021/cr4004902

[262] C. L. McFearin, D. K. Beaman, F. G. Moore, and G. L. Richmond, From Franklin to today: Toward a molecular level understanding of bonding and adsorption at the oil–water interface. *J. Phys. Chem. C*, **113**(4):1171–1188, 2009, DOI:10.1021/jp808212m

[263] M. Bonn, Y. Nagata, and E. H. G. Backus, Molecular structure and dynamics of water at the water–air interface studied with surface-specific vibrational spectroscopy. *Angew. Chem. Int. Ed.*, **54**(19):5560–5576, 2015, DOI:10.1002/anie.201411188

[264] J. G. Davis, K. P. Gierszal, P. Wang, and D. Ben-Amotz, Water structural transformation at molecular hydrophobic interfaces. *Nature*, **491**(7425):582–585, 2012, DOI:10.1038/nature11570

[265] A. Tuntomo, C. L. Tien, and S. H. Park, Optical constants of liquid hydrocarbon fuels. *Combust. Sci. Technol.*, **84**(1–6):133–140, 1992, DOI:10.1080/00102209208951849

[266] J. E. Bertie, M. K. Ahmed, and H. H. Eysel, Infrared intensities of liquids. 5. Optical and dielectric constants, integrated intensities, and dipole moment derivatives of H_2O and D_2O at 22 °C. *J. Phys. Chem.*, **93**:2210–2218, 1989, DOI:10.1021/j100343a008

[267] S. Strazdaite, J. Versluis, E. H. G. Backus, and H. J. Bakker, Enhanced ordering of water at hydrophobic surfaces. *J. Chem. Phys.*, **140**(5):054711, 2014, DOI:10.1063/1.4863558

[268] E. Tyrode and J. F. D. Liljeblad, Water structure next to ordered and disordered hydrophobic silane monolayers: A vibrational sum frequency spectroscopy study. *J. Phys. Chem. C*, **117**(4):1780–1790, 2013, DOI:10.1021/jp310732f

[269] S. Strazdaite, J. Versluis, and H. J. Bakker, Water orientation at hydrophobic interfaces. *J. Chem. Phys.*, **143**(8):084708, 2015, DOI:10.1063/1.4929905

[270] P. Stöckel, I. M. Weidinger, H. Baumgärtel, and T. Leisner, Rates of homogeneous ice nucleation in levitated H_2O and D_2O droplets. *J. Phys. Chem. A*, **109**(11):2540–2546, 2005, DOI:10.1021/jp047665y

[271] H. S. Frank and M. W. Evans, Free volume and entropy in condensed systems III. Entropy in binary liquid mixtures; Partial molal entropy in dilute solutions; Structure and thermodynamics in aqueous electrolytes. *J. Chem. Phys.*, **13**(11):507–532, 1945, DOI:10.1063/1.1723985

[272] D. N. Glew, Aqueous solubility and the gas-hydrates. The methane–water system. *J. Phys. Chem.*, **66**(4):605–609, 1962, DOI:10.1021/j100810a008

[273] P. Aryal, F. Abd-Wahab, G. Bucci, M. S. P. Sansom, and S. J. Tucker, A hydrophobic barrier deep within the inner pore of the TWIK-1 K2P potassium channel. *Nat. Commun.*, **5**:4377, 2014, DOI:10.1038/ncomms5377

[274] A. Ehringhaus, Beiträge zur Kenntnis der Dispersion der Doppelbrechung einiger Kristalle. *N. Jb. Min. Geol. Paläont. Abt. B.*, **41**:342–419, 1917

[275] H. W. Fairbairn, *Structural petrology of deformed rocks*. Addison-Wesley, 1954, ISBN:1-114-77882-6

[276] C. C. Langway, Jr., *Ice fabrics and the universal stage*. Technical Report 62, U. S. Army Snow Ice and Permafrost Research Establishment, 1958

[277] H. Groenzin, *Sum-frequency studies of single crystalline ice I_h*. Ph.D. thesis, Tufts University, 2007

[278] P. Mohr, D. B. Newell, and B. N. Taylor, CODATA recommended values of the fundamental physical constants: 2014. arXiv:1507.07956 [physics.atom-ph]

Summary

Water is an extraordinary substance. It owes its characteristic anomalous properties to a network of strong hydrogen bonds present between water molecules. Ice is frozen water. In bulk ice, water molecules hold regular positions in the crystal. Nevertheless, the behaviour of ice can be dynamic and exciting, especially at the surface. At temperatures well below bulk melting, the surface of ice is covered by a liquid premelted layer. This water layer governs many geophysical processes and may be a significant factor in the low friction of ice.

This thesis describes the properties of ice and related systems at the molecular level. For this purpose we employ a variety of spectroscopic techniques and make use of stretching vibrations as sensitive probes of the molecular structure. The position, amplitude, and width of the stretching bands are utilized to describe the molecular properties and structure. The scientific insights from these studies are summarized below.

As a first experiment, we study the dissipation of vibrational energy using pump–probe spectroscopy. An intense pump pulse resonantly excites OD stretches of dilute HDO molecules and the population dynamics are probed using a time-delayed probe pulse. In ice we find the dissipation of the vibrational energy to decelerate with increasing temperature. The vibrational lifetime is observed to increase from 480 ± 40 fs at 25 K to 860 ± 60 fs at 265 K. These lifetimes are remarkably shorter than the vibrational lifetime in the liquid phase, which has a value of 1.7 ± 0.1 ps at 274 K and increases to 2.24 ± 0.09 ps at 343 K. The increase in vibrational lifetime with temperature is quite unusual because the vibrational lifetime generally decreases with temperature.

We also investigate the vibrational lifetime of similar water molecules in a hydrated lithium nitrate crystal. The crystal water contains OD groups with three distinct hydrogen bonds. The vibrational lifetime of the three hydrogen-bonded species is observed to increase with decreasing hydrogen-bond strength. Furthermore, the vibrational lifetime is found to decrease with temperature, which is qualitatively the opposite to the observed behaviour in ice.

The observed temperature dependencies can be well explained from a relaxation mechanism in which the OD vibration relaxes via energy transfer to a combination tone involving a bending mode of HDO or H_2O. The vibrational lifetime are determined by the spectral overlap of the OD stretching mode and the acceptor mode. For ice, the spectral overlap decreases when temperature increases. For the OD stretching modes in hydrated lithium nitrate, the opposite holds and the spectral overlap increases with temperature. The frequency dependence of the spectral overlap also explains the differences in vibrational lifetime of the OD vibrations. The OD modes with strong hydrogen bonds have better spectral overlap with the acceptor mode than the OD modes with

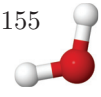

weak hydrogen bonds, hence the vibrational lifetime is observed to increase with decreasing hydrogen-bond strength.

The surface structures of ice and liquid water are studied using phase-resolved sum-frequency generation spectroscopy. In this technique a broad-band infrared pulse is overlapped at the surface with a visible pulse to generate sum-frequency light. The efficiency of this light-conversion process is strongly enhanced when the infrared light is resonant with a surface vibration. The spectral response is used to characterize the molecular surface structure of basal ice. At 150 K we observe 7 modes in the sum-frequency spectrum, of which 2 modes are absent in the bulk. These 2 modes are assigned to the outermost water molecules with an incomplete hydrogen-bond configuration. When increasing the temperature we find the crystalline surface to become disordered above ~185 K. At temperatures starting from 245 K we observe the surface of ice to be covered by a layer of liquid water, i.e. the hydrogen bonds of this premelted layer are indistinguishable from supercooled water.

In another experiment we study the extent of resonant molecular coupling towards the surfaces of ice and liquid water using isotope substitution. For isotopically dilute HDO in D_2O, the OH stretch vibration is effectively uncoupled from the surrounding OD oscillators owing to the frequency mismatch. The sum-frequency spectra of isotopically diluted ice and H_2O ice at 245 K strongly differ. This indicates that the OH stretches at the surface of H_2O ice are strongly influenced by intermolecular couplings, which leads to a delocalization of the vibrations. For liquid water, the difference between the surface spectra of neat and isotopically diluted water is found to be much smaller. The intermolecular coupling of the H_2O vibrations at the surface of liquid water is thus concluded to be smaller in comparison with the bulk, resulting in localized vibrations. The OH stretch vibrations are thus found to be much more delocalized at the surface of H_2O ice than at the surface of liquid H_2O. This is explained from a difference in surface order. The surface of ice is highly ordered and the homogeneity of the hydrogen-bond network leads to a large delocalization of the vibrations. The surface of liquid water is more disordered and the resulting heterogeneity of the hydrogen-bond strengths leads to a localization of the vibrations. Furthermore, for isotopically diluted liquid water and ice the surface spectra bear a striking similarity with the corresponding bulk spectra. This implies that the hydrogen-bond strengths at the surface of both liquid water and ice to resemble the bulk values.

Finally, we employ sum-frequency scattering spectroscopy to study the surface structure of nanoscopic water and oil droplets in emulsion. In this technique the infrared and visible pulses generate sum-frequency photons all around the droplets' surface. The scattered sum-frequency photons yield a spectrum of the vibrations at the water–oil interface. We investigate the effect of freezing of the constituents on the interfacial structure of oil-in-water emulsions. The freezing of oil is observed to lead to deviations from the spherical shape of liquid oil droplets. The freezing of the water matrix leads to a strong distortion of the oil droplets in case the oil is liquid, but has little effect on frozen oil particles.

In a final experiment we characterize the surface structure of water droplets

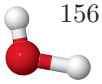

in oil. The hydrogen-bond network at the surface of water droplets is found to possess a much enhanced tetrahedral structure compared to a planar air–water interface. The increase is much larger than observed in previous studies of planar liquid hydrophobic–water interfaces. The observed spectral difference is similar to that of a planar air–water surface at a temperature that would be 60 K lower.

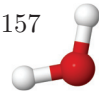

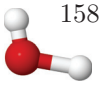

Samenvatting

Water is een fantastische substantie, helemaal als het bevroren is. Wat onmogelijk lijkt wordt mogelijk. Je kunt dan zowaar over water lopen. IJs is erg glad en het is nog leuker om erop te schaatsen! Waarom ijs zo glad is, is nog steeds niet helemaal goed begrepen. De afgelopen 150 jaar heeft een aantal grote natuurkundigen zich met deze vraag bezig gehouden. Het is duidelijk dat dit te maken moet hebben met een waterlaagje op ijs. Denk aan een stroeve keukenvloer die spekglad wordt als je er water op morst.

Gladheid heeft alles te maken met hoe oppervlakken over elkaar heen bewegen. Op een microscopische schaal zien de meeste oppervlakken eruit als schuurpapier, zelfs als ze er met het blote oog wél glad uit zien. De vele in elkaar hakende pieken en dalen verhinderen dat twee oppervlakken makkelijk over elkaar heen glijden. Het aanbrengen van een smeermiddel vermindert het contact en zorgt ervoor dat het glijden veel soepeler verloopt. IJs heeft van nature zo'n smeermiddel in zich, namelijk water. Er doen verschillende theorieën de ronde over de oorsprong van het laagje water op ijs.

Vaak wordt beweerd dat de druk van je schaats ervoor verantwoordelijk is dat het ijs een beetje smelt. Vloeibaar water is ruim 9 % compacter dan ijs, waardoor ijs onder druk zijn smeltpunt iets verlaagt. De druk van een schaats op het ijs leidt tot een smeltpuntverlaging van een paar tienden graad. In de praktijk blijkt het ook mogelijk te zijn om bij lagere temperaturen te schaatsen. Bovendien schiet ook iets lichts als een ijshockeypuck, zonder dat deze veel druk uitoefent, met groot gemak over het ijs. Naast de druk moeten er dus ook andere effecten een rol spelen.

Twee andere mechanismen bieden een betere verklaring. Daarvan is de meest geaccepteerde dat de beweging van je schaats over ijs een waterlaagje creëert. De wrijvingswarmte zorgt er namelijk voor dat er een dun laagje water smelt waar de schaats vervolgens zonder veel wrijving overheen kan glijden. Dit effect houdt zichzelf in stand: Indien het waterlaagje afwezig is, is er geen smering waardoor er veel wrijving is. Door de vrijgekomen wrijvingswarmte smelt het oppervlak van het ijs en ontstaat er een waterlaagje. Het betreft slechts een heel dun laagje, omdat ijs weinig wrijving geeft doordat het glad is en het smelten van ijs veel energie kost.

Daarnaast speelt een ander effect ook nog een rol. Ook zonder wrijvingswarmte kan ijs namelijk nat zijn. Het oppervlak van ijs is dat uit zichzelf al. Dat komt doordat de kristalstructuur van ijs aan het oppervlak ophoudt. Middenin het ijskristal worden de watermoleculen door andere moleculen op hun plek vastgehouden. Voor de moleculen aan de buitenkant geldt dit in mindere mate, waardoor deze moleculen beweeglijker zijn en er een soort waterlaagje ontstaat. De dikte van het waterlaagje is sterk afhankelijk van de temperatuur.

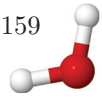

Hoe dichter de temperatuur bij 0 °C is, des te dikker is het waterlaagje. Het belang van dit laagje voor de gladheid van ijs is nog niet goed duidelijk. Dat komt mede doordat er nog weinig bekend is over de eigenschappen van het waterlaagje op het meest fundamentele niveau. In dit proefschrift gaan wij hier dieper op in. De geringe grootte van watermoleculen in combinatie met hun ultrasnelle dynamica maakt het uitdagend hier meer inzichten over te vergaren. Slechts enkele technieken zijn hiervoor geschikt.

In dit proefschrift hebben we de moleculaire eigenschappen van ijs onderzocht door naar trillingen van watermoleculen te kijken. Bij de paginanummers van dit proefschrift staan watermoleculen afgebeeld. Als je de pagina's snel omslaat zie je ze vibreren. De werkelijke vibraties zijn ontzettend snel. Je zou per seconde 1000000000000000 (10^{15}) pagina's moeten omslaan om de watermoleculen met hun werkelijke frequentie te zien vibreren. De precieze trillingsfrequentie wordt sterk beïnvloed door de configuratie van de watermoleculen. Zo is de strekfrequentie van watermoleculen in ijs lager dan in vloeibaar water. Dat komt doordat de onderlinge verbindingen van watermoleculen (zogeheten waterstofbruggen) in ijs sterker zijn dan in vloeibaar water.

De molecuulvibraties van water kunnen worden aangeslagen met behulp van licht. Daarvoor moet het licht wel de juiste trillingsfrequentie hebben, oftewel resonant zijn. Door vervolgens de frequentie en intensiteit van het licht te analyseren kunnen allerlei moleculaire eigenschappen worden afgeleid. Deze tak van wetenschap heet spectroscopie. In dit proefschrift hebben we met behulp van verscheidene spectroscopische technieken de moleculaire eigenschappen en structuur van ijs onderzocht.

Het oppervlak van ijs hebben we bestudeerd met behulp van somfrequentiegeneratie spectroscopie. Deze techniek maakt het mogelijk om alleen de vibraties van moleculen aan het oppervlak zichtbaar te maken, en niet de vibraties van moleculen die diep in de kristalstructuur zitten en in veel grotere getallen aanwezig zijn. Aan de hand van de gemeten oppervlaktevibraties hebben wij waargenomen dat er een waterlaagje aanwezig is aan het oppervlak van ijs, zelfs bij temperaturen ver onder het smeltpunt (−30 °C). Er blijkt geen verschil te zijn in de sterkte van de waterstofbruggen tussen de watermoleculen in het waterlaagje op ijs en aan het oppervlak van vloeibaar water bij eenzelfde temperatuur.

Naast het oppervlak van ijs hebben we ook het oppervlak bestudeerd van druppeltjes in emulsies, zowel van waterdruppeltjes in olie als van oliedruppeltjes in water. De watermoleculen aan het oppervlak van vloeibare waterdruppeltjes in olie blijken geordender te zijn dan watermoleculen aan een niet-gekromd oppervlak met lucht. Een dergelijk verschil nemen we niet waar indien de waterdruppeltjes in olie bevroren zijn en ze kleine ijskristallen vormen.

We hebben tevens het bevriezen van oliedruppeltjes in water onderzocht. Daarbij hebben we afzonderlijk zowel het bevriezen van de olie als het bevriezen van het omringende water onderzocht door het type olie te variëren. Een interessant aspect is daarbij dat olie krimt als het bevriest in tegenstelling tot water dat uitzet als het ijs wordt. Wij hebben gevonden dat het bevriezen van de oliedruppeltjes resulteert in een vervorming ten opzichte van de sferische symmetrie

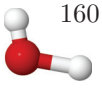

van vloeibare oliedruppeltjes. Het effect van het bevriezen van het omringende water op de oliedruppeltjes wordt sterk bepaald door de toestand waarin de oliedruppeltjes zich bevinden. Het bevriezen van het omringende water leidt tot sterke vervormingen van vloeibare oliedruppeltjes, maar heeft geen effect op reeds bevroren oliedruppeltjes.

Tenslotte hebben we in andere experimenten zuurstof–waterstof-vibraties bestudeerd van watermoleculen in een kristalrooster. Bij verschillende temperaturen hebben we gemeten hoe lang deze vibraties voortduren nadat ze zijn aangeslagen door een korte lichtflits. Dat hebben we gedaan voor zowel watermoleculen in ijs als voor watermoleculen opgesloten in een zoutkristal. Het blijkt dat de levensduur van de zuurstof–waterstof-vibraties in ijs en het zoutkristal een tegenovergesteld temperatuursverloop kennen; wanneer de temperatuur hoger wordt, neemt de levensduur van de watervibraties in ijs toe, terwijl de levensduur in het zoutkristal afneemt. In het algemeen wordt de levensduur van een vibratie bepaald door de mate waarin deze zijn energie kan overdragen. Op eenzelfde manier trilt een vrije gitaarsnaar veel langer dan wanneer je er een hand tegenaan legt. De vibraties van watermoleculen blijken hun energie beter over te kunnen dragen bij een toenemende sterkte van de waterstofbruggen. De sterkte van de waterstofbruggen hangt af van de configuratie van de watermoleculen. Het verschil in de configuratie tussen de watermoleculen in ijs en in het zoutkristal verklaart in beide gevallen het gevonden temperatuurverloop.

Met deze experimenten hebben we het begrip over de moleculaire eigenschappen van ijs vergroot. Het verhaal is echter nog niet af. Over veel eigenschappen bestaat nog onzekerheid en andere zijn nog onbekend. Door gebruik te maken van meer geavanceerde experimentele technieken zal het in de toekomst ook mogelijk zijn om de dynamica van watermoleculen aan het oppervlak van ijs te meten. Daarmee zullen we de bijzondere eigenschappen van ijs nog beter gaan begrijpen.

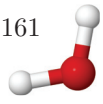

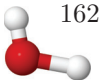

Acknowledgments

Experimental physics is the domain of teamwork and this thesis has been no exception. I am sincerely grateful for the support of many people, to some of which I would like to express my gratitude here.

First of all I would like to thank my promotor Huib Bakker. He is an outstanding scientist and has been an excellent mentor. I admire his great scientific knowledge and ability to quickly read problems, as well as his good-temper and his relaxed demeanour in spite of his always busy schedule. I deeply appreciate how he has been engaged in both the progress of my projects and my personal well-being. I felt greatly supported throughout my Ph.D., including during the difficult moments. We share a passion for cycling and I will never forget our encounter in the last bend of the ascent to Alpe d'Huez during La Marmotte.

Secondly, I would like to thank my co-promotor Mischa Bonn. We set up a fruitful collaboration studying the structure of ice when he moved to the Max Planck Institute for Polymer Research in Mainz just before the start of my time at AMOLF. I am grateful for his explanations on the principles of the sum-frequency generation technique. I would also like to acknowledge the experience on the growth of single crystal ice and feedback on data interpretation of Ellen Backus, Alejandra Sánchez, and Marc-Jan van Zadel in making this cooperation a success.

I thank Sylvie Roke and Nikolay Smolentsev at EPFL for their hospitality in welcoming me to their lab and for our successful collaboration on the freezing of emulsions. I would like to thank Nikolay for spending two weeks at AMOLF to teach me the ins and outs of sum-frequency scattering experiments and for preparing the emulsions.

I would like to express my gratitude to Yves Rezus, for being a great teacher and for taking the time to explain numerous aspects of spectroscopy. I am also grateful for his detailed reading of the manuscript and his constructive suggestions. I hope that one day we will settle on the rightful owner of that bottle of wine.

Hinco Schoenmaker has been indispensable for his technical support and I envy him for his creativity and skills in solving all kinds of practical problems. Dion Ursem has also greatly helped me out and has been of particular value to the growth of single crystal ice. I expect that the completion of my Ph.D. research will free up some time for the both of you!

The skills and experience of Jan Versluis with the laser setup have saved me a lot of time. I am also grateful for his input on the interpretation of data and for our fruitful discussions.

During the last four years, it has been a pleasure to have been surrounded

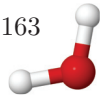

by the great and stimulating colleagues in the research groups of Huib and Yves with whom I have had many productive discussions and shared even more laughs. I want to thank them for the open atmosphere and their kind help: Oleg Selig generously shared his infrastructure on the data analysis of the 2D pump–probe measurements, Eliane and Roberto cooperated with enthusiasm in a caffeine project. I also thank my other fellow colleagues for their helpful insights and all good vibrations: Aleksandr, Artem, Bart, Biplab, Carien, Christina, Giulia, Harmen, Jiri, Janneke, Johannes, Konrad, Lianne, Liyuan, Maarten, Marcin, Niels, Niklas, Roel, Sietse, Simona, Stephan, and Wouter. Many thanks to you all!

In addition, I would like to thank Mark, Christiaan, and Benjamin for being friends as well as colleagues at AMOLF.

The AMOLF Institute is a fantastic place to perform scientific research. One of the foundations of this climate is the great willingness to help of all experts and craftsmen from the support departments. I would like to honour their fantastic contributions for extending the possibilities of my research and for making my life a lot easier. I acknowledge Dirk Jan, Henk-Jan, Iliya, and Ricardo for their numerous designs of custom-made mechanical equipment and for their help in creating compelling graphics. A big thank you as well to the colleagues from the mechanical workshop: Jan, Henk, Mark, Menno, Niels, Ricardo, Tom, Wim, and Wouter, for the fine pieces of craftsmanship they delivered. I enjoyed our work together and I am grateful for all advice and assistance in my personal projects. Duncan, Erik, Idsart, Jan and Ronald provided excellent electronics support. I want to thank Ivo and Sjoerd for their view on the data acquisition software. André, Carl, Richard, Rutger, and Wiebe are acknowledged for their IT service. I also thank Silvia from the library for finding even the most obscure books and articles for me.

I want to thank my paranimphs Martin Makkenze and Bram Bet for their readiness to assist me during my defence. Together with Martin I achieved the peak of my cycling adventures, making it from Amsterdam to Paris in one ride. Together with Bram, I look forward to the next adventure on Cuba.

I am grateful for the friends I made during my years of study in Utrecht and Zurich, and for how we have explored the world of physics together.

Finally, I want to thank my family and friends for their encouragements, as well as their interest and patience during my many mini-lectures and practical experiments. In particular I want to thank Renske who played a significant role in my life over the past few years. She helped me through all critical moments and proofread large parts of this thesis. I also want to thank my dear parents Mirjam & Cees, my brother Jochem, and my sister Marieke for their unconditional love and their unfaltering support along the paths I take.

Amsterdam, October 2016

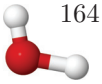

About the author

Wilbert Smit (Amsterdam, 4 June 1989) grew up in Hoofddorp and completed his secondary education at the KSH grammar school in 2007. He then studied Mathematics and Physics at Utrecht University and was awarded both his B.Sc. degrees cum laude in 2010. To pursue his Master's degree in Physics he subsequently moved to ETH Zurich. Wilbert spent the summer of 2011 at CERN, Geneva, working together with Dr. Werner Lustermann for the purposes of an internship. In 2012 he received his M.Sc. ETH in Physics, writing a theoretical dissertation in the field of solid-state physics under the supervision of Prof. Dr. Manfred Sigrist.

In 2012 Wilbert joined the group of Prof. Dr. Huib Bakker at the AMOLF Institute in Amsterdam to embark on his Ph.D. research employing ultrafast spectroscopy techniques to study ice, resulting in this thesis. His Ph.D. research projects on monocrystalline ice have been carried out in conjunction with the research group of Prof. Dr. Mischa Bonn at the Max Planck Institute for Polymer Research in Mainz. During his Ph.D. research, he also spent several weeks at the EPFL collaborating with Prof. Dr. Sylvie Roke to study the freezing behaviour of emulsions using sum-frequency scattering spectroscopy. Among other activities, in his free time Wilbert loves experiencing the slipperiness of ice on his ice skates.

Jaap Edenbaan, Amsterdam, 2013

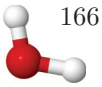

About the cover

The painter Hendrick Avercamp (1585–1634) was born in Amsterdam, but spent most of his live in the city of Kampen. Avercamp was mute and nicknamed 'de Stomme van Campen' (the Mute of Kampen). The absence of his sense of hearing likely strengthened his other senses. The many details in his paintings are signs of a sharp sight and a watchful eye. His life coincided with an exceptionally cold period with severe and long winters, known as the Little Ice Age. Winter was a harsh time, but the ice and snow also brought many opportunities for leisure, which he captured in his art. The winter scene on the cover of this thesis shows a crowded frozen lake where people of all walks of life have congregated. Avercamp shows us the many social interactions and activities on the ice. We find people engaged in conversation, playing a game of colf, dancing on their skates, as well as carrying out their normal day-to-day activities on and around the ice. The winter scene contains many anecdotal elements. Try to spot the following details:

- ☐ Someone who fell through the ice
- ☐ An eel fisher bringing home his catch
- ☐ An elderly lady, begging
- ☐ A person slipping
- ☐ A man urinating
- ☐ A couple stealing a kiss
- ☐ A birdhouse
- ☐ A bird trap
- ☐ Two pairs of buttocks
- ☐ A greyhound
- ☐ Graffiti
- ☐ An iceboat sailing

Hendrick Avercamp, *Winter Landscape with Ice Skaters*, circa 1608